

LA TROBE UNIVERSITY

MASTERS THESIS

Wavefront Propagation Simulation of X-ray Interference Nanolithography

Author:

Jerome KNAPPETT

Supervisor:

Dr. Grant VAN RIESSEN

Co-Supervisor:

Dr. David HOXLEY

Co-Supervisor:

Prof. Brian ABBEY

A thesis submitted in fulfilment of the requirements for the degree of

Masters of Science

November 5, 2021

Declaration of Authorship

I, Jerome KNAPPETT, declare that this thesis titled, "Wavefront Propagation Simulation of X-ray Interference Nanolithography" and the work presented in it are my own. I confirm that:

- This work was done wholly or mainly while in candidature for a degree at this University.
- Where any part of this thesis has previously been submitted for a degree or any other qualification at this University or any other institution, this has been clearly stated.
- Where I have consulted the published work of others, this is always clearly attributed.
- Where I have quoted from the work of others, the source is always given. With the exception of such quotations, this thesis is entirely my own work.
- I have acknowledged all main sources of help.
- Where the thesis is based on work done by myself jointly with others, I have made clear exactly what was done by others and what I have contributed myself.

Signed:

Date:

Abstract

Future extreme ultraviolet (EUV) lithography for high-volume manufacturing is expected to transition from 13.5 nm to 6.7 nm wavelength sources to keep pace with the demand for device scaling predicted by Moore's Law. However, there are many challenges that must be overcome as critical dimensions approach the single-digit nanometer scale. It has been widely recognized that these challenges include the availability of suitable light sources, and interrelated effects associated with the source properties and nanoscale mask roughness.

EUV interference lithography (EUV-IL) using synchrotron radiation has recently emerged as a powerful tool for understanding key aspects of the 6.7 nm lithographic process. An EUV-IL exposure and metrology instrument is currently in development for use at the coherent imaging branch of the SXR beamline of the Australian Synchrotron. The aim of this work was to construct a comprehensive model of the SXR beamline and proposed EUV-IL optics to evaluate the achievable lithographic performance at 6.7 nm wavelength, and thus to explore photomask design constraints.

A complete model of the undulator source and beamline optics was constructed using the Synchrotron Radiation Workshop physical optics code. The intensity distribution, coherence, and polarisation properties of a wavefront propagated from the source to the photomask plane, was evaluated with respect to the known properties and the requirements for 6.7 nm EUV-IL. The EUV-IL aerial image formation was simulated for a two-beam configuration using model photomasks based on binary gratings in transmission geometry. The aerial image intensity and contrast are shown to depend on the partial coherence of the illumination and the structure of the grating as expected from theory. It is further shown that while the model allowed control over the source polarisation, further work is required to simulate polarisation-dependent mask diffraction.

Finally, the model was used to study the effect of mask surface roughness on the quality of aerial images. Multiple quality metrics are evaluated for their sensitivity to the effects of roughness magnitude and roughness correlation length. The results of this study provide a basis for the optimization of source properties, mask design and lithography processes that will be applied at the SXR beamline.

Acknowledgements

A great debt of gratitude is owed to my supervisor Dr. Grant van Riessen, who has gone above and beyond his requirements to instruct me during these past two years. The work presented in this thesis would not have been possible without his efforts. My co-supervisors, Dr. David Hoxley and Prof. Brian Abbey, have both been a monumental aid in developing this thesis, and giving me a much-needed push when I was struggling for direction.

This work was supported by an Australian Government Research Training Program Scholarship.

Many thanks to Trey Guest, whose Masters thesis paved the way for this research project.

Thanks to Bruce Cowie, whose meticulous documentation of the Soft X-ray beamline gave me information I did not even know I needed.

Thanks to my fellow students, with whom I have spent days and nights studying or procrastinating. We did it. Our time is come. Let us dine.

Thank you to my family, Mum, Bill, Jamie, Frith, Caleb and Kezia. Thank you for your support. I wish we could have seen each other more over the last two years and I hope to make up for lost time.

Of course, thank you to my partner Octavia for putting up with being locked down with someone who is glued to a computer screen. Your continued support has been invaluable during this entire project. I cannot wait to celebrate with you.

*For my own future light source,
whose properties are yet to be determined.*

Contents

DECLARATION OF AUTHORSHIP	I
ABSTRACT	III
ACKNOWLEDGEMENTS	V
CHAPTER 1 INTRODUCTION & BACKGROUND	1
1.1 THE DEVELOPMENT OF SHORT-WAVELENGTH INTERFERENCE LITHOGRAPHY	1
1.2 THESIS OBJECTIVE AND OUTLINE.....	3
1.3 A NOTE ON CONTRIBUTIONS.....	4
CHAPTER 2 LITERATURE REVIEW	5
2.1 BEUV LITHOGRAPHY	5
2.2 INTERFERENCE LITHOGRAPHY	7
2.3 SYNCHROTRON RADIATION	9
2.3.1 <i>Undulator Radiation</i>	10
2.4 INTERFERENCE AND DIFFRACTION WITH PARTIALLY COHERENT LIGHT	13
2.4.1 <i>Coherence</i>	13
2.4.1.1 Partial Coherence.....	15
2.4.1.2 Interference Due to Partially Coherent Light.....	16
2.4.2 <i>Polarisation</i>	18
2.4.2.1 The Stokes Vector.....	20
2.4.2.2 Partial Polarisation	22
2.4.2.3 Interference & Polarisation.....	23
2.4.2.4 Polarisation & Interference Lithography.....	24
2.4.3 <i>Interaction at BEUV Wavelengths</i>	29
2.4.4 <i>Diffraction Efficiency</i>	30
2.5 COMPUTATIONAL LITHOGRAPHY	33
2.5.1 <i>Computational Wavefront Propagation</i>	35
2.5.2 <i>Partially Coherent Representations</i>	35
2.5.3 <i>Computational Requirements & Limitations</i>	36
CHAPTER 3 METHOD OF WAVEFRONT PROPAGATION AND AERIAL IMAGE QUALITY METRICS	39
3.1 WAVEFRONT PROPAGATION	39
3.1.1 <i>Discrete Fourier Sampling</i>	42
3.1.2 <i>Implementation of Wavefront Propagation</i>	44
3.1.3 <i>Partially Coherent Propagation</i>	47
3.2 POLARISATION.....	49
3.3 PHOTOMASK SURFACE ROUGHNESS	50
3.4 AERIAL IMAGE EVALUATION AND QUALITY METRICS.....	51
3.4.1 <i>Normalized Image Log-Slope</i>	52
3.4.2 <i>Line Edge and Line Width Roughness</i>	52
3.4.3 <i>Contrast</i>	54
3.4.3.1 Michelson Contrast	54
3.4.3.2 Root Mean Squared Contrast.....	54
3.4.3.3 Fourier Contrast	55
3.4.3.4 Integrated Optical Density.....	55
3.4.3.5 Mean Dynamic Range.....	56
3.5 VALIDATION OF CONTRAST AND QUALITY METRICS.....	57

CHAPTER 4 EXPERIMENTAL METHODS	61
4.1 INTRODUCTION	61
4.2 PROPOSED EUV-IL TECHNICAL DESIGN.....	62
4.3 THE SXR-I BEAMLINE	62
4.3.1 <i>Storage Ring & Electron Beam</i>	63
4.3.2 <i>APPLE II Undulator</i>	63
4.3.3 <i>Beamline Optics</i>	64
4.4 INTERFERENCE LITHOGRAPHY OPTICS	66
4.4.1 <i>Grating Mask Model</i>	66
4.4.1.1 Grating Representation.....	68
4.4.1.2 Absorber Surface Roughness.....	69
4.4.2 <i>Implementation</i>	70
4.4.3 <i>Diffraction Efficiency</i>	71
4.4.4 <i>Mask material properties</i>	72
4.4.5 <i>Mask Geometry and Aerial Image Distance</i>	73
4.4.6 <i>Summary</i>	75
CHAPTER 5 VALIDATION OF SOURCE, BEAMLINE AND MASK MODEL	77
5.1 INTRODUCTION	77
5.2 THE SOURCE	77
5.2.1 <i>Source Polarisation</i>	82
5.3 THE BEAMLINE	87
5.4 MASK ILLUMINATION	90
5.5 DIFFRACTION EFFICIENCY	92
5.6 PARTIAL COHERENCE	97
5.6.1 <i>The Effect of Secondary Source Size on Spatial Coherence</i>	100
5.7 SUMMARY	104
CHAPTER 6 SOURCE AND MASK EFFECTS ON AERIAL IMAGE QUALITY	106
6.1 INTRODUCTION	106
6.2 AERIAL IMAGE FORMATION	106
6.2.1 <i>Effect of Photon Block Diffraction</i>	109
6.3 EFFECT OF PARTIAL COHERENCE AND POLARISATION ON AERIAL IMAGE FORMATION	112
6.3.1 <i>Partially Coherent Aerial Image Formation</i>	113
6.3.1.1 <i>The Effect of Source Polarisation on Aerial Image Contrast</i>	115
6.3.1.1.1 Effect of Polarisation and Grating Pitch.....	116
6.3.1.1.2 Partially Coherent Propagation and Polarisation	118
6.3.2 <i>Aerial Image Contrast and Source Properties</i>	121
6.4 EFFECT OF MASK PROPERTIES ON AERIAL IMAGE	122
6.4.1 <i>Partially Coherent Illumination of Rough Masks</i>	123
6.4.1.1 Qualitative Description of Aerial Images.....	124
6.4.1.2 Quantitative Description of Aerial Images.....	128
6.4.2 <i>Aerial Image Quality Metrics and Roughness</i>	131
6.5 DISCUSSION	132
CHAPTER 7 CONCLUSION.....	137
7.1 FUTURE WORK	139

List of Abbreviations

- BDA – Beam Defining Aperture
BEUV – Beyond Extreme Ultraviolet
BEUV-IL – Beyond Extreme Ultraviolet Interference Lithography
CWT – Coupled Wave Theory
DFT – Discrete Fourier Transform
DUV – Deep Ultraviolet
EUV – Extreme Ultraviolet
EUV-IL – Extreme Ultraviolet Interference Lithography
EUVL – Extreme Ultraviolet Lithography
FFT – Fast Fourier Transform
FTAM – Fourier Transfer Alignment Method
HVM – High Volume Manufacturing
IC – Integrated Circuit
IL – Interference Lithography
IRDS – International Roadmap for Devices and Systems
LPP – Laser Produced Plasma
LER – Line Edge Roughness
LWR – Line Width Roughness
NEXAFS – Near Edge X-Ray Absorption Fine Structure
NILS – Normalised Intensity Log-Slope
OPP – Optical Projection Printing
PGM – Planar Grating Monochromator
RCWA – Rigorous Coupled Wave Analysis
RMS – Root Mean Squared
SEM – Scanning Electron Microscopy
SRW – Synchrotron Radiation Workshop
SSA – Secondary Source Aperture
SXR – Soft X-ray
SXR-I – Soft X-ray Imaging
WBS – White Beam Slits
XRNF – X-ray Nanofabrication Facility
YDS – Young's Double Slit

Chapter 1

Introduction & Background

1.1 The Development of Short-Wavelength Interference Lithography

Moore's Law states that the level of integrated circuit (IC) complexity that can be manufactured for minimal cost is an exponential function of time, and the minimal cost of manufacturing an IC decreases at an almost inversely proportional rate with respect to time. These two statements mean the cost of making any IC at optimal transistor density levels remains essentially constant in time whilst the complexity doubles [1]. Moore's law is the main driver of growth in the semiconductor industry. The single most important factor in the advancement of Moore's law is the steady improvement of lithography techniques [2].

Photolithography is a process used to pattern ICs. The practice involves transferring an image to a photosensitive material. The term lithography comes from the Greek 'lithos' and 'grapho', meaning stone and to write, respectively; the 'stone' in the case of photolithography is typically a photosensitive resist and the 'writing' is a complex intensity pattern [3]. High-Volume Manufacturing (HVM) of ICs is currently undertaken using Projection Lithography or Optical Projection Printing (OPP) implementing deep ultraviolet (DUV) and more recently extreme ultraviolet (EUV) radiation.

In OPP, a patterned mask is illuminated using partially coherent light (Figure 1.1.1). The scattered light is then collected and refocused by projection optics which demagnifies the pattern and projects it onto a photoresist wafer [4,5]. Interference Lithography (IL) creates a standing wave intensity pattern by coherently illuminating a diffraction grating (Figure 1.1.1). The resulting interference intensity pattern at the image plane (aerial image) is then transferred to a photoresist film [6]. IL is not currently applied to IC fabrication as it cannot meet the HVM throughput requirement of 100 wafers patterned per hour and it is

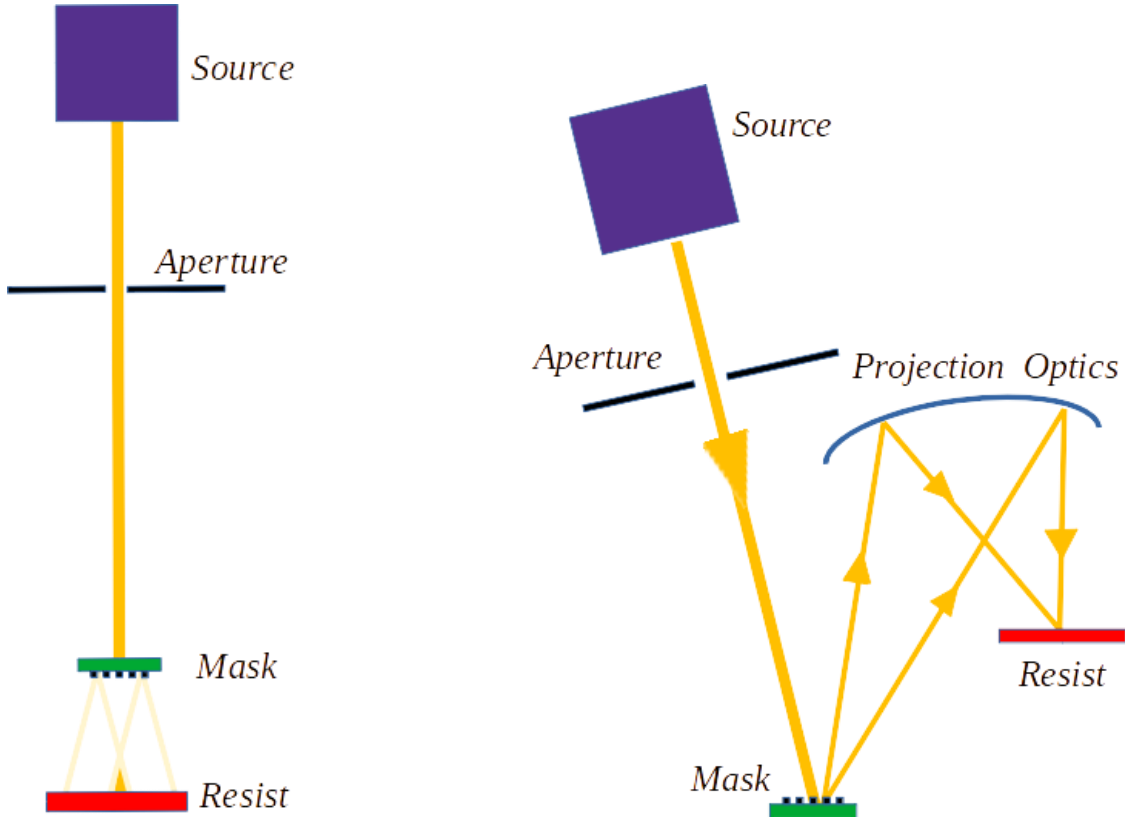


Figure 1.1.1: Simplified layouts of different photolithography geometries. Each diagram shows only essential elements and omits focusing optics. (LEFT): An interference lithography system. The aperture controls spatial coherence of the illumination. Light passing through the mask is diffracted, forming interference fringes at the aerial image plane. (RIGHT): A projection lithography system. The aperture controls the spatial coherence of the illumination. Light passing through the mask is refocused and demagnified by the projection optics onto the aerial image plane. Reflective optics are used due to lack of suitable material for refractive optics at EUV wavelengths.

limited to producing periodic patterns. However, IL is widely used in a research capacity [7], as a means to evaluate and refine the lithography process.

Device scaling in the semiconductor industry is driven primarily by reductions of patternable feature size in lithography processes, which are due largely to a move to smaller wavelength sources [8]. The progression of feature size from the 500 nm node to 350 nm and then to 90 nm and 32 nm nodes has been propelled by the progress of sources in the visible (365 nm) to Deep Ultra-Violet (DUV) (248 – 157 nm) and onto Extreme Ultra-Violet (EUV) (13.5 nm) spectra [9]. As of 2019 EUV Lithography (EUVL) is used for HVM of advanced semiconductor chips. Synchrotron radiation sources are not used for commercial implementation of EUVL, but they do play an essential part in research and development [10–14].

EUV lithography will eventually hit its resolution limit, set by the diffraction of light with the highest feasible numerical aperture [6]. In order to keep pace with Moore's law and to meet the 3.5 nm technology node defined by the International Roadmap for Devices and Systems (IRDS) a move to smaller wavelength sources will be necessary [9]. The wavelength chosen for lithography beyond 13.5 nm is 6.x nm which resides in the Beyond EUV (BEUV) regime [15]. This choice is reinforced by the fact that BEUV and EUV resists have similar radiation chemistry. This means that effects occurring at shorter wavelengths (such as the long mean-free-path of secondary electrons) can be controlled in a similar manner [6].

The scarcity of suitable EUV sources for IL means that computational modelling of the EUV-IL process has taken on a larger role in research and development. Accurate simulations of the IL process at EUV wavelengths can inform the technical design of sources for EUV-IL. The properties of materials at EUV and BEUV wavelengths can be critically evaluated and the effects of source and mask properties on the generation of interference fringes can be more thoroughly understood.

1.2 Thesis Objective and Outline

This thesis will provide a pathway for the implementation of an IL research capability at the Australian Synchrotron through the construction of an in-depth computational model of the Soft X-ray Imaging (SXR-I) beamline, focusing specifically on the propagation of a partially coherent wavefront through a model interference lithography mask. The new X-ray Nanofabrication Facility (XRNF) will be a short wavelength (BEUV) lithography end station at the SXR-I beamline at the Australian Synchrotron. The XRNF will allow for scalable, large-area manufacturing of sub-20 nm nano-structures and will be crucial in addressing the need for advanced HVM at sub-10 nm scale in the coming decade [16]. Accurate modelling of the beamline and lithographic image formation process is required to inform the technical design of the XRNF facility, grating-based photomasks and the lithography processes that will be implemented.

In this work the theory behind BEUV Interference Lithography will be outlined in Chapter 2, as well as the method of implementation of computational models of the process. Chapter 3 will explain wavefront propagation and the details of different methods of

contrast evaluation of the intensity of aerial images obtained from interference lithography. In Chapter 4 the experimental methods undertaken for this project are explained in detail, including the geometry of the beamline model and the interference grating masks generated for simulation. The source and beamline are validated in Chapter 5 as well as the ability of the model to accurately represent the process of BEUV interference lithography. Chapter 6 details the results of simulations of the effect of grating masks with modelled roughness on aerial image formation. Conclusions and recommendations for future work are given in Chapter 7.

1.3 A Note on Contributions

The simulations presented in this work made extensive use of code in the SRW library [17] and extensions provided by the Wavefront Propagation (WPG) [18] project. Custom codes developed by Grant van Riessen were used for batch processing of simulations. Custom code to generate grating masks and analyse aerial images were developed jointly by the author and Grant van Riessen. Construction, optimisation and use of the model using these codes was done by the author.

Chapter 2

Literature Review

2.1 BEUV Lithography

In 2009 the semiconductor industry announced that sources would be needed for future 6.x nm optical lithography [19]. The 6.7 nm wavelength was chosen as it meets requirements for available light sources and the reflectivity of multilayer optics[20]. However, reducing the wavelength from 13.5 nm (EUV) to 6.7 nm (BEUV) comes with difficulties. As incident wavelength decreases the peak and integrated reflection coefficients of mirrors decreases as well, which increases the challenges in developing suitable reflective optics and reflective masks for Optical Projection Printing (OPP) [21]. Line-edge roughness in photoresist patterning also increases when moving from EUV to BEUV, the cause of which is still to be clearly determined but may be a result of photon shot noise [22].

It has been recognised since the move from Deep Ultraviolet (DUV) to EUV sources that photomask defectivity is the most vital problem with short wavelength lithography. Small ‘phase defects’ in the form of distortions in the multilayer coating of materials have a non-negligible effect on the aerial image [23]. The wavelength dependence of the optical properties of material defects means it is difficult to predict the EUV and BEUV properties of a defect from measurements at DUV or longer wavelengths [24]. This is typically due to the lack of suitable EUV sources for mask evaluation. Even so, the benefits of a reduced wavelength will outweigh the difficulties as the resolution for lithography processes is dependent on wavelength. The Rayleigh equation gives the critical dimension of an image formed using an exposure tool with numerical aperture, NA as:

$$CD = \frac{k_1 \lambda}{NA}$$

2.1.1

where k_l is a constant factor depending primarily on the material properties of the resist and properties of the illumination. The total resolution blur of an image formed by a photoresist has been found to decrease when moving from EUV to BEUV [25]. Resolution blur is dependent on the blur caused by secondary electrons, $b_{electron}$, due to scattering, and the optical resolution blur, $b_{optical} = CD/2$. While $b_{optical}$ decreases with wavelength, $b_{electron}$ increases due to the increased energy of photoelectrons, and total resolution blur reaches a minimum for wavelengths around 3 – 5 nm [26]. Total resolution blur, b_i , is given by the relationship:

$$b_i = \sqrt{b_{optical}^2 + b_{electron}^2}. \quad 2.1.2$$

EUV to BEUV lithography sources for manufacturing and research are typically of two varieties; Laser Produced Plasma (LPP) sources and Synchrotron sources. LPP sources for generating radiation at 13.5 nm have typically used tin (Sn) droplets, which are excited by two laser pulses, the first to expand the droplet and the second, to create plasma and EUV light. For BEUV sources at 6.x nm, gadolinium and terbium (Gd and Tb) are the most suitable for high brightness as they produce strong resonant emissions at 6.5 – 6.7nm [15,27,28]. The strongest lines result from 4p-4f and 4p-4d emissions in the spectra of Ag (Gd XVII & Tb XIX) through Rh (Gd XX & Tb XXI) [19]. LPP sources are the most viable candidate for high volume manufacturing (HVM) [29], however there are various issues in the laser system design for LPP EUV to BEUV sources [30]. The biggest issue is the generation of debris which damages collector optics and limits the lifetime of optical systems [31]. For LPP sources, the conversion efficiency also decreases with wavelength, from 5% at 13.5 nm to 1.2 – 1.5% at 6.7 nm [27].

Synchrotron EUV to BEUV sources do not have these problems and have been used to advance Interference Lithography (IL) for research and development, particularly photoresist testing, characterisation and evaluation [12,32,33]. They have also been used to demonstrate the ability of IL to create high resolution, large-area nano-structures [13,34]. Synchrotron EUV radiation sources are of little interest to HVM due to cost and complexity. As materials used for focusing optics are highly absorbent at BEUV, any source used for lithography must have high brightness to achieve good lithographic performance.

The diffraction and interferometric techniques that Beyond Extreme Ultraviolet Interference Lithography (BEUV-IL) is based on require coherent illumination to achieve their ultimate resolution[27]. Undulators in use at synchrotrons are therefore a potential source, due to their narrow energy spectrum, high brightness, partial coherence and the ability to easily tune the wavelength of the emitted radiation[35]. As implied by Equations 2.1.1 & 2.1.2, a tuneable wavelength source allows for the exploration of wavelength for optimal resolution and consideration of the photochemistry of new resist technology.

2.2 Interference Lithography

Interference lithography is a popular tool for nanopatterning and lithography research and has been implemented successfully using synchrotron sources [36,37]. The simplicity of IL makes it ideal to study the interaction of EUV radiation with photoresists at a higher resolution than the scanners typically used for HVM. This makes it a powerful and relatively low-cost method for photoresist testing and evaluation [38–40]. The higher throughput of EUV to Soft X-Ray (SXR) IL compared to traditional lithographic techniques such as e-beam and laser IL, and its ability to exceed the resolution of projection lithography, makes it a perfect candidate for high resolution patterning [5,41]. The EUV-IL tool at the Swiss Light Source has been used to demonstrate patterning at 8 nm half-pitch [42].

In IL, light incident on a grating diffracts at multiple angles, θ_m , corresponding to orders, m , governed by the grating equation. For a monochromatic beam of wavelength, λ , incident at angle, θ_i , on a grating with period, p_G , the angle of diffraction of the m^{th} order beam is given by [43]:

$$\sin \theta_m = \frac{m\lambda}{p_G} + \sin \theta_i .$$

2.2.1

A typical IL grating mask contains multiple gratings that each result in diffracted beams of multiple orders. As shown in Figure 2.2.1, some of these beams will interfere at the image plane. The distance, z_0 , from the mask to the image plane for a particular order is given by the spacing between the gratings, d , and the diffraction angle θ_m [43]:

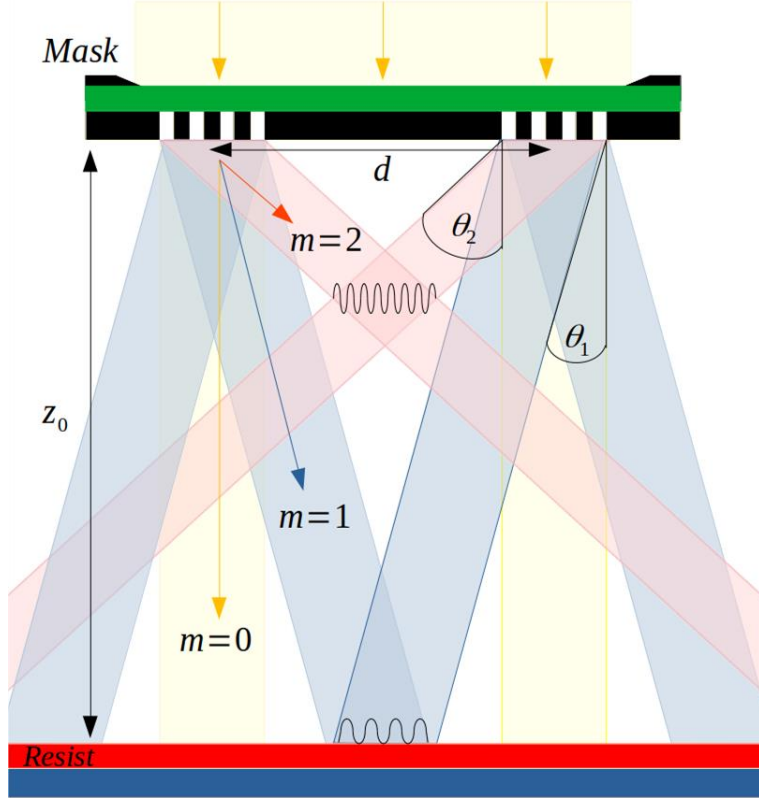


Figure 2.2.1: Schematic of an Interference Lithography setup using a binary grating mask. The first order ($m=\pm 1$) beams form an aerial image at the image plane, a distance z_0 from the mask, which is then transferred onto a photoresist. The zero order ($m=0$) and second order ($m=2$) diffracted beams are also shown.

$$z_0 = \frac{d}{2\tan\theta_m} . \quad 2.2.2$$

The simplest interference lithography setup consists of two plane waves intersecting at an angle $2\theta_m$ creating a standing wave pattern with period, p , given by:

$$p = \frac{\lambda}{2\sin\theta_m} . \quad 2.2.3$$

The interference pattern formed at the image plane is known as the aerial image, the resolution of which is denoted by the half-pitch, $HP=p/2$. For a beam normally incident upon a grating Equation 2.2.1 and Equation 2.2.3 can be combined to show

$$HP = \frac{\lambda}{4\sin\theta_m} = \frac{p_G}{4m} \quad 2.2.4$$

so the ultimate resolution for a first order aerial image is $p_G/4$ [44]. Equation 2.2.4 implies that sub-10 nm patterning by EUV-IL requires a grating mask with $p_G < 40$ nm, which is easily achievable through electron beam lithography [45]. The right side of Equation 2.2.4 is independent of λ , which shows the achromatic nature of the resolution of IL.

The depth of focus (*DoF*) of the image plane for an Interference Lithography system can be very large. Depending on the total width of the gratings, the *DoF* of an ideal mask illuminated with normal incidence, coherent illumination, can be thought of as effectively infinite [47]. For partially coherent illumination the depth of focus can be calculated from the coherence width, W_c , at the plane of the interference grating [46]:

$$DoF = \frac{W_c}{\tan(2\theta_m)}.$$

2.2.5

The finite grating size has been found to cause the fringes of an aerial image to be non-uniform, with an envelope that resembles zero-order Fresnel diffraction from an aperture [48]. The effect is heavily dependent on the geometry of the grating mask and beamline optics, which can be optimised for high flux and visibility in the aerial image plane [14,48].

A major limitation of IL is the limited area of the aerial image, however, techniques have been developed to overcome this. Step-and-repeat scanning exposure techniques can be implemented which allow for the fast patterning of large-area periodic structures much larger than the exposure area [19,40]. This technique can be utilised to create structures up to 2×2 cm from single patterned areas of the order of several 10×10 μm [49].

2.3 Synchrotron Radiation

Synchrotron radiation facilities provide high energy radiation by accelerating an electron beam through periodic magnetic structures and are used the world over for lithographic experiments [32,34,50–53]. Synchrotron undulator sources have recently been used for research into creating high-resolution (sub-10 nm), periodic nano-structures using EUV-IL [54–57]. At present, most synchrotron-based IL facilities are optimised for 13.5 nm radiation and have not been applied extensively to BEUV-IL (< 13.5 nm).

2.3.1 Undulator Radiation

While not ideal sources for HVM, undulator radiation has many qualities that make it well suited to BEUV research. It is a continuously tuneable source, allowing for fine selection of wavelength. It has high spectral brilliance, which is desirable for short-wavelength lithography. It is also highly spatially coherent, which is essential for reaching the ultimate resolution in BEUV-IL [11].

Figure 2.3.1 shows a relativistic charged particle inside an undulator. An undulator accelerates the relativistic charged-particle beam of a synchrotron perpendicular to its motion which causes large amounts of electromagnetic radiation to be emitted in a tight cone of angular dispersion $1/\gamma$, where γ is the Lorentz factor given by [58]:

$$\gamma = \frac{1}{\sqrt{1 - v^2/c^2}}.$$

2.3.1

The magnetic field at the axis of a planar undulator with magnetic period λ_U and peak field B_0 is a harmonic function of the longitudinal position z [59]:

$$B_y(z, x = 0, y = 0) = B_0 \cos\left(\frac{2\pi z}{\lambda_U}\right).$$

2.3.2

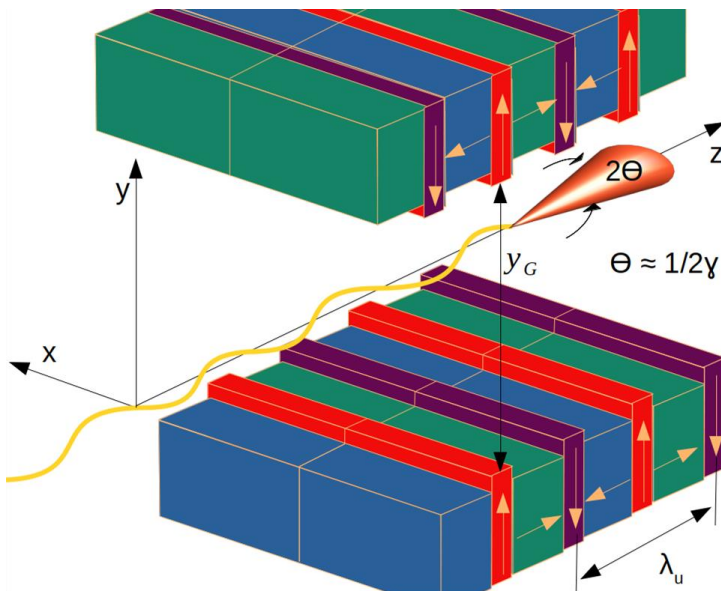


Figure 2.3.1: A relativistic electron traversing an undulator. The periodic magnetic field causes the electron to oscillate and emit radiation in a tight cone. The period of the undulator is labelled λ_u , the undulator gap is labelled y_G .

In the frame of an electron moving with highly relativistic velocity, $v \approx c$ the periodic structure is moving towards it with a Lorentz contracted period. The transverse velocity of the electron can be written as

$$v_x = \frac{Kc}{\gamma} \sin\left(\frac{2\pi z}{\lambda_U}\right)$$
2.3.3

where K is the magnetic deflection parameter. For a typical undulator, $K \leq 1$ and the oscillations of the electron are contained within the central radiation cone which causes interference effects and leads to cone narrowing, higher spectral brightness and partial coherence. The deflection parameter is given by:

$$K = \frac{eB_0\lambda_U}{2\pi mc}.$$
2.3.4

K can be controlled by varying the undulator vertical gap, y_G , which will alter the magnetic field strength B_0 [35]. Undulator radiation is thus highly tuneable and covers a wider range of wavelengths than laboratory sources [60]. The wavelength of undulator radiation can be determined by the ‘undulator equation’ [35]:

$$\lambda_m = \frac{1}{m} \frac{\lambda_U}{2\gamma^2} \left(1 + \frac{\kappa^2}{2} + \gamma^2 \theta^2\right),$$
2.3.5

where m is an integer defining the undulator harmonic and θ is the angle of emission from the optical axis so that $\theta = 0$ represents on axis radiation. An undulator produces harmonics at λ_U/m intervals from the fundamental harmonic ($m=1$). The spectral bandwidth $\Delta\lambda$ of each harmonic depends on the number of magnetic periods, N [61]:

$$\left(\frac{\Delta\lambda}{\lambda}\right)_m = \frac{1}{mN}.$$
2.3.6

Undulator radiation can be highly polarised [58], and the polarisation may be manipulated by shifting the relative positions of the rows of magnets used in some undulator designs [62]. The default position shown in Figure 2.3.1 results in linear horizontal polarisation, while Figure 2.3.2 shows how shifting each row of magnets by a factor of $\lambda_U/2$ will give linear vertical polarisation, and shifts of $\lambda_U/4$ and $3\lambda_U/4$ will lead

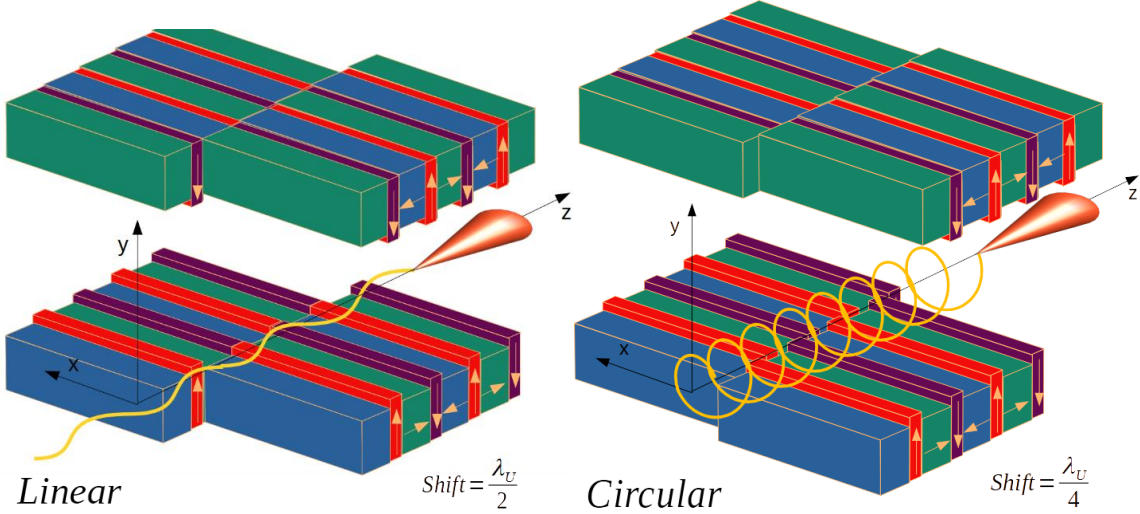


Figure 2.3.2: Undulator configurations used to obtain the desired beam polarisation. Shifting the magnet rows by distances of fractions of the undulator period will give linear vertical polarisation (left), or circular polarisation (right)

to both right and left circular polarisation [63].

The power produced by an undulator for the fundamental harmonic in the central radiation cone is given by:

$$\bar{P}_{cen} = \frac{\pi e \gamma^2 I}{\epsilon_0 \lambda_U} \frac{K^2}{(1 + K^2/2)^2} f(K), \quad 2.3.7$$

where e is the fundamental electron charge, ϵ_0 is the permittivity of free space and $f(K)$ is a multiplicative factor associated with the transfer of power from the fundamental ($m=1$) to higher harmonics ($m>1$) [64]. The spectral brilliance, B of an undulator source is proportional to the photon flux $\Phi(E)$ (measured in photons/second at a specific energy, within 0.1% bandwidth) and inversely proportional to source size and angular divergence [65]:

$$B(E) = \frac{\Phi(E)}{4\pi^2 \sigma_x \sigma'_x \sigma_y \sigma'_y} = \frac{\Phi(E)}{4\pi^2 \epsilon_x \epsilon_y} \quad 2.3.8$$

where ϵ_x and ϵ_y are the horizontal and vertical beam emittance respectively. Power and photon flux are related by [35]:

$$P [W] \approx 5.034 \times 10^{15} \lambda [nm] \Phi(E) \left[\frac{\text{photons}}{s} \right]. \quad 2.3.9$$

For example, at 6.7 nm wavelength, a power of one watt corresponds to a photon flux of approximately 3.373×10^{16} photons per second, where each photon has energy of ~ 185 eV. For coherent x-ray experiments a high-quality source is characterised by high brightness and low emittance. The x-ray beam emittance of a synchrotron source is directly related to the emittance of the electron beam in the storage ring [66]. Low emittance storage rings are thus necessary for synchrotron experiments that require high brightness, such as EUV-IL.

2.4 Interference and Diffraction with Partially Coherent Light

2.4.1 Coherence

Coherence of a light source is a measure of the relationship between the electric field at two separate points in space and time and can be divided into two categories, *spatial coherence* and *temporal coherence*. Spatial coherence is directly related to the size and angular divergence of the source emitting radiation and temporal coherence is related to the spectral bandwidth. If an electric field is known at one point in space and time, the degree to which it can be predicted at another point after some time τ is described by the mutual coherence function, Γ [35,67]. For a pair of points, (x_1, y_1) , (x_2, y_2) , on a two-dimensional plane:

$$\Gamma(x_1, y_1, x_2, y_2, \tau) \equiv \langle E^*(x_1, y_1, t)E(x_2, y_2, t + \tau) \rangle. \quad 2.4.1$$

Normalising the mutual coherence function gives the complex degree of coherence:

$$\gamma_{1,2}(x_1, y_1, x_2, y_2, \tau) = \frac{\Gamma(x_1, y_1, x_2, y_2, \tau)}{\sqrt{\langle |E(x_1, y_1, t)|^2 \rangle} \sqrt{\langle |E(x_2, y_2, t)|^2 \rangle}} \quad 2.4.2$$

with $|\gamma_{1,2}| = 1$ corresponding to a completely coherent source and $|\gamma_{1,2}| = 0$ an incoherent source. In the case of zero time delay ($\tau=0$), Equation 2.4.1 reduces to the mutual intensity, J , [68]:

$$J(x_1, y_1, x_2, y_2) = \Gamma(x_1, y_1, x_2, y_2, 0) = \langle E^*(x_1, y_1)E(x_2, y_2) \rangle \quad 2.4.3$$

which describes a quasimonochromatic source. The normalised form is the degree of spatial coherence [69]:

$$\gamma(x_1, y_1, x_2, y_2) = \frac{J(x_1, y_1, x_2, y_2)}{[\langle |E(x_1, y_1)|^2 \rangle \langle |E(x_2, y_2)|^2 \rangle]^{1/2}}. \quad 2.4.4$$

When $(x_1, y_1) = (x_2, y_2)$, $\gamma = 1$ and J reduces to the intensity of the beam. The mutual intensity is a useful measure of the coherence of a beam [70]. In the case of a paraxial beam with uniform polarisation, a scalar treatment of J as in Equation 2.4.3 is adequate. However, when considering a partially polarised beam the vector nature of the electromagnetic field must be taken into account [71]. In this case the mutual intensity may be represented by a 2×2 matrix containing the statistical correlation between all transverse components of the electric field at any pair of points [70]:

$$\begin{aligned} J(x_1, y_1, x_2, y_2) &= \begin{bmatrix} J_{xx}(x_1, y_1, x_2, y_2) & J_{xy}(x_1, y_1, x_2, y_2) \\ J_{yx}(x_1, y_1, x_2, y_2) & J_{yy}(x_1, y_1, x_2, y_2) \end{bmatrix} \\ &= \begin{bmatrix} \langle E_x^*(x_1, y_1) E_x(x_2, y_2) \rangle & \langle E_x^*(x_1, y_1) E_y(x_2, y_2) \rangle \\ \langle E_y^*(x_1, y_1) E_x(x_2, y_2) \rangle & \langle E_y^*(x_1, y_1) E_y(x_2, y_2) \rangle \end{bmatrix} \end{aligned} \quad 2.4.5$$

where E_x and E_y are the horizontal and vertical components of the electric field respectively. If $(x_2, y_2) = (x_1 + \Delta x, y_1 + \Delta y)$, then the width of $J(x_1, y_1, x_1 + \Delta x, y_1 + \Delta y)$ as a function of point separation $(\Delta x, \Delta y)$ is the correlation length. The *spatial coherence length* can then be defined with respect to the full-width at half maximum [69]. For an object to be considered coherently illuminated its extent, σ_o , must be less than the spatial coherence length of the incident beam. A radiation source at a distance D from a pinhole of size d , can be considered spatially coherent if it satisfies the condition:

$$\frac{\sigma_o}{D} < \frac{\lambda}{d}. \quad 2.4.6$$

So high spatial coherence for synchrotron sources can be obtained by increasing the propagation distance, D , between the source and endstation. As the flux over the area, σ_o ,

will decrease with propagation due to beam divergence, a compromise between coherence and flux must then be considered when designing a synchrotron beamline.

2.4.1.1 Partial Coherence

Undulator light sources are partially coherent [64]. The coherent fraction, ζ , of a beam is the ratio of coherent flux, Φ_{coh} , to photon flux and can be used to describe the degree of coherence of a source [72,73]:

$$\zeta = \frac{\Phi_{coh}(E)}{\Phi(E)} = \left(\frac{\lambda}{4\pi}\right)^2 \frac{1}{\epsilon_x \epsilon_y}, \quad 2.4.7$$

with

$$\Phi_{coh} = B(E) \left(\frac{\lambda}{2}\right)^2, \quad 2.4.8$$

where $B(E)$ is the spectral brilliance, defined for an undulator source in Equation 2.3.8. An incoherent source such as a bending magnet or LPP can be implemented for IL through the use of a cascaded grating interferometer, however the method is extremely sensitive to misalignment and grating quality which can lead to a degradation in performance which limits the size and acceptable divergence [46,74].

For experiments that require coherent illumination such as IL, the fraction of usable power is set by the longitudinal (temporal) and transverse (spatial) coherence lengths of the source, l_t and, l_s . The temporal coherence length is dependent on energy spread, given by [75]:

$$l_t = \frac{\lambda^2}{2\Delta\lambda} \quad 2.4.9$$

and the spatial coherence length is related to the source size σ , and angular divergence σ' , given by [76]:

$$\frac{(2\pi\sigma')^2}{\lambda^2} = \frac{1}{4\sigma^2} + \frac{1}{l_s^2}. \quad 2.4.10$$

The longitudinal coherence in the illumination at a photomask can be improved using a monochromator as a spectral filter to reduce $\Delta\lambda$, while the transverse coherence can be improved by spatial filtering with collimating slits.

The reflective illumination optics used in synchrotron based EUV-IL, and the projection optics used in EUV for high volume manufacturing, allow for a broader spectral bandwidth than refractive elements used in lithography at lower energy. While the resolution of IL is bandwidth insensitive, as shown in Equation 2.2.4, the optical properties of the materials comprising the photomask and resist are sensitive to changes in energy. This leads to considerations of temporal coherence. For low emittance sources such as an undulator, the effects of temporal coherence on aerial image formation can be safely ignored, especially if optical elements are in use to limit bandwidth. The monochromatic illumination assumption remains valid for typical EUV-IL applications [77,78].

2.4.1.2 Interference Due to Partially Coherent Light

Detailed knowledge of the mutual coherence function over an aperture is essential in order to fully describe resulting interference [79]. The degree of coherence, $|\gamma|$, of radiation in the aperture plane can be determined through analysis of the fringe visibility, V , of the far-field interference pattern from radiation passing through a Young's Double Slit (YDS) of various slit separations. Fringe visibility is determined by comparing the maximum central intensity I_{max} to its nearest minimum I_{min} [67,80]:

$$V = \frac{I_{max} - I_{min}}{I_{max} + I_{min}} = \frac{2\sqrt{(I_1 I_2)}}{I_1 + I_2} |\gamma_{1,2}(\tau)|. \quad 2.4.11$$

Assuming each slit is illuminated with equal intensity ($I_1 = I_2$), then $V = |\gamma|$, and the coherence length, l_c , in the plane of the YDS can be determined as the slit separation at

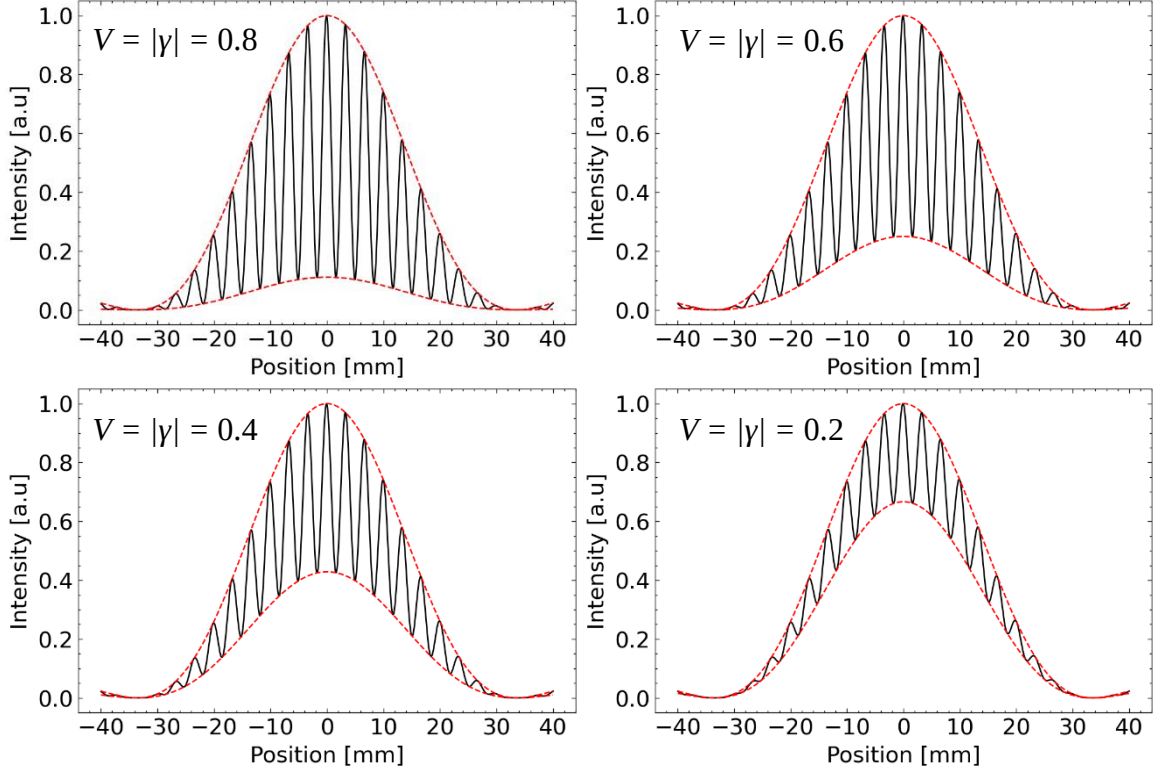


Figure 2.4.1: The representation of the effect of partial coherence on visibility of a YDS diffraction pattern, created using Equation 2.4.12. As the slit separation is increased, the visibility of the interference fringes decreases. The coherence length can then be determined as the slit separation at which V is reduced to a desired limit.

which $|\gamma|$ is reduced to a chosen limit, typically 0.88 [80,81]. A demonstration of this is shown in Figure 2.4.1

The far-field intensity line profile with central intensity, I_0 , at a distance, z , from a YDS with slit size β and separation, a , illuminated by a source with degree of coherence γ , can be modelled using [80]:

$$I(x) = I_0 \left[\text{sinc} \left(\frac{\pi a x}{\lambda z} \right) \right]^2 \left\{ 1 + \gamma \left[\text{sinc} \left(\frac{\pi \Delta \lambda x}{\lambda z} \right) \right] \times \left[\text{sinc} \left(\frac{\pi \delta \beta}{\lambda z} \right) \right] \cos \left(\frac{2\pi \beta x}{\lambda z} \right) \right\}, \quad 2.4.12$$

where δ is the detector resolution.

Knowledge of coherence must also be considered when describing propagation through or reflection from a rough surface. Surface roughness will introduce phase variation in a transmitted (or reflected) beam that will lead to interference in the image plane for sufficiently coherent illumination. This manifests as random intensity variation known as speckle [82]. The contrast of the speckle pattern formed depends on the surface

roughness of the object [83], and the coherence of the illumination [84]. The correlation of coherence, surface roughness and speckle contrast is such that analysis of speckle images produced by coherent illumination is a commonly used method to assess surface roughness [85–87]. Coherence is intentionally reduced in some imaging applications to suppress speckle [84,88].

2.4.2 Polarisation

A fully polarised beam of quasimonochromatic light can be described by an electromagnetic vector field $\vec{E}(x, y, z, t)$ [71]. Taking propagation in the z -direction, the z -components of the electromagnetic vector describing the beam are negligible and can be ignored. The electric field vector can then be written in terms of its horizontal component E_x and vertical component, E_y , so that

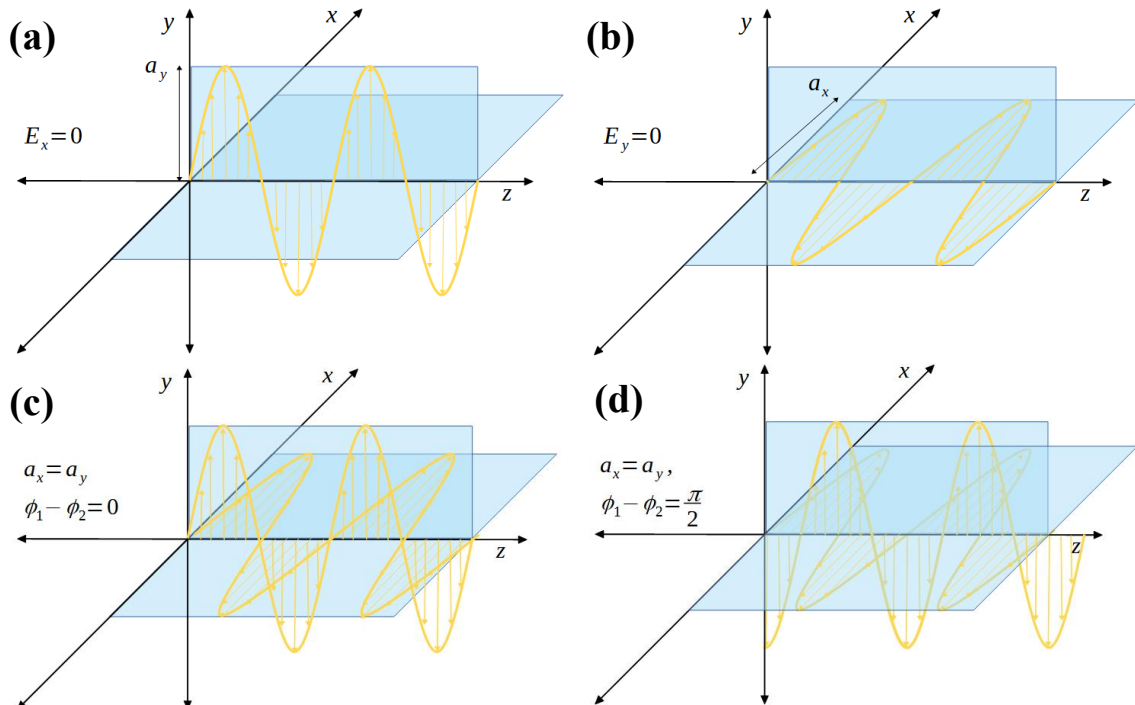


Figure 2.4.2: The electric field of light in different polarisation states. (a) linear vertical, (b) linear horizontal, (c) linear 45°, (d) circular polarisation.

$$\vec{E}(x, y, t) = \vec{E}_x(t) + \vec{E}_y(t)$$

$$= a_x(t) \exp[i(\phi_1(t) - \omega t)] \hat{x} + a_y(t) \exp[i(\phi_2(t) - \omega t)] \hat{y}$$
2.4.13

where a_x, a_y , are the amplitudes in the x and y components of the field, ϕ_1 , and ϕ_2 , are the phases and $\omega/2\pi$ is the frequency. The polarisation is described by the relative amplitude and phase of E_x and E_y . If the phase difference, $\delta = \phi_1 - \phi_2 = 0$, the beam is linearly polarised. If each component is of equal amplitude, $a_1 = a_2$, and $\delta = \pm \frac{\pi}{2}$, then the beam is circularly polarised. In any other case the beam is elliptically polarised [89]. In the case in which the electric field oscillates completely in the horizontal plane, $E_y = 0$, or vertical plane, $E_x = 0$, the beam is said to be linearly horizontally polarised or linearly vertically polarised respectively [90], as shown schematically in Figure 2.4.2 (a) and (b).

By eliminating the dependence of Equation Error! Reference source not found. on position and time, the polarisation ellipse (Figure 2.4.3) that the electric field vector traces as it propagates is obtained. For $\delta = \phi_1 - \phi_2$:

$$\frac{E_x^2}{a_x^2} + \frac{E_y^2}{a_y^2} - \frac{2E_x E_y}{a_x a_y} \cos \delta = \sin^2 \delta,$$
2.4.14

Equation 2.4.14 describes an ellipse oriented at an angle, χ , with the x and y axes given by [67]:

$$\tan(2\chi) = \frac{2a_x a_y \cos \delta}{a_x^2 - a_y^2}.$$
2.4.15

The polarisation ellipse of a beam of light can be described using the eccentricity, e , the orientation, χ , and the chirality (direction of rotation). However, this ellipse only describes perfectly polarised beams. For a complete description of the polarisation state of a beam the degree of polarisation, P , must be known [91]. This can be obtained from the *Stokes vector*.

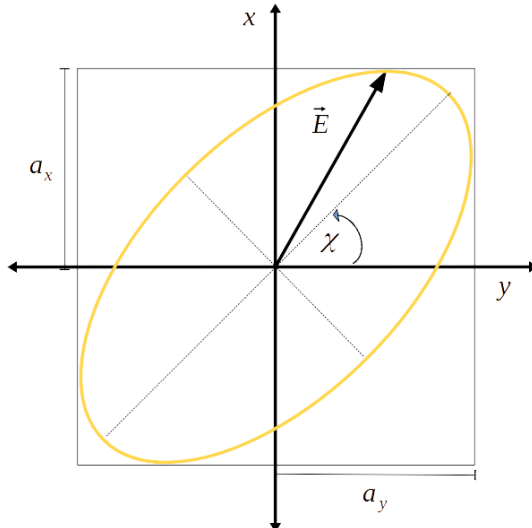


Figure 2.4.3: The polarisation ellipse. The shape the endpoint of the electric field vector traces as it propagates.

2.4.2.1 The Stokes Vector

The Stokes vector, \hat{S} , is a set of four values known as the Stokes parameters. It can describe the polarisation state of a polarised, partially-polarised and unpolarised beam and is the simplest method of predicting the result of adding two incoherent beams [90]. The Stokes parameters can be obtained from the time-average of J (Equation 2.4.14). This is acceptable since, although the polarisation ellipse (Figure 2.4.3) changes shape slowly in comparison to the frequency of the field oscillations, it changes extremely fast in comparison to the duration of any possible measurement [92]. The Stokes parameters are thus given by

$$S_0 = \langle a_x^2 \rangle + \langle a_y^2 \rangle$$

$$S_1 = \langle a_x^2 \rangle - \langle a_y^2 \rangle$$

$$S_2 = \langle 2a_x a_y \cos\delta \rangle$$

$$S_3 = \langle a_x a_y \sin\delta \rangle$$

2.4.16 - a, b, c, d

where the brackets denote the time average [93]. From Equation 2.4.16 it can be seen that S_0 is simply the intensity of the beam, while S_1 , S_2 , and S_3 describe the polarisation state. When $S_1 = \pm 1$ the polarisation ellipse reduces to a line along the horizontal ($S_1 = +1$) or vertical ($S_1 = -1$) axes. When $S_2 = \pm 1$ the polarisation ellipse is reduced to a line oriented $+45^\circ$ ($S_2 = +1$) or -45° ($S_2 = -1$) with respect to the x axes. When $S_3 = \pm 1$ the polarisation

ellipse becomes a circle and the polarisation state is right ($S_3 = +1$) or left ($S_3 = -1$) circular [89]. If there is an equally weighted mix of either state described by the corresponding Stokes parameter it will reduce to 0 [67]. The Stokes vector is then written as

$$\hat{S} = \begin{bmatrix} S_0 \\ S_1 \\ S_2 \\ S_3 \end{bmatrix} = \begin{bmatrix} a_x^2 + a_y^2 \\ a_x^2 - a_y^2 \\ 2a_x a_y \cos\delta \\ 2a_x a_y \sin\delta \end{bmatrix}$$

2.4.17

which is typically normalised to the intensity so that

$$s_n = \frac{S_n}{S_0}, \quad n \in (0, \dots, 3)$$

2.4.18

and the value of each parameter falls between 0 and 1 [71]. The Stokes vector of a beam can be measured using wave-plates or simply four polarising filters, as shown in [93]. The normalised Stokes vectors for completely polarised beams with simple geometry are known as the degenerate polarisation states,

$$s_{LHP} = \begin{pmatrix} 1 \\ 1 \\ 0 \\ 0 \end{pmatrix}, s_{LVP} = \begin{pmatrix} 1 \\ -1 \\ 0 \\ 0 \end{pmatrix}, s_{L+45} = \begin{pmatrix} 1 \\ 0 \\ 1 \\ 0 \end{pmatrix},$$

$$s_{L-45} = \begin{pmatrix} 1 \\ 0 \\ -1 \\ 0 \end{pmatrix}, \quad s_{RCP} = \begin{pmatrix} 1 \\ 0 \\ 0 \\ 1 \end{pmatrix}, \quad s_{LCP} = \begin{pmatrix} 1 \\ 0 \\ 0 \\ -1 \end{pmatrix}.$$

2.4.19

These describe linearly polarised beams with horizontal (*LHP*), vertical (*LVP*) and $\pm 45^\circ$ polarisation (*L+45 P*, *L-45 P*) as well as right (*RCP*) and left (*LCP*) circularly polarised beams [93]. Therefore, for completely polarised beams

$$S_0^2 = S_1^2 + S_2^2 + S_3^2.$$

2.4.20

2.4.2.2 Partial Polarisation

Any partially polarised beam can be considered as an incoherent superposition of an unpolarised beam of intensity, S_0^N , and a completely polarised beam of intensity S_0^P so that

$$S_0 = S_0^N + S_0^P, \quad 2.4.21$$

with the intensity of each component given by [92]:

$$S_0^N = S_0 - (S_1^2 + S_2^2 + S_3^2)^{1/2} \quad \text{and} \quad S_0^P = (S_1^2 + S_2^2 + S_3^2)^{1/2}. \quad 2.4.22$$

The *degree of polarisation*, P , expresses the fraction of energy contained in the polarised part of the beam [71]. The degree of polarisation can then be obtained through the Stokes parameters by the relation

$$P = \frac{S_0^P}{S_0} = \frac{(S_1^2 + S_2^2 + S_3^2)^{1/2}}{S_0}, \quad 2.4.23$$

where $0 \leq P \leq 1$. $P=1$ and $P=0$ represent a completely polarised and unpolarised beam respectively [67]. This can be used to find the Stokes vector of the completely polarised component, S_P , of a partially polarised beam

$$S_P = \begin{pmatrix} S_0 \\ S_1 \\ S_2 \\ S_3 \end{pmatrix}_P = \frac{1}{P} \begin{pmatrix} S_0 \\ S_1 \\ S_2 \\ S_3 \end{pmatrix} - \frac{1-P}{P} \begin{pmatrix} 1 \\ 0 \\ 0 \\ 0 \end{pmatrix}_N \quad 2.4.24$$

where the column vector with subscript N denotes the Stokes vector for natural light [67]. The angle of orientation, χ , and the ellipticity, e , can also be obtained through the Stokes parameters with the relations

$$\chi = \frac{1}{2} \tan^{-1} \left(\frac{S_2}{S_1} \right), \quad \text{and} \quad e = \left[\frac{2\sqrt{S_1^2 + S_2^2}}{1 + \sqrt{S_1^2 + S_2^2}} \right]^{1/2}. \quad 2.4.25-a, b$$

Therefore, with the chirality taken from the sign of S_3 , the complete polarisation state of the beam can be described using just the Stokes vector [91].

2.4.2.3 Interference & Polarisation

Just as two incoherent beams in the same polarisation state will not interfere [94], orthogonally polarised beams, even if completely coherent, will not produce interference fringes [95]. Although the significance of the polarisation state of a beam of light in an interference pattern has long been known [81,92,94,96] there are still recent developments in understanding being made [70]. An alternative description of the degree of polarisation of a beam is the measure of the correlation between equal intensity, orthogonal electric field components at each point. A quasimonochromatic, partially polarised beam can be represented at a plane (x, y) perpendicular to the propagation direction by the 2×2 polarisation matrix \mathbf{J} (Equation 2.4.5) [71]. The Stokes parameters of the beam are then given by linear combinations of the elements of \mathbf{J} [96]:

$$\begin{aligned} S_0(x_1, y_1, x_2, y_2) &= J_{xx}(x_1, y_1, x_2, y_2) + J_{yy}(x_1, y_1, x_2, y_2) \\ &= \langle E_x^*(x_1, y_1) E_x(x_2, y_2) \rangle + \langle E_y^*(x_1, y_1) E_y(x_2, y_2) \rangle \end{aligned} \quad 2.4.26$$

$$\begin{aligned} S_1(x_1, y_1, x_2, y_2) &= J_{xx}(x_1, y_1, x_2, y_2) - J_{yy}(x_1, y_1, x_2, y_2) \\ &= \langle E_x^*(x_1, y_1) E_x(x_2, y_2) \rangle - \langle E_y^*(x_1, y_1) E_y(x_2, y_2) \rangle \end{aligned} \quad 2.4.27$$

$$\begin{aligned} S_2(x_1, y_1, x_2, y_2) &= J_{xy}(x_1, y_1, x_2, y_2) + J_{yx}(x_1, y_1, x_2, y_2) \\ &= \langle E_x^*(x_1, y_1) E_y(x_2, y_2) \rangle + \langle E_y^*(x_1, y_1) E_x(x_2, y_2) \rangle \end{aligned} \quad 2.4.28$$

$$\begin{aligned} S_3(x_1, y_1, x_2, y_2) &= i[J_{xy}(x_1, y_1, x_2, y_2) - J_{yx}(x_1, y_1, x_2, y_2)] \\ &= i[\langle E_x^*(x_1, y_1) E_y(x_2, y_2) \rangle - \langle E_y^*(x_1, y_1) E_x(x_2, y_2) \rangle] \end{aligned} \quad 2.4.29$$

The matrix, \mathbf{J} , and its determinant $|\mathbf{J}|$ can be used to calculate the degree of polarisation, P , of the electric field at any point in the plane [68]:

$$P = \sqrt{1 - \frac{4|J|}{(J_{xx} + J_{yy})^2}}. \quad 2.4.30$$

A practical measure for degree of polarisation of a beam can be made in a similar manner to that of the degree of coherence [97]. The electric field from two partially polarised beams originating from a Young's two-pinhole interference experiment will show modulation in each Stokes parameter at the image plane. The visibility of the oscillations can be given by:

$$V_n(x, y) = \frac{\max[S_n(x, y)] - \min[S_n(x, y)]}{\max[S_n(x, y)] + \min[S_n(x, y)]}, \quad n \in (0, \dots, 3). \quad 2.4.31$$

In the case that the electric field is identical at each pinhole in the incident plane (x_0, y_0), the visibilities of the Stokes parameter modulations are identical to the normalised Stokes parameters. The degree of polarisation can then be obtained from [71]:

$$P(x_0, y_0) = \left[\sum_{n=1}^3 V_n^2(x, y) \right]^{1/2} \quad 2.4.32$$

2.4.2.4 Polarisation & Interference Lithography

The interference pattern generated in n -beam IL can be understood as the superposition of the electric field vectors of each beam. The electric field vector of the n^{th} beam, with amplitude, A_n , initial phase, ϕ_n , and frequency, ω , is given by:

$$\vec{E}_n = A_n \vec{p}_n \exp[i\vec{k} \cdot \vec{r} + \phi_n] \quad 2.4.33$$

where $\vec{r} = (\hat{x}, \hat{y}, \hat{z})$ is the position vector, \vec{p}_n , and \vec{k}_n , are the polarisation vector and the wavevector respectively, given by:

$$\begin{aligned} \vec{p}_n = & -(cos\theta_n cos\varphi_n cos\chi_n - sin\theta_n sin\chi_n) \hat{x} \\ & -(cos\theta_n sin\varphi_n cos\chi_n + cos\theta_n sin\chi_n) \hat{y} - (sin\theta_n cos\chi_n) \hat{z}, \end{aligned} \quad 2.4.34$$

and

$$\hat{k} = k \sin\theta_n \cos\varphi_n \hat{x} + k \sin\theta_n \sin\varphi_n \hat{y} + k \cos\theta_n \hat{z}, \quad 2.4.35$$

where θ_n is the incident angle, determined by Equation 2.2.1, χ_n is the orientation angle and φ_n is the azimuthal angle of the n^{th} beam. The intensity of the aerial image formed by an N -beam IL experiment is described by [98]:

$$\begin{aligned} I &= \sum_{n=1}^N \vec{E}_n \cdot \sum_{m=1}^N \vec{E}_m^* \\ &= \sum_{n=1}^N \sum_{m=1}^N A_n \vec{p}_n \cdot A_m \vec{p}_m \cdot \exp[i(\vec{k}_n - \vec{k}_m) \vec{r} + \phi_n - \phi_m]. \end{aligned} \quad 2.4.36$$

For two beams with equal amplitudes A , zero initial phases and opposite azimuthal angles, $\varphi_1=0^\circ$, and $\varphi_2=180^\circ$, the electric fields of each diffracted beam are:

$$E_1 = A \vec{p}_1 \exp[i(kx \sin\theta - kz \cos\theta)],$$

$$E_2 = A \vec{p}_2 \exp[i(-kx \sin\theta - kz \cos\theta)]. \quad 2.4.37$$

It can be seen from Equation 2.4.36 and Equation 2.4.37 that the contrast of the resulting interference pattern will depend on the polarisation of each beam [41]. For two-beam interference, the direction of the polarisation vector of each beam plays a critical role in determining the resulting interference pattern. The contrast in the image plane will depend on whether the electric field polarisation at the incident plane of the grating is parallel to the grating lines (TE-TE), perpendicular (TM-TM) or a mixture of TE & TM.

For the two beams described in Equation 2.4.37, the angle χ_n is taken relative to the horizontal x-axis, so $\chi=0$ corresponds to a horizontal polarisation and will be considered TE-TE for a horizontal grating, while $\chi=90^\circ$ corresponds to vertical polarisation (TM-TM for a horizontal grating). The polarisation vectors of the two beams for TE-TE and TM-TM interference lithography configurations are then:

$$\vec{p}_1^{TE} = y \cdot \hat{y}, \quad \vec{p}_2^{TE} = y \cdot \hat{y} \quad 2.4.38$$

and

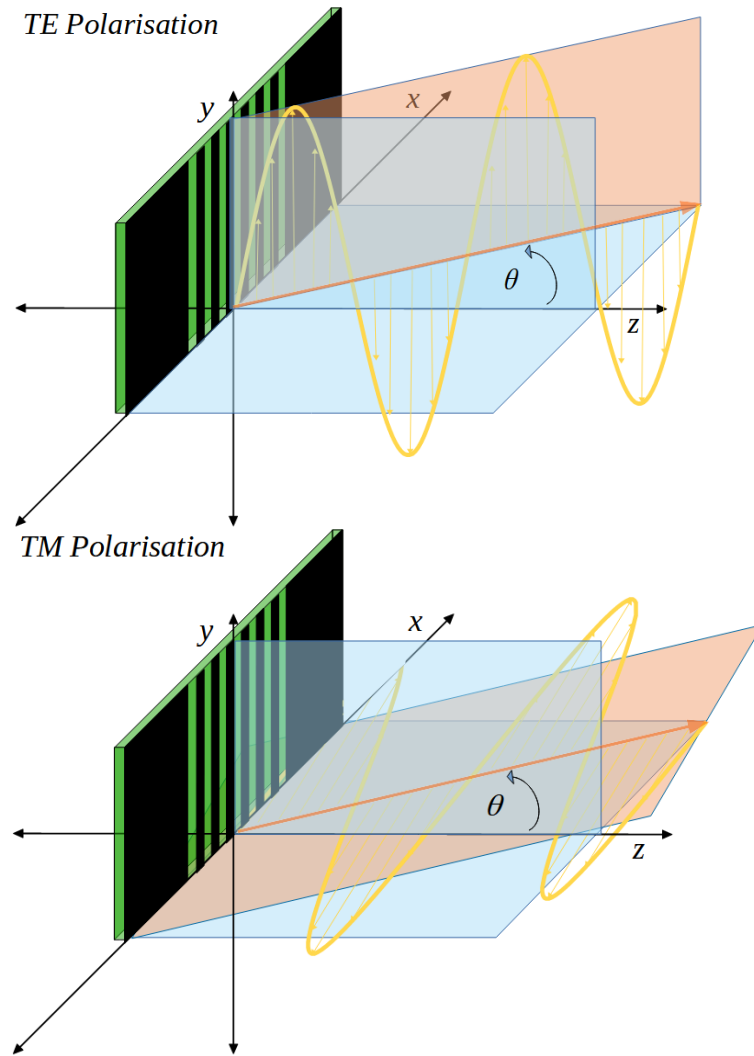


Figure 2.4.4: Diffracted beams with TE and TM polarisation. The polarisation vector of the incident TE polarised beam is unaffected by diffraction from the grating and oscillations of the electric field occur only in the y-direction. The polarisation vector of the incident TM polarised beam is affected by diffraction, introducing a z-component into the electric field oscillation.

$$\vec{p}_1^{TM} = y\cos\theta\hat{x} + z\sin\theta\hat{z}, \quad \vec{p}_2^{TM} = y\cos\theta\hat{x} - z\sin\theta\hat{z}. \quad 2.4.39$$

Figure 2.4.4 shows the diffracted E_I beam for both TE and TM incident polarisation. The electric field vectors describing each beam are then:

$$\vec{E}_1^{TE} = A \exp[i(kx\sin\theta - kz\cos\theta)]y\hat{y},$$

$$\vec{E}_2^{TE} = A \exp[i(-kx\sin\theta - kz\cos\theta)]y\hat{y} \quad 2.4.40$$

and

$$\vec{E}_1^{TM} = A \exp[i(kx \sin \theta - kz \cos \theta)](y \cos \theta \hat{x} + z \sin \theta \hat{z}),$$

$$\vec{E}_2^{TM} = A \exp[i(-kx \sin \theta - kz \cos \theta)](y \cos \theta \hat{x} + z \sin \theta \hat{z})$$

2.4.41

and the Stokes vectors describing each beam are given by Equation 2.4.17:

$$\hat{S}_1^{TE} = \begin{bmatrix} A^2 \exp[2i(kx \sin \theta - kz \cos \theta)]y^2 \\ -A^2 \exp[2i(kx \sin \theta - kz \cos \theta)]y^2 \\ 0 \\ 0 \end{bmatrix},$$

$$\hat{S}_2^{TE} = \begin{bmatrix} A^2 \exp[2i(-kx \sin \theta - kz \cos \theta)]y^2 \\ -A^2 \exp[2i(-kx \sin \theta - kz \cos \theta)]y^2 \\ 0 \\ 0 \end{bmatrix},$$

2.4.42

and

$$\hat{S}_1^{TM} = \begin{bmatrix} A^2 \exp[2i(kx \sin \theta - kz \cos \theta)]y^2 \cos^2 \theta \\ A^2 \exp[2i(kx \sin \theta - kz \cos \theta)]y^2 \cos^2 \theta \\ 0 \\ 0 \end{bmatrix},$$

$$\hat{S}_2^{TM} = \begin{bmatrix} A^2 \exp[2i(-kx \sin \theta - kz \cos \theta)]y^2 \cos^2 \theta \\ A^2 \exp[2i(-kx \sin \theta - kz \cos \theta)]y^2 \cos^2 \theta \\ 0 \\ 0 \end{bmatrix},$$

2.4.43

which, after normalising reduce to the linear vertical and linear horizontal degenerate polarisation states shown in Equation 2.4.19. So, $s_1^{TE} = s_2^{TE} = s_{LVP}$, and $s_1^{TM} = s_2^{TM} = s_{LHP}$. The two beams will create interference patterns with intensity described by:

$$I^{TE-TE} = 2A^2 + 2A^2 \cos(2kx \sin \theta),$$

2.4.44

and

$$I^{TM-TM} = 2A^2 + 2A^2 \cos(2kx \sin \theta) \cos(2\theta). \quad 2.4.45$$

For EUV-IL using linearly polarised illumination, rotating the mask will lead to a change in polarisation direction of the beam with respect to the mask gratings. The intensity distribution of an aerial image after propagation through a mask rotated at an angle α is then given by [41]:

$$I = 2A^2 \cos^2(\alpha) [2 + \cos(2kx \cos(\alpha) \sin(\theta)) \cos(2\theta) + 2 \cos(2kx \cos(\alpha) \sin(\theta))] \quad 2.4.46$$

The visibility of TE-TE interference fringes is independent of the diffraction angle as the polarisation vector remains orthogonal to the direction of propagation. The visibility of TM-TM interference fringes however, varies with the difference in angles $|\theta_1 - \theta_2|$ and is given by [69]:

$$V_{TM} = \cos(\theta_1 - \theta_2). \quad 2.4.47$$

As the angle of diffraction is determined only by the incident wavelength, λ , and grating pitch, p_G , the visibility can be written as

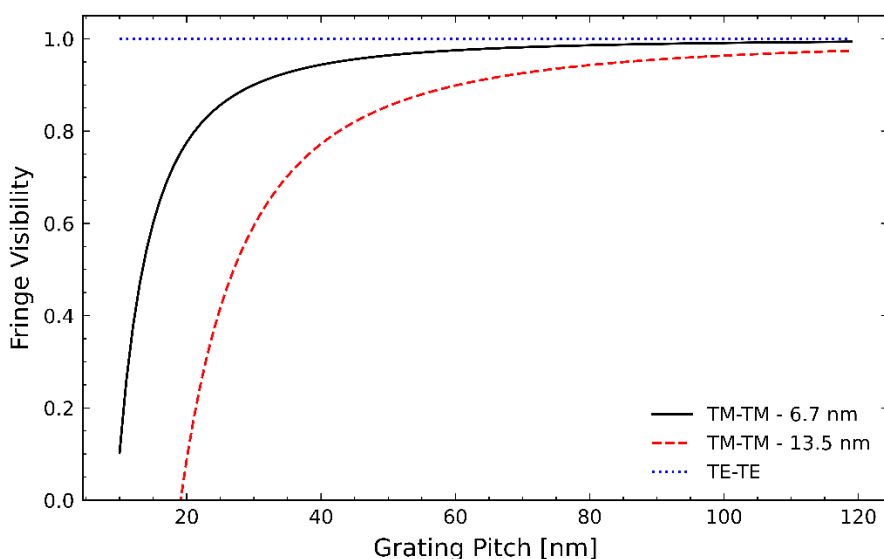


Figure 2.4.5: The visibility of interference fringes produced by TE-TE and TM-TM interference lithography at 13.5 nm and 6.7 nm as a function of grating pitch, calculated using Equation [Error! Reference source not found.](#). No loss of

visibility is seen for TE-TE polarised beams, and the loss of visibility for TM-TM polarised beams is dependent on the incident wavelength.

$$V_{TM} = 1 - 2 \left(\frac{\lambda}{p_G} \right)^2. \quad 2.4.48$$

Figure 2.4.5 shows the visibility as a function of grating pitch for 13.5 nm (EUV) and 6.7 nm (BEUV) for two-beam TM-TM lithography. It indicates that for a TM polarised incident beam, 6.7 nm light is less sensitive to polarisation dependent contrast reduction than a 13.5 nm beam with the same polarisation.

2.4.3 Interaction at BEUV Wavelengths

The interaction of light with matter can be described using the complex refractive index n :

$$n = 1 - \delta + i\beta = 1 - \frac{n_a r_e \lambda^2}{2\pi} f^0(\omega), \quad 2.4.49$$

where n_a is the atomic density per unit volume of the material, r_e is the classical electron radius, δ and β are both wavelength dependent, real numbers, which are much less than unity in magnitude [65]. The frequency dependent, complex scattering factor, $f^0(\omega)$, can be separated into real and complex components [35,81]:

$$f^0(\omega) = f_1^0(\omega) - i f_2^0(\omega). \quad 2.4.50$$

A database of real and complex scattering factors of elements from $Z = 1 - 92$ and photon energies from $h\nu = 50 - 30,000$ eV has been compiled, with f_1^0 being derived numerically and f_2^0 using theoretical models based on previously measured absorption spectra [99].

The absorption and phase shift of a wavefield after interaction with matter can be obtained from the β and δ components of Equation 2.4.49 respectively. The absorption of a wavefield incident on a slab of a single material of projected thickness, $T(x, y)$, and uniform density, propagating in the z direction, can be described by the Beer's law of absorption:

$$I(x, y, z = z_0) = \exp[-2k\beta T(x, y)]I(x, y, z = 0) \quad 2.4.51$$

where $I(x, y, z = z_0)$ is the intensity of the exit surface wavefield, and $I(x, y, z = 0)$ is the intensity of the incident wavefield. The phase shift introduced in the exit wavefield after the same interaction is given by [65]:

$$\Delta\phi = \frac{2\pi}{\lambda} \delta T(x, y). \quad 2.4.52$$

2.4.4 Diffraction Efficiency

The diffraction of incident light passing through a grating mask arises due to the spatially periodic modulation of the complex refractive index (Equation 2.4.49) inside the mask [100]. The groove profile of the grating determines its diffraction characteristics. Blazed gratings exhibit saw-tooth grooves and gratings using rectangular grooves are known as laminar gratings [101]. The *diffraction efficiency*, η , and how it varies with incident wavelength and spectral order ($m=0,1,2,\dots$) is an important measure of quality in a grating [102].

A single diffraction grating will diffract multiple beams or different orders, m , at angles, θ_m , given by Equation 2.2.1, leading to intensity peaks when viewed at an image plane (see Section 2.2, Figure 2.2.1). The spacing between the intensity peaks of each order is given by [103]:

$$\Delta x_m = \frac{\lambda z}{p_G} \left(\frac{1}{\cos \theta_m} + \frac{\sin^2 \theta_m}{\cos^3 \theta_m} \right), \quad 2.4.53$$

where p_G is the period of the grating and z is the distance from the grating to the image plane. The absolute diffraction efficiency, η_A , of a grating is the ratio of the intensity contained within a particular diffraction order, I_m , to the total intensity, I , of the incident wavefront. While the relative diffraction efficiency, η , is the ratio of I_m to the incident intensity contained within the area of the grating, I_{inc} , simply given by [102]:

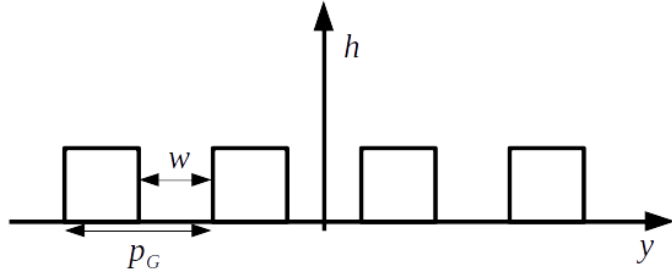


Figure 2.4.6: Line profile of the height of a single Laminar diffraction grating taken perpendicular to the grating lines. The period is p_G and the width of the transparent spacing is w .

$$\eta_m = \frac{I_m}{I_{inc}}$$

2.4.54

For transmission gratings the diffraction efficiency can be accurately described analytically providing the period of the grating is much larger than the incident wavelength ($p_G \gg \lambda$) and the grating is thin ($T \ll \lambda$). The relative diffraction efficiency of an ideal transmission grating of thickness, T , with groove width, w , is given by:

$$\eta_{m=0} = 1 - 4 \left(\frac{p_G}{w} \right) \left(1 - \frac{p_G}{w} \right) \sin^2 \left(\frac{\pi \Delta n T}{\lambda} \right),$$

2.4.55

and

$$\eta_{m \neq 0} = \left[\frac{\sin \left(\frac{m \pi p_G}{w} \right) \sin \left(\frac{\pi \Delta n T}{\lambda} \right)}{\frac{m \pi}{2}} \right]^2$$

2.4.56

where, Δn , is the change in refractive index between the transparent and opaque lines in the grating [100]. The profile of an ideal, square-wave, laminar transmission grating is shown in Figure 2.4.6. For such a grating the even orders have zero efficiency. Ignoring thickness effects, the expression for $\eta_{m \neq 0}$ simplifies to:

$$\eta_{m=odd} = \frac{w^2}{p_G^2} \operatorname{sinc}^2 \left(\frac{mw}{p_G} \right).$$

2.4.57

The term w/p_G is known as the duty cycle, f . For a transmission grating with a duty cycle $f = 0.5$, the first-order diffraction efficiency is $\eta_1 \approx 0.1013$, so approximately 10.13% of the intensity incident upon the grating is diffracted into the $m=1$ order beam.

An ideal phase grating can suppress the zero-order beam by introducing a π phase shift to the beam passing through the grating lines leading to destructive interference. This leads to an increase in first-order order diffraction efficiency for a phase mask with the geometry shown in Figure 2.4.6. For a phase grating with a duty cycle of 0.5, the relative efficiency is then

$$\eta_m = \text{sinc}^2\left(\frac{m}{2}\right), \quad \text{for } m \neq 0, \quad 2.4.58$$

and the maximum efficiency of the 1st order diffracted beam increases to $\approx 40.53\%$ [103]. The 1st order diffraction efficiency is of most importance for EUV-IL grating masks as we typically rely on interference between the $m = \pm 1$ beams from spatially separated gratings to form an aerial image.

Interference Lithography grating masks can contain multiple laminar gratings, arranged symmetrically about the centre of a grating mask (Figure 2.4.7). The number of gratings determines the number of interfering beams and the intensity pattern in the resulting aerial image. It also affects the absolute diffraction efficiency, η_A^{IL} , of an IL mask. For an n beam IL grating mask, assuming uniform, coherent illumination, the absolute diffraction efficiency is given by $\eta_A^{IL} = n\eta_A$ [6].

In the case of a linearly polarised incident beam, the diffraction efficiency will depend on the angle of polarisation in relation to the orientation of the grating (*TE-TE/TM-TM – See Section 2.4.2.4*). For an unpolarised incident beam the efficiency will fall between the TE and TM efficiencies [102].

Optimising diffraction efficiency is an important part of the EUV-IL mask development process. At wavelengths below 13.5 nm and grating pitch below tens of nanometres (required to realise the promised BEUV-IL patterning resolution), the condition

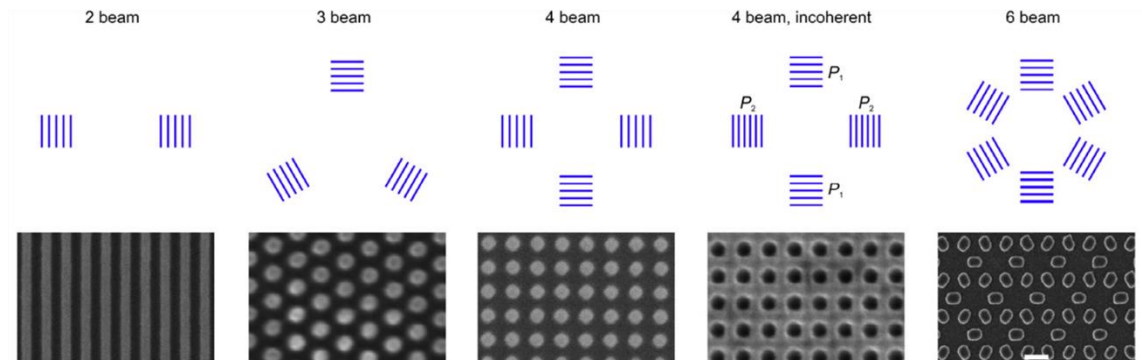


Figure 2.4.7: Interference lithography grating masks with multiple gratings and configurations (above), coupled with the resulting interference patterns generated (below). Reprinted from Microelectronic Engineering, Vol 143, N. Mojarrad, J. Gobrecht, Y. Ekinici, ‘Interference Lithography at EUV and Soft X-ray Wavelengths’, Page 56, Copyright 2015, with permission from Elsevier [4].

($p_G \ll \lambda$ and $T < \lambda$) is violated and Equation 2.4.56 is invalid. When the period of a grating is approaches the wavelength, it is necessary to solve Maxwell’s equations rigorously in order to accurately determine grating efficiency. Rigorous Coupled Wave Analysis (RCWA) is widely used for this purpose [104]. RCWA has been used to estimate diffraction efficiency and inform grating design for 13.5 nm and 6.5 nm lithography [105].

Limited work has been done to estimate the effects of fabrication artefacts on grating diffraction efficiency [106–108]. However, it has been found that at EUV, small variations in surface roughness may have a substantial impact on the diffraction efficiency due to scattering [109]. Consideration of artefacts in the mask surface is of particular importance as the grating pitch is reduced [110]. Some of the advantages of RCWA are lost for complex, aperiodic structures (such as a random rough surface) or illumination that can only be represented accurately by many Fourier components (representative of real sources) [111].

2.5 Computational Lithography

Computational Lithography is the process of using computational models to improve the patterning capabilities of lithographic processes. The advancement of computational lithography has been a major factor in the scaling of semiconductor devices in accordance with Moore’s law and EUV modelling has the potential to extend optical lithography scaling for future nodes [112].

The first model of a lithography process was the ‘ABC model’ of the image forming properties of a positive photoresist and this has served as a base for all future lithography

simulations [113]. Today, computational models for IL are able to accurately demonstrate the influence of wavefront phases in multiple-beam setups [40], asses the sensitivity of an Extreme Ultraviolet Interference Lithography (EUV-IL) pattern to alignment of the diffraction grating mask [32], and simulate EUV photoresist interactions to a level of complexity that takes into account contributions of photon absorption, random chemical reactions [114], and the effect of wavelength on line-edge roughness [22]. While not always the prominent method of a lithography experiment, computational lithography is often used in conjunction with IL systems to improve accuracy and validate models [77,115].

A complete computational lithography model would include an accurate representation the entire lithography process, including formation of an aerial image at the plane of a photoresist, the resist photochemistry, stochastic formation of a latent image in the resist, and the development process. This work will focus only on the aerial image formation process, as (for reasons outlined in Chapter 1) we are specifically interested in what lithographic performance can be achieved with the Apple II undulator source used at the Australian Synchrotron (AS) SXR-I beamline. Future metrology at the proposed X-ray Nanofabrication Facility (XRNF) will allow for direct aerial image characterisation and optimisation with respect to source properties, which will greatly aid research into mask requirements for future 6.7 nm sources.

Simulation of source and image formation is typically implemented through an analytical model. An analytical model is primarily quantitative and represents a system using a set of mathematical equations which are then solved for a final state [116]. These models typically omit higher-order effects, such as mask shadowing and topography, as they are assumed to have little impact on the image forming process. At short wavelengths, this assumption becomes less valid [22]. Analytical models also have difficulties representing imperfect optics [112]. For a complete understanding of the process from a source to the image plane a wavefront propagation model is necessary. Wavefront propagation models are able to simulate a Synchrotron beamline from the radiation emitted by electrons traversing an undulator source, (described in Section 2.3.1) to interactions with optical elements and along the beamline and finally arriving at the aerial image plane [117].

2.5.1 Computational Wavefront Propagation

Wavefront propagation models are being used increasingly to aid in the design, commissioning and experimental application of modern high-brightness and high-coherence light source facilities [118]. One widely used model that implements computational wavefront propagation is Synchrotron Radiation Workshop (SRW) [17]. SRW can compute radiation emitted from a relativistic electron moving through an arbitrary magnetic field. This radiation is then propagated using a near-field or far-field propagator depending on the distance from the source to the first optic. A series of propagation steps is implemented with propagators between elements and each optical element being represented with a transmission function [119]. The propagation is undertaken using discrete free-space propagators, explained in detail in Chapter 3.1.

The transmission functions representing all transmission geometry optical elements in this work follow the projection approximation. This assumes that an object is sufficiently thin so that any scattering occurring inside is weak enough to negligibly perturb the path of the radiation through the object [65]. The transmission function modifies the amplitude and phase of the wavefront differently at different horizontal and vertical positions in the plane in which the sample is located. For a material with uniform material composition and density, these transmission objects can be generated from a two-dimensional (x, y) map of the object thickness [119]. The exit surface wavefront can then be obtained by simply multiplying the initial wavefront by a transmission term, defined by the refractive index of the material, n , and the thickness, T [120]:

$$\psi_{exit\ surface} = \psi_{initial} \times \exp\left(-ik \sum_j \delta_j T_j\right) \times \exp\left(-k \sum_j \beta_j T_j\right).$$

2.5.1

2.5.2 Partially Coherent Representations

Recent computational models have developed sufficient complexity to allow for the representation of partially coherent wavefield propagation. 13.5 nm EUV plasma sources have been successfully modelled using ray tracing and a coupled wave theory (CWT) to simulate spatial coherence [121]. Temporal coherence effects have also been successfully

modelled for EUV [77], and EUV-IL using Monte Carlo sampling of a Lorentzian spectral distribution to investigate the effect on aerial image contrast [121].

Synchrotron Radiation Workshop (SRW) uses numerical free-space Fourier optics propagators to simulate light propagating through various optical systems [122]. SRW uses an analytical treatment of quadratic phase terms to reduce memory and CPU (compared to Fresnel free-space propagation) while maintaining accuracy. Thus, partially coherent simulations are undertaken in a fraction of the time of previous simulations using standard Fresnel propagation (described in Section 3.1) [118]. SRW has been used to implement detailed source-to-detector models to test coherent scattering. The results agree with experimentally measured intensity distributions in terms of speckle contrast and its dependence on beamline configuration [119]. Partially coherent simulations are done using a Monte-Carlo approach to average the single electron characteristics over the phase-space volume of the electron beam [122].

2.5.3 Computational Requirements & Limitations

A major limitation of computational lithography is the computational complexity of modelling optical systems and partially coherent beams [118]. In lieu of continuous representations, models must rely on discrete representations of wavefronts and optics. High-resolution models rely on sampling at higher spatial frequencies which increases the required time for executing a simulation [123]. A complete computation model of the image formation process in lithography is required to be able to model the characteristics of sources, non-ideal optics, partial coherence, and polarisation. Ideally this would require high spatial resolution, quantitative intensity, and phase distributions at every point in the beamline. Defects with lengths scales of ~ 1 nm would need to be modelled for beamline optics included in beamlines containing tens of elements over tens of meters.

For wavefront propagation implementing Fast-Fourier-Transforms (FFTs), such as Synchrotron Radiation Workshop (SRW), the numerical complexity, O , scales as $O[N\log(N)]$, where N is the total number of data points in each wavefront. This is further increased when partially coherent propagation methods are needed. In the case of partially coherent propagation in SRW, propagating the wavefront from N_e electrons, O , is given by [124]:

$$O[N_e N \log(N)].$$

2.5.2

This complexity greatly increases the computational time of simulations. For SRW simulations, the run time can be significantly reduced by using Python scripts instead of the in-built graphical user interface [122].

An important challenge for computational lithography is the simulation of defects in the photoresist and mask [125]. Although the treatment of masks is improving with new cleaning methods and thin-film coatings for masks (pellicles) there will always be defects to consider [126–128]. The effect of various types of defects on image formation depends on the wavelength of illumination, so at-wavelength metrology is required to identify and characterise defects. This is not widely available at BEUV wavelengths. The effects of mask surface roughness, LER, and other defects may be more important at shorter wavelengths. The role of partial coherence and polarisation should also be considered [24].

Chapter 3

Method of Wavefront Propagation and Aerial Image Quality Metrics

3.1 Wavefront Propagation

A light field can be described by a complex scalar wavefunction, $\Psi(x, y, z, t)$. This wavefunction can be separated into a superposition of monochromatic wavefields of frequency, ω , with real spatial components $\psi_\omega(x, y, z)$ and a time dependant component, $\exp(-i\omega t)$, using a Fourier transform:

$$\Psi(x, y, z, t) = \frac{1}{\sqrt{2\pi}} \int_0^\infty \psi_\omega(x, y, z) \exp(-i\omega t) d\omega.$$
3.1.1

Considering a light field in a 2 dimensional plane, each monochromatic component, $\psi_\omega = (x, y, z = 0)$, can then be further decomposed into a linear combination of plane wave components with spatial frequency, $k = \sqrt{k_x^2 + k_y^2 + k_z^2}$, over an area of phase space $dk_x dk_y$ [65]:

$$\psi_\omega(x, y, z = 0) = \frac{1}{2\pi} \iint \psi'_\omega(k_x, k_y, z = 0) \exp[i(k_x x + k_y y)] dk_x dk_y,$$
3.1.2

where ψ'_ω is representative of the Fourier transform, \mathcal{F} , of the wavefront ψ_ω and has the inverse property [67]:

$$\mathcal{F}^{-1}(\mathcal{F}(\psi_\omega)) = \mathcal{F}^{-1}(\psi'_\omega) = \psi_\omega.$$
3.1.3

For propagation in a vacuum, the wavefield at any parallel plane, $\psi_\omega(x, y, z > 0)$, can be found by multiplying each two dimensional plane wave in its Fourier decomposition with the free space propagator, $\exp[izk_z]$:

$$\psi_\omega(x, y, z > 0) = \frac{1}{2} \iint \psi'_\omega(k_x, k_y, z = 0) \times \exp[i(k_x x + k_y y)] \exp\left[iz\sqrt{k^2 - k_x^2 - k_y^2}\right] dk_x dk_y \quad 3.1.4$$

Equation 3.1.4 can be simplified using the angular spread representation, representing this process through free space diffraction in which each point in the wavefront propagates individually. This approach implements the diffraction operator, D_z :

$$D_z = \mathcal{F}^{-1} \exp\left[iz\sqrt{k^2 - k_x^2 - k_y^2}\right] \mathcal{F}, \quad 3.1.5$$

The propagated wavefront then becomes:

$$\psi_\omega(x, y, z) = D_z \psi_\omega(x, y, z = 0). \quad 3.1.6$$

Over small distances, we can assume that the each of the non-negligible components of the wavefront propagate with a small divergence with respect to the propagation distance. The wavefield is then considered paraxial, which leads to the binomial approximation:

$$\sqrt{k^2 - k_x^2 - k_y^2} \approx k - \frac{k_x^2 + k_y^2}{2k}, \quad 3.1.7$$

and the diffraction operator becomes:

$$D_z \approx D_z^F \equiv \exp(ikz) \mathcal{F}^{-1} \exp\left[\frac{-iz(k_x^2 + k_y^2)}{2k}\right] \mathcal{F}, \quad 3.1.8$$

where D_z^F is the Fresnel diffraction operator [65]. So, the propagated wavefield becomes:

$$\begin{aligned} \psi_\omega(x, y, z) &\approx D_z^F \psi_\omega(x, y, z = 0) \\ &= \exp(ikz) \mathcal{F}^{-1} \exp\left[-\frac{iz(k_x^2 + k_y^2)}{2k}\right] \mathcal{F} \psi_\omega(x, y, z = 0). \end{aligned} \quad 3.1.9$$

This operator is implemented for numerical wavefront propagation in SRW, as mentioned in Section 2.5.1. The Fresnel diffraction operator (Equation 3.1.8) can be rewritten using the convolution theorem

$$\mathcal{F}[f(x, y) * g(x, y)] = 2\pi \{\mathcal{F}[f(x, y)]\} \times \{\mathcal{F}[g(x, y)]\}, \quad 3.1.10$$

where $f(x, y) * g(x, y)$ is the two dimensional convolution of the two functions $f(x, y)$ and $g(x, y)$, defined by:

$$f(x, y) * g(x, y) = \iint_{-\infty}^{\infty} f(x', y') g(x - x', y - y') dx' dy'. \quad 3.1.11$$

The propagated wavefield can be obtained from the convolution of the unpropagated wavefield with, \mathcal{P} , the real-space form of the Fresnel diffraction operator. The propagated wavefield can then be written as:

$$\begin{aligned} \psi_{\omega}(x, y, z) &= \psi_{\omega}(x, y, z = 0) * \mathcal{P}(x, y, z) \\ &= -\frac{ik \exp(ikz)}{2\pi z} \left\{ \psi_{\omega}(x, y, z = 0) * \exp\left[\frac{ik(x^2 + y^2)}{2z}\right] \right\}, \end{aligned} \quad 3.1.12$$

where \mathcal{P} is given by:

$$\mathcal{P}(x, y, z) = -\frac{ik \exp(ikz)}{2\pi z} \exp\left[\frac{ik(x^2 + y^2)}{2z}\right]. \quad 3.1.13$$

Using the convolution formula (Equation 3.1.11), Equation 3.1.12 can be written in a convenient form for numerically computing diffraction:

$$\begin{aligned} \psi_{\omega}(x, y, z) &= -\frac{ik \exp(ikz)}{2\pi z} \iint_{-\infty}^{\infty} \psi_{\omega}(x', y', z = 0) \\ &\quad \times \exp\left[\frac{ik}{2z} [(x - x')^2 + (y - y')^2]\right] dx' dy'. \end{aligned} \quad 3.1.14$$

Rearranging and expanding, the propagated wavefront can then be written as:

$$\begin{aligned}\psi_\omega(x, y, z) = & -\frac{ik \exp(ikz)}{2\pi z} \exp\left[\frac{ik}{2z}(x^2 + y^2)\right] \iint_{-\infty}^{\infty} \psi_\omega(x', y', z=0) \\ & \times \exp\left[\frac{ik}{2z}(x'^2 + y'^2)\right] \exp\left[-\frac{ik}{z}(xx' + yy')\right] dx' dy'.\end{aligned}\quad 3.1.15$$

For propagation over distances much greater than the length scale of the unpropagated wavefield, the $\exp\left[\frac{ik}{2z}(x'^2 + y'^2)\right]$ term in Equation 3.1.15 can be ignored and the Fraunhofer diffraction integral can be used to calculate the propagated wavefield [65]:

$$\begin{aligned}\psi_\omega(x, y, z) \approx & -\frac{ik \exp(ikz)}{2\pi z} \exp\left[\frac{ik}{2z}(x^2 + y^2)\right] \\ & \times \iint_{-\infty}^{\infty} \psi_\omega(x', y', z=0) \exp\left[-\frac{ik}{z}(xx' + yy')\right] dx' dy'.\end{aligned}\quad 3.1.16$$

For a monochromatic wavefield with wavelength, λ , that has a non-negligible magnitude only over a region of space with maximum dimension, σ_{max} , the minimum propagation distance, z_p , for the Fraunhofer diffraction integral to be valid is given by the relation

$$\frac{\sigma_{max}}{\lambda} \ll z_p. \quad 3.1.17$$

3.1.1 Discrete Fourier Sampling

The discrete Fourier transform (DFT) is the implementation of the Fourier transform seen in Section 3.1 through sampled data of a finite step size [129]. For a continuous wavefront, the DFT sampled at N intervals is given by [130]:

$$\mathcal{F}\{\psi[x, y]\} = \psi'[k_x, k_y] = \sum_{x=0}^{N-1} \sum_{y=0}^{N-1} \psi[x, y] \exp\left(\frac{2\pi i(k_x x + k_y y)}{N}\right). \quad 3.1.18$$

A method for reducing the computational time while obtaining the same results of a DFT is the Fast Fourier Transform (FFT) [131]. For a FFT to sufficiently represent a continuous wavefront it must be adequately sampled. The sampling requirement is given

by the Nyquist frequency, W , which is defined as twice the highest frequency present in the wavefront [132]. Inadequately sampling images will result in aliasing, and folding in of information containing spatial frequencies outside of those represented in the sampled data [133]. A wavefield in Fourier space will be adequately sampled in two-dimensions if the following condition is satisfied:

$$\left(\frac{N}{W}\right)^2 \geq 2 \rightarrow N \geq \sqrt{2}W.$$

3.1.19

The sampling frequency must be sufficiently greater than the Nyquist frequency to satisfactorily represent phase [134]. For an electric field extending a distance, σ_{max} , in space, the sampling interval is defined as:

$$dN = \frac{\sigma_{max}}{N}.$$

3.1.20

When propagating the wavefield over a distance Δz , sufficient sampling by Equation 2.4.19 requires that the phase shift between adjacent points is less than π . It can be shown that the minimum sampling interval for a paraxial field propagated through free space is then:

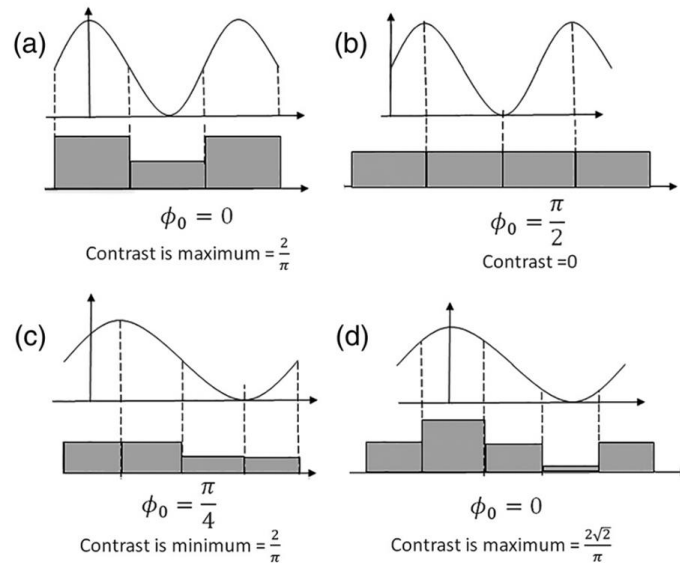


Figure 3.1.1: The effect of discrete sampling on the contrast of an intensity distribution with different initial phase ϕ_0 . Reprinted from Journal of Electronic Imaging, Vol 27, No 1, T. Battula et al, 'Contrast Computation Methods for Interferometric Measurement of Sensor Modulation Transfer Function', Page 4, Copyright 2018, with permission from SPIE [135].

$$dN \leq \frac{\Delta z \lambda}{\sigma_{max}}.$$

3.1.21

As shown in Figure 3.1.1, inadequate sampling of an aerial image intensity distribution may lead to errors in the measured contrast due to the phase of the wavefront [135].

3.1.2 Implementation of Wavefront Propagation

In Synchrotron Radiation Workshop (SRW), Synchrotron Radiation (SR) is propagated using Scalar Diffraction theory through Fourier Optics methods. The wavefield is represented by the transverse components of the complex electric field, $\vec{E}_\perp(x, y, z)$, and paraxial propagation is implemented using discrete FFTs as discussed in Section 3.1.1 [136]. The direct approach of Equation 3.1.14 to propagate a wavefield between two planes requires very high-density sampling as explained in Section 3.1.1. Special cases can be identified for which approximations can reduce the computational cost. The special cases that are implemented in SRW are described in Table 3.1. Propagator number 1 in SRW uses a method to reduce sampling density requirements outlined in Section 3.1.1 which saves considerable memory and increase CPU performance compared to propagator #0 (Table 3.1) [137], which uses Equation 3.1.14. A full description of the method can be found in Ref. 118. This method, named the Quadratic Term Propagator, assumes the unpropagated electric field has a quadratic term in its phase, and has the form:

Table 3.1: Propagators used in SRW, and the corresponding equation used to implement the propagation.

Case	Propagator Number	Method	Equation
Standard Propagation	0	Two FFTs	3.1.14
Moderate Propagation (Assuming Quadratic Phase)	1	Two FFTs	3.1.24
Far-field Propagation	2	One FFT	3.1.16
Propagation from Waist	3	One FFT	
Propagation to Waist	4	One FFT	

$$E_{\perp}(x, y, z = 0) = U_{\perp}(x, y, z = 0) \exp \left\{ \frac{ik}{2} \left[\frac{(x - x_0)^2}{R_x} + \frac{(y - y_0)^2}{R_y} \right] \right\}, \quad 3.1.22$$

where R_x, R_y are the radii of wavefront curvature in the horizontal and vertical planes, and (x_0, y_0) are the coordinates of the centre point. Substituting Equation 3.1.22 into Equation 3.1.14, rearranging and applying the convolution theorem (Equation 3.1.10) gives:

$$\begin{aligned} U_{\perp}(x, y, z) &\approx \frac{k^2 \exp(ikz)}{(2\pi)^2} \left[\frac{R_x R_y}{(R_x + z)(R_y + z)} \right]^{\frac{1}{2}} \iint_{-\infty}^{\infty} U'_{\perp}(\theta_x, \theta_y, z = 0) \\ &\times \exp \left[-\frac{ikz}{2} \left(\frac{R_x}{R_x + z} \theta_x^2 + \frac{R_y}{R_y + z} \theta_y^2 \right) \right] \exp \left[ik \left(\frac{R_x x + zx_0}{R_x + z} \theta_x + \frac{R_y y + zx_0}{R_y + z} \theta_y \right) \right] dk_x dk_y \end{aligned} \quad 3.1.23$$

where $U'_{\perp}(\theta_x, \theta_y, z = 0)$ is the Fourier transform of the unpropagated electric field after subtraction of the quadratic phase terms (shown in Equation 3.1.22), $U_{\perp}(x, y, z = 0)$. The propagated electric field can then be found from:

$$E_{\perp}(x, y, z) = U_{\perp}(x, y, z) \exp \left\{ \frac{ik}{2} \left[\frac{(x - x_0)^2}{R_x + z} + \frac{(y - y_0)^2}{R_y + z} \right] \right\}. \quad 3.1.24$$

The quadratic terms are often the dominant terms in the complex electric field phase and define the divergence of the beam. In order to accurately propagate using discrete FFTs the electric field must be sampled so that all oscillations are resolved, so by subtracting the quadratic phase terms from the unpropagated electric field before applying FFTs, the sampling requirements of the unpropagated wavefield are greatly reduced and the memory requirements and CPU efficiency are improved drastically [118,137]. In some cases the CPU efficiency of fully-coherent propagation implemented in SRW is even higher than the efficiency of geometrical ray-tracing simulations, which typically emit wave-optical effects and require additional code to describe source properties [138].

In the case in which the beam is being propagated to or from a waist (a sufficiently small aperture), the quadratic term propagators cannot be effectively applied. This

limitation is due to phase effects that occur as the beam passed through its focus. In the case of propagation to a waist the problem arises when [118]:

$$R_x + \Delta z = 0, \quad R_y + \Delta z = 0,$$

3.1.25

where R_x and R_y are the radii of curvature of the wavefront in the horizontal and vertical planes. For propagation from a waist the problem is due to there being no significant quadratic phase terms. To circumvent this problem, new values of R_x and R_y are chosen that only slightly deviate from the actual values but also make sure the relation in Equation 3.1.25 is not satisfied.

The wavefield after propagation through an optical element can be written in a general form as [18]:

$$E(x, y, z, \omega) \approx \iint dx' dy' \mathcal{K}(x, y, x', y', \omega) E(x', y', z = 0, \omega),$$

3.1.26

where \mathcal{K} is the kernel, which for free space is [139]:

$$\mathcal{K}(x, y, x', y', \omega) \approx -\frac{ik}{2\pi\Delta z} \exp\left[\frac{ik}{2\Delta z} [(x - x')^2 + (y - y')^2]\right].$$

3.1.27

By altering the kernel, propagation through any element can be achieved. Most optical elements in a beamline are considered thin optical elements satisfying the projection approximation. For propagation through these elements the kernel can be written as:

$$\mathcal{K}(x, y, x', y', \omega) \approx \mathbf{T}(x', y', \omega) \delta(x' - x) \delta(y' - y)$$

3.1.28

where $\mathbf{T}(x', y', \omega)$ is the complex transmission function for the element and δ is the delta function. For thin elements the transmission function determines the wavefield at the exit plane, for extended optical elements such as mirrors and gratings the kernel from the above equation does not hold. In such cases a new kernel is defined depending on the specific element, as outlined in detail in [18].

3.1.3 Partially Coherent Propagation

While fully coherent propagation is implemented in SRW through the propagation of radiation emitted by a single relativistic electron traversing an undulator (Equation 3.1.29), partially-coherent propagation can be undertaken by extending the simulation to the spontaneous emission from the entire electron beam [122,124,138,140,141]. The complex electric field of the emitted radiation resulting from a single electron with instant relative velocity, $\vec{\beta}(\tau)$, is given by [139]:

$$\vec{E}_0 = \frac{ie\omega}{c} \int_{-\infty}^{\infty} \left[\vec{\beta}(\tau) - \vec{n}(\tau) \left[\frac{1+ic}{\omega R(\tau)} \right] \right] R^{-1}(\tau) \exp \left[i\omega \left(\tau + \frac{R(\tau)}{c} \right) \right] d\tau, \quad 3.1.29$$

where, ω , is the cyclic frequency, $\vec{n}(\tau)$, is the unit vector in the direction from electron position to observation point, $R(\tau)$, is the distance from electron to observation point, τ , is the integration variable with respect to time, c , is the speed of light and, e , is the electron charge.

The spectral photon flux per unit surface of radiation emitted by the entire electron beam can be separated by contributions from temporally coherent, I_{CSR} , and incoherent, I_{ISR} , radiation, and is described by:

$$\frac{dN_{ph}}{dtd\Sigma(d\omega/\omega)} = \frac{c^2\alpha I_e}{4\pi^2 e^3} (I_{ISR} + I_{CSR}), \quad 3.1.30$$

where, I_e is the electron beam current, N_{ph} , is the number of photons and, α , is the fine-structure constant. Since electron bunch lengths in storage rings are typically much greater than the wavelength of radiation emitted (in the order of sub-mm to cm), each emission is therefore temporally incoherent in the spectral range from infrared to hard x-rays. This means the dominant contribution in Equation 3.1.30 comes from temporally incoherent radiation [142], which can be calculated by averaging the squared amplitude of the electric field from each electron over the phase space area of the electron beam. The total electric field, $\langle |\vec{E}_\omega| \rangle$, can be obtained from [143]:

$$\begin{aligned}
\langle |\vec{E}_\omega|^2 \rangle &= I_{ISR} + I_{CSR} \\
&= \int \left| E_{\omega 0} \left(x, y, x_{e0}, y_{e0}, z_{e0}, x'_{e0}, y'_{e0}, \delta\gamma_{e0} \right) \right|^2 \\
&\quad \times f \left(x_{e0}, y_{e0}, z_{e0}, x'_{e0}, y'_{e0}, \delta\gamma_{e0} \right) dx_{e0} dy_{e0} dz_{e0} dx'_{e0} dy'_{e0} d\delta\gamma_{e0} \\
&\quad + (N_e - 1) \left| \int E_{\omega 0} \left(x, y, x_{e0}, y_{e0}, z_{e0}, x'_{e0}, y'_{e0}, \delta\gamma_{e0} \right) \right. \\
&\quad \left. \times f \left(x_{e0}, y_{e0}, z_{e0}, x'_{e0}, y'_{e0}, \delta\gamma_{e0} \right) dx_{e0} dy_{e0} dz_{e0} dx'_{e0} dy'_{e0} d\delta\gamma_{e0} \right|^2
\end{aligned}$$

3.1.31

where, N_e , is the number of electrons, $x_{e0}, y_{e0}, x'_{e0}, y'_{e0}$, are the horizontal and vertical coordinates in phase space of each electron and, $\delta\gamma_{e0}$, is the relative energy and z_{e0} is the initial longitudinal position. The function $f(x_{e0}, y_{e0}, z_{e0}, x'_{e0}, y'_{e0}, \delta\gamma_{e0})$, is known as the particle density function which is assumed to be normalised to 1 when integrated so that, $\int f \left(x_{e0}, y_{e0}, z_{e0}, x'_{e0}, y'_{e0}, \delta\gamma_{e0} \right) dx_{e0} dy_{e0} dz_{e0} dx'_{e0} dy'_{e0} d\delta\gamma_{e0} = 1$ [139]. Equation 3.1.31 may be simplified for cases in which the horizontal and vertical motion as well as the energy of the electron are uncorrelated [144], or when the squared electric field amplitude does not depend on all 6 phase space variables [139].

Random initial phase space coordinates of each electron are generated using the Monte-Carlo method [144,145], with more electrons needed to accurately represent electron beams with greater emittance and therefore less coherence [143]. The propagation of the electric field of each electron is done coherently, using the methods outlined in Section 3.1.2, so no modification to the propagators in Table 3.1 is needed. The partially coherent intensity after propagation is then calculated by averaging the intensity distributions from propagated electric fields from each electron, seeded over the phase space inhabited by the beam [122,138,146–149].

The main obstacle with the Monte-Carlo method is the low computational efficiency, especially in cases of large electron beam emittance [138], in which the number of electrons

needed to accurately represent the source could be in excess of one hundred thousand [144]. Some of this difficulty can be overcome since the electric fields from each electron are independent and so the process is easily parallelized with multiple processors on servers or computer clusters with multiple cores [122,139].

3.2 Polarisation

Linear polarisation at an arbitrary angle, χ , can be achieved by altering the amplitude of the horizontal and vertical magnetic field components of the undulator, B_x and B_y using the relation [150]:

$$\chi = \tan^{-1} \left(\frac{B_x}{B_y} \right).$$

3.2.1

In physical undulators this is controlled through varying the phase shift of the relative rows of undulator magnets as described in 2.3.1, while in the SRW code the values of each magnetic field component can be entered directly. As long as the peak magnetic field magnitude, $|B|$, is kept constant, the deflection parameter, K , (given by Equation 2.3.4) will be unchanged,

where:

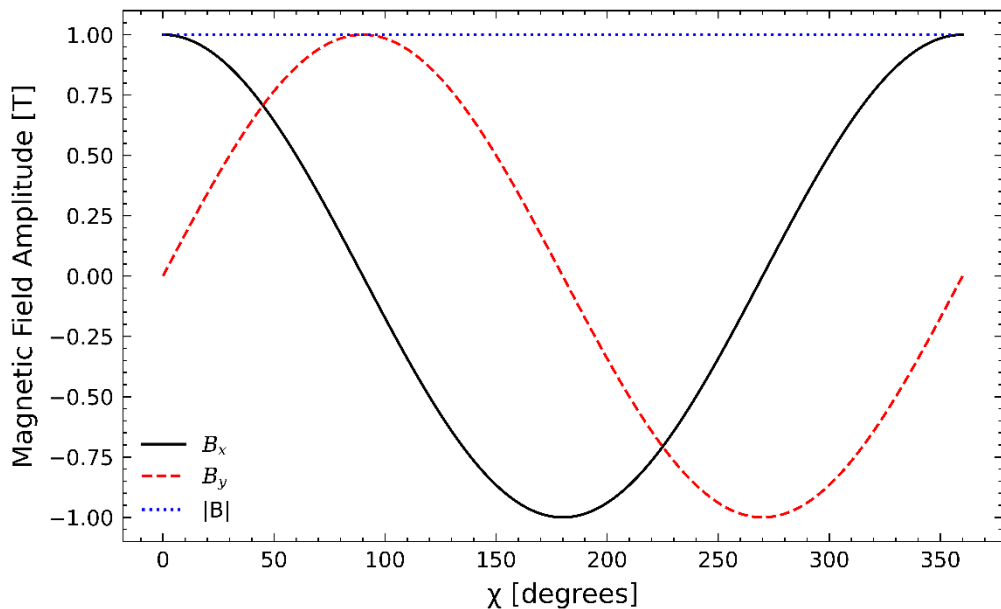


Figure 3.2.1: The relationship between each magnetic field component B_x , B_y and the angle of polarisation of the beam, for a constant peak magnetic field $|B|$.

$$|B| = \sqrt{B_x^2 + B_y^2}.$$
3.2.2

the relationship between each magnetic field component and the polarisation angle is shown in Figure 3.2.1.

Circular polarisation states can be created by setting, $B_x = B_y$, and adding a phase offset of $\pi/2$ to either magnetic field component as described in Section 2.3.1. With elliptical polarisation resulting $B_x \neq B_y$.

A partially polarised beam can then be created by summing the stokes parameters of multiple linearly polarised beams with varied polarisation angles. Unpolarised light¹ can be represented by the sum of just two independent beams of light with equal intensity and perpendicular polarisation states [151].

3.3 Photomask Surface Roughness

Non-ideal mask properties must be taken into consideration when designing EUV/SXR lithography systems. Surface roughness in a grating mask will introduce phase variations in the transmitted wavefront. The amount of variation introduced will depend on the material properties of the mask, such as refractive index (shown in Section 2.4.3) and thickness.

EUV mask roughness is known to lead to increased line-width roughness (LWR) in the patterns produced in the photoresist [135]. In this work we are concerned with transmission grating masks (see Section 2.4.4) that consist of two thin layers: the absorber and substrate. Roughness at the surface of each layer may result from the fabrication processes. Surface roughness can be modelled as either deterministic or random. Deterministic roughness profiles are modelled with a simple periodic modulation of the material, which is easy to implement but does not accurately represent real surfaces [152].

¹¹ The single APPLE-II undulator in use at the SXR-I beamline at the Australian Synchrotron is unable to create an unpolarized source. An unpolarized source can be created by using two APPLE-II undulators back-to-back, which is the case at the Diamond Light Source referenced in [150].

The typical measurement for surface roughness is the RMS roughness σ , given by the standard deviation of surface height:

$$\sigma = \left[\frac{1}{N} \sum_{x=0}^N Z(x)^2 \right]^{1/2}.$$

3.3.1

RMS roughness is an important parameter used to characterise the quality of optical surfaces and its effects are widely studied in the design and optimisation of coherent X-ray beamlines [43,126]. However, a variety of surface structures with correlation over different length scales may have the same RMS value. Rough surfaces with height correlation representative of that found due to fabrication artefacts can be modelled analytically [153]. Correlation lengths in each direction in the surface plane of a photomask may be defined as the average distance between two points with the same surface height. Correlated roughness may be generated by constructing a randomly rough surface with the distribution of heights at each pixel given by a Gaussian distribution, with height given by σ , and a variable width. By convolution with a Gaussian of width equal to the correlation length in x and y a roughness profile with variable correlation lengths can be generated [152].

3.4 Aerial Image Evaluation and Quality Metrics

The quality of a lithographic process is determined by many interacting properties related to the source, optics, mask, photoresist, and wafer. In this work we are interested in only the lithographic quality of the EUV-IL aerial image, which should be maximised in the optimisation of source and optical parameters. We are also interested in quantitative evaluation of the effect of mask roughness. It is desirable to identify a figure-of-merit that can be used to compare the lithographic quality of aerial images. Lithographic quality is usually determined from morphological characterisation of the pattern transferred to the photoresist [153]. It may be possible that contributions to pattern quality from processes associated with the exposure and development of the resist can be evaluated and separated from the aerial image with carefully designed experiments and models [155]. However, the process to do so is complex, and depends on the availability of appropriate resist models. The measurement process itself may even introduce particular sources of systematic error [156]. Alternatively, some figures of merit that are widely discussed in the literature

can be applied to evaluate the quality of the aerial image. In this Section, several metrics that can be used to evaluate the quality of an aerial image interference pattern or grating are introduced. In Chapter 6 the suitability of these metrics is investigated in terms of their quality as figures of merit for aerial image formation evaluation.

3.4.1 Normalized Image Log-Slope

The slope of the intensity profile in an aerial image as a function of its position is a measure of the rate of transition between dark and light fringes. For this to be a useful metric it must first be normalised by dividing by the intensity at the point of measurement. The position coordinate is then normalised as well by multiplying the obtained log-slope by the nominal linewidth, w , to obtain the Normalized Image Log-Slope (NILS) [155]:

$$NILS = w \frac{d\ln(I)}{dx} \quad 3.4.1$$

The NILS is the industry standard for assessing the usefulness of an aerial image in patterning a photoresist [156]. The NILS has been used to evaluate the effects of numerical aperture, wavelength, feature size, and objective comparison of different lithographic tools through its relationship with focus. As focus increases the slope of the intensity of an aerial image also increases, and the higher the slope of the intensity the better the patterning ability of the aerial image [157].

3.4.2 Line Edge and Line Width Roughness

For a two-dimensional representation of a nanostructured surface, the deviation of the actual edge contour from a straight line is described by the edge roughness. For structures defined by lines and spaces such as IL grating masks and aerial images, this is classified by the line edge roughness (LER), and line width roughness (LWR). LER describes the variation in the line centre position, while LWR describes the variation in width [158]. As EUVL moves to smaller critical dimensions, the acceptable LWR and LER is decreased [110,159,160], and so further progress is needed in understanding the principle causes. In the past, LER has been considered primarily in the pattern produced in the photoresist. However, it has been shown that mask surface roughness introduces LER into an aerial

image due to phase variations introduced [161–163]. The extent to which surface roughness in the grating mask contributes to LER is not fully understood [110].

Estimates of LER and LWR for EUV-IL aerial images can be obtained through measurements of two-dimensional intensity distribution. The LWR calculations in this work follow the method outlined by I. Mochi *et al* [154], for analysis of scanning electron microscopy (SEM) images of lithographic patterns. The LWR of the aerial image is estimated through calculation of the average standard deviation of the intensity line widths. If the trailing and leading edge profiles of the i^{th} intensity fringe are defined as $T_i(x)$ and $L_i(x)$ respectively, and $1 < x < M$ is the pixel coordinate of the profiles, the line width profile, $W_i(x)$, can be calculated as

$$W_i(x) = T_i(x) - L_i(x).$$

3.4.2

For an aerial image containing N intensity fringes, the average standard deviation all the lines in the image, $\bar{\sigma}$, is then

$$\bar{\sigma} = \frac{1}{N} \sum_{i=1}^N \sqrt{\frac{1}{M-1} \sum_{x=1}^M (W_i(x) - \mu_i)^2}$$

3.4.3

where μ_i is the average calculated line width. The LWR is then calculated as

$$LWR = 3\bar{\sigma}.$$

3.4.4

As pointed out in Ref. 156, the LWR as defined by Equation 3.4.4 is affected by systematic errors that arise from the measurement, typically by SEM, of the pattern transferred to a wafer. Low spatial frequency components of the LWR are not sampled in the measurement of a small area of the pattern, while the presence of high-frequency noise in the SEM image causes an overestimate of LW [164,165]. For the analysis of simulated aerial images in this work, it is assumed that these effects can be neglected.

3.4.3 Contrast

Contrast is the most widely used method for evaluating the quality of interference generated by a grating as it depends on many technical factors [166]. Contrast of the aerial image in interference lithography is an important property because higher aerial image contrast generally leads to lower LER and LWR in the pattern transferred to the photoresist [167,168]. While the contrast of an interference pattern is important, so too is the contrast of the mask itself. In this work we consider only binary gratings that have a simple periodic structure as described in Section 2.4.4.

Mask contrast may be measured from a line profile of the thickness of the grating perpendicular to the grating lines (Shown in Figure 2.4.6). A grating with perfect contrast will have zero height inside the grooves of the grating and a constant height everywhere else. Mask contrast is related to diffraction efficiency as the efficiency of a grating is dependent on the thickness, as mentioned in Section 2.4.4. The definition of mask contrast may extend to the case of a non-ideal binary mask, such as one that includes defects in the absorber or substrate. Defects in the mask will change contrast measurement of the mask as they will alter the measured height profile.

3.4.3.1 Michelson Contrast

The Michelson contrast of an image is often referred to as the visibility, V , and is the standard method of evaluating the quality of interference fringes [166]. V is explained in section 2.4.1.2, defined by Equation 2.4.11. Using only the Michelson contrast as a metric for image quality can have disadvantages. For an oscillating intensity pattern the extreme values recorded will depend on the sampling frequency compared to the fringe period and whether there is a phase offset present, seen in Figure 3.1.1 [135]. As the Michelson contrast relies on extreme values, it is sensitive to noise [166].

3.4.3.2 Root Mean Squared Contrast

The Root Mean Squared (RMS) Contrast, C_{RMS} , is a less noise sensitive method for calculating the apparent contrast of an interference pattern or grating [169]. The RMS contrast is the standard deviation of the intensity values, I , measured in an image of N

pixels. It is calculated by normalising the intensity and computing the mean value, defined in Equation 3.4.5. The RMS Contrast for an aerial image in interference lithography can be computed from an entire two-dimensional image or by taking a line profile perpendicular to the grating structure [170]:

$$C_{RMS} = \sqrt{\frac{1}{N} \sum_{x=0}^N \left[\frac{I(x) - \bar{I}}{\bar{I}} \right]^2}. \quad 3.4.5$$

3.4.3.3 Fourier Contrast

The Fourier contrast is a method for determining the contrast from the relative amplitude of the fundamental spatial frequency of an image. The amplitude of the fundamental is found from a discrete FFT of the intensity profile over the direction perpendicular to the interference fringes [171]. The contrast, $C_{Fourier}$, is obtained from:

$$C_{Fourier} := \frac{\sqrt{2 \sum_k |\psi'[k_y]|^2 - |\psi'[0]|^2}}{|\psi'(0)|}, \quad 3.4.6$$

where, ψ' , is the continuous, one-dimensional wavefront intensity profile, k_y is the wavevector component perpendicular to interference fringes and $\psi'[k_y]$ is the discrete FFT of ψ along k_y . The factor $\sqrt{2}$ is included for direct comparison to Michelson Contrast [135].

A method of optimising Fourier contrast has been demonstrated to be useful in locating the image plane in a lithographic-quality imaging system [172]. The benefit of the Fourier contrast method is that it is insensitive to noise however the calculation can be time-consuming [166]. The frequencies obtained can also show spectral leakage if the pixel width used does not fit the spatial frequency in an integer number , this appears as a broadening of the peaks in the discrete FFT [135].

3.4.3.4 Integrated Optical Density

Optical density was first introduced as a measure of the quality of a photographic negative [173]. The perfect negative was one that showed a linear variation of optical density with

the log of exposure, and negatives which quickly changed from low to high optical density when exposed were deemed high contrast [155]. The integrated optical density is obtained by generating a histogram of the recorded intensity values across an image. For an image with N pixels and G distinct intensity values, a histogram is drawn by finding the number, H , of pixels that have a recorded intensity value, i , and plotting $H(i)$ against i . From this we can find the integral optical density, defined by [166]:

$$I_{od} = \sum_{i=0}^{G-1} iH(i). \quad 3.4.7$$

The contrast of an image is directly related to the optical density, if the optical density is too high or low the image is unbalanced and the contrast will be low, in this way the optical density can represent the global performance of an image. For an image to have maximum contrast it must contain exactly half of its pixels at its maximum intensity value and half at the minimum value. The integrated optical density of such an image depends only on the total number of intensity values and the number of pixels:

$$I_{od_max} = \frac{G - 1}{2} N. \quad 3.4.8$$

By relating the measured optical density to its theoretical maximum, the contrast of imbalance, C_{im} , can be obtained:

$$C_{im} = \begin{cases} \frac{I_{od}}{I_{od_max}}, & I_{od} \leq I_{od_max} \\ 2 - \frac{I_{od}}{I_{od_max}}, & I_{od} \geq I_{od_max} \end{cases}. \quad 3.4.9$$

This measure of contrast is inaccurate for analysing images with a low dynamic range, as they would be found to have high contrast.

3.4.3.5 Mean Dynamic Range

The dynamic range of an aerial image is defined as the difference between the lower and upper bound intensity values. This simple measure does not reflect anything inside the most extreme values and can be easily affected by noise in an image and thus is not

practically useful [174]. The mean dynamic range is found by first separating the histogram of intensity levels referred to in Section 3.4.3.4 into upper and lower parts, divided along the mean intensity level value, μ , given by:

$$\mu = \frac{\sum_{i=0}^{G-1} i H(i)}{\sum_{i=0}^{G-1} H(i)}. \quad 3.4.1_0$$

The average intensity value of each part is then calculated in a similar way:

$$I_{lower} = \frac{\sum_{i=0}^{\mu} i H(i)}{\sum_{i=0}^{\mu} H(i)}, \quad I_{upper} = \frac{\sum_{i=\mu}^{G-1} i H(i)}{\sum_{i=\mu}^{G-1} H(i)}. \quad 3.4.1_1$$

The mean dynamic range is then given as

$$C_{MDR} = \frac{I_{upper} - I_{lower}}{I_{upper} + I_{lower}}. \quad 3.4.1_2$$

This method is noise sensitive and is inaccurate as a measure of contrast for images containing mostly dark pixels with small areas of high intensity. However, combining, C_{MDE} , with, C_{im} , leads to a composite measure of contrast, $C_{composite}$, which is superior to each separate method and represents both balance of intensity and dynamic range:

$$C_{composite} = C_{MDR} \cdot C_{im}. \quad 3.4.1_3$$

Composite contrast will only reach a maximum value when both, C_{MDE} , and C_{im} , are at a maximum simultaneously so it is not affected by noise values that have a low number of occurrences or are at a low intensity. This method is limited when the fringe pattern being analysed is dominated by noise as it will then only represent the contrast of the noise instead of the intensity fringes [166].

3.5 Validation of Contrast and Quality Metrics

While the contrast of intensity fringes resulting from TE-TE polarised radiation is independent of grating spacing, at BEUV wavelengths the contrast of aerial images produced by TM-TM polarised incident light is expected to decrease significantly for masks with grating pitch, p_G , below ~ 20 nm (outlined in Section 2.4.2.4). Figure 3.5.1 shows aerial

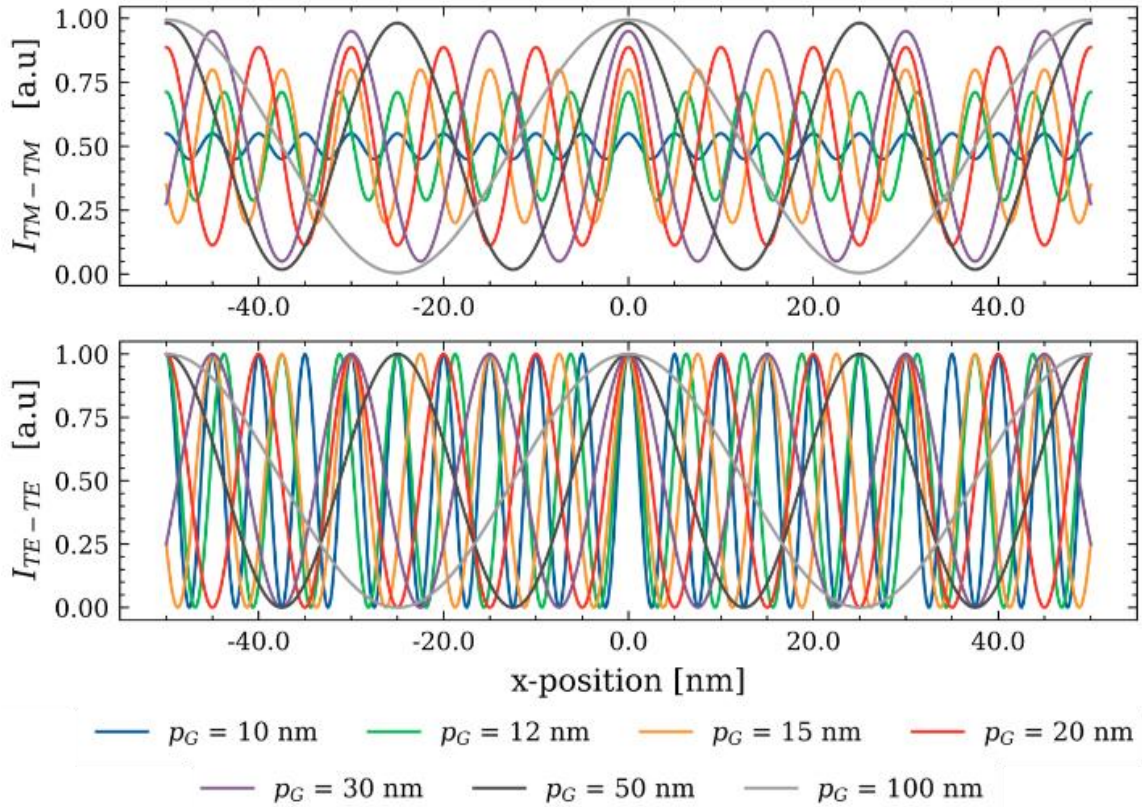


Figure 3.5.1: Aerial image intensity fringes resulting from TM-TM (top) and TE-TE (bottom) polarised BEUV radiation incident on IL grating masks with varied pitch (p_G). Below 20 nm pitch the visibility of fringes produced by TM-TM polarised beams is highly dependent on p_G , while the visibility of fringes produced by TE-TE polarised beams is independent of grating pitch.

images produced by gratings with varied pitch, generated from Equation 2.4.44 and Equation 2.4.45 to evaluate the accuracy of each contrast metric in analysing polarisation dependant aerial images. The accuracy of each metric in the presence of high noise in the aerial image, as shown in Figure 3.5.3 was also evaluated.

The Michelson, RMS, and NILS metrics exhibit the expected decrease in contrast for TM-TM polarised incident radiation and constant contrast for TE-TE polarisation. As shown in Figure 3.5.2, the Fourier, composite, and imbalance contrast metrics do not follow the expected contrast reduction for TM-TM polarised beams or the constant contrast for TE-TE polarised beams as shown in Figure 2.4.5. The Fourier contrast shows unexpected variation for both TE-TE and TM-TM polarised aerial images, which can be attributed to a combination of the finite size of the aerial images and the constant spatial sampling, leading to errors in the calculated spatial frequency for some aerial images. The imbalance and composite contrast metrics are not correlated with changes in contrast in TM-TM aerial

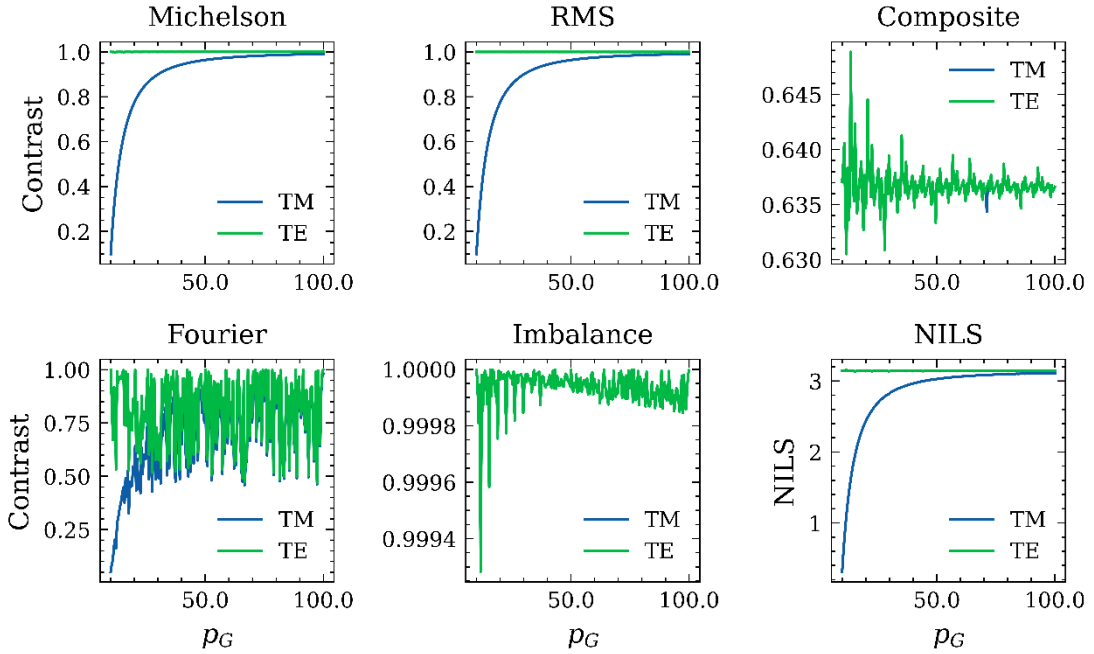


Figure 3.5.2: Contrast of ideal TE-TE (labelled TE) and TM-TM (labelled TM) polarised IL aerial images, shown in Figure 3.5.1, measured by each metric outlined in this chapter. The expected relationship between grating pitch and contrast is seen only in Michelson, RMS and NILS contrast metrics, while Fourier, Composite and Imbalance contrast methods show deviation from expected values.

images, indicating they are not sensitive to changes in aerial image contrast due to source polarisation.

RMS, composite, Fourier, and imbalance contrast metrics are shown in Figure 3.5.3 to be less sensitive to noise in an aerial image interference pattern. A noise model was implemented to add random fluctuations of constant amplitude to the aerial image, the number of fluctuations per unit frequency is known as the noise density, ρ . Ideal TE-TE interference intensity was generated Equation 2.4.44 and then modified with increasing noise density. The Michelson contrast and NILS show increased error over small values of ρ compared to other metrics shown in Figure 3.5.3. The NILS was found to be the most sensitive to noise in an aerial image and is not reliably computed for spectral noise density over $\rho = 1 \text{ Hz}^{-1}$. The Fourier contrast was found to be the least sensitive to noise, however it was unreliable when evaluating loss of aerial image contrast due to polarisation. The Fourier contrast was thus left out of all further analysis in this work.

RMS contrast was shown to be the most reliable metric for evaluating loss of aerial image contrast due to polarisation, even in the presence of significant noise. Although a significant variation in contrast was seen for a noise density of $\rho = 150 \text{ Hz}^{-1}$, this level of

noise is not expected for the aerial images formed in this project. Although, in the case of high-coherence, the speckle introduced by a rough mask surface could resemble those shown in Figure 3.5.3 with high noise density [175]. RMS contrast was therefore considered the best metric for evaluating aerial image contrast for interference lithography.

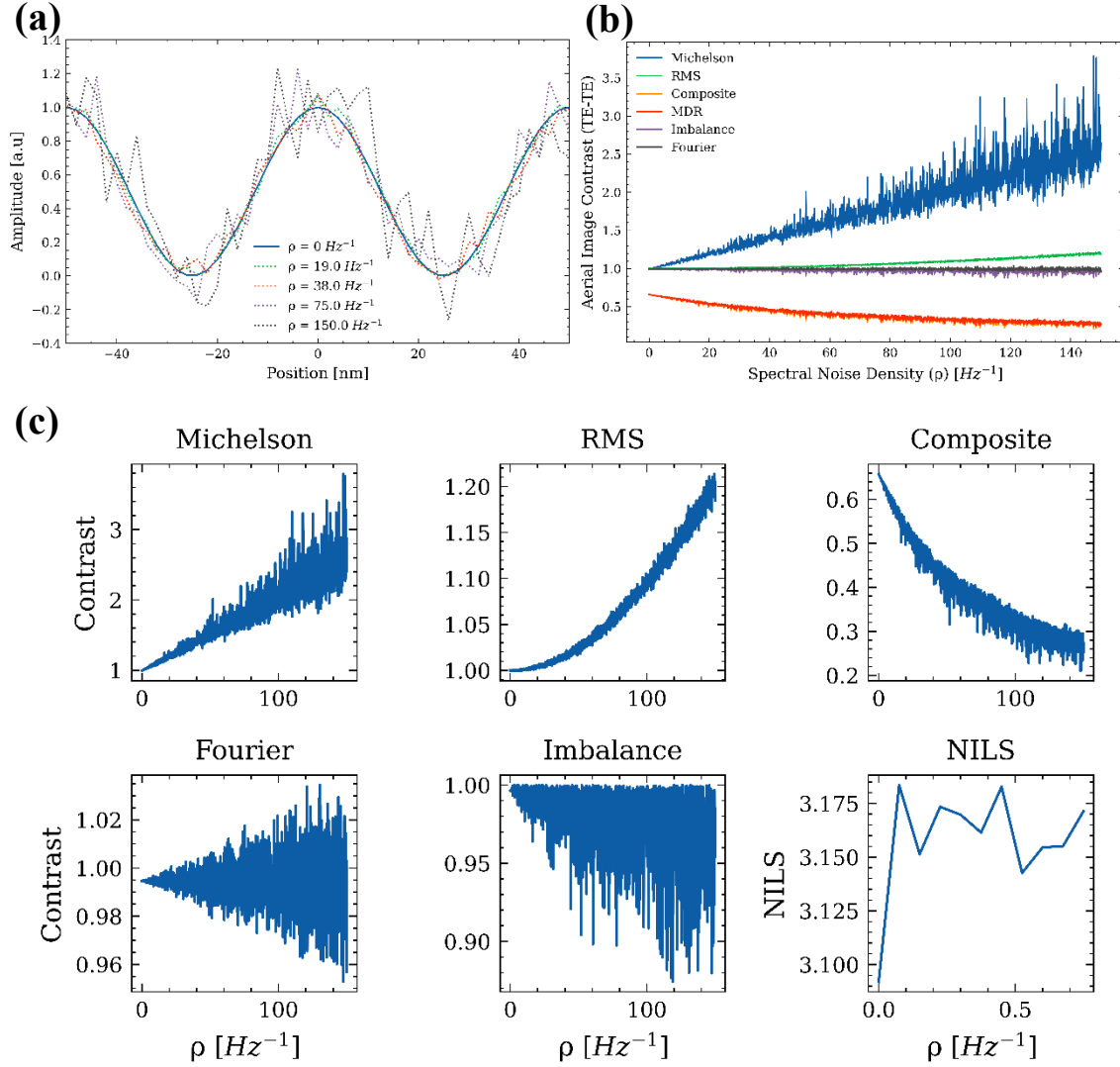


Figure 3.5.3: The contrast as noise is added to an aerial image intensity pattern resulting from a TE-TE polarised beam incident on a two-beam IL grating. (a) The aerial image intensity pattern with added noise. (b) Comparison of contrast by each metric. (c) Separate contrast metrics, including NILS.

Chapter 4

Experimental Methods

4.1 Introduction

This chapter describes the implementation of a model of the Soft X-ray Imaging (SXR-I) source, beamline, and proposed interference lithography optical components. The existing SXR-I beamline, proposed EUV-IL implementation and performance requirements are briefly described. The implementation of a model using the framework provided by Synchrotron Radiation Workshop (SRW) codes [17,122] is then explained. Applying the model to the simulation of partially coherent wavefront propagation from the source, through the beamline and model photomask is described in Chapter 5.

This Chapter includes a description of the model of laminar grating based masks for use in transmission geometry. They include a substrate layer, absorber layer (grating), and aperture layer (photon stop). Grating surface roughness, characterised by the root-mean-square height variations and transverse correlation lengths was included for the purpose of evaluating the effect of mask fabrication artefacts on the quality of the aerial image that is formed. In this Chapter, the mask resolution and efficiency requirements are discussed, along with the constraints on the grating mask dimensions and their relationship to the aerial image location and spatial separation of the first-order image.

Synchrotron Radiation Workshop (SRW) [17] was used for the source and wavefront propagation calculations mentioned in Sections 4.3.3, 4.4.2, and 4.4.3, with custom extensions to run batch simulations to test specific beam and mask properties. The grating generation, surface roughness and contrast evaluation code used in Section 4.4.1 and 4.4.2 was written by the author and Grant van Riessen. The code to calculate diffraction efficiency of the mask seen in Section 4.4.3 was written by the author for use on the complex electric field calculated by SRW.

4.2 Proposed EUV-IL Technical Design

The EUV-IL facility proposed for construction at the Australian Synchrotron will use the Soft X-ray Imaging beamline [176], which is based around an elliptically polarising APPLE-II undulator source. The key optical components include a toroidal mirror, a planar grating monochromator, and a cylindrical mirror. The beamline images the source onto secondary source apertures. The beamline is currently configured to produce a highly demagnified image of the secondary source using diffractive optics for coherent imaging research. The proposed EUV-IL configuration uses an unconventional transmission geometry and requires a relatively large, partially coherent beam. In this work we investigate a simplified optical layout that dispenses with the refocusing optic and places the photomask nominally located at the plane where a diffractive optic has previously been used for coherent diffractive imaging applications [177–179].

At the time of writing the development of interference lithography at the SXR-I beamline of the Australian Synchrotron is at an early stage. The endstation, which is currently under construction at La Trobe University, will combine interference lithography and at-wavelength coherent imaging metrology using an EUV detector. The metrology capability will be important for optimising lithographic processes at extremely high resolution.

An intended application of the IL endstation is nanometre-scale periodically patterned surfaces for nanophotonic and nanoplasmonic structures, and functional materials. Another is the evaluation of photoresist performance and the compromise between resolution (half-pitch), sensitivity (dose) and line-edge roughness (LER). To meet the requirements for these applications, and to make effective use of the metrology capabilities, this work is primarily concerned with using the model to evaluate aerial image formation at half-pitch below 25 nm using 6.7 nm radiation. As explained in Section 4.4, grating photomasks that are compatible with this requirement, and fabrication constraints, are based on a Ni₃Al grating of thickness 20 nm and grating pitch 100 nm.

4.3 The SXR-I Beamline

A comprehensive model of the Soft X-ray Imaging beamline at the Australian Synchrotron

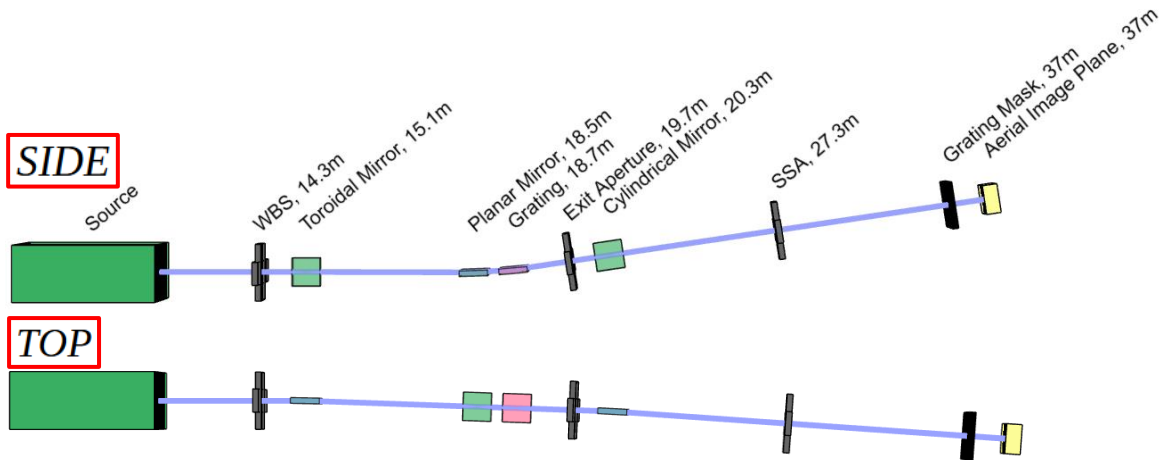


Figure 4.3.1: The model of the Imaging Branch of the Soft X-ray Spectroscopy Beamsline used for this experiment viewed side-on and from above. The names and distance from source of each element are given. Generated from the 3D beamsline function in SRW.

was created in SRW with parameters taken from descriptions in the literature [66,180–182]. The component models of the source and beam transport optics are described below.

4.3.1 Storage Ring & Electron Beam

The storage ring and electron beam was modelled with parameters taken from Refs. 66, 181, and 183, and listed in Table 4.1. The flux at the exit plane of the undulator is a limited by the storage ring current I_0 , which is maintained at 0.2 A at the Australian Synchrotron. The low vertical beam emittance, ε_y , leads to high brightness at the undulator exit plane [8].

Table 4.1: Key values for the Australian Synchrotron storage ring. Parameters obtained from Refs. 66, 181, and 183

Parameter	Value
E_0	3.01 GeV
I_0	0.2 A
σ_E	0.1021 %
ε_x	10 nm rad
ε_y	0.009 nm rad
β_x	9 m
β_y	3 m

4.3.2 APPLE II Undulator

The APPLE-II undulator was modelled as an ideal undulator with magnetic fields defined from the undulator length, L , magnetic period, λ_U , and number of periods, N , of the values obtained from Refs. 66, and 181, shown in Table 4.2. SRW library functions were used to calculate the magnetic field along the undulator axis and to simulate the trajectory of a

Table 4.2: Key values for the APPLE-II undulator used for the SXR-I beamline at the Australian Synchrotron. K_u , which determines B_u , was adjusted to produce a fundamental harmonic at 184.76 eV. Values obtained from Refs. 66, and 181

Parameter	Value
L_u	Undulator Length
λ_u	Undulator Period Length
B_u	Peak Magnetic Field
K_u	Deflection Parameter
N_u	Number of Undulator Periods

Table 4.3: Horizontal (B_x) and vertical (B_y) magnetic field components as well as phase offset values for producing different beam polarisation states. The values listed are for producing a peak magnetic field (B_u) of 0.46111878 T.

Beam Polarisation	B_x	B_y	Phase offset - X	Phase offset - Y
Linear Horizontal	0 T	0.46111878 T	0 rad	0 rad
Linear Vertical	0.46111878 T	0 T	0 rad	0 rad
Linear 45°	-0.326060216 T	0.326060216 T	0 rad	0 rad
Circular Right	0.326060216 T	0.326060216 T	$\pi/2$ rad	0 rad

relativistic electron from the storage ring described in Section 4.3.1 and, consequently, the radiation characteristics of the source. A detailed description of the method is described in [117]. The deflection parameter K_U was adjusted to produce a fundamental harmonic at 184.76 eV (6.7106 nm wavelength).

The horizontal and vertical components of the magnetic field of the Apple II undulator along with the phase offsets of each component were adjusted to induce degenerate beam polarisation states as outlined in Table 4.3. A beam with an arbitrary degree of polarisation was simulated by addition of linear polarisation states at various angles as outlined in Section 3.2

4.3.3 Beamline Optics

Models of each of the optical elements of the beamline, including mirrors, apertures and a planar grating monochromator were constructed using SRW, with parameters taken from technical documents provided by the supplier of beamline components Oxford FMB, and documents supplied by Bruce Cowie, Refs. 63, and 182. Parameters are shown in Table 4.4. A representation of the optical layout is shown in Figure 4.3.1. Optical elements were created to represent the drift space between each element.

Table 4.4: The geometry of the optical elements used in the model of the SXR-IL beamline. The defining characteristic for a Mirror element type is given as the major radius, R , and minor radius, ρ . The defining characteristic for a grating element is given as the line spacing, and for a mask element as the period, p_G , and grating separation, d . Values obtained from Refs. 63 and 182.

Element Name	Element Type	Propagation Distance	Distance from Source	Dimensions	Defining Characteristic	Incident Angle
White Beam Slit	Aperture	14.3 m	14.3 m	4×3 mm	N/A	90°
Toroidal Mirror	Mirror	12.12 m	15.12 m	420×30 mm	$R = 6669.6 \text{ m}$ $\rho = 5.2619 \text{ m}$	1°
Planar Mirror	Mirror	3.38 m	18.50 m	460×50 mm	N/A	2°
Grating	Grating	0.2 m	18.70 m	150×20 mm	250 lines/mm	1.1728°
Exit Aperture	Aperture	1.0 m	19.70 m	10×20 mm	N/A	90°
Cylindrical Mirror	Mirror	0.6 m	20.30 m	240×40 mm	$R = 100 \text{ km}$ $\rho = 0.24433 \text{ m}$	1.5°
Secondary Source Aperture	Aperture	7.0 m	27.30 m	200×200 μm	N/A	90°
Beam Defining Aperture	Aperture	9.7 m	37.0 m	100×100 μm	N/A	90°
Grating Mask Aperture	Aperture	0.0 m	37.0 m	10×40 μm	N/A	90°
Grating Mask	Mask	0.0 m	37.0 m	10×40 μm	$p_G = 100 \text{ nm}$ $d = 27.5 \mu\text{m}$	90°

The white beam slits (WBS) are used to stop off-axis radiation and to define the beam size. The 4×3 mm size is typical for experiments undertaken at the beamline. The planar mirror at 18.5 m and the grating at 18.7 m together make up a plane grating monochromator (PGM). The 250 lines/mm² grating was chosen from the two available one of the two options available in the SXR-I beamline because it provides greater efficiency for 6.7 nm wavelength. The beam exiting the grating then passes through the exit aperture, which gives the option of reducing the output of the beam from the grating. This aperture is not needed and is kept fully open at 10×20 mm. A cylindrical mirror then focuses the beam vertically at 7 m onto the secondary source aperture (SSA), with an expected demagnification of ∼2. The angular dispersion of the light due to the PGM comes into focus in the plane of the SSA, so that the beam is spectrally filtered by the vertical size of the SSA. For the 250 l/mm grating at 185 eV photon energy and a vertical SSA opening of 200 μm, the expected resolving power is ∼1100. Unusually for a beamline, the horizontal and vertical focus points of the beam are separated longitudinally along the beamline, so that the horizontal focus is located ∼3 m before the plane of the SSA. The SSA therefore acts as an ideal secondary source in the vertical direction, but non-ideal in the horizontal. The beam is then propagated

to the beam defining aperture (BDA), which, in practice, primarily serves to block light scattered off-axis by upstream optical elements.

All mirrors were modelled as ideal, with zero roughness. Propagation through the apertures was done with the assumption of zero transmission through the aperture material. SSA size was chosen to be smaller than the FWHM of the beam at the plane it is placed , which causes the amount of transmitted power to be significantly reduced. However, the transverse coherence is increased, and the number of pixels required represent a wavefront with adequate sampling is reduced, which is important for limiting the computational costs of propagation.

For propagation through elements, the propagation was typically undertaken by implementing the Fresnel diffraction operator (Equation 3.1.8) using two FFTs. Drift through free space was implemented using Fresnel propagation with semi-analytical treatment of the quadratic phase term, mentioned in Section 2.5.3. The propagation parameters such as sampling rate and range were chosen for each element to satisfy oversampling requirements mentioned in Section 3.1.1. The resizing and resolution factors chosen for the propagation parameters (*Appendix. Figure 7.1.1*), with the dimensions of beamline elements listed in Table 4.4 lead to a resolution of 2.5 nm (h) \times 2.5 nm (v) at the mask plane, and a 2.5 nm (h) \times 240 nm (v) resolution at the aerial image plane for simulations involving a horizontally oriented, 100 nm pitch grating.

This work is concerned primarily with the formation of the aerial image. No attempt is made to model the interaction between the beam and photoresist. When propagating between optics a perfect vacuum was assumed.

4.4 Interference Lithography Optics

4.4.1 Grating Mask Model

Masks were modelled as a stack of three layers, comprised of a substrate, absorber and photon block layer and the projection approximation was assumed. A two-beam interference grating mask was generated (Figure 4.4.2) with dimensions shown in

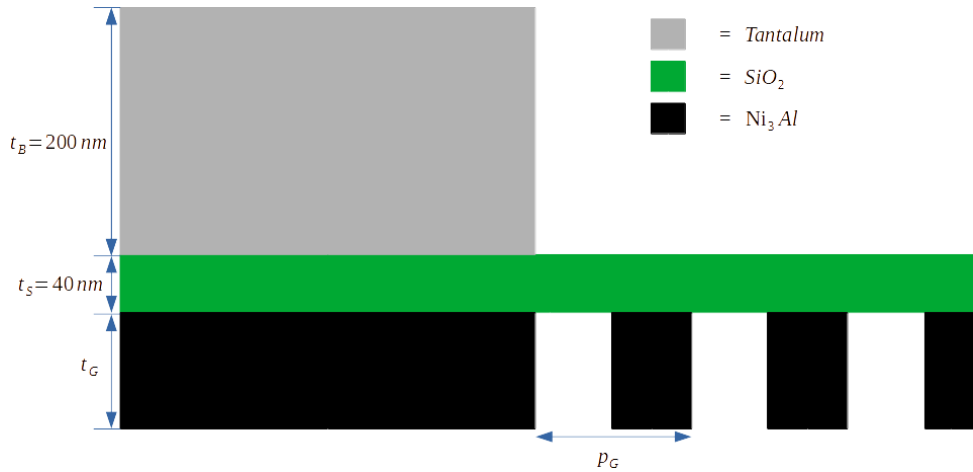


Figure 4.4.1: A diagram of the ideal mask generated for modelling interference lithography. The mask consisted of a 200 nm tantalum absorber layer; a 40 nm SiO_2 substrate layer and Ni_3Al grating layer of thickness t_g .

Table 4.5: The physical properties of materials used in the grating mask model. Density of Ni_3Al was obtained from V. Luong et al [184], attenuation lengths, δ and β values for Ni_3Al , δ and β values and density of tantalum and SiO_2 were obtained from Henke database [99].

Material	Density	δ	β	Attenuation Length
Tantalum	16.65 g/cm ²	1.356156×10^{-2}	1.939377×10^{-2}	27.53364 nm
SiO_2	2.2 g/cm ²	9.401009×10^{-2}	$5.30286832 \times 10^{-3}$	0.100688 μm
Ni_3Al	0.95 g/cm ²	2.530307×10^{-2}	$1.22133737 \times 10^{-2}$	43.72202 nm

Figure 4.4.1. The model masks consisted of 3 separate layers, each with a resolution of 2.5 nm (h) \times 2.5 nm (v).

The mask comprised of a 200 nm layer of Tantalum, a 40 nm layer of SiO_2 and a layer of Ni_3Al of thickness t_g , with material properties shown in Table 4.5. The Tantalum acted as a photon block to stop any transmission everywhere outside the area occupied by the gratings. The SiO_2 was the substrate with high transmission and the Ni_3Al was the absorber material in which gratings were defined.

The computational complexity inherent in the wavefront propagation methods used in this work (described in Section 3.1) introduces constraints on the mask model and parameters that can be examined. A compromise must be made between the area of the grating mask and the resolution at which it and the illuminating wavefield, can be represented. This, in turn has consequences for the model's sensitivity to effects of partial coherence and nanoscale mask roughness. As described in Section 2.4.4, the first-order diffraction efficiency of a grating mask, which is an important determinant of lithographic

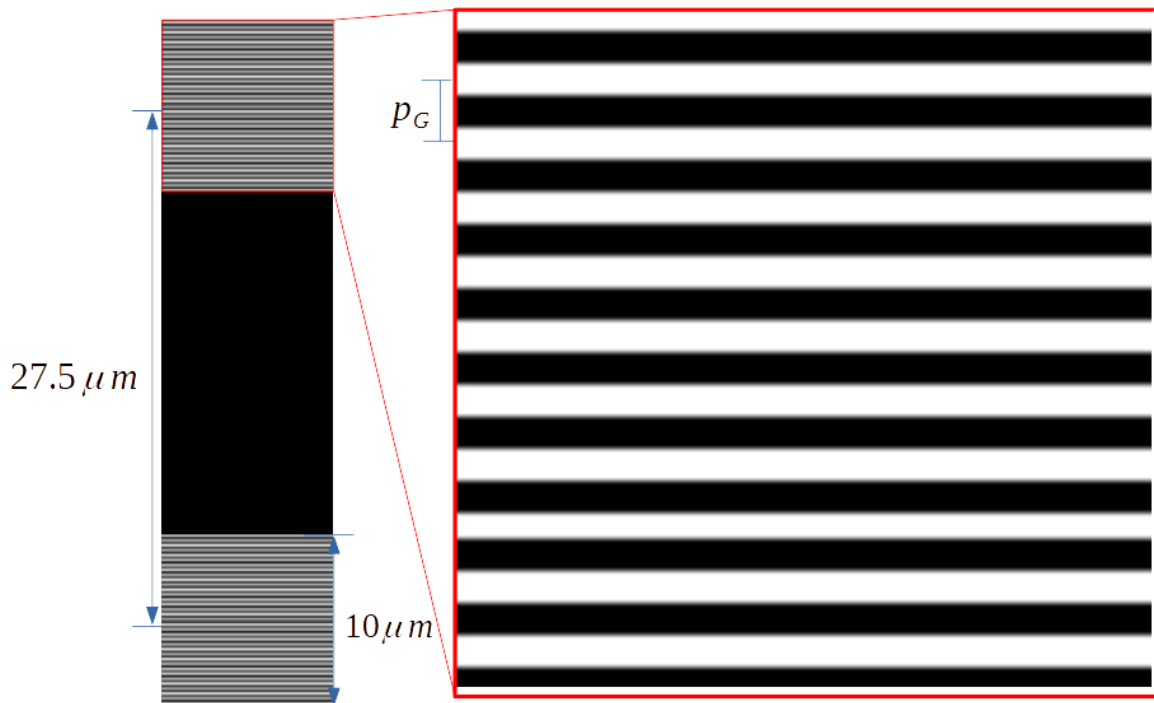


Figure 4.4.2: A diagram of the grating mask generated for modelling interference lithography. The white areas indicate Ni_3Al of thickness t_g and the black areas represent empty space. The entire mask is shown on the left oriented vertically, and a zoomed in section of the grating is shown on the right. The relevant dimensions are labelled.

performance, is a function of grating pitch and thickness. The optimal thickness for diffraction efficiency of 107.5 nm, discussed in Section 5.5, and the small grating pitch required for nanometre pattern half-pitch, together represent an extreme challenge for mask fabrication. The optimal thickness also violates the assumptions required for the simple approach to modelling the interaction of the EUV radiation with the mask in this work, the effect of this are discussed further in Section 5.5. In consideration of the above, two-grating photomasks with a pitch of 100 nm and a thickness of 20 nm are mostly used.

4.4.1.1 Grating Representation

The gratings were modelled as Laminar gratings with lines consisting of uniform density Ni_3Al of thickness t_g , with material properties obtained from Refs 99 and 186, listed in Table 4.5. A duty cycle of 0.5 was chosen as it offers the highest efficiency for $m = 1$ order diffraction as shown in Section 2.4.4. Two $10 \mu m \times 10 \mu m$ gratings with pitch p_G were oriented on the mask as shown in Figure 4.4.2, with the centre of each grating separated by $27.5 \mu m$. A pitch of $p_G = 100 \text{ nm}$ was chosen for most trials as it provided a suitable balance between intended mask resolution for the proposed EUV-IL facility at the AS and model

resolution which determines the computational cost of simulations. Figure 4.4.2 shows the mask model oriented vertically, but horizontal orientation was also used, in which case the entire mask model was rotated 90°.

4.4.1.2 Absorber Surface Roughness

The mask model was extended to include surface roughness in the absorber layer. The roughness model was implemented using the method described by Garcia and Stoll [152]. A two-dimensional random roughness map was first created with a Gaussian distribution of Δh , shown in Figure 4.4.3. The width of the Gaussian distribution was given by a chosen RMS roughness value (defined by Equation 3.3.1). Correlation was then introduced to the roughness map in the horizontal and vertical directions by convolution with a two-dimensional Gaussian of widths given by the correlation lengths in each direction. The result was then added to the absorber thickness map. The variation of surface height in each direction is given by an autocovariance function which is proportional to the correlation length.

The roughness model can be closely related to roughness characteristics obtained from Atomic Force Microscopy (AFM) of mask layer surfaces, which can be implemented to measure both surface roughness and correlation lengths for surfaces [185].

A representative example of the process of adding a surface roughness profile to an

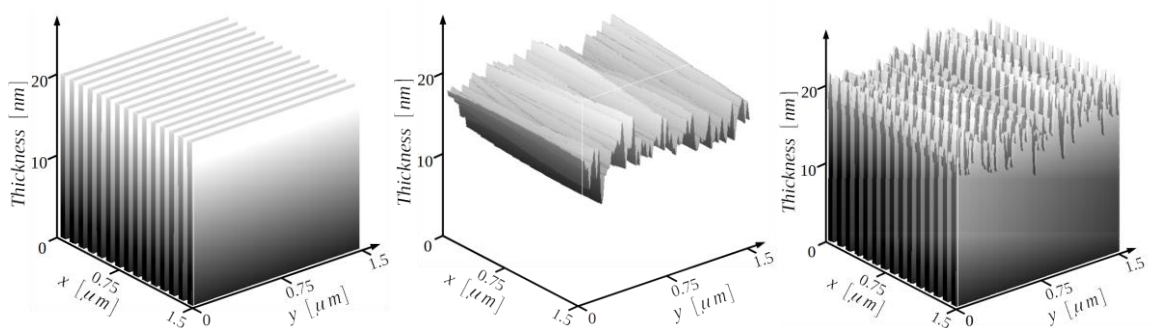


Figure 4.4.3: The process of generating grating masks with variable roughness. (left): The ideal grating with no roughness is generated. (centre): A roughness profile is generated. (right): The roughness is added to the ideal grating. Each surface plot shown is only a $1.5 \mu\text{m} \times 1.5 \mu\text{m}$ section taken from a larger area generated across the entire mask structure.

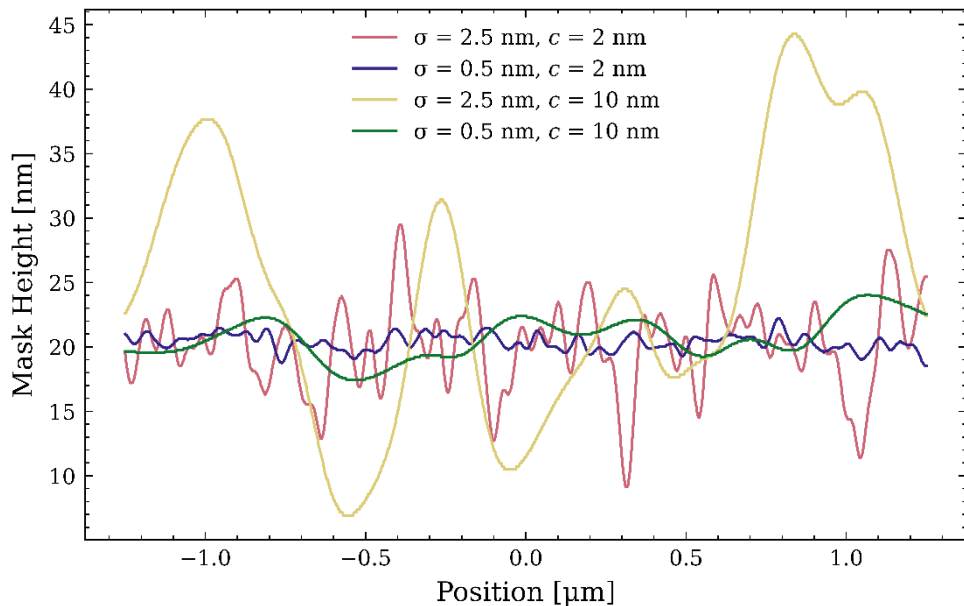


Figure 4.4.4: Line profiles of generated mask surfaces with varied roughness parameters. Four mask profiles with RMS roughness values $\sigma = 2.5 \text{ nm}$ & $\sigma = 0.5 \text{ nm}$ each with correlation lengths: $c = 2.0 \text{ nm}$ and $c = 10.0 \text{ nm}$. Shown for a mask of 20 nm thickness.

absorber thickness map is shown in Figure 4.4.3. The roughness is characteristic of the roughness that results from the deposition and etching processes that are typically used to fabricate masks. Line profiles of absorber thickness maps with added surface roughness can be seen in Figure 4.4.4, showing the differences in roughness profiles when varying the RMS roughness, σ , and the roughness correlation length, c . For each roughness profile, σ and c were varied and a plot of height distribution and autocovariance was generated.

4.4.2 Implementation

Custom code was written to generate grating masks, with each layer of the mask represented by a $N \times N$ array of values representing thickness in $2.5 \text{ nm} \times 2.5 \text{ nm}$ columns of the material. A “Sample” optical element type as implemented in SRW was used, together with the density and attenuation length given in Table 4.5, to construct the transmission function that was included in the wavefront propagation model.

Propagation of the wavefront through each layer of the mask model assumed that the projection approximation defined in Section 2.5.1 was valid. The thickness of the aperture layer was chosen to ensure over 99% absorption at 6.7 nm. At 200 nm thickness the projection approximation is not strictly valid, but the small error that this introduces is not

considered significant and does not justify multislice approaches (described in Appendix) that are much more computationally expensive. For propagation of light with a wavelength of 6.7 nm through an object with lateral resolution of 2.5 nm, multislice requires a minimum slice thickness as defined by K. Li *et al* [123], of ~ 9.3 nm. This would have increased computational time of each propagation an unreasonable amount, even for simulations with masks modelled with 20 nm thickness. The fastest partially coherent propagation in this work was completed in ~ 7 hours, with propagation through the mask being the most time-consuming propagation step due to the high spatial resolution needed at the mask plane. To evaluate the potential issues that may arise from the assumption of the projection approximation at the mask, diffraction efficiency calculations taken by propagation through the mask were compared to calculations by Rigorous Coupled-Wave Theory (RCWA) [188,189].

4.4.3 Diffraction Efficiency

As mentioned above, the assumption of the projection approximation at each layer of the mask model is not strictly accurate and the effects of this assumption need to be evaluated. The diffraction efficiency of the mask model calculated by propagation through each layer assuming the projection approximation was evaluated against efficiency calculations

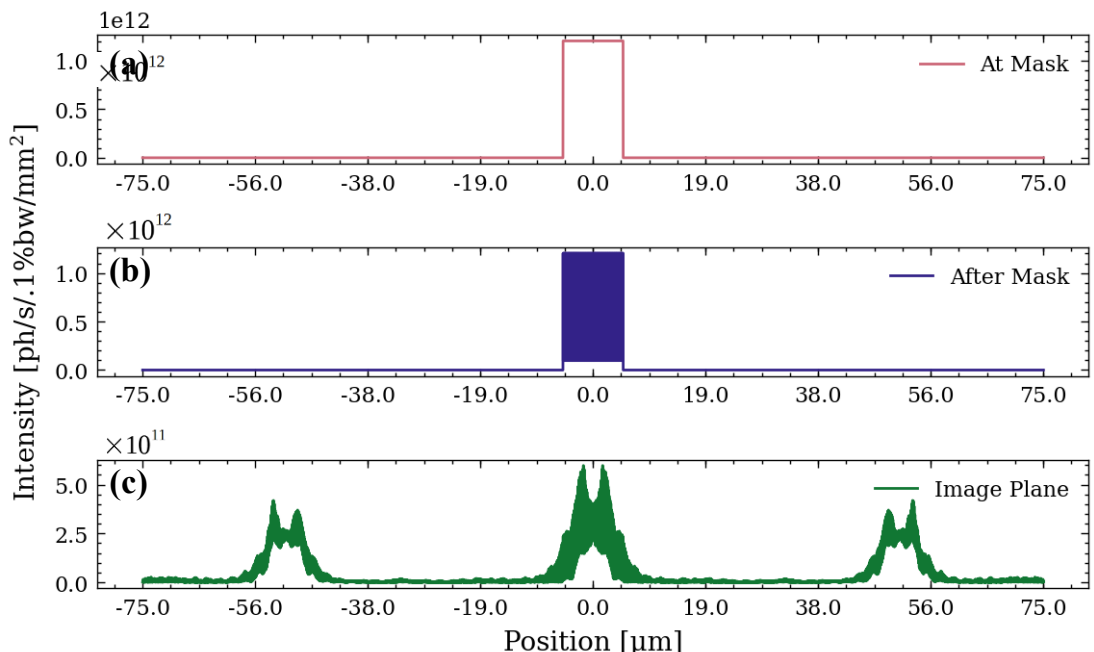


Figure 4.4.5: Incident (a), exit (b), and propagated (c), wavefield intensity for evaluating the diffraction efficiency of a single Ni₃Al grating.

obtained through RCWA. To calculate the diffraction efficiency of the ideal grating mask model, a simplified source and optical model was constructed, consisting simply of a Gaussian source, and grating mask at 3 m from the source. For the case of diffraction from a single grating, an aperture with equal dimensions to the grating was placed immediately before the grating to select only the intensity of the beam over the area of the grating (Figure 4.4.5a). The model gaussian beam was large enough at the mask plane that the intensity distribution over the area of the mask was essentially uniform. The beam was then propagated through the grating and the exit surface wave was recorded before propagation to the image plane. The intensity at the image plane was assumed to be symmetrical about the horizontal plane so only the horizontal profile was analysed.

The process was then repeated for the case of a two-beam interference grating, with the tantalum photon block layer taking the place of the aperture. The sum of the intensity of each diffracted order produced by each grating, I_m , as well as the sum of the intensity over the aerial image was then compared to the incident beam intensity over the area occupied by both gratings to obtain the relative diffraction efficiency.

The diffraction efficiency values generated for single and two-grating mask models was evaluated against theory outlined in Section 2.4.4 and Rigorous Coupled-Wave Theory (RCWA) calculations by B. Haydon [188,189], using the same material properties and mask geometry.

4.4.4 Mask material properties

Initial, fully coherent propagation trials (shown in Section 6.2) used a mask with thickness of 72 nm, oriented vertically, with 100 nm pitch and geometry shown in Figure 4.4.2. The wavefield was propagated using fully coherent propagation methods outlined in Section 3.1.

Partially coherent propagation trials to evaluate effects of mask roughness (shown in Section 6.4.1) used a set of 25 masks of 20 nm thickness with varied roughness profiles. Masks for these trials were oriented horizontally. RMS roughness values of 0.5, 1, 1.5, 2 and 2.5 nm were used with vertical correlation lengths of 2, 4, 6, 8 and 10 nm. Each combination of RMS roughness and correlation length was generated for a total of 25 masks.

The wavefield was propagated through each mask using partially coherent propagation methods outlined in Section 3.1.3.

Trials to evaluate the effects of polarisation on aerial image contrast (shown in Section 6.3.1) used a mask thickness of 109 nm as simulations were done before it was recognised that reasonable efficiency could be achieved with 20 nm thick masks. Grating masks were generated with varied grating pitches of 40 nm and 24 nm for fully coherent propagation trials. This was decreased to 24 nm and 14 nm for partially coherent propagation trials.

After propagation through each mask the intensity at the image plane was analysed using contrast metrics detailed in Section 2.1.1. The effect of source properties such as polarisation and coherence, as well as mask properties such as grating pitch, RMS roughness and correlation length on the aerial image intensity distribution was investigated.

4.4.5 Mask Geometry and Aerial Image Distance

Using Equation 2.2.2 and assuming zero divergence of each diffracted 1st order beam, the range over which two first order beams would interfere and produce an aerial image was evaluated for different grating geometries. The range of interference of the 1st order beams was called the focal depth and was used to determine acceptable propagation distances for each simulation. The focal depth depends also on the wavelength of the incident beam – as the angle at which each order is diffracted is dependent on wavelength, the size of each

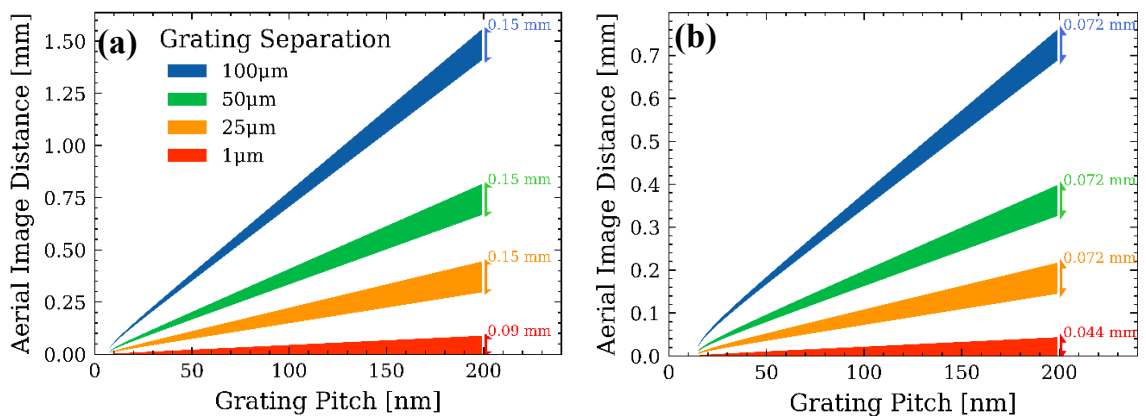


Figure 4.4.6: Aerial image distance and range vs. grating pitch (pg) for IL using a mask with two $10 \times 10 \mu\text{m}$ gratings, separated by $100 \mu\text{m}$, $50 \mu\text{m}$, $25 \mu\text{m}$ & $1 \mu\text{m}$. The focal depth for $pg=200 \text{ nm}$ is displayed for each grating separation. (LEFT): IL using BEUV radiation ($\lambda=6.7 \text{ nm}$). (RIGHT): IL using EUV radiation ($\lambda=13.5 \text{ nm}$).

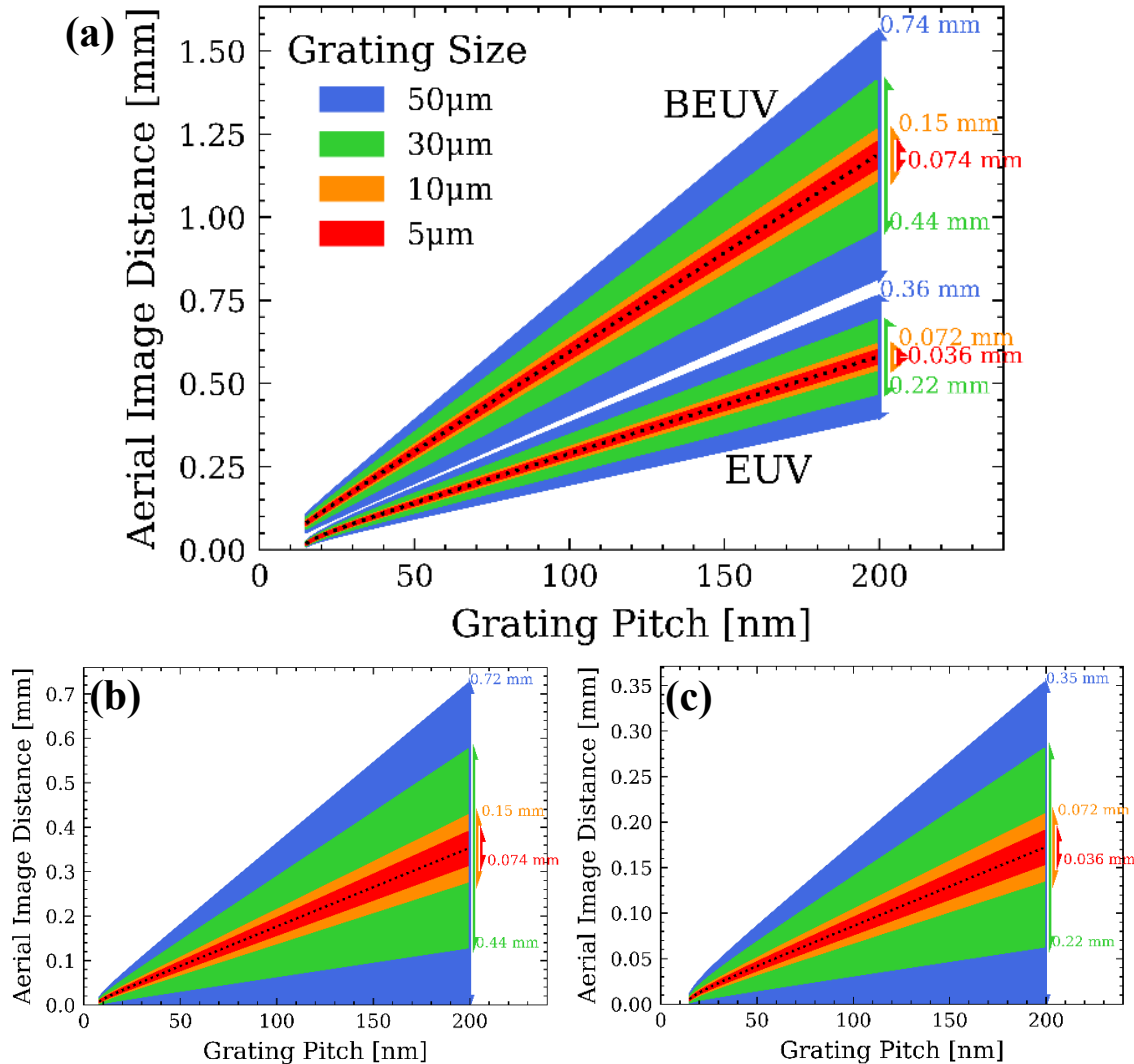


Figure 4.4.7: (a): Aerial image distance and depth of field vs. grating pitch (p_G) for IL using a mask with two gratings separated by $23.75 \mu\text{m}$, with dimensions $50 \mu\text{m}$, $30 \mu\text{m}$, $10 \mu\text{m}$ & $5 \mu\text{m}$. The depth of field for $p_G=200 \text{ nm}$ is displayed for each grating size. (b): IL using BEUV radiation ($\lambda=6.7 \text{ nm}$). (c): IL using EUV radiation ($\lambda=13.5 \text{ nm}$). A significant increase in both aerial image distance and range is seen for BEUV compared to EUV.

grating – as larger gratings will interfere over a larger longitudinal distance, and the grating pitch which, along with wavelength, determine the angle of diffraction. Figure 4.4.6 shows that for gratings with dimensions less than the separation length, focal depth for gratings with equal pitch is independent of grating separation. It also shows that the propagation distance to the aerial image plane is highly dependent on grating separation and wavelength, which is consistent with Equation 2.2.2. This is a significant consideration as the maximum grating separation is determined by the coherence length of the beam, as gratings separated by distances greater than the coherence length will not be coherently illuminated and will therefore show a loss in aerial image contrast. There is also a significant increase in aerial

image distance for IL in the BEUV (Figure 4.4.6a) regime compared to EUV (Figure 4.4.6b).

Figure 4.4.7 shows the dependence of focal depth on grating size and pitch. The cones representing focal depth for both BEUV and EUV are compared, with a significant increase in both for BEUV ($\lambda=6.7$ nm) compared to EUV ($\lambda=13.5$ nm). Grating size will then play a leading role in the size of the patternable area in an IL system.

4.4.6 Summary

A representative model of the SXR-I beamline was successfully constructed for evaluation of EUV-IL at 6.7 nm. The implementation of the source, beam transport optics and propagation was described in this chapter. As well as a detailed description of the dimensions of optics and the interference grating mask. The method of mask generation was described in detail, including material properties used and the addition of roughness profiles. The roughness parameters used in experiment were listed as well as mask geometry for each trial. Preliminary evaluation of the effect of mask geometry on aerial image distance and focal depth was undertaken to determine an acceptable range of propagation distances for aerial image evaluation.

The method of propagation through each layer of the mask the detailed in 4.4.1.1 assumed the projection approximation to be valid which was indicated as a possible limitation of the model. Each optical element described in Section 4.3.3 was modelled with no roughness and a perfect vacuum was assumed for drift between elements. While models for evaluating other EUV-IL beamlines typically use wavefront propagation only up to the mask plane [14,48], this work includes propagation through a multilayer mask with modelled surface roughness and up to the aerial image plane.

In the following chapter the application of the model to simulate the propagation of a partially coherent wavefield from the source to the aerial image plane is described. The source model is validated against the theoretical description in Section 2.3.1, and key optical properties of the beamline model are compared to available experimental data to establish the reliability of the model.

Chapter 5

Validation of Source, Beamline and Mask Model

5.1 Introduction

In this Chapter the model of the source and beamline is validated, and the characteristics of the aerial image formed by partially coherent wavefront propagation through the complete model of source, beamline and mask is also presented. The properties of the source and the wavefront propagated through the beamline are compared to the theory outlined in Section 2.3, to known parameters of the Soft X-ray Beamline at the Australian Synchrotron and to other existing models [64,182,183]. The ability of the source model to represent polarisation is evaluated, and the polarisation of the wavefield at the mask plane is compared to the theory outlined in Section 2.4.2. The intensity and phase of the propagated wavefield at the mask plane is evaluated for a monochromatic beam of 6.7 nm wavelength. The diffraction efficiency obtained from fully coherent propagation of a Gaussian source through a simplified beamline and the multi-layer mask model described in Section 4.4.1 is compared to theory outlined in Section 2.4.4. Finally, the ability of the model to represent the source's partial coherence is evaluated, and the effect of the secondary source aperture size on the coherence at the mask plane is investigated.

5.2 The Source

The periodic magnetic field of the model APPLE-II undulator in use at the SXR-I beamline at the Australian Synchrotron is shown in Figure 5.2.1, along with the trajectory of a 3.01 GeV electron. The field was calculated using the parameters listed in Table 4.1 and Table 4.2 for different configurations of the four independently movable periodic magnetic structures illustrated in Figure 2.3.1. When configured for a photon beam with linear polari-

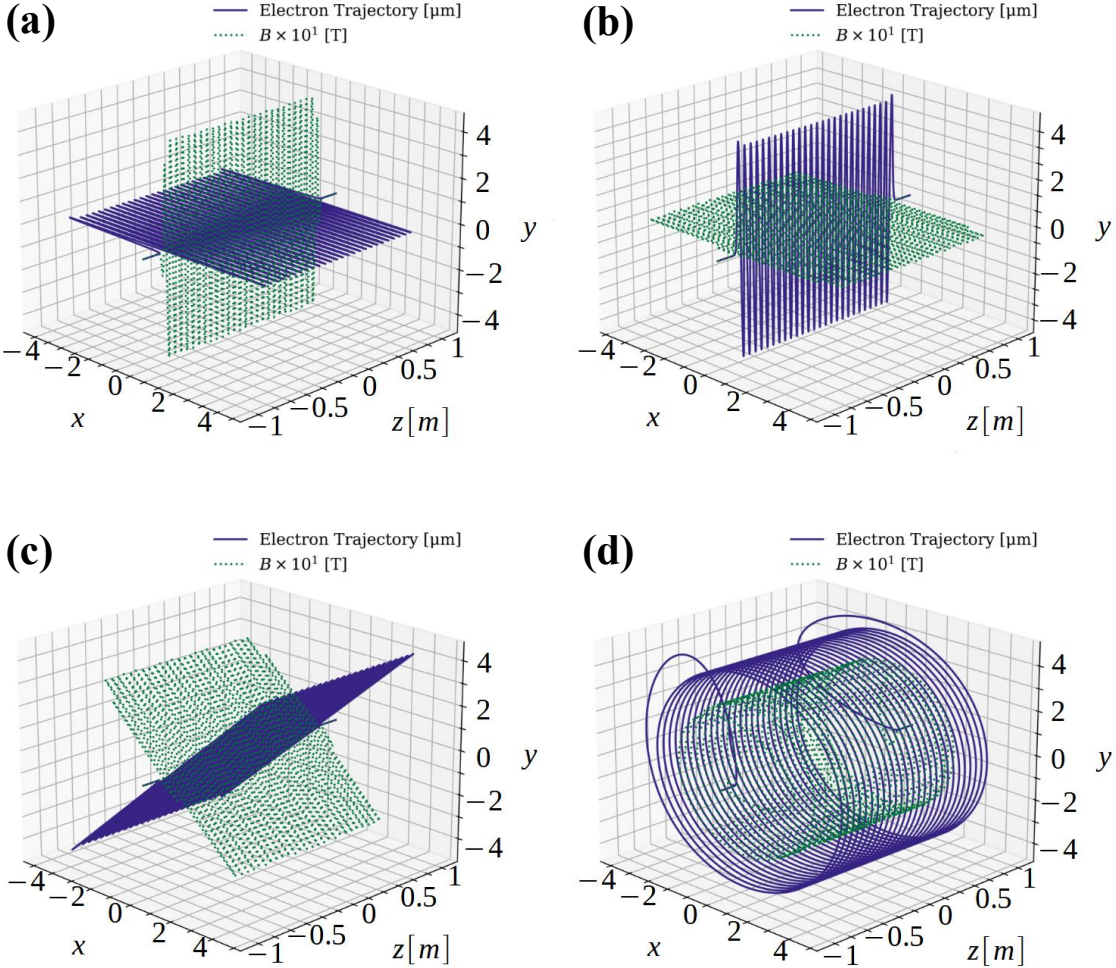


Figure 5.2.1 : Undulator magnetic field (green) and the trajectory of a 3.01 GeV electron (blue) for the magnetic field configured for (a) linear horizontal polarisation, (b) linear vertical polarisation, (c) linear 45-degree polarisation, and (d) circular-right polarisation. The undulator was modelled using SRW codes with the parameters given in section 4.3.2. The magnetic field amplitude and phase offset for each configuration are listed in Table 4.3.

-sation (Figure 5.2.1a,b,c), the expected sinusoidal field variation is seen with an amplitude of $|B_0| = 0.461$ T, and period of 75 mm, which is consistent with Equation 2.3.2. The trajectory of a 3.01 GeV electron through this magnetic field is perpendicular to the applied field and transverse to the optical axis and shows a maximum lateral displacement of 6.544 μm. The linear horizontally polarised beam (Figure 5.2.1a) is used throughout this work, unless explicitly stated otherwise. The polarisation of the photon beam produced for linear horizontal and linear vertical configurations with a finite emittance electron beam is considered in Section 6.3.1.

Multi-electron simulations (described in Section 3.1.3) represent the effect of the finite emittance of the stored electron beam, using parameters in Table 4.1. The single electron

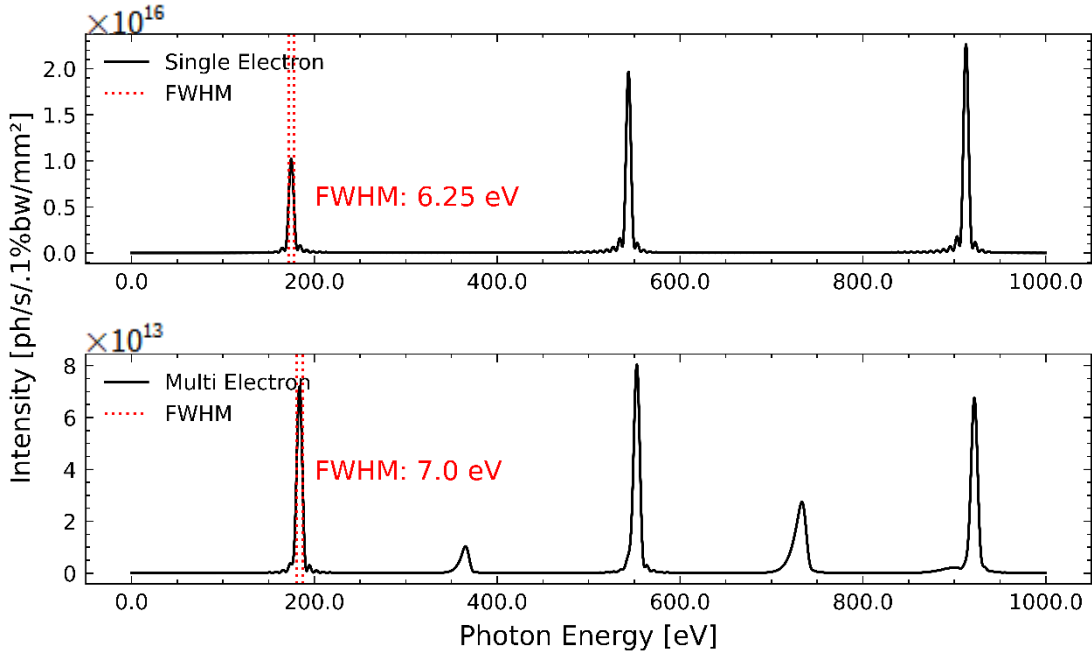


Figure 5.2.2: Single electron (top) and multi-electron (bottom) intensity spectrum of undulator harmonics at 2 m from the source, generated in SRW. The first five harmonics are presented, although only odd orders are visible for the single electron spectrum. The single electron spectrum considers only the on-axis intensity, while the multi-electron spectrum takes into account the intensity through a $10 \times 10 \mu\text{m}$ aperture. The FWHM of the fundamental harmonic is shown for both cases. The fundamental is centred at 184.76 eV as required for 6.7106 nm radiation. The maximum intensity of the fundamental harmonic is $1.02 \times 10^{16} \text{ ph/s/.1\%bw/mm}^2$, which drops to $2.54 \times 10^{15} \text{ ph/s/.1\%bw/mm}^2$ for the multi-electron spectrum

and on-axis multi-electron emission spectrum of the modelled APPLE-II undulator is shown in Figure 5.2.2 and contains the expected harmonic structure, with the fundamental harmonic centred at 184.76 eV (6.7106 nm), as required. For the single electron spectrum, the FWHM is 6.25 eV, with a full width of 13.9 eV and a peak intensity of $1.02 \times 10^{16} \text{ ph/s/.1\%bw/mm}^2$. For the multi-electron spectrum, the energy of the fundamental harmonic is spread out so that the FWHM increases to 7.0 eV, with a full width of ~ 16.1 eV. The peak intensity is lower ($7.19 \times 10^{13} \text{ ph/s/.1\%bw/mm}^2$) because off-axis radiation is excluded by a $10 \times 10 \mu\text{m}$ aperture at 2 m from the source. The multi-electron spectrum also shows even order harmonics, which are suppressed in the single electron calculation which is restricted to on-axis radiation. The single electron full width of the fundamental harmonic is in reasonable agreement with the value of $\Delta E = 14.81$ eV (0.268 nm) expected from Equation 2.3.6 and the parameters in Table 4.2. In practice, a narrow bandwidth is selected by the plane grating monochromator in the beamline and the asymmetric shape of the harmonic is therefore also of no significance. For the simulations described in this work, a single wavelength is propagated from the source. This is a reason-

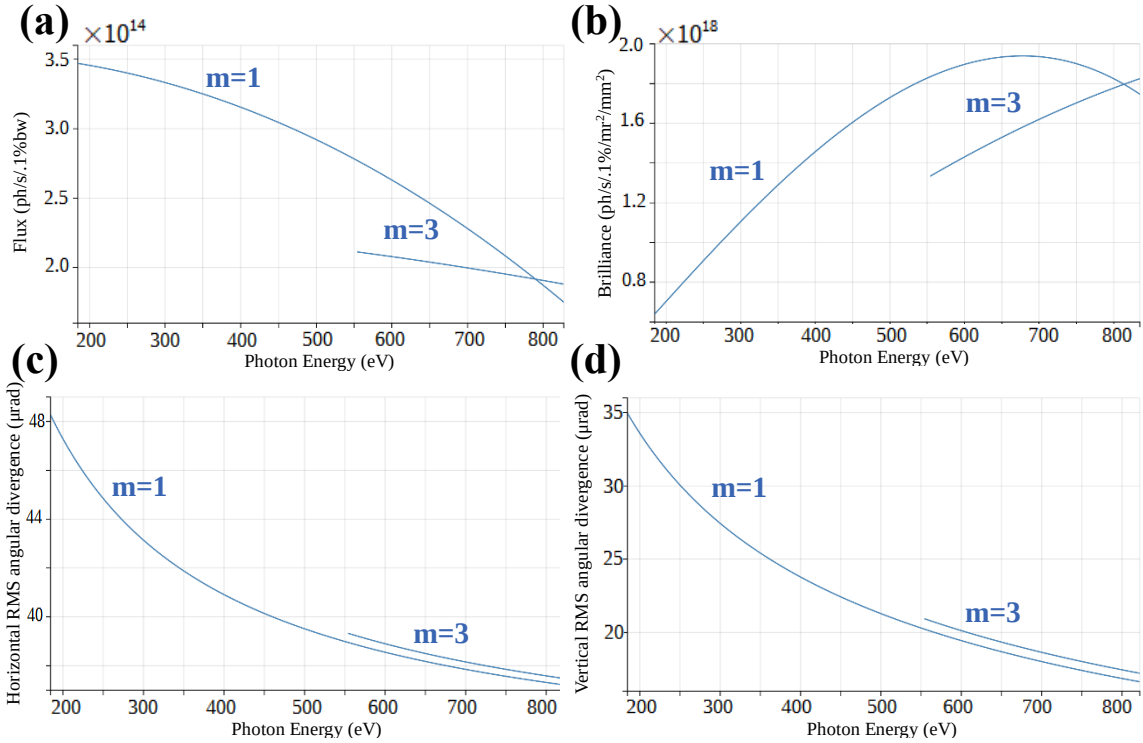


Figure 5.2.3 : The brightness (a), flux (b), horizontal and vertical RMS divergence (c), (d) of the first and third undulator harmonics as a function of photon energy for total polarisation components. The horizontal axis (photon energy) starts at the peak energy of the fundamental harmonic (184.76 eV).

-able approximation given the high resolving power of the plane grating monochromator (Section 4.3.3).

Equation 2.3.4 gives undulator deflection parameter $K = 3.23$, for $B_0 = 0.461$ T, which is in reasonable agreement with the nominal value of the undulator at the Soft X-ray beamline at the Australian Synchrotron expected for the same fundamental harmonic energy, (see Table 4.2). The photon flux, brilliance, horizontal and vertical RMS divergence of the first and third harmonic at 20 m from the source is shown in the calculated turning curves shown in Figure 5.2.3. The peak brilliance for the first harmonic occurs at ~ 700 eV and falls to less than half the peak value at the beam energy of primary interest in this work (184.76 eV). The large flux ($\sim 3.5 \times 10^{14}$ ph/s/.1%) (Figure 5.2.3a) of the first undulator harmonic but low brilliance ($\sim 6.5 \times 10^{17}$ ph/s/.1%/mr²/mm²) (Figure 5.2.3b) at 184.76 eV (6.7 nm) is a consequence of the relatively large divergence of the first harmonic (Figure 5.2.3c,d). The horizontal and vertical RMS divergence peak at the desired beam energy, with a peak horizontal RMS divergence of 48.1 μrad, and a peak vertical RMS divergence of 35.0 μrad.

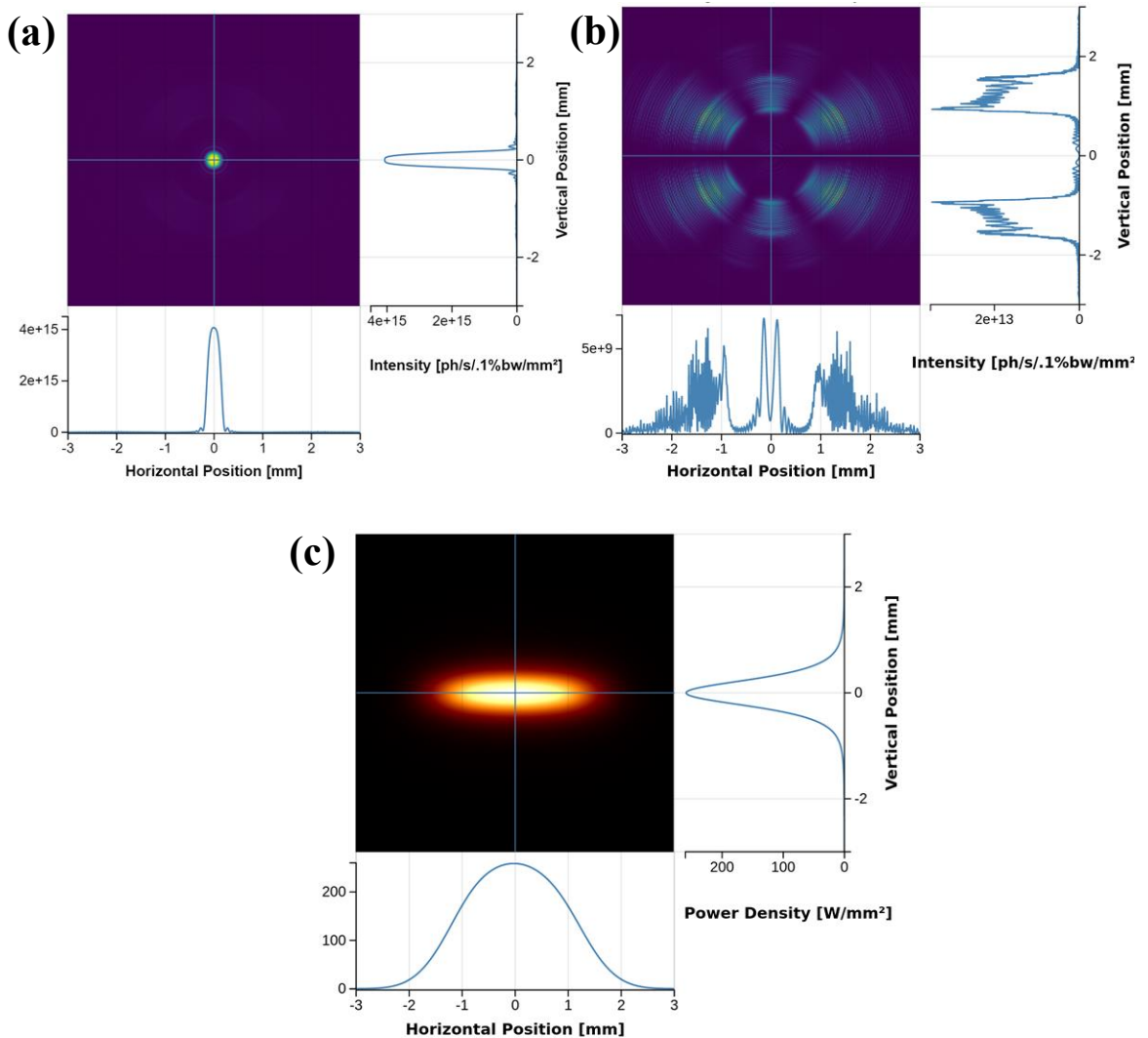


Figure 5.2.4 : The wavefront characteristics at 3 m from the model source for the undulator field shown in Figure 5.2.1-a. The intensity of the horizontally (a) and vertically (b) polarised components of the wavefield and power distribution (c) are shown. Power density is shown for the total polarisation component and undulator spectrum. Intensity is shown only for a single energy, $E = 184.76$ eV.

The peak in the linear horizontal polarised part of the wavefront at 3 m from the undulator (Figure 5.2.4a) is 4.07×10^{15} ph/s/.1%bw/mm². The peak vertically polarised intensity (Figure 5.2.4b) is 2 orders of magnitude less at 3.50×10^{13} ph/s/.1%bw/mm² and primarily off the optical axis such that it will be blocked by the first aperture (white beam slit). The power density distribution is much wider than the intensity distribution as it is given for all beam energies. It is also wider in the horizontal compared to vertical due to the asymmetric source emittance (Table 4.1).

5.2.1 Source Polarisation

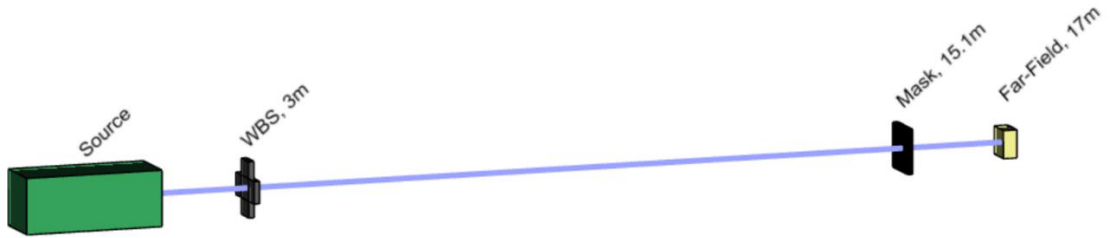


Figure 5.2.5: A simplified beamline representation, consisting of only elements up to the M1 plane of the SXR-I beamline at the Australian Synchrotron. The mask element can represent a grating mask or a YDS depending on the experiment. Generated using Sirepo/SRW [122].

To simplify the evaluation of the polarisation characteristics of the undulator source a simplified beamline model was constructed, shown in Figure 5.2.5. The model consisted only of an undulator source and optical elements up to the M1 plane of the SXR-I beamline (Table 4.4). The wavefront before and after each optical element was inspected to ensure the beam was adequately sampled at each plane. The polarisation of the beam was controlled by varying the horizontal and vertical components (B_x , B_y), of the Apple-II undulator magnetic field, and the offset in each direction, as described in Table 4.3. The Stokes parameters at every pixel, $S_n(x, y)$, were computed for beams generated for each combination of undulator parameters shown in Table 4.3 and propagated to the M1 mirror plane. Each Stokes parameter was then normalised to the maximum intensity so that

$$s_n(x, y) = \frac{S_n(x, y)}{\max[S_0(x, y)]} \quad 5.2.1$$

and the normalised Stokes parameters, $s_n(x, y)$, for each polarisation state are shown in Figure 5.2.6.

Each Stokes parameter shown in Figure 5.2.6 tends to 0 when the beam intensity is zero, which is expected from the definition of the Stokes parameters outlined in Section 2.4.2.1. For comparison to the degenerate stokes vectors (Equation 2.4.19), the average of each normalised Stokes component, \bar{s}_n , was taken over the area of the beam, discretely sampled by, N_x , and N_y , pixels in the horizontal and vertical directions respectively, so that:

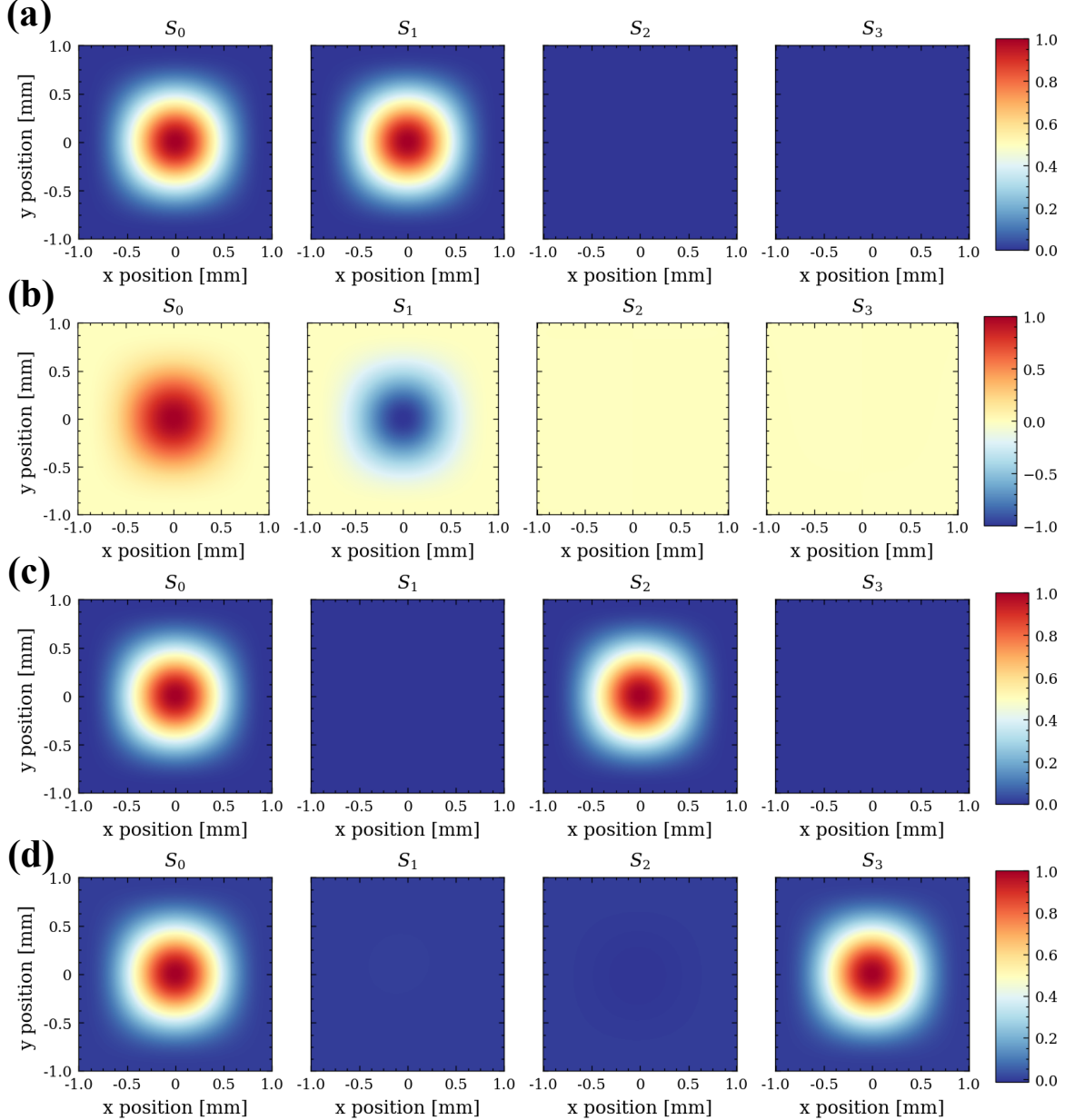


Figure 5.2.6: The normalised Stokes parameters for each beam undulator magnetic configuration shown in Figure 5.2.1, which produces (a) linear horizontal polarisation, (b) linear vertical polarisation, (c) linear 45° polarisation, and (d) circular-right polarisation.

$$\bar{s}_n = \frac{1}{N_x N_y} \left[\sum_{x=0}^{N_x} \sum_{y=0}^{N_y} s_n(x, y) \right].$$

5.2.2

The averaged Stokes components for each of the beams generated from parameters shown in Table 4.3 were found to be in agreement with the degenerate states (Equation 2.4.19, Section 2.4.2.1) showing that the undulator model is capable of recreating any degenerate polarisation state. To evaluate the ability of the model to generate a partially polarised beam, the magnetic field was varied to create linearly polarised beams with

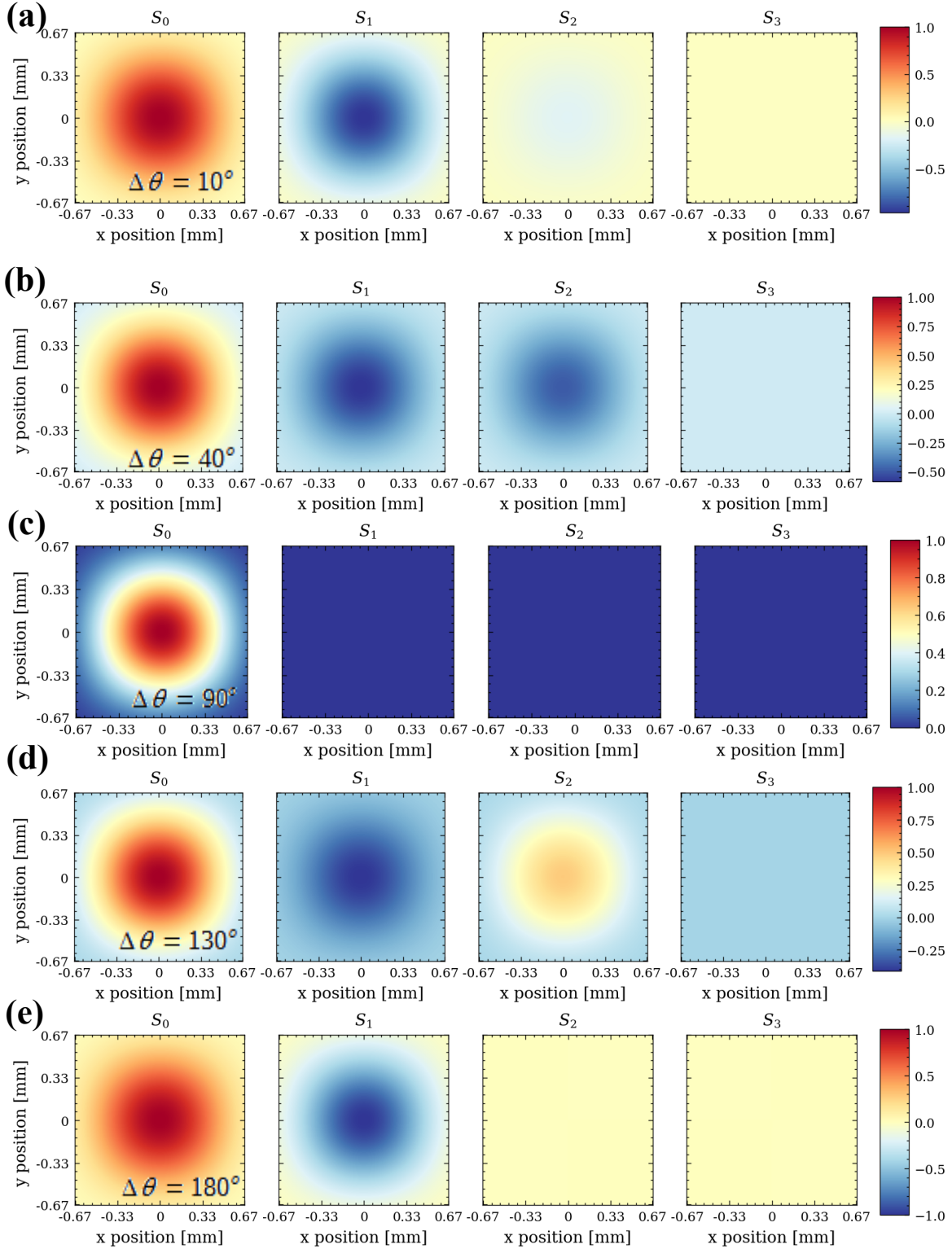


Figure 5.2.7: The Stokes parameters resulting from summing two linearly polarised beams with various angular separation. (a) $\Delta\theta = 10^\circ$. (b) $\Delta\theta = 40^\circ$. (c) $\Delta\theta = 90^\circ$. (d) $\Delta\theta = 130^\circ$. (e) $\Delta\theta = 180^\circ$. At $\Delta\theta=180^\circ$ S_3 reduces to 0 and at $\Delta\theta=90^\circ$ the resulting Stokes parameters are that of an unpolarised beam. S_3 remains at 0 for all beams as all summed beams are linearly polarised with no phase offset in the electric field

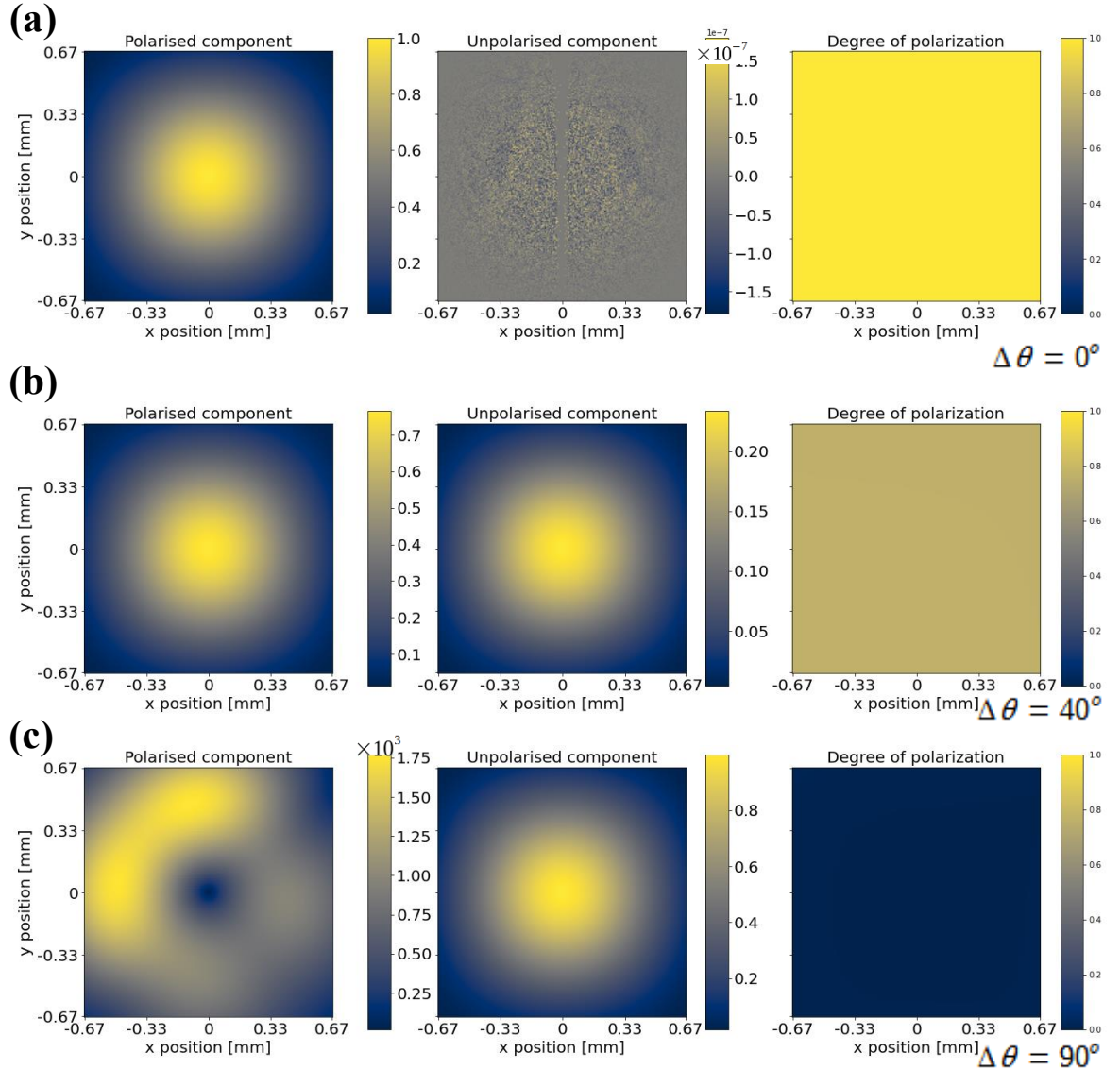


Figure 5.2.8: The polarised and unpolarised components and degree of polarisation for sum of linearly polarised beams with varied angular separation ($\Delta\theta$). (a) $\Delta\theta = 0$ (A single beam). (b) $\Delta\theta = 40^\circ$. (c) $\Delta\theta = 90^\circ$. As angular separation increases up to 90° the polarised component of the beam becomes less prominent, the degree of polarisation decreases, and the proportion of the beam in the unpolarised component increases,

polarisation orientations from 0° to 180° in steps, $\Delta\theta$, of 10° (using Equation 3.2.1). The Stokes parameters of the two of the set of propagated beams were then summed and normalised to unity. The Stokes parameters of the normalised sum of components with various angular distributions are shown in Figure 5.2.7. S_1 and S_2 vary with angular separation but the values of S_0 and S_3 are unchanged. At an angular separation of 180° , S_2 reduces to zero. When the angular separation of the two linearly polarised beams is 90° the resulting Stokes parameters are that of an unpolarised beam. This behaviour of the Stokes

parameters as the linearly polarised beams were added is consistent with theory outlined in Section 2.4.2.1.

Figure 5.2.8 shows the polarised and unpolarised components of various summed beams, calculated at every pixel from Equation 2.4.22, and the degree of polarisation at every pixel calculated from Equation 2.4.23. This figure shows that each individual beam is completely polarised (Figure 5.2.8a), as the degree of polarisation is unity across the entire beam and the polarised component is equal to the normalised intensity (s_0) shown in Figure 5.2.6a. As the angular separation of the summed beams increases, the degree of polarisation of the resulting beam decreases, confirming that the model can be used to generate a beam with an arbitrary degree of polarisation. The beam resulting from two orthogonally polarised beams (Figure 5.2.8c) shows a degree of polarisation of zero at the centre point which agrees with theory and previous tests.

Figure 5.2.9 shows that when summing beams of different polarisation orientation, the average degree of polarisation decreases with increasing angular distribution of the summed beams. The degree of polarisation of the resulting beam decreases steadily until it reaches a minimum when the polarisation angles of the summed beams differ by 90° . This is as expected, as the tendency of the resulting polarisation vector to any direction decreases as each additional beam is included in the sum. The relationship between the angular separation of two linearly polarised beams, $\Delta\theta$, and the average degree of polarisation of their sum, P , was found to be

$$P = |\cos(\Delta\theta)|.$$

5.2.3

This further validates the ability of the model to represent a beam with an arbitrary degree of polarisation.

It has been shown that the model presented is capable of reproducing beams with any polarisation state desired, including linear polarisation at arbitrary angles and elliptical/circular polarisation. Combined with the method shown for generating a beam with an arbitrary degree of polarisation, this allows the model to be used to recreate the polarisation characteristics of the Apple II undulator source of the SXR-I beamline.

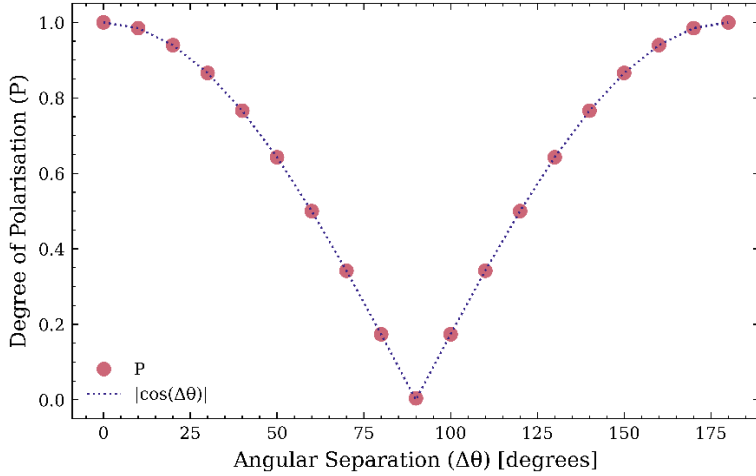


Figure 5.2.9: The average degree of polarization of a beam resulting from the sum of two linearly polarised beams with increasing angular separation between their polarisation vectors. As the angular separation increases up to 90° , the degree of polarization decreases and reaches a minimum of 0 when the two beams are polarised orthogonally to one another. When the beams are polarised at 180° to one another the degree of polarization of the resulting beam is 1.

5.3 The Beamline

The beam was propagated to each optical element shown in Figure 4.3.1 using both single electron (fully coherent) and multi-electron (partially coherent) propagation methods outlined in Section 3.1. The intensity was evaluated at each optical element to ensure adequate sampling and suitable propagation parameters. Figure 5.3.1 shows the beam intensity at key elements in the beamline propagated using both single and multi-electron propagation. The fully coherent nature of the single electron propagation leads to significant intensity variation due to coherent diffraction from apertures which is smoothed when propagated using multi-electron propagation. At the exit aperture plane (Figure 5.3.1a), cylindrical mirror plane (Figure 5.3.1b), and SSA plane (Figure 5.3.1c), the intensity fringes seen in the single electron intensity are no longer visible when viewed for multi-electron propagation. This smooth intensity distribution at the exit aperture plane is in agreement with intensity generated from ray tracing software Shadow for the SXRI beamline [63]. The intensity at the grating mask plane (Figure 5.3.1d) shows considerable variation when fully coherent propagation methods are used, which is unacceptable for IL as the grating would not be uniformly illuminated. The intensity variation in the central $100 \times 100 \mu\text{m}$ area of the fully coherently propagated wavefield is 15%. This variation is smoothed to just 7% over the same area when partially coherent propagation methods are used. The dimensions

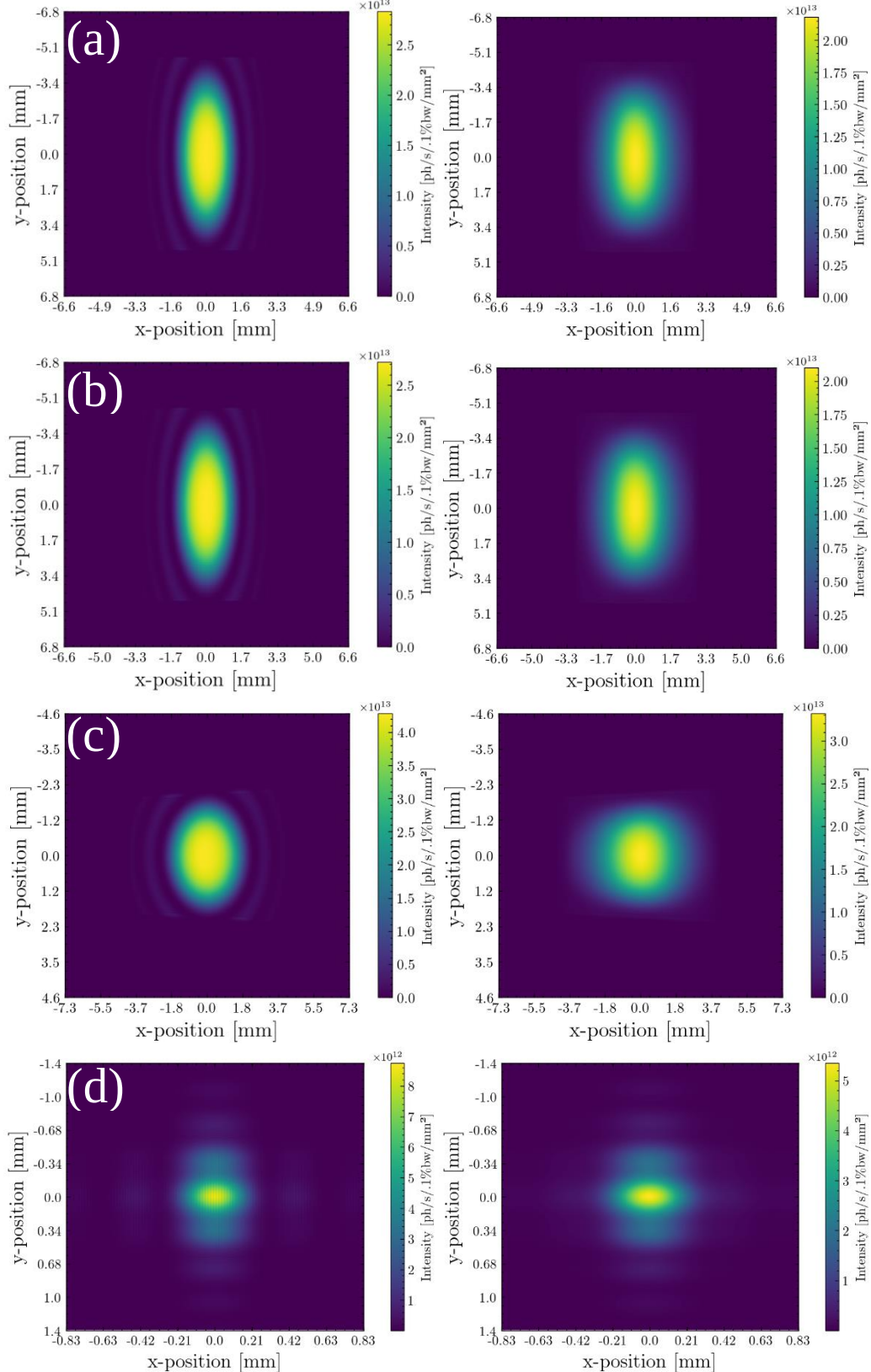


Figure 5.3.1: The beam intensity at different elements in the beamline obtained through fully coherent, single electron propagation (LEFT) and partially coherent, multi-electron propagation (RIGHT). (a) Intensity at exit aperture plane. (b) Intensity at cylindrical mirror (M1) plane. (c) Intensity at secondary source aperture plane, (d) Intensity at grating mask plane. At every plane the single electron intensity shows intensity variation due to coherent diffraction that is smoothed in the case of multi-electron propagation.

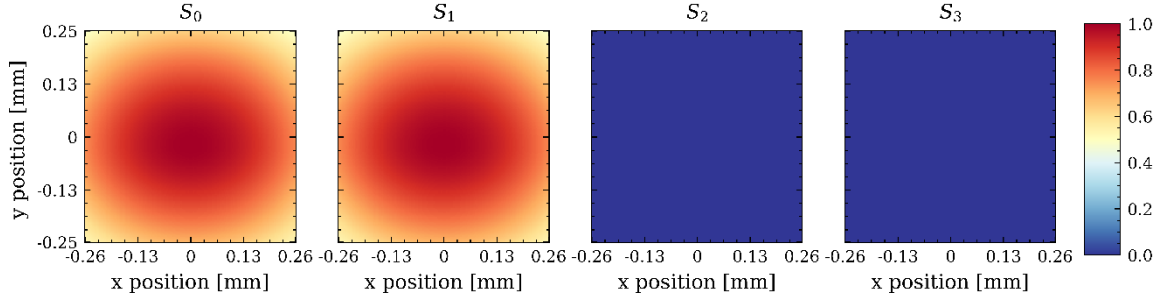


Figure 5.3.2: The Stokes parameters calculated for a beam propagated to the grating mask plane in the model of the SXRI beamline. The values of each stokes parameter is representative of a beam in a linear horizontal polarisation state with a high degree of polarisation.

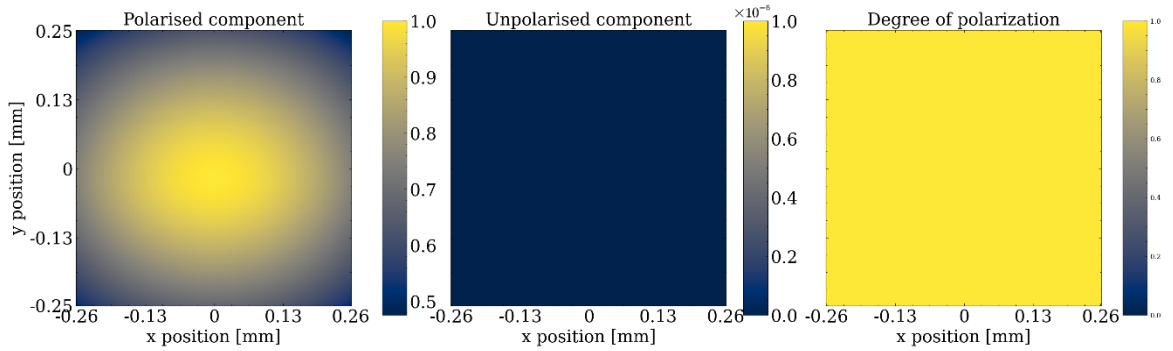


Figure 5.3.3: The polarised and unpolarised components of the beam at the mask plane, as well as the degree of polarisation across the beam. The beam can be seen to be highly polarised as the degree of polarisation at all points does not drop lower than 0.999991, The unpolarised component is of the beam has a maximum of $\sim 3.5 \times 10^{-6}$ compared to 1 in the polarised component.

of the intensity seen at the mask plane are similar to dimensions observed by a fluorescence screen located at the end of the beamline that is used for visual observations. The beam was found to be adequately sampled at each plane according to theory outlined in Section 3.1.1.

The polarisation properties of the wavefront propagated through the beamline to the mask plane shown in Figure 4.3.1 were evaluated using the same method used to evaluate the source polarisation in Section 5.2.1. The Stokes parameters calculated for the wavefront at the mask plane are shown in Figure 5.3.2. The Stokes parameters shown are consistent with linear horizontal polarisation as outlined in Section 2.4.2.1 indicating the polarisation of the source is maintained throughout the beamline. The polarised and unpolarised components of the propagated wavefield shown in Figure 5.3.3 show that the wavefield is highly polarised at the mask plane. This is confirmed by the degree of polarisation which is ~ 1 at every sampled point of the wavefront (Figure 5.3.3c).

5.4 Mask Illumination

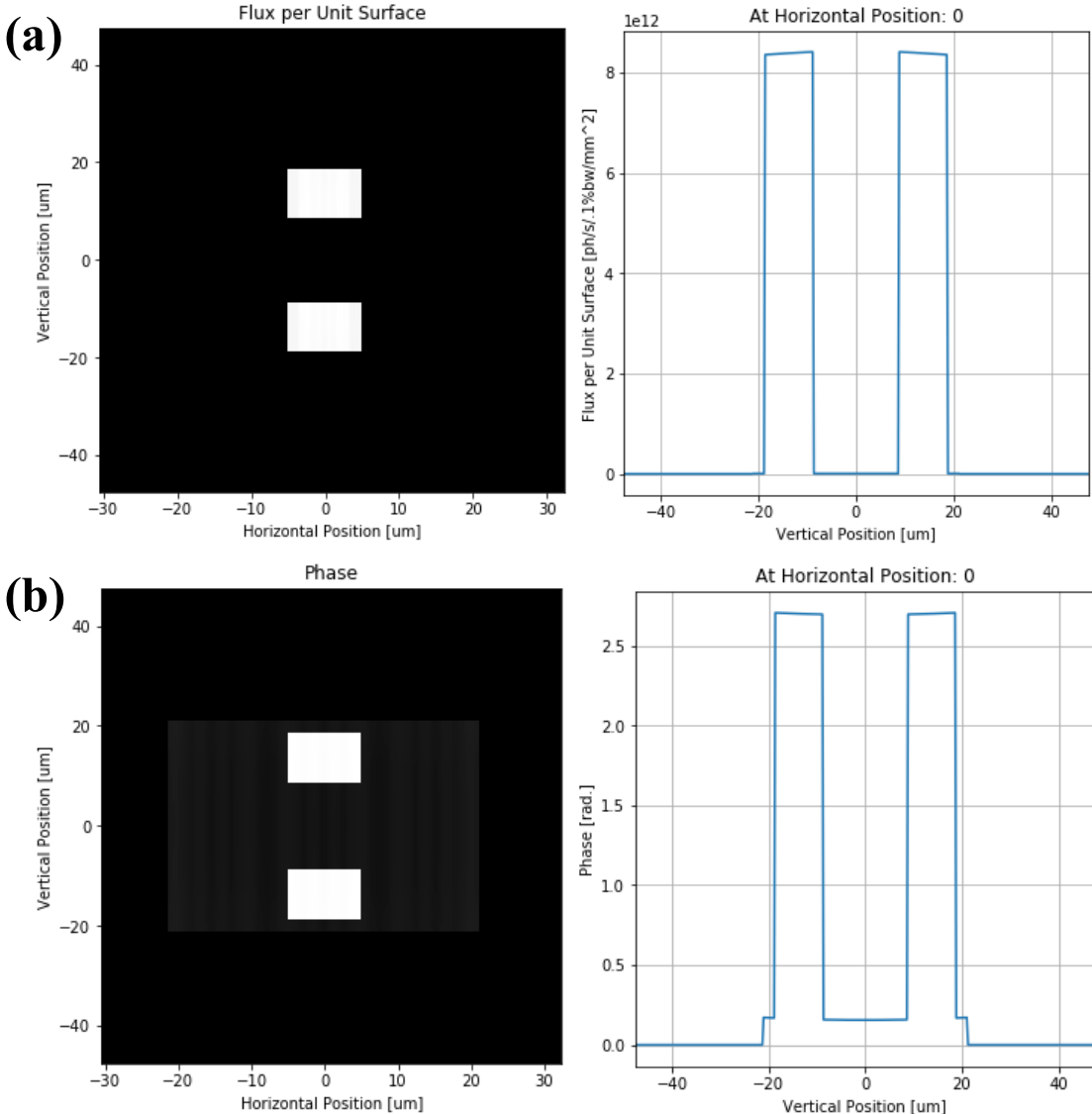


Figure 5.4.1 : The wavefront intensity (a) and phase (b) at the mask plane immediately after the tantalum photon block layer. The intensity shows a small amount of transmission through the centre of the block layer and interference due to the circular BDA. The phase shows symmetry across the mask.

The wavefront at the mask plane, immediately after fully coherent propagation through the Tantalum photon block layer of the mask model described in Section 4.4.1 shows nearly uniform intensity distribution in the transmitted intensity (Figure 5.4.1). In the area of the gratings the intensity varies by ~1%, with a peak intensity of $\sim 8.4 \times 10^{12}$ ph/s/.1%bw/mm². The transmission through the photon block mask layer is $\sim 0.075\%$, so contamination of the aerial image from zero-order transmission through the mask will not have to be considered for high efficiency gratings. The effect of transmission through the mask will become more significant for low-efficiency gratings and may have to be

considered. The phase of the wavefront at the grating plane is symmetric about $x = 0$ across the mask and shows a negligible radial variation over the area of the gratings. This indicates a symmetrical wavefront with low divergence which is ideal for ensuring high contrast interference.

Figure 5.4.2 shows the wavefront intensity and phase after propagation through the entire mask shown in Section 4.4.1. The grating thickness, t_g was set to 107.5 nm. The peak intensity seen in Figure 5.4.2 is unaffected for areas not occupied by grating lines. Transmission of $\sim 0.7 \times 10^{12}$ ph/s/.1%bw/mm² is seen in the grating lines as shown in the

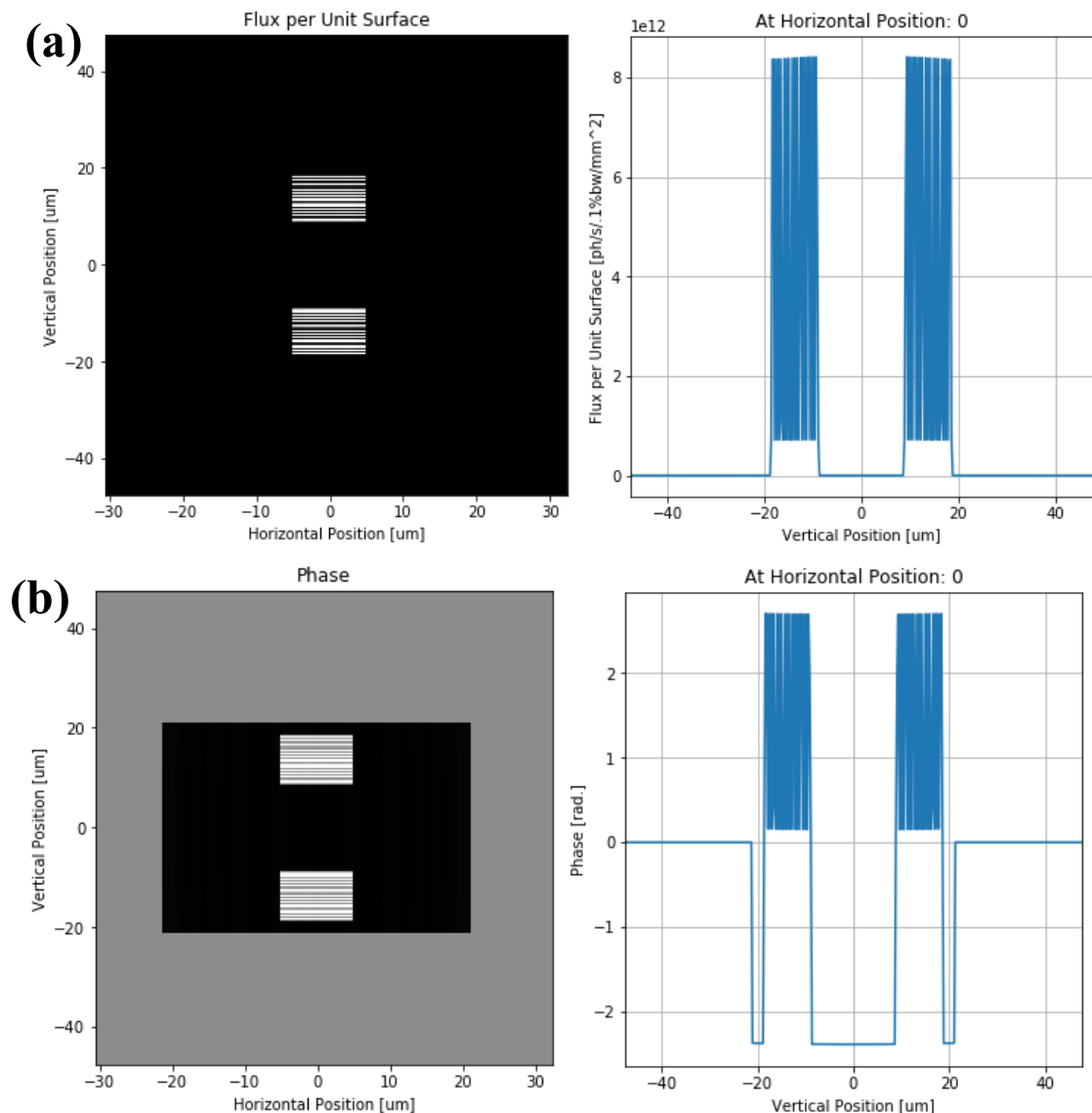


Figure 5.4.2 : The wavefront intensity (a) and phase (b) at the mask exit plane immediately after the propagation through the entire three-layer mask. The 100 nm grating line period is not observable at this scale, due to resolution the lines appear much larger. The phase shows symmetry across the mask.

vertical line profile (Figure 5.4.2), which gives a transmission through the absorber layer of $\sim 8\%$. The phase of the illumination at the grating exit plane is shown to be symmetrical over the grating with an average phase shift of 2.5 rad introduced in the transmitted wavefront. The phase distribution of the wavefield in areas not occupied by grating lines is again seen to be highly uniform indicating low divergence and sufficient conditions for high contrast interference at the image plane.

5.5 Diffraction Efficiency

As indicated in Section 4.4, the consequences of the assumption of the projection approximation for each layer of the mask model (shown in 4.4.1) may lead to inaccuracies

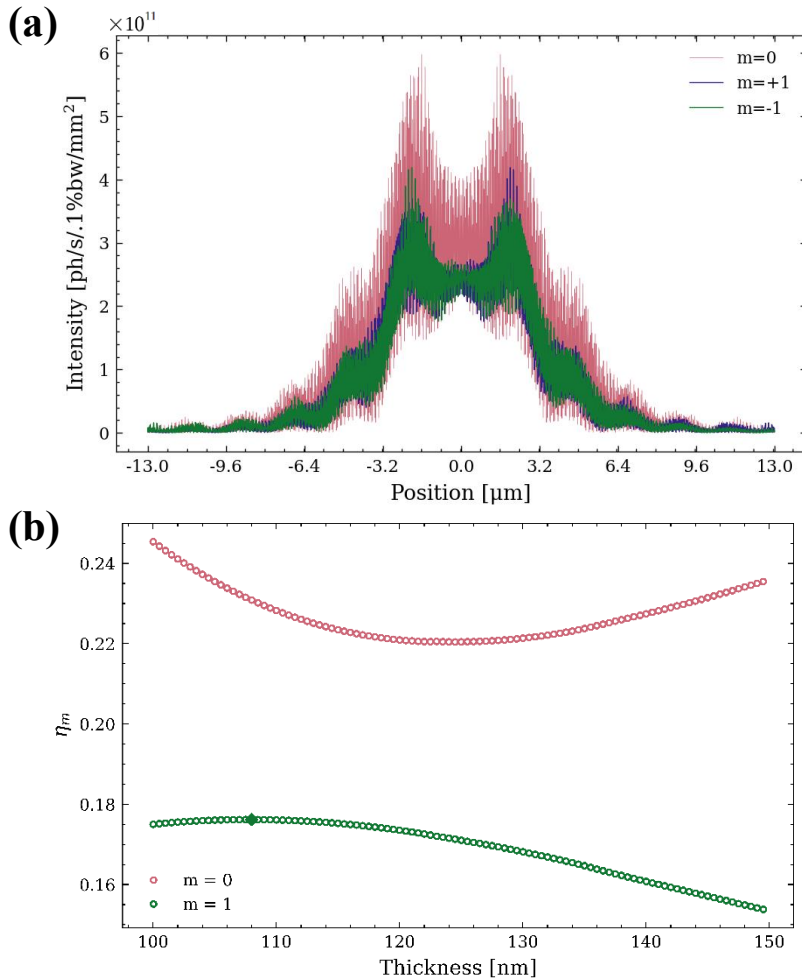


Figure 5.5.1: (a): Overlaid intensity distributions for $m=0$, $m=+1$, $m=-1$ diffracted beams from an Ni_3Al single grating (seen in Figure 4.4.5c). The $m=1$ and $m=-1$ orders are translated so the centre of each order is aligned with that of the zero-order diffracted beam. (b): Zeroth (red) and first (green) order diffraction efficiency as a function of grating thickness for a single Ni_3Al grating. Minimum efficiency for $m=0$ is 0.22, which occurs at grating thickness of 124.5 nm. Maximum efficiency for $m=1$ of 0.18 occurs at grating thickness of 108 nm.

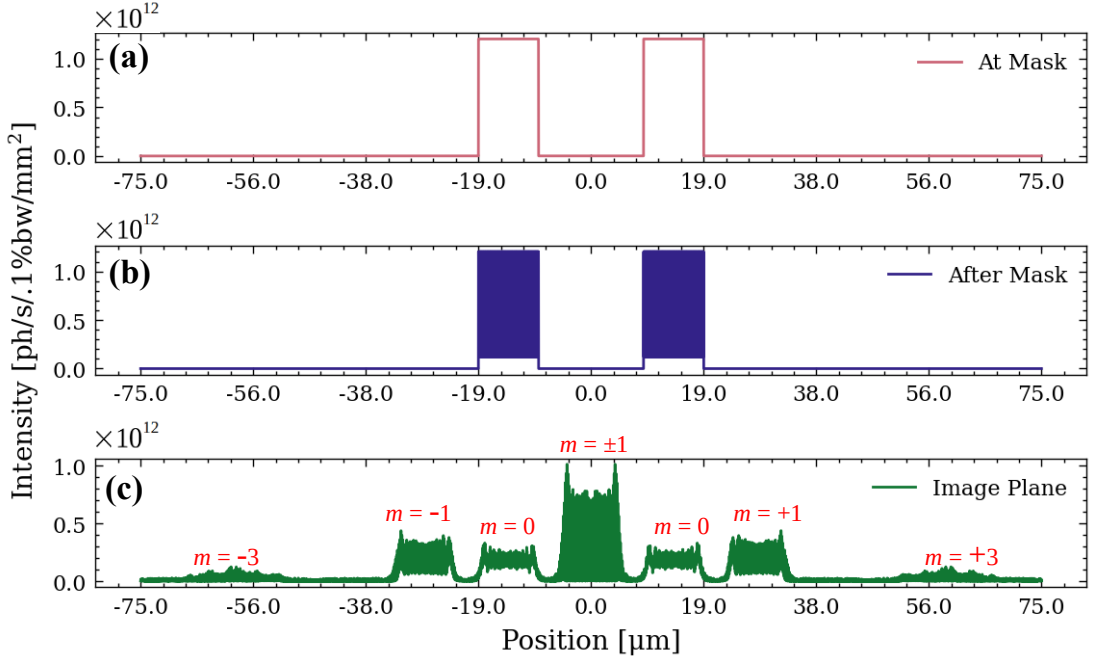


Figure 5.5.2: Incident (a), exit (b), and propagated (c) wavefield intensity for evaluating the diffraction efficiency of an Ni₃Al two-grating mask.

in the generation of an aerial image. The diffraction efficiency values obtained for different grating thickness using the wavefront propagation approach in this work can be compared to the diffraction efficiency obtained by RCWA to evaluate the impact of neglecting mask thickness effects. To evaluate the diffraction efficiency of a Ni₃Al grating mask for EUV-IL using the wavefront propagation approach, a Gaussian beam was propagated through an ideal mask model of a single and two-beam IL grating mask as outlined in Section 4.4.3. The optical properties of Ni₃Al for 6.7 nm incident radiation are listed in Table 4.5. The intensity of each diffracted order after propagation (Figure 4.4.5c) was compared to the incident intensity over the area of the grating (Figure 4.4.5a).

Figure 5.5.1 shows the overlaid intensity distributions for each diffracted order for a single, Ni₃Al diffraction grating, and the efficiency as the grating thickness was increased from 100 nm to 150 nm. The maximum first-order efficiency was found to be $\eta_1 = 0.18$, occurring at a grating thickness of $t = 108$ nm. The minimum zero-order efficiency was found to be $\eta_0 = 0.22$, occurring at a grating thickness of $t = 124.5$ nm.

The process was repeated to evaluate the efficiency of a two-grating IL mask. The intensity of each diffracted order after propagation, as well as the intensity contained in the

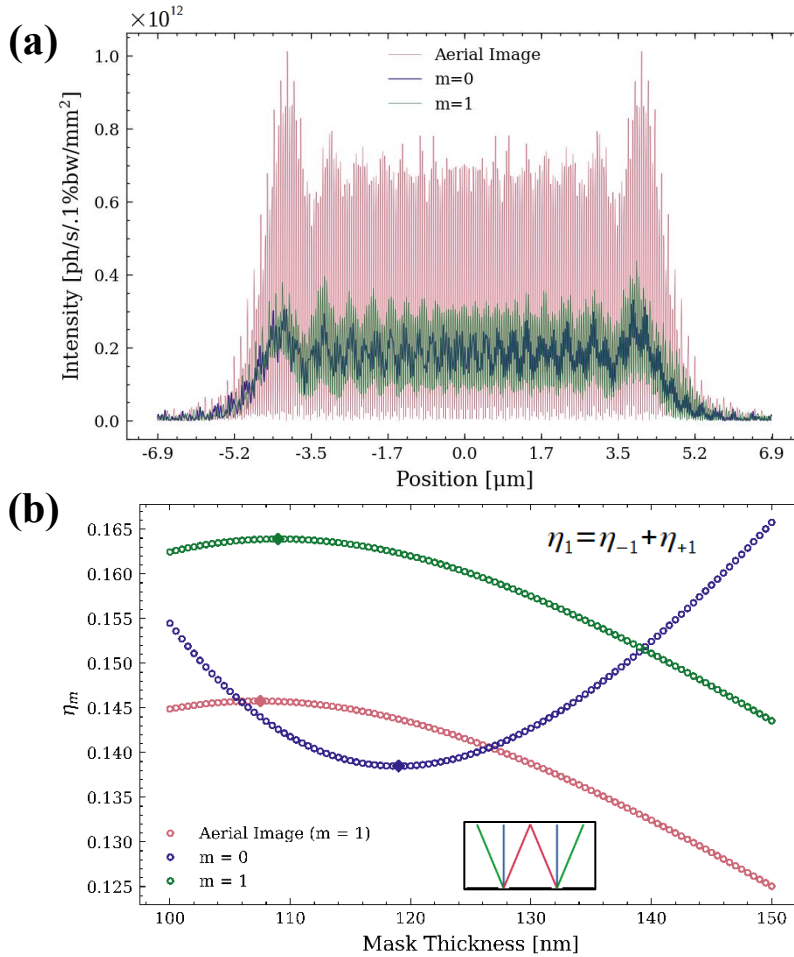


Figure 5.5.3: (a): Overlaid intensity distributions of the 0th and 1st order diffracted beams, and the 1st order aerial image, propagated to the image plane (seen in Figure 5.5.2-c).(b): Efficiency vs. thickness for an Ni₃Al, two-grating interference mask. Inset shows a simple diagram of each diffracted beam, $m=0$ and $m=1$ efficiencies were taken as the sum of efficiencies from each grating. Minimum efficiency for $m=0$ is 0.1384, which occurs at grating thickness of 119 nm. Maximum efficiency for $m=1$ of 0.1639 occurs at grating thickness of 109 nm. Maximum aerial image ($m=1$) efficiency is 0.1458, occurring at 107.5 nm thickness.

aerial image (shown in Figure 5.5.2c) was compared to the incident intensity over the area of each grating (Figure 5.5.2a). The aerial image intensity profile shown in Figure 5.5.2c is a low resolution, representative profile only generated for evaluation of diffraction efficiency. No other analysis was performed regarding on aerial images generated for this section. A full description and analysis of aerial images is undertaken in Section 6.2.

Figure 5.5.3 shows the overlaid intensity distributions for each diffracted order for a two-beam, Ni₃Al diffraction grating mask, and the efficiency as the mask thickness was increased from 100 nm to 150 nm. The efficiency of each order was taken as the sum of the efficiencies from each grating so that $\eta_1 = \eta_{-1} + \eta_{+1}$. The first order efficiency was taken as the sum of the efficiencies of the non-interfering first order intensit-

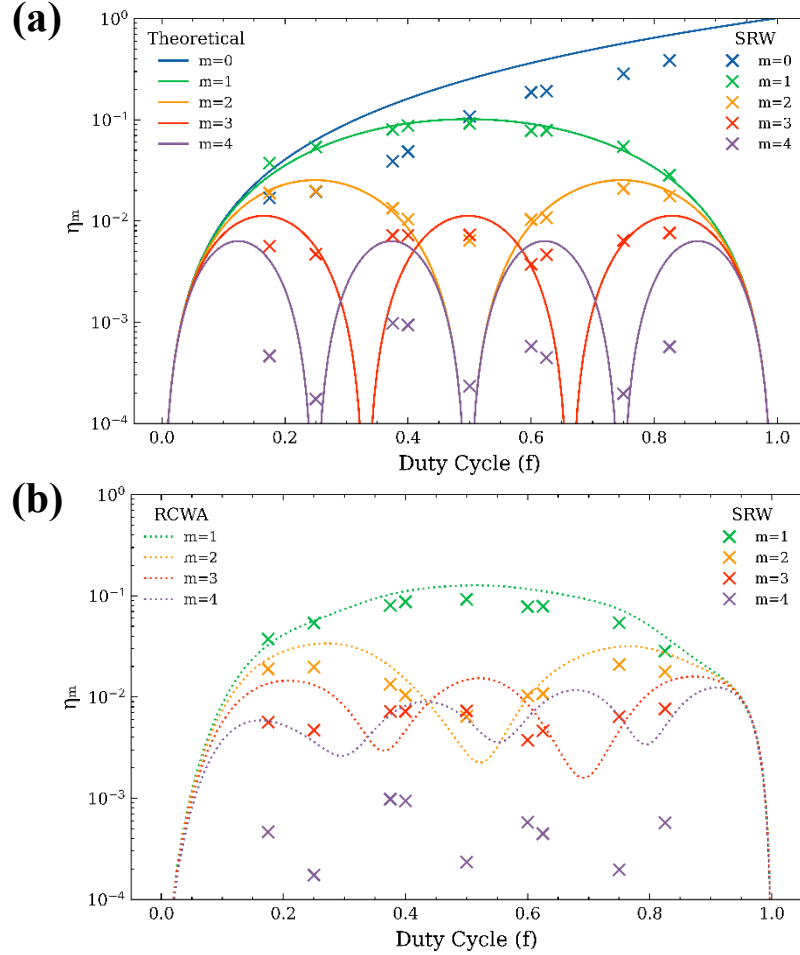


Figure 5.5.4: Efficiency of a single grating with varied duty cycle. (a): Efficiency obtained from propagation method. (b): Efficiency obtained numerically from theory outlined in Section 2.4.4.

-ties ($m = +1$, and $m = -1$ in Figure 5.5.2c), while the first order aerial image efficiency, η_I^{AE} , was taken as the sum of the efficiencies of the interfering first order intensities ($m = \pm 1$ in Figure 5.5.2c). The maximum first-order efficiency was found to be $\eta_I = 0.16$, occurring at a grating thickness of, $t = 109$ nm. The minimum zero-order efficiency was found to be $\eta_0 = 0.14$, occurring at a grating thickness of $t = 119$ nm. The maximum first-order aerial image efficiency was found to be $\eta_I^{AE} = 0.15$, coinciding with a 107.5 nm thick Ni₃Al mask. The difference in the maximum and minimum intensity value calculated across the area of the gratings in each case is $< 0.1 \times 10^8$ ph/s/.1%bw/mm² which is $< 1 \times 10^{-5}\%$ variation in intensity. The maximum variation in phase across the area of the mask is $< 1 \times 10^{-7}$ rad, indicating sufficiently large wavefront curvature, for the assumption that the incident beam can be considered a plane wave to be valid.

Grating masks with different duty cycles ($f = 0.175, 0.25, 0.375, 0.4, 0.5, 0.6, 0.625, 0.75, 0.825$), 100 nm pitch, and 107.5 nm thickness were created using methods shown in Section 4.4.1. The efficiency of diffracted orders $m = 0, 1, 2, 3, 4$, were calculated for each mask and compared to the expected values from Equation 2.4.57. The discrepancies seen in Figure 5.5.4 are expected as Equation 2.4.57 assumes an ideal transmission grating with zero thickness and ($p_G >> \lambda$). The efficiency of the first order beam is in the best agreement with theory.

Table 5.1: Peak efficiency values and their corresponding mask thicknesses obtained through propagation in SRW and RCWA with various refractive index and attenuation length values. Results obtained for the efficiency of a single grating and a two-grating mask are included. Refractive index database values were obtained from Ref. 99, measurement values were taken from Ref. 188 and 189.

Single Grating:	δ	β	ρ	η_1 max	Thickness
SRW	2.530307×10^{-2}	$1.22133737 \times 10^{-2}$	0.95 g/cm^2	0.18	108 nm
RCWA (database)	2.530307×10^{-2}	$1.22133737 \times 10^{-2}$	0.95 g/cm^2	0.13	118.4 nm
RCWA (measurement)	2.40×10^{-2}	1.75×10^{-2}	0.95 g/cm^2	0.14	110.3 nm
Two Gratings:	δ	β	ρ	η_1 max	Thickness
SRW (each grating)	2.530307×10^{-2}	$1.22133737 \times 10^{-2}$	0.95 g/cm^2	0.16	109 nm
SRW (aerial image)	2.530307×10^{-2}	$1.22133737 \times 10^{-2}$	0.95 g/cm^2	0.15	107.5 nm
RCWA (database)	2.530307×10^{-2}	$1.22133737 \times 10^{-2}$	0.95 g/cm^2	0.11	112.4 nm
RCWA (measurement)	2.40×10^{-2}	1.75×10^{-2}	0.95 g/cm^2	0.13	105.3 nm

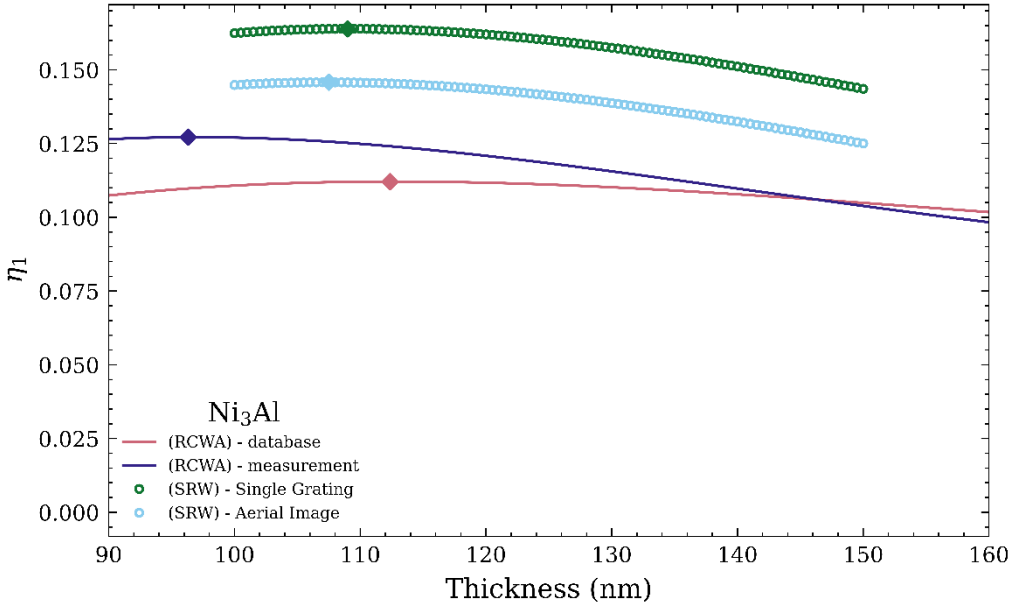


Figure 5.5.5: Comparison of efficiency values obtained from wavefront propagation through an ideal Ni₃Al mask using SRW to values obtained from RCWA [188,189], for the same value of the complex refractive index and for an experimentally measured value.

The diffraction efficiency as a function of mask material thickness for Ni₃Al single and two-grating masks with 100 nm pitch were compared to results obtained from Rigorous Coupled-Wave Analysis (RCWA) [188,189], using the same complex refractive index and attenuation values for Ni₃Al shown in Table 4.5 (Section 4.4.1) as well as empirical values obtained from x-ray absorption measurements at the SXR-I beamline (Figure 5.5.5). A Ni₃Al film was deposited in alternating layers of Ni and Al by physical vapor deposition (PVD) and annealed at 500° C for 1 hour. X-ray absorption was measured over the photon energy range 90 – 160 eV and the real part of the refractive index was obtained via Kramers-Kronig transformation [188,189].

Figure 5.5.4a shows close agreement between efficiency values calculated from SRW and theory, with the smallest differences between SRW and analytical values occurring for $m = 1$. Figure 5.5.4b shows that the closest agreement between efficiency values obtained from SRW and RCWA also occurs for $m = 1$. As the diffracted order is increased, the differences in efficiency values are greater. Figure 5.5.5 and Table 5.1 show disagreement in calculated efficiencies obtained from the propagation method in SRW and the analytical method of RCWA ranging from ~14% to ~26%. For a two-grating mask, RCWA found the peak first-order efficiency to be 0.11 when using values for the Ni₃Al refractive index from the Henke database [99], and 0.13 when using measured refractive index values. For a single grating, RCWA found the peak efficiency to be 0.13 when using refractive index values from the Henke database [99], and 0.14 when using experimental values. The deviation of the RCWA efficiency values from the $\eta_1 = 0.18$ value obtained from the propagation method, and the systematic difference in values obtained through propagation can be attributed to limitations in the projection approximation at this thickness. The close agreement seen between diffraction efficiency values calculated from theory, RCWA and the SRW wavefront propagation method is sufficient to justify using the projection approximation in this work.

5.6 Partial Coherence

The aerial images resulting from partially coherent propagation through the entire beamline model described in Section 4.3 and a two-grating IL mask with geometry shown in Section 4.4.1 were compared for 100, 1000, 2000, 3000, 4000, 5000 and 10000 simulated

electrons. The minimum number of electrons needed to accurately represent the partially coherent source was evaluated. The mask was oriented with the gratings separated horizontally to capture the effects of finite horizontal spatial coherence. The horizontal electron beam emittance is significantly greater than the vertical emittance and so the number of electrons needed to accurately sample the phase space occupied by the beam is greater.

Figure 5.6.1 shows the aerial images generated for different numbers of simulated ele-

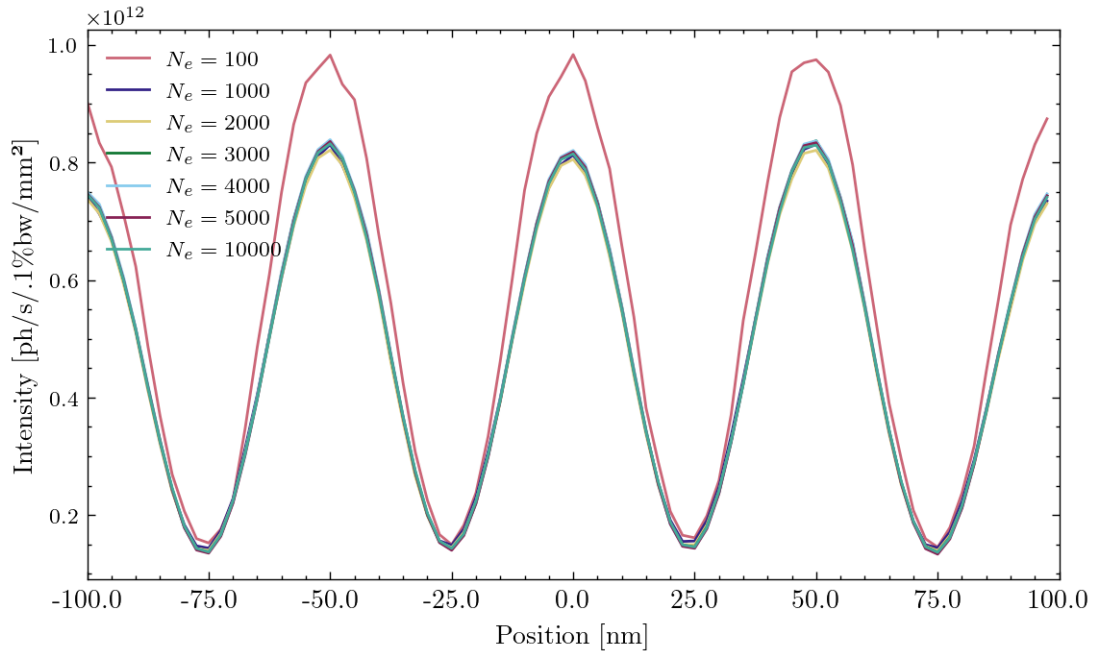


Figure 5.6.1: The aerial image intensity generated using partially coherent propagation, shown for $N_e = 100, 1000, 2000, 3000, 4000, 5000$ and 10000 simulated electrons. The maxima of the interference fringes can be seen to drop significantly when comparing the results from 100, 1000 and 2000 electrons. The difference between propagation using 5000 electrons and 10000 electrons is negligible.

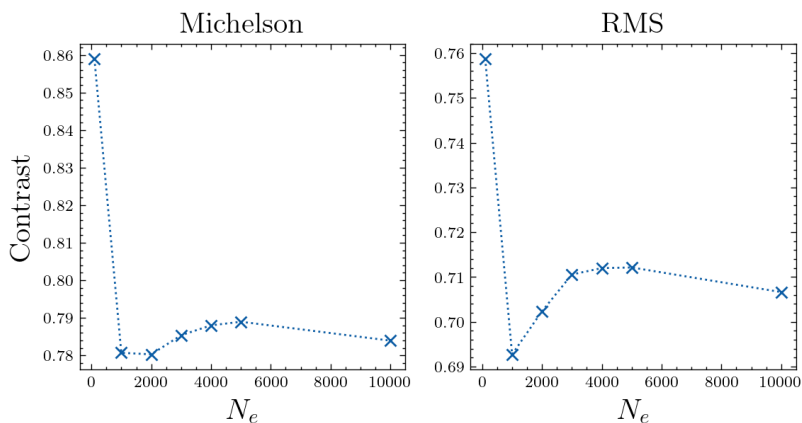


Figure 5.6.2: Contrast calculations for aerial images generated through multi-electron propagation with different numbers of simulated electrons (N_e). The aerial images are shown in Figure 5.6.1.

-ctrons, N_e . The height of the intensity fringes decreases significantly as N_e increases from 100 to 1000 and increases slightly from $N_e = 2000$ to $N_e = 3000$. For $N_e > 2000$ the variation is minimal with increased electrons. No significant variation is seen in the aerial images generated from N_e from 3000 to 10000 indicating that the phase space occupied electron beam is adequately sampled when $N_e = 3000$.

The Michelson contrast (visibility), and RMS contrast of the aerial images shown in Figure 5.6.1 was calculated by methods described in Section 2.1.1 and is shown in Figure 5.6.2. Both contrast metrics show a steep drop in contrast from 100 to 1000 simulated electrons, and a small increase in contrast from 2000 to 3000 simulated electrons which is consistent with the change seen in the aerial images in Figure 5.6.1. From 3000 to 10000 simulated electrons the visibility stays ~ 0.79 , which the RMS contrast remains ~ 0.71 . A

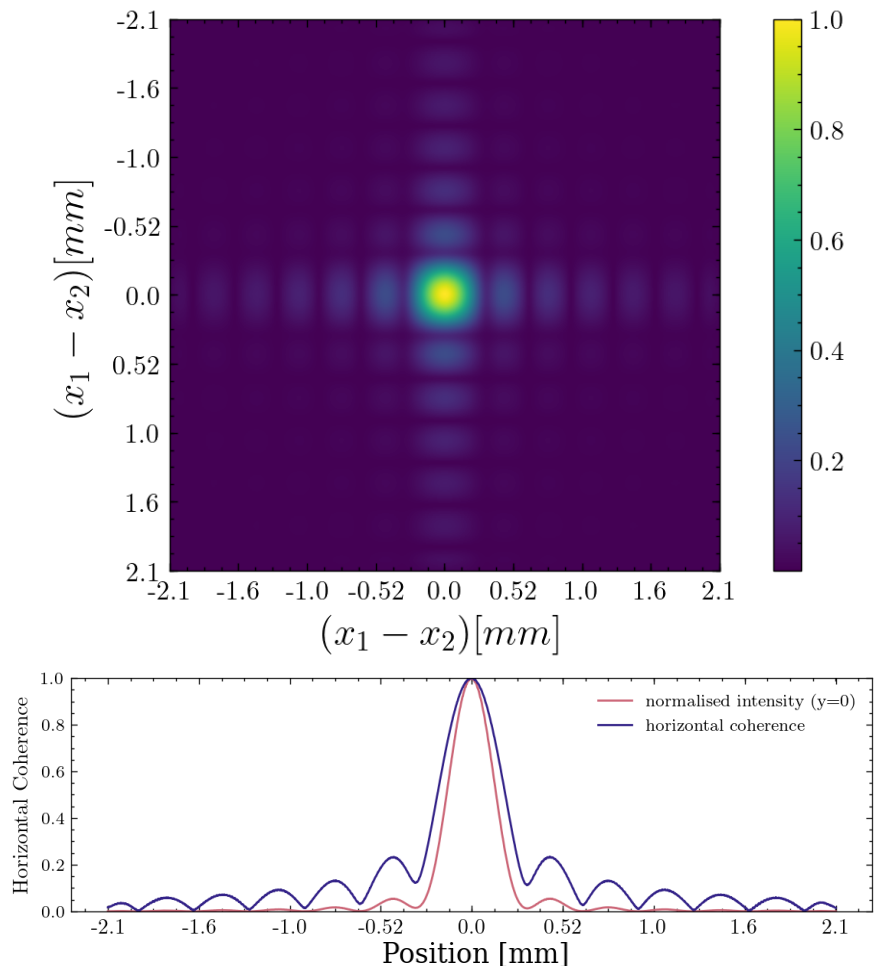


Figure 5.6.3: Horizontal coherence profile of the wavefield at the mask plane. Line profiles through the normalised point separated horizontal coherence profile (TOP), give the horizontal coherence and normalised intensity (BOTTOM). The horizontal coherence length was estimated as the width of the coherence profile at 0.8. For a SSA of 200 μm horizontal width the horizontal coherence length was estimated to be 230 μm .

small variation in contrast is still seen for $N_e > 3000$, however the computational cost of each propagation is increased with the number of simulated electrons (Equation 2.5.2). As a compromise 4000 electrons were simulated for all partially coherent propagations presented hereafter.

The complex electric field of the beam at the plane of the mask was used to compute the two-dimensional coherence function using theory outlined in Section 2.4.1. An estimate of the horizontal coherence length was taken as the width of the normalised coherence profile at 0.8 of the maximum value. Figure 5.6.3 shows the horizontal coherence profile of the beam used to generate the aerial images shown in Figure 5.6.1 for a SSA of 200 μm horizontal width. The horizontal coherence length at the mask plane for a SSA of 200 μm horizontal size was estimated to be 230 μm . This is significantly larger than the dimensions of the mask, indicating that the grating can be considered coherently illuminated at this SSA setting.

The transverse coherence of the SXRI beamline at 1 keV photon energy has previously been measured at the mask plane by Tran *et al* [187], using an array of Young Double Slits (YDS) oriented vertically with a range of slit separation distances. The same method was used for a 6.7 nm wavelength beam and a YDS array with maximum slit separation of 30 μm . No significant loss of visibility of the interference fringes was found for the largest YDS slit separation even when the beamline SSA horizontal size was increased to 1100 μm . This implies that the horizontal coherence length for 6.7 nm is always greater than 30 μm .

5.6.1 The Effect of Secondary Source Size on Spatial Coherence

The effect of the secondary source aperture (SSA) size on spatial coherence and intensity at the mask plane was investigated by adjusting the horizontal and vertical dimensions of the SSA and evaluating the wavefield at the mask plane. Figure 5.6.4 shows the horizontal coherence profiles for the SXR-I beamline at the mask plane for a SSA of horizontal widths 100 μm , 200 μm and 300 μm . The maximum horizontal coherence length obtained was 460 μm for a SSA of horizontal size 100 μm . The minimum horizontal coherence length attained was 160 μm for a secondary source slit of horizontal size 300 μm . Similar analysis was undertaken on the vertical profile of the wavefield at the mask plane for SSA vertical widths of 100 μm , 125 μm , 150 μm , and 200 μm . The maximum estimated vertical cohere-

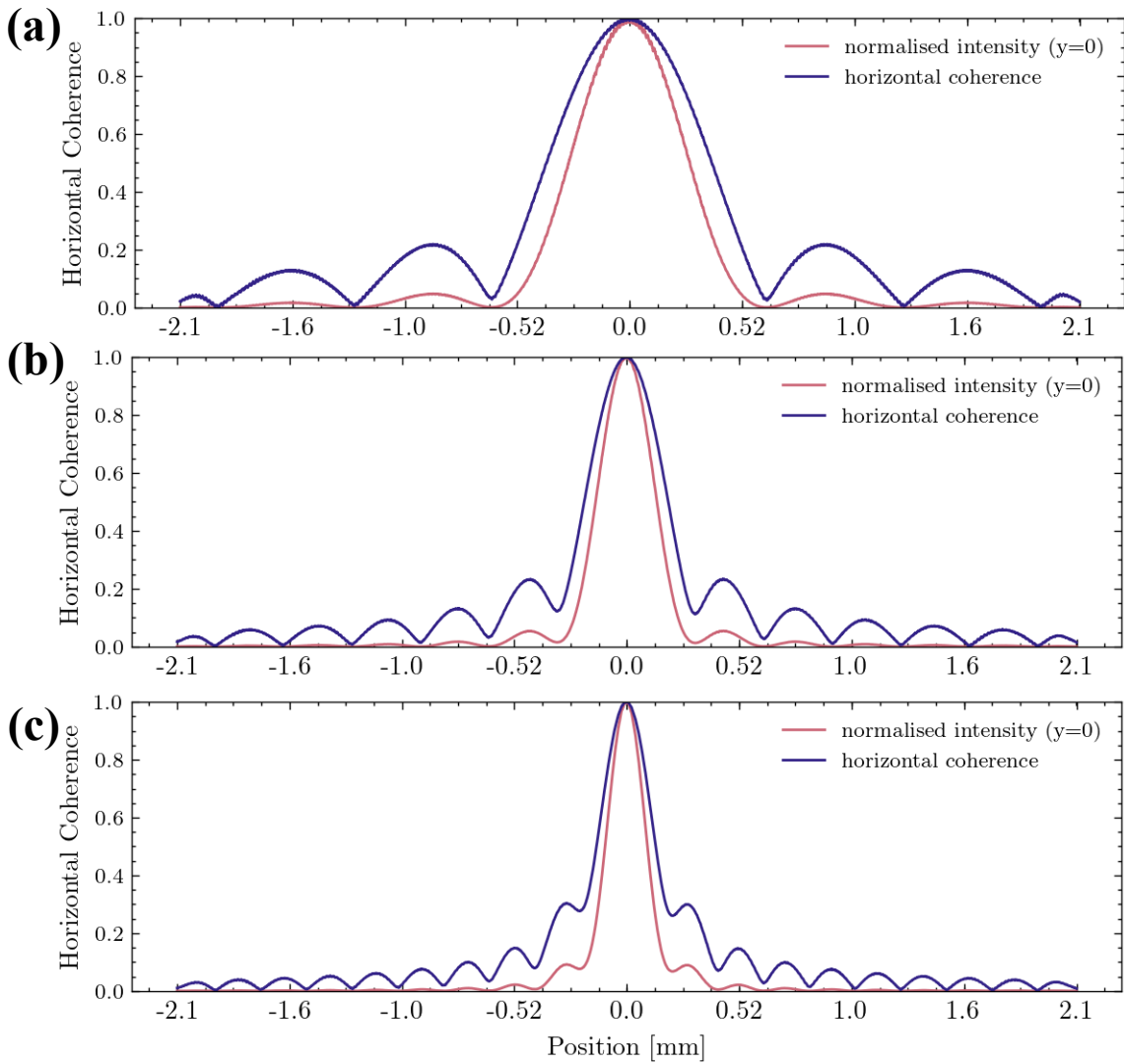


Figure 5.6.4: Horizontal coherence profiles at the mask plane generated for SSA of horizontal size from 100 (a), 200 (b), and 300 (c) microns. An estimate of the coherence length was taken to be the width of the coherence profile at a value of 0.8. The coherence length as a function of secondary source slit width is shown in Figure 5.6.5.

-nce length was 460 μm for a SSA of 100 μm vertical width, with a minimum coherence length of 280 μm for a vertical SSA size of 200 μm .

Figure 5.6.5 shows the estimated horizontal and vertical coherence lengths as a function of SSA size. The decrease in coherence length with greater SSA size is expected as from theory outlined in Section 2.4.1. The consistently larger vertical coherence length compared to horizontal when measured for the same SSA size is also expected, as the vertical emittance of the source (given in Table 4.1) is significantly smaller than the horizontal emittance.

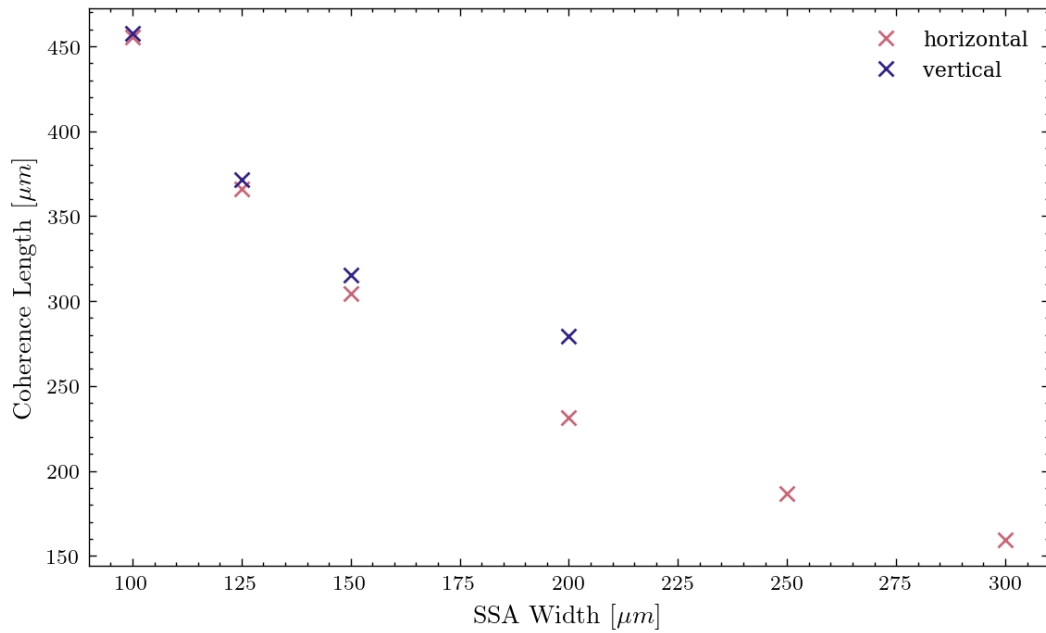


Figure 5.6.5: Estimated horizontal (red) and vertical (blue) coherence length at the mask plane for various secondary source slit sizes. The coherence length is seen to decrease as slit width increases as expected. The coherence length in both directions was found to be larger than the dimensions of the mask models shown in Figure 4.4.1 for horizontal SSA < 300 μm and vertical SSA < 200 μm.

The minimum horizontal and vertical coherence lengths of 160 μm and 280 μm are both significantly larger than the largest dimension of the mask used in this project. The mask can therefore be considered coherently illuminated for all SSA widths below 300 μm in the horizontal and 200 μm in the vertical. This suggests that further optimisation of the beamline is possible such as increasing the size of the WBS or SSA to provide more flux as further loss in coherence can be tolerated for the advantage of more flux.

Figure 5.6.6 shows the relationship between horizontal SSA size, coherence length and total flux at the mask plane. The vertical SSA size was kept to a constant 200 μm. The maximum total flux obtained at the mask plane was $\sim 1.5 \times 10^{15}$ ph/s/0.1%bw, for a 300 μm horizontal SSA. This is a ~ 3 factor increase in the total flux of 0.5×10^{15} ph/s/0.1%bw obtained from a 100 μm horizontal SSA. This increase in flux comes at the cost of coherence, with the horizontal coherence length decreasing by a factor of ~ 2.9 for the same change in SSA size. Since the horizontal coherence length is still significantly larger than the mask dimensions the benefits from the increased flux at the mask plane will outweigh the costs of the reduction in horizontal coherence.

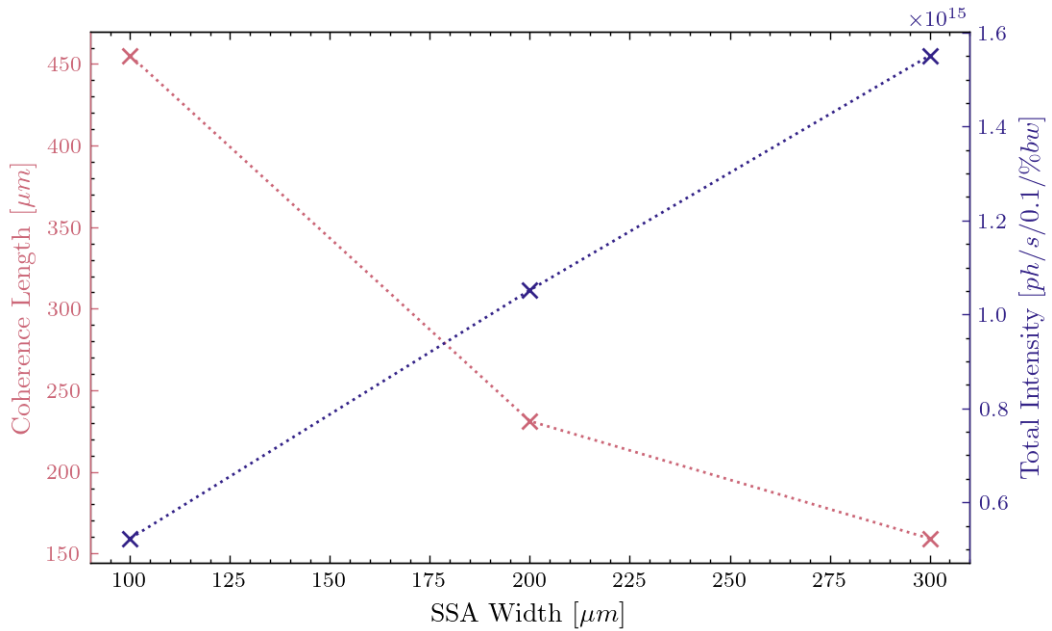


Figure 5.6.6: The horizontal coherence length vs total flux at the mask plane for different SSA horizontal size and vertical size of 200 μm . Increased coherence comes at a cost of total flux. The dotted lines between points are added to guide the eye only.

Comparing the 1.5×10^{15} ph/s/0.1%bw maximum flux at the mask to the intensity reported at other beamlines in use for EUV-IL gives an indication of the future performance of the XRNF facility at the AS. Scaling the flux by the ratio of the bandwidth at which it is calculated to the bandwidth of the monochromator when operating in zero-order so that the entire first harmonic centred at 185 eV (shown in Figure 5.2.2) is used to illuminate the mask gives an estimated flux of $\sim 1 \times 10^{17}$ ph/s/3.7%bw. This approximation allows for a more accurate comparison to other beamlines and is representative of the flux at the mask when the monochromator is set to allow zero order diffraction. This is acceptable as EUV-IL is achromatic. However, the effect of higher order harmonics would have to be considered for a rigorous treatment.

The flux of different beamlines taken from the literature are listed in Table 5.2. The SLS, SSRF and COSAMI² beamlines all show higher flux at the mask plane when compared to the maximum flux obtained in this work [191–193]. However, the beamlines listed all operate at lower energies and the lower flux is expected from the SXR-I undulator when moving from 92 eV to 185 eV. While the maximum flux at the mask plane obtained

² As COSAMI is still in the conceptual phase of development, the flux mentioned is only an estimate.

Table 5.2: The flux of different beamlines and sources currently used for EUV-IL and the maximum flux at the mask plane obtained from simulation of the SXR-I beamline in this work. Flux values at mask for SLS, COSAMI and SSRF beamlines were taken from Refs. 191, 192 and 193.

	Photon Energy (eV)	Flux at Mask
SXR-I	185	1×10^{17} ph/s/3.7%bw
SLS	92	3×10^{15} ph/s/4%bw
COSAMI	92	1.2×10^{15} ph/s/0.1%bw
SSRF [193]	85	2.4×10^{15} ph/s/2.6%bw
	92	3.6×10^{15} ph/s/2.6%bw
	150	0.93×10^{15} ph/s/2.6%bw

for these simulations is already optimal, as stated earlier, further improvements can easily be made by increasing the horizontal and vertical size of the SSA or the WBS. These changes would be made at the cost of coherence at the mask plane, but for the grating dimensions used in this work the SSA could be increased from 100 μm to 300 μm without a significant change in the coherence length at the mask plane.

5.7 Summary

In this Chapter we have shown that the end-to-end model of the SXR-I beamline and proposed EUV-IL configuration described in Chapter 4 can be used to simulate the formation of EUV-IL aerial images with the orders and period expected from theory. SRW codes were used to construct the model source and optical elements and implement numerical wavefront propagation from the source to the aerial image plane. The key components of the APPLE-II undulator source were compared against theory outlined in Section 2.3, known parameters of the SXR-I beamline at the Australian Synchrotron and existing models and were found to be in satisfactory agreement. The model was determined to be capable of accurately modelling the aerial image at the expected image plane.

The model was found to be capable of representing the polarisation of the source. The polarisation properties were found to be unaffected after propagation through the beamline model. The diffraction efficiency calculated from propagation through the mask model shown in Section 4.4.1 was compared to values calculated using RCWA. The differences found for mask thickness of around 100 nm were significant, with diffraction efficiency systematically overestimated by using the wavefront propagation model. This can be attributed to effects of mask thickness that are neglected in the simplified treatment of wavefront propagation through the mask model. Further work is required to confirm how

the effect scales with mask thickness, but the preliminary investigation over the range 100–150 nm indicates that the defining characteristics of a binary grating are adequately represented in the model.

The model was found to accurately represent the partially coherent source, and the minimum number of simulated electrons to reproduce the effects of partial coherence was found to be 4000. An estimate of the horizontal spatial coherence length at the mask plane was calculated as 460 μm .

The ability to accurately represent source polarisation and coherence throughout the beamline and the quantifiable model of intensity at the mask and aerial image plane lends credence to the suitability of the model to aid in the development of the EUV-IL configuration for the SXR-I beamline at the Australian Synchrotron.

Chapter 6

Source and Mask Effects on Aerial Image Quality

6.1 Introduction

The design of the EUV-IL capability that is in development for the SXR-beamline of the Australian Synchrotron must be informed by the constraints on the source and mask properties that can be identified by simulation. In particular, the relationship of the properties of the mask and illumination to the quality of the aerial image must be accurately modelled, and quantified.

In this Chapter, the model that was described in Chapters 4 and 5 is evaluated to establish if simulations of wavefront propagation can be reliably applied to the study of aerial image formation. The quality metrics for aerial image assessment introduced in Section 3.4 are evaluated for their sensitivity to the effects of systematic variation in source properties such as coherence and polarisation, and mask properties such as mask surface RMS roughness and roughness correlation length. Limitations in accepted aerial image quality metrics such as Michelson contrast and NILS are considered and the potential for alternative metrics to be used for optimising source, beamline, and mask parameters are discussed. The Chapter ends with a discussion of what further work is required to apply these observations and to extend the model to overcome limitations to EUV-IL performance and to define photomask design rules.

6.2 Aerial Image Formation

Figure 6.2.1 shows the wavefront at the aerial image plane, after partially coherent propa-

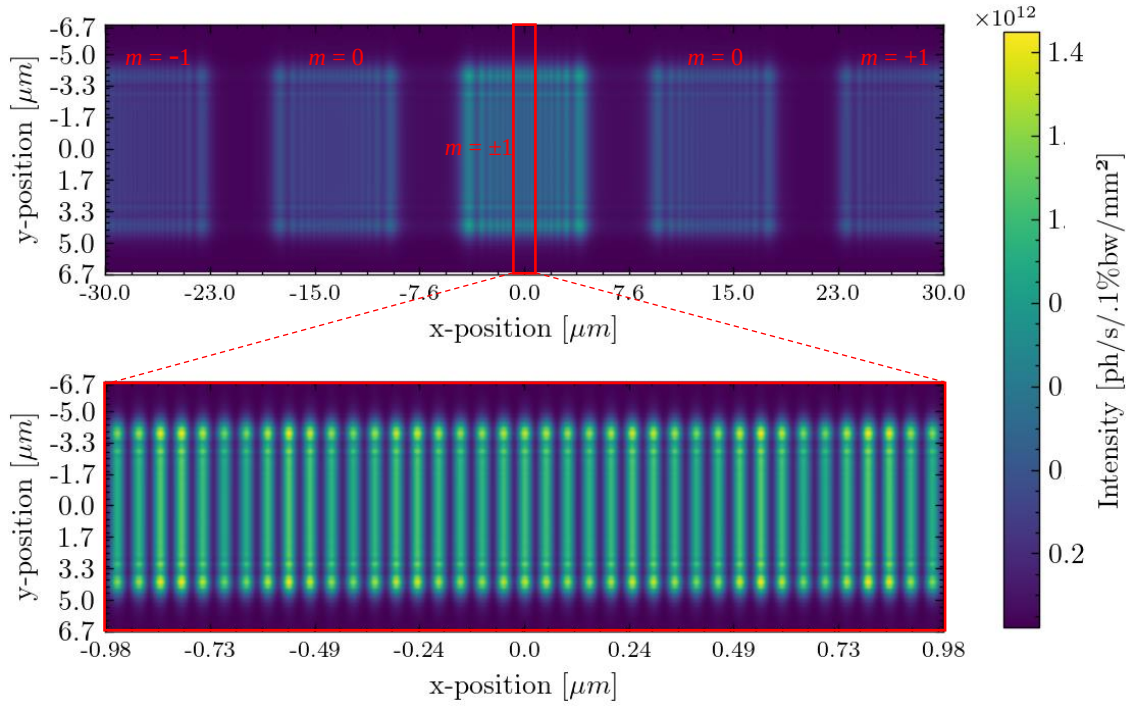


Figure 6.2.1 : Aerial image intensity from propagation through mask shown in Figure 4.4.2 and further 204.44 μm propagation after the mask. Interference of the 1st order beams can be seen in the centre of the image. The pixel size at the image plane was 2.5 nm (h) \times 240 (v) nm.

-gation of a 6.7 nm beam from the source through the beamline described in Section 4.3. A model mask stack was used with Ni₃Al absorber layer described in Section 4.4.1 and 204.44 μm of free space. The propagation distance used was the optimal distance given by Equation 2.2.4. The Ni₃Al mask layer used was 107.5 nm thick with a 100 nm grating pitch. All other mask geometry was the same as shown in Figure 4.4.2. The interfering first order ($m=\pm 1$) beams can be seen to have the highest intensity, which is consistent with the results for a high efficiency two-grating mask seen in Section 5.5. The zero order ($m=0$) beams can be seen at either side of the interfering $m=\pm 1$ beams, with non-interfering first order beams ($m=\pm 1$) situated to either side of each zero-order beam. First order interference occurs at the centre of the image plane as expected.

The aerial image forms where the $m=\pm 1$ beams overlap at the optical axis. Inspection of Figure 6.2.1 confirms that the wavefront propagation simulation can provide an aerial image with the expected characteristics from a horizontally oriented two-grating mask with 100 nm pitch. The choice of grating pitch was chosen as it provides a suitable balance between intended mask resolution and computational cost, as explained in Section 4.4.1.1. A horizontal ($y = 0$) line profile through the aerial image is shown in Figure 6.2.2. The int-

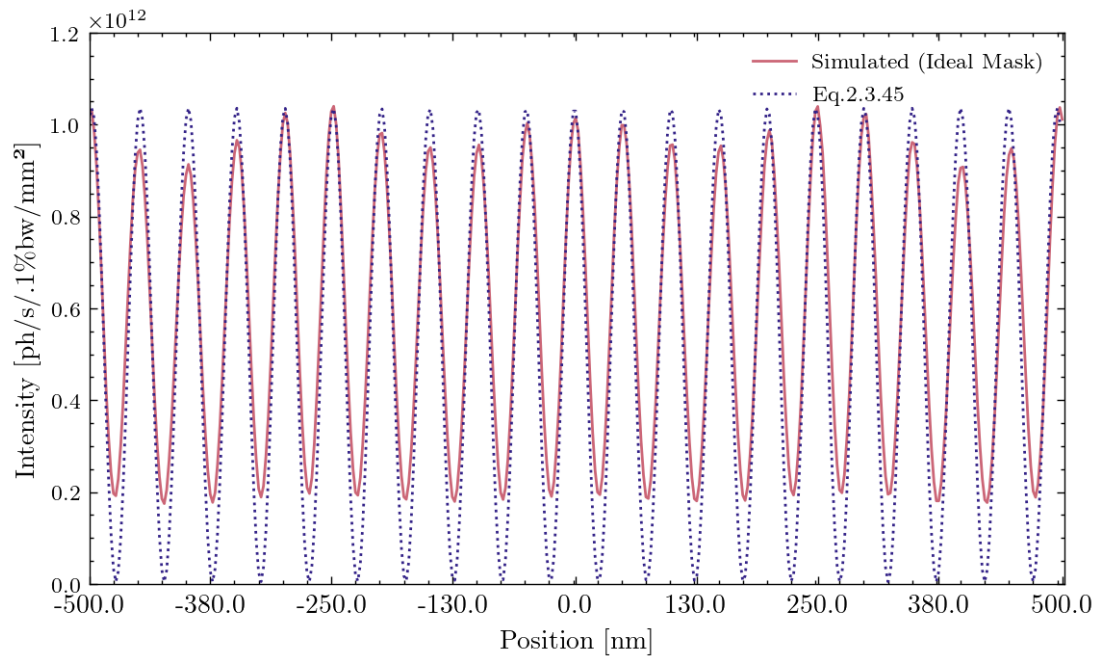


Figure 6.2.2 : Intensity profile taken along a horizontal strip at the centre ($y=0$) of the aerial image shown in Figure 6.2.1. The simulated intensity is compared to the model intensity from Equation 2.4.44 for a beam with polarisation direction parallel to the incident beam (TE-TE). The period and peak-to-peak intensity are in close agreement. The modulation in peak intensity in the simulation result follows the envelope of Fresnel diffraction from a single-slit.

Intensity profile is compared to the model intensity of a vertically polarised wavefield incident on a grating mask with horizontal lines (TE-TE), generated from Equation 2.4.44. The profile shows a sinusoidal pattern with a period of 50 nm. This agrees with Equation 2.2.4 which predicts a half-pitch of 25 nm from a grating with a period of 100 nm. The simulated aerial image also shows greater than zero intensity at minima, which is characteristic of a loss of contrast. Possible causes for this, such as partial coherence of the illuminating wavefield or diffraction from the photon block layer of the mask stack are investigated in the following sections.

The sinusoidal intensity pattern is accompanied by additional structure that appears as sharp bands of reduced intensity in the fringes along the horizontal and vertical directions. The latter is more clearly seen in the profile (Figure 6.2.2). These intensity variations arise from the coherent diffraction from the finite gratings that are bound by square apertures in the photon stop layer of the mask stack. This is discussed in Section 6.2.1.

6.2.1 Effect of Photon Block Diffraction

As shown in Section 4.4.1 (Figure 4.4.1 and Figure 4.4.2), the gratings in the mask model are finite and each bounded by an aperture in the photon block layer. As outlined in Section 2.2 and seen in Figure 6.2.2, Fresnel diffraction from the aperture in the photon block layer of a grating mask can introduce variation in the peak intensity of fringes in an aerial image. The peak intensity height variation is related to the dimensions of the grating masks and can lead to a reduction in aerial image contrast. This effect would also affect the uniformity of a pattern that could be transferred onto the photoresist. The wavefield was propagated through only the photon block layer of the mask to the aerial image plane using partially coherent methods described in Section 3.1.3. The relationship between the intensity peak height variation and diffraction from the photon block layer of the grating mask was evaluated. Figure 6.2.3 shows the aerial image intensity from a two-beam grating mask of 100 nm pitch, 20 nm thickness and dimensions shown in Figure 4.4.2 as well as the zero-order diffracted intensity from a single aperture of the same dimensions as the grating used.

The relationship between the single aperture diffraction and the aerial image peak intensity variations that was shown by Meng *et al* [48], for a two-grating mask of larger

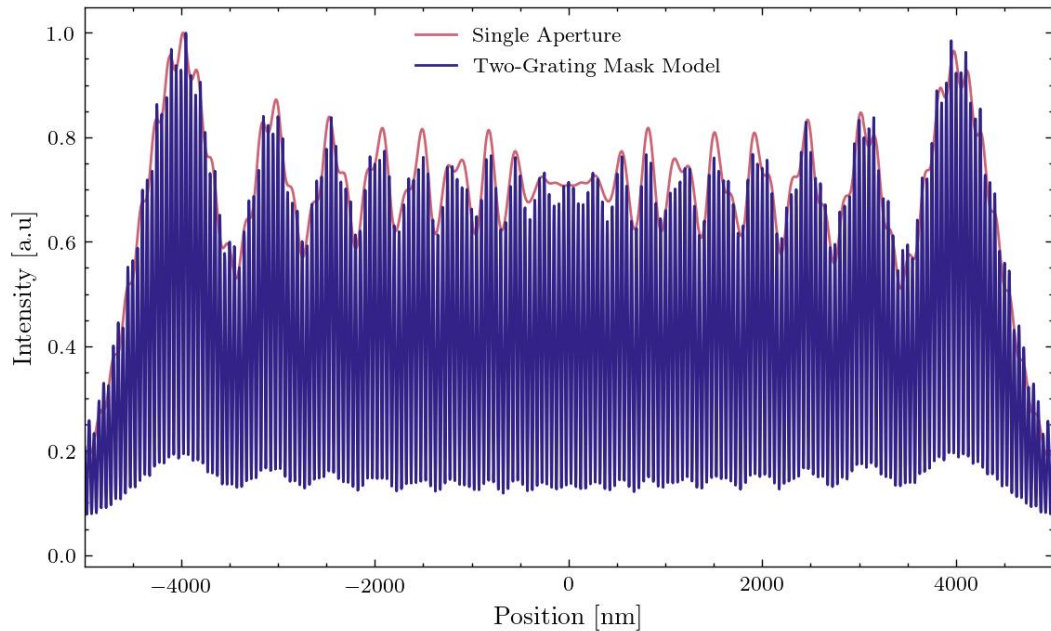


Figure 6.2.3: Intensity at the aerial image plane from a two-grating mask with 100 nm pitch, overlaid with zero-order Fresnel diffraction intensity from a single aperture of the same dimensions as the gratings (red).

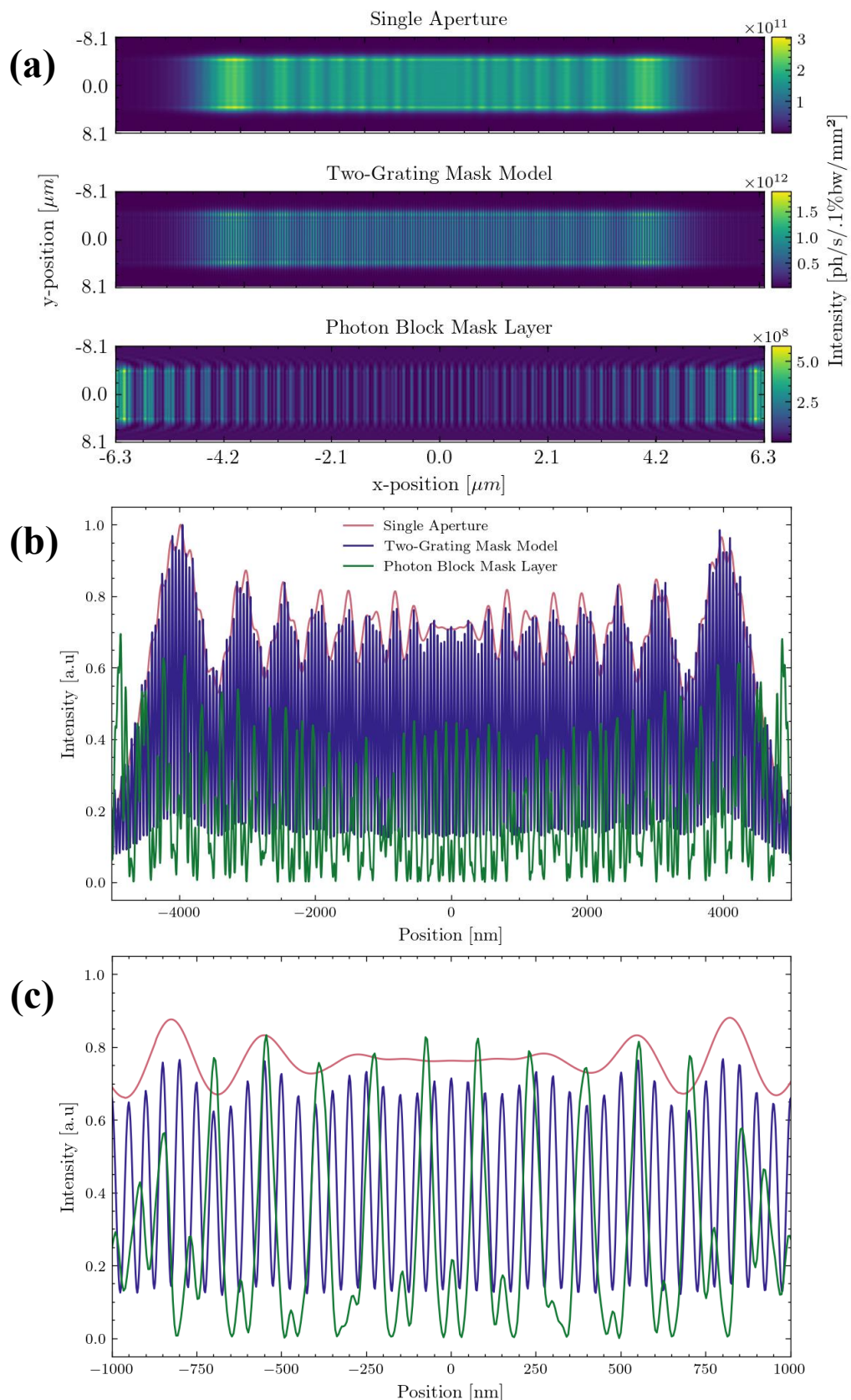


Figure 6.2.4: Two-dimensional (a), and one-dimensional (b),(c), profiles of the aerial image intensity from a horizontally oriented, two-grating mask with 100 nm pitch and dimensions shown in Figure 4.4.2, intensity from diffraction from an aperture of the same size as the gratings, and first-order diffraction from the photon block layer of the grating mask.

dimensions is seen in Figure 6.2.3. However, the envelope the aerial image does not exactly follow the shape of the single aperture diffraction intensity, which can be seen most clearly in the centre of Figure 6.2.3. This indicates that the envelope of the aerial image from a two-grating IL mask is not simply characterised by diffraction from a finite grating as a single aperture. To better understand the cause of the intensity envelope, the exit surface wave from the single $10 \times 10 \mu\text{m}$ aperture, from the pair of like apertures in the photon block mask layer, and from the complete two-grating mask stack ($10 \times 10 \mu\text{m}$ grating size, $27.5 \mu\text{m}$ separation and 100 nm pitch) was propagated separately to the aerial image plane. The resulting intensity at the aerial image plane is compared in Figure 6.2.4.

Line profiles at $y = 0$ through Figure 6.2.4a are shown in Figure 6.2.4b,c. The shape of the envelope has characteristics corresponding to diffraction from the two apertures of the photon block layer of the grating mask. The relationship between the modulation in height of intensity fringes in the aerial image and the geometry of the grating mask is thus more complex than can be described by diffraction from a single aperture alone. This may be of more importance if the illumination is not uniform across each grating.

The intensity envelope of the aerial image not only introduces variation in the height of the intensity fringes, but it also affects the minima of intensity fringes (Figure 6.2.4b,c). As shown in Section 5.6, the degree of coherence at the mask is very high so the partial coherence does not account for this increase in minima. The envelope of the intensity minima seen in Figure 6.2.3 and Figure 6.2.4b,c, is periodic and follows a similar pattern to the envelope of the intensity peaks, but with smoother variation that more closely follows the shape of the single aperture diffraction intensity. The effect of this combination of increased intensity minima and modulation of intensity maxima is a reduction in the contrast in the aerial image that is dependent on the dimensions of the grating. For the aerial image shown in Figure 6.2.4, the Michelson and RMS contrast values were reduced by 14% and 11% respectively when compared to the contrast of the analytical aerial image given by Equation 2.4.44. For the same comparison, the NILS was reduced by 25%. This indicates that the effect of the grating dimensions on aerial image formation is significant and must be accounted for to produce high contrast aerial images.

The effects of diffraction from the photon block layer on the aerial image is dependent on the grating geometry. The propagation distance between the grating and aerial image

plane depends on the diffraction angle, which is a function of grating pitch, photon energy, and the grating separation (Equation 2.2.2). This dependence suggests that the peak height modulation may be more significant for small grating pitch but can be reduced by carefully choosing the combination of grating area and grating separation. For the work presented in this chapter, our choice of mask geometry is restricted by computational constraints and our particular interest in high-resolution patterning (small grating pitch). The peak height variations are undesirable for lithographic patterning, but they do not significantly impede further investigation of source and mask effects.

6.3 Effect of Partial Coherence and Polarisation on Aerial Image Formation

The characteristics of an aerial image formed from EUV-IL depend not only on mask geometry as outlined in Section 2.2 but also on the properties of the illuminating wavefield. In Section 2.4 it was shown that source properties such as coherence and polarisation can significantly affect the contrast of an aerial image. In this section we use the model of the source, beamline, and mask to quantitatively evaluate their effect on EUV-IL aerial image formation.

Accurate modelling of the effects of source properties on aerial image formation is essential to fully understand the beam characteristics needed for high-quality lithographic patterning. In this Section, the effect of partial coherence of the wavefront at the mask plane on aerial image formation is evaluated by propagating a partially coherent wavefront through the a two-grating IL mask and to the image plane using methods described in Section 3.1.3. The grating mask is oriented horizontally, with 100 nm pitch, 20 nm Ni₃Al absorber layer thickness and grating separation of 27.5 nm as shown in Figure 4.4.2. The effect of changes in partial coherence on the aerial images is investigated by adjusting the size of the secondary source aperture (SSA) as in Section 5.6, and evaluating the aerial image contrast by metrics defined in Section 2.1.1

The polarisation characteristics in the wavefront at the aerial image plane are evaluated through analysis of the intensity of the horizontally and vertically polarised components of the aerial image. The effect of the polarisation orientation of a linearly polarised beam on aerial image contrast is evaluated by changing the source parameters as shown in

Section 5.2.1 and propagating through horizontally oriented grating masks of various pitch using fully coherent and partially coherent propagation methods shown in Section 3.1.

6.3.1 Partially Coherent Aerial Image Formation

As discussed in Section 2.4, the ability to form interference fringes is directly related to the coherence of a light source. For any evaluation of the interference capabilities of an IL apparatus it is therefore necessary to include an accurate representation of the coherence of the source and beam in use. To evaluate the effect of finite spatial coherence on aerial image formation, the multiple electron source model and partially coherent propagation methods outlined in Section 3.1.3 were employed. 4000 electrons were used for the partially coherent propagation at 6.7 nm as it was shown in Section 5.6 to be a sufficient number to accurately represent the partially coherent aerial image formed using the undulator source at the SXR-I beamline from a $200 \mu\text{m}$ (h) \times $200 \mu\text{m}$ (v) SSA and a 100 nm pitch, horizontally oriented, two-beam grating mask with $27.5 \mu\text{m}$ grating separation and $10 \times 10 \mu\text{m}$ grating size.

In Section 5.6 the two-dimensional coherence functions calculated using theory outlined in Section 2.4.1 were used to estimate the coherence length of the wavefield at the mask plane for different Secondary Source Aperture (SSA) sizes. In this Section, the aerial images obtained from three different SSA horizontal settings are evaluated. The relationship between coherence length and aerial image contrast is thus investigated.

Figure 6.3.1 shows the aerial images resulting from varying the horizontal SSA size from $100 \mu\text{m}$ to $300 \mu\text{m}$. The grating dimensions used were the same as in the previous section: 100 nm pitch, 20 nm Ni₃Al absorber layer thickness, and geometry as shown in Figure 4.4.2. The average intensity contained in each interference fringe was reduced with SSA size. This agrees with Figure 5.6.6 which shows that the flux at the mask decreases with SSA size. The average intensity in the aerial image when moving from a $300 \mu\text{m}$ to $200 \mu\text{m}$ horizontal SSA is reduced by 43%, and when moving from $300 \mu\text{m}$ to $100 \mu\text{m}$ horizontal SSA the reduction in mean intensity is 76%. The decrease in the intensity fringe minima seen in Figure 6.3.1a can be attributed to decreased flux at the aerial image plane and is not caused by an increase in the degree of coherence. As shown in Section 5.6, the mask is coherently illuminated for all SSA settings used. This is confirmed by the aerial

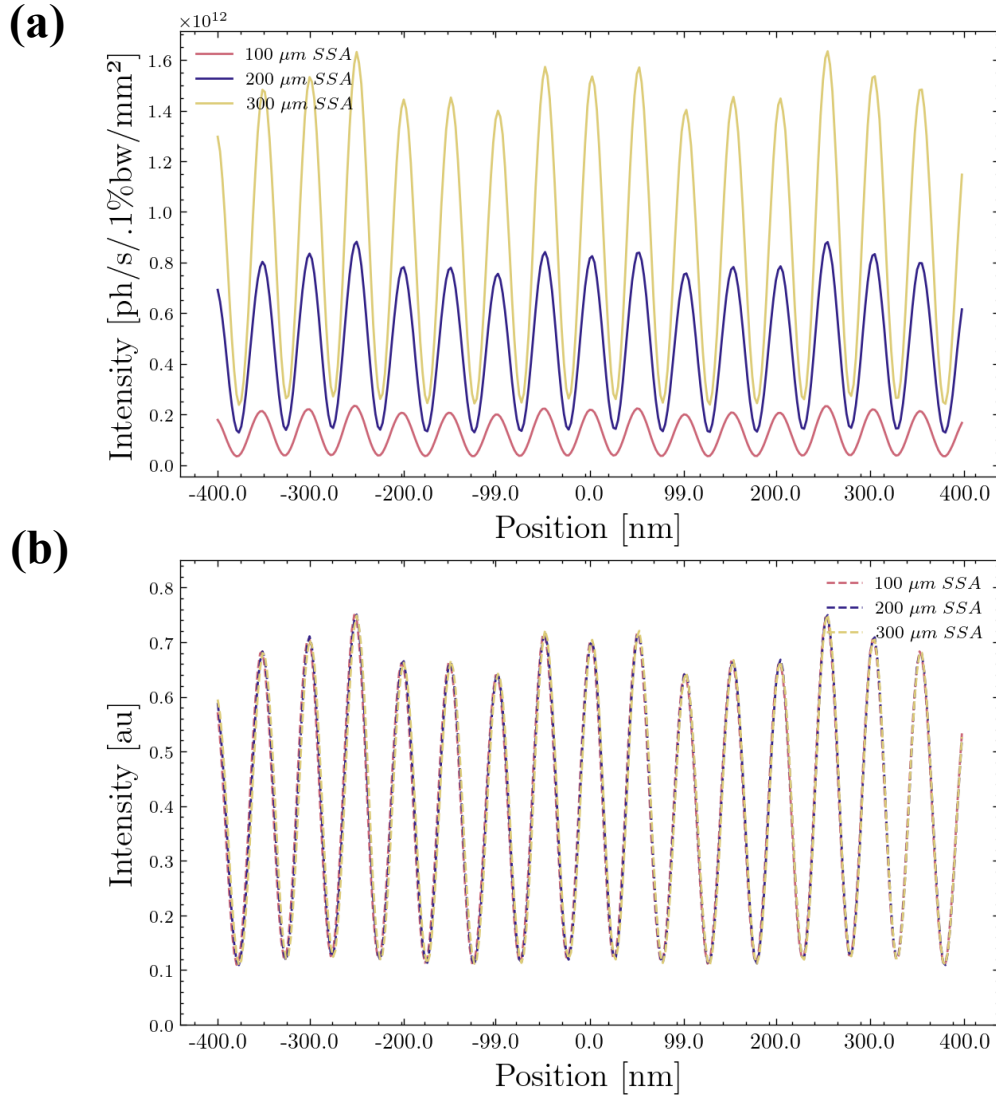


Figure 6.3.1: (a) Line profiles through aerial images generated from different horizontal SSA sizes. Two-grating, Ni₃Al masks with 20 nm thickness, 100 nm pitch and 27.5 micron grating separation, oriented horizontally were used for each trial, with 6.7 nm incident illumination. (b) The same aerial image intensity profiles shown in (a), normalised to their mean value.

image profiles when they are normalised to their mean intensity, which is shown in Figure 6.3.1b.

The normalised profiles shown in Figure 6.3.1b appear identical to each other, indicating that no loss in contrast is seen due to a decrease in coherence of the illuminating wavefield. The envelope of the aerial image intensity is unchanged for difference SSA settings, indicating the divergence and flux of the wavefield at the mask plane has little effect on the modulation of intensity fringes in the aerial image. This confirms that for these SSA sizes the dominant effect on aerial image contrast is the flux at the mask plane. No

loss in contrast is seen for reduced coherence of the wavefield, proving that the masks are coherently illuminated for all horizontal SSA widths below 300 μm . For IL masks with these dimensions, reducing the SSA size shows no benefit in aerial image contrast. Larger SSA settings are thus ideal for higher flux at the mask plane and high contrast aerial images. The results indicate that larger IL masks are possible with the SSA sizes used. Masks as large as the minimum horizontal coherence length of 160 μm will be coherently illuminated with the largest SSA size evaluated.

6.3.1 The Effect of Source Polarisation on Aerial Image Contrast

Modelling the effects of different beam polarisation on the aerial image contrast is important to fully understand constraints on photomasks and the source that are required to achieve high quality aerial images. In this Section, the intensity of the horizontal and vertical components of the wavefield of a highly linear horizontally and vertically polarised 6.7 nm source were compared at the aerial image plane for horizontally oriented two-grating IL masks of various pitch. The polarisation of the wavefield at the aerial image plane was evaluated against the polarisation at the mask plane that was discussed in Section 5.3. As described in Section 2.4.2.4, the effect of polarisation on aerial image contrast scales with wavelength and is weak for 6.7 nm. The effect is also inversely proportional to grating pitch as shown by Figure 2.4.5. To evaluate the loss of contrast of aerial images formed by TE-TE and TM-TM polarisation at 6.7 nm the total aerial image intensity was analysed for two-grating IL masks with different grating pitch. The contrast of aerial images generated from fully coherent and partially coherent propagation methods shown in Section 3.1 was compared to the expected contrast differences shown in Section 2.4.2.4.

As the language used when describing total polarisation of a wavefield and the polarisation components of a wavefield can quickly become hard to decipher, in this section when referring to the total polarisation state of the wavefield, the terms TE and TM will be used. When referring to the separate polarised components of the intensity the terms horizontal polarisation and vertical polarisation will be used. The gratings used in this section were all oriented horizontally (so the grating lines were oriented vertically), and so

TE and TM polarised wavefields correspond to those shown in Figure 2.4.4. Linear vertical and linear horizontal polarisation correspond to TE and TM respectively.

6.3.1.1 Effect of Polarisation and Grating Pitch

As shown in Section 2.4.2.3 and 2.4.2.4, for a linearly polarised beam, the orientation of polarisation in relation to the orientation of grating lines in an IL mask will affect the resulting contrast of an aerial image. As grating pitch decreases, the contrast of an aerial image formed from TM-TM polarised diffracted beams will decrease, while the contrast of an aerial image formed from TE-TE polarised beams will be unchanged (as described in Section 2.4.2.4). As IL mask configurations often include multiple gratings oriented perpendicular to one another (shown in Figure 2.4.7, Section 2.4.4) the effects of polarisation for IL masks with more than two gratings cannot be ignored. The reduction in contrast from polarised beams will become more significant as the desired half pitch of aerial images decreases (shown in 2.4.2.4, Figure 2.4.5).

Two-beam, Ni₃Al grating masks were generated with varied grating pitch, p_G , over the range 14 nm to 40 nm using methods outlined in Section 4.4.1. Each mask was oriented horizontally and used to generate aerial images from TE and TM polarised beams. The gratings were modelled as 107.5 nm thick with all other grating parameters the same as shown in Figure 4.4.2. Fully coherent propagation methods shown in Section 3.1 were initially used with the intention of separating the effects of polarisation orientation from the loss of aerial image contrast due to partial coherence seen in Section 6.3. The contrast of each aerial image was compared for TE-TE and TM-TM polarisation states for each grating pitch, following the approach described by Wang *et al* [98]. For initial simulations utilising fully coherent propagation, the simplified beamline model shown in Figure 5.2.5 was used to avoid potentially confounding the effects of coherent diffraction from upstream beamline elements.

Figure 6.3.2 shows the horizontal profiles of aerial image intensity fringes formed from fully coherent propagation through two-beam IL grating masks with grating pitch 24 nm and 40 nm, oriented horizontally. The visibility of the intensity fringes from TM-TM polarised beams do not show the expected reduction in contrast outlined in Section 2.4.2.4.

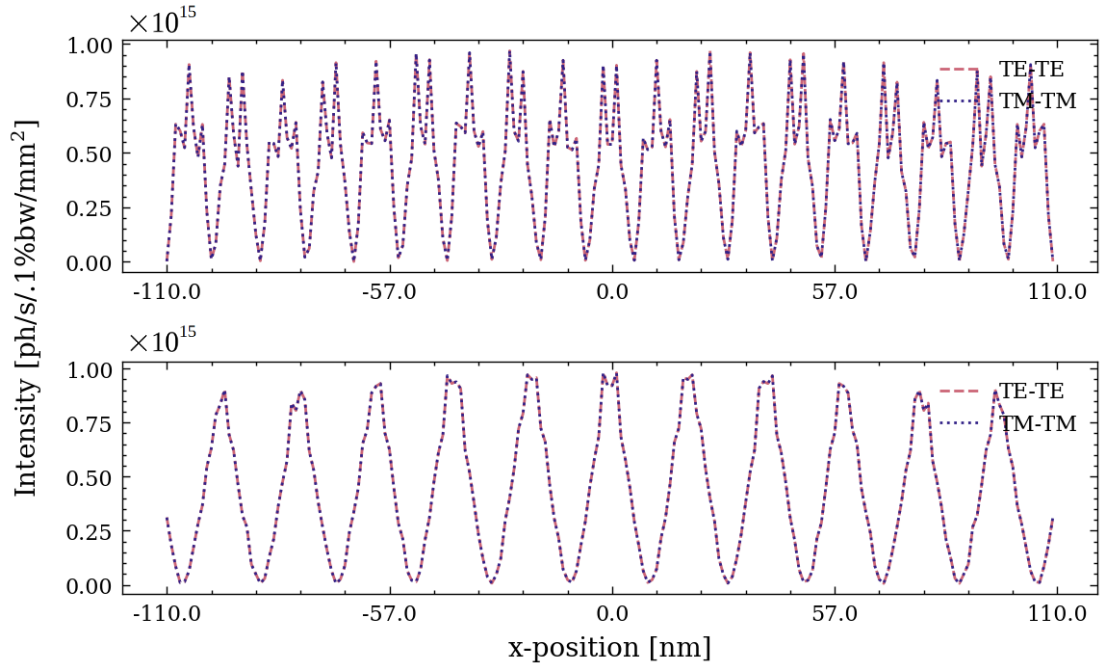


Figure 6.3.2: Aerial image intensity profiles from TE-TE (purple) and TM-TM (pink) polarised beams. Profiles were obtained by fully coherent propagation of 6.7 nm radiation through the beamlne shown in Figure 5.2.5, and Ni₃Al two-grating masks with grating pitch of 24 nm (top) and 40 nm (bottom), each with 107.5 nm thickness and dimensions shown in Figure 4.4.2. There is no difference in contrast. While the average peak intensity is similar for each aerial image, the quality of the intensity fringes is significantly reduced for the 24 nm pitch grating mask.

In fact, the aerial images produced by each beam polarisation are identical. This shows a limitation in the model, in that fully coherent propagation method is unable to fully reproduce polarisation dependent effects of aerial image formation.

Although the sum of the vertically and horizontally polarised intensity components of each aerial image shows identical fringes independent of the beam polarisation (Figure 6.3.2), the horizontal and vertical polarisation intensity components shown in Figure 6.3.3 for the grating of 40 nm pitch show significant differences. While the aerial image formed from TM-TM polarised beams shows a central maximum at horizontal position $x = 0$ for both polarisation components, the TE-TE aerial image shows inversion in the intensity minima and maxima of the horizontal component. The TM-TM aerial image intensity also shows a much smaller proportion of intensity contained in its vertical polarised component than the TE-TE aerial image contains in its horizontal polarised component. The fraction of horizontally polarised intensity in the TE-TE aerial image is more than a factor of 2×10^5 greater than the fraction of vertically polarised intensity in the TM-TM aerial image. The polarisation at the mask plane for each wavefield was thoroughly evaluated in Section 5.2.1 and no discrepancies between TE and TM polarised wavefields were found before propaga-

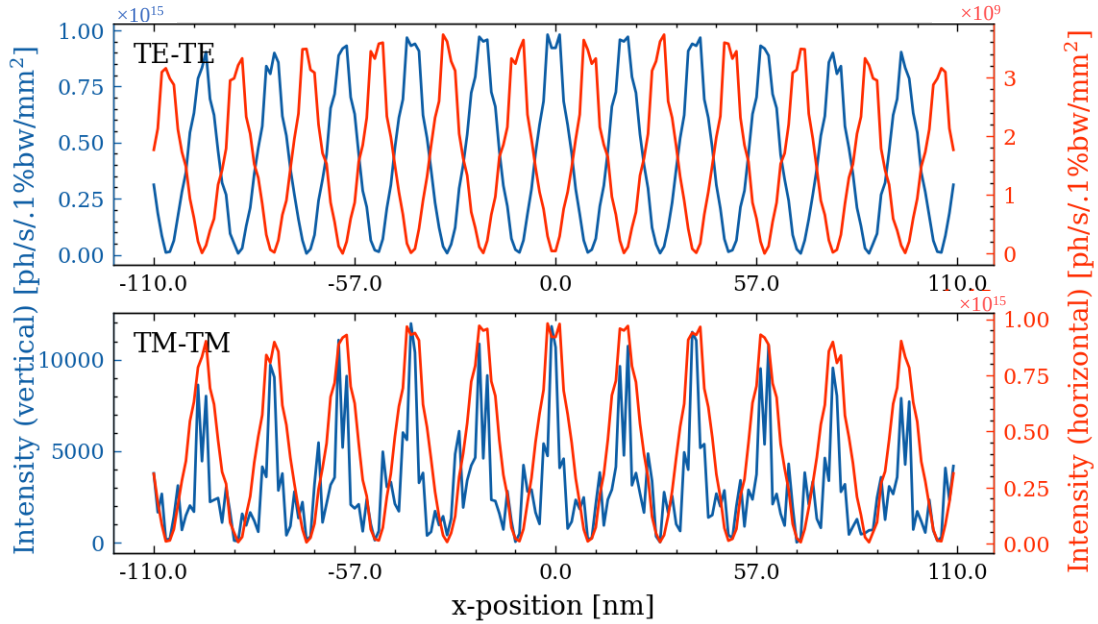


Figure 6.3.3: The vertically (blue) and horizontally (red) polarised components of the TE-TE (top) and TM-TM (bottom) aerial image intensities shown in Figure 6.3.2 obtained by fully coherent propagation of 6.7 nm radiation through the beamline shown in Figure 5.2.5, and a Ni₃Al two-grating masks with grating pitch of 40 nm, 107.5 nm thickness and dimensions shown in Figure 4.4.2. In the aerial image formed by the TE-TE polarised beams, the maxima of the vertically polarised intensity component coincide with minima of the horizontally polarised intensity component. In the TM-TM generated aerial images the maxima and minima of both polarisation components coincide.

-tion through the mask. While the propagator employed for the wavefront interaction with the mask does not explicitly include polarisation dependant scattering, Figure 6.3.3 is consistent with the grating mask acting as a weak polariser, with vertically polarised light absorbed more strongly than horizontally polarised light. This would imply the grating lines act on the wavefield in a similar way to a wire-grid polariser, which polarises incident light perpendicular to the orientation of the lines [90].

6.3.1.2 Partially Coherent Propagation and Polarisation

To further investigate whether the model accurately represents the effects of beam polarisation on aerial image contrast at 6.7 nm, Ni₃Al grating masks with $p_G = 24$ nm and 14 nm, and dimensions shown in Figure 4.4.2 were used to generate aerial images by the partially coherent propagation methods outlined in Section 3.1.3. As in the previous section, the grating masks were oriented horizontally and aerial images were generated from linearly vertically polarised (TE), and linearly horizontally polarised (TM) wavefields. The

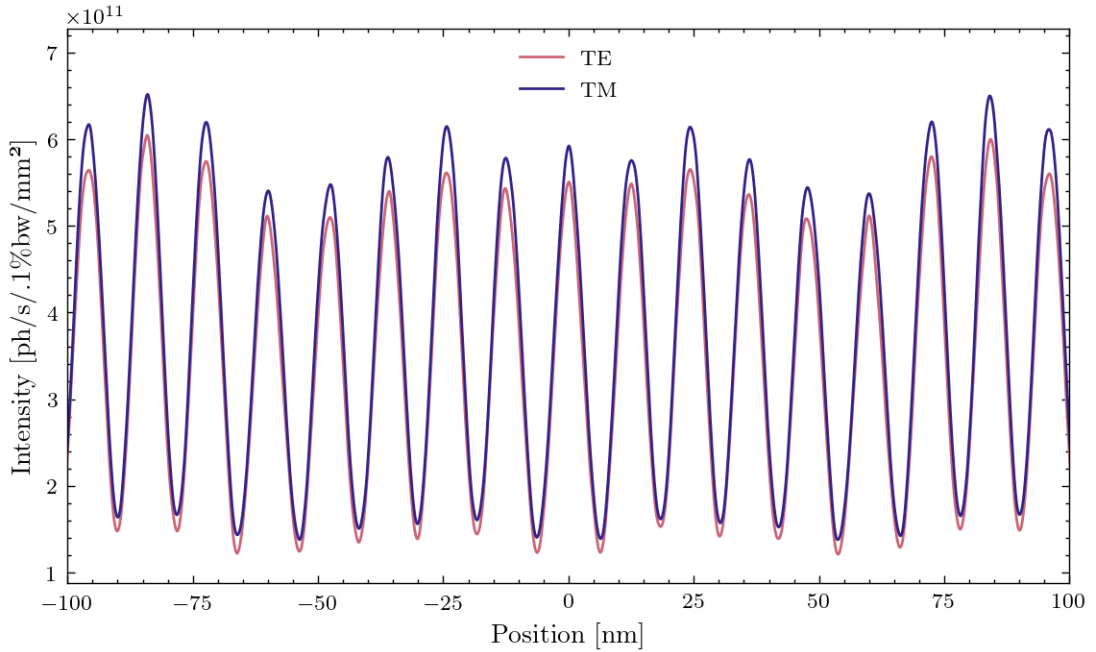


Figure 6.3.4: The aerial image intensity from partially coherent propagation through a grating mask with $p_G = 24 \text{ nm}$ for both TE-TE (pink) and TM-TM (purple) polarised beams.

Table 6.1: Calculated contrast values of the aerial images shown in Figure 6.3.4 (grating pitch of 24 nm). The contrast of a TM-TM aerial image generated by Equation 2.4.45 calculated for each metric is given as a comparison.

$p_G = 24 \text{ nm}$	C_M
TE-TE (calculated)	0.72
TM-TM (calculated)	0.70
Theory (TE-TE)	1.00
Theory (TM-TM)	0.84

partially coherent propagation used 4000 electrons to accurately represent the coherence properties of the beam as shown in Section 5.6.

Figure 6.3.4 shows line profiles taken perpendicular to the aerial image intensity fringes from the 24 nm pitch grating mask for TE-TE and TM-TM polarised beams. The calculated contrast of each aerial image is listed in Table 6.1. The ~16% reduction in aerial image contrast that would be expected from theory outlined in Section 2.4.2.4 for gratings with this pitch and 6.7 nm incident light is not seen. Instead, only a 3% reduction is seen. This could be attributed to effects of diffraction from the photon block layer of the mask dominating the reduction in contrast at this grating pitch, as described in 6.2.1. The Michelson contrast calculations show values less than 0.8 (seen in Table 6.1), which is greater than the expected loss of contrast due to TM-TM polarisation at a grating pitch of 24 nm from 6.7 nm incident light.

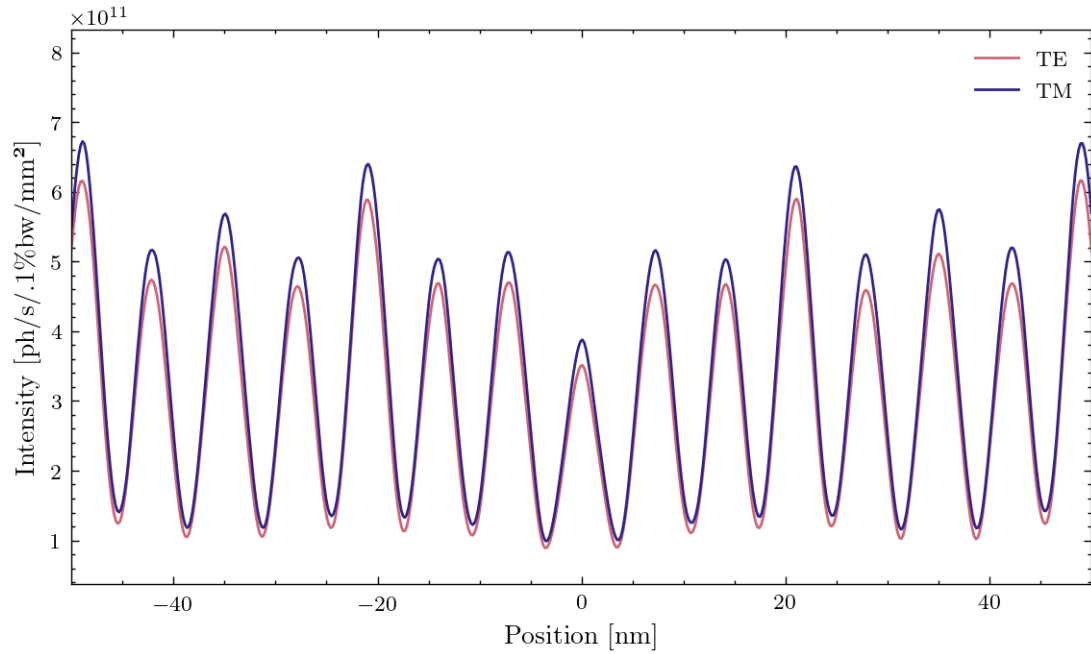


Figure 6.3.5: The aerial image intensity from partially coherent propagation through a grating mask with $p_G = 14 \text{ nm}$ for both TE-TE (pink) and TM-TM (purple) polarised beams.

Table 6.2: Calculated contrast values of the aerial images shown in Figure 6.3.5 (grating pitch of 14 nm). The contrast of a TM-TM aerial image generated by Equation 2.4.45 calculated for each metric is given as a comparison.

$p_G = 14 \text{ nm}$	C_M
TE-TE (calculated)	0.82
TM-TM (calculated)	0.82
Theory (TE-TE)	1.00
Theory (TM-TM)	0.54

To further evaluate whether the effects of polarisation angle on aerial image contrast are represented in the model, the pitch of the grating mask was decreased to 14 nm. All other grating dimensions were kept constant. Figure 6.3.5 shows the aerial image intensity profiles for TE-TE and TM-TM polarised beams diffracted from a two-beam grating mask with 14 nm pitch. The TM-TM aerial image shows consistently greater intensity across all peaks, however the calculated Michelson contrast of each aerial image is identical. The 46% expected loss for a grating of 14 nm pitch and a wavelength of 6.7 nm is not seen. Table 6.2 lists the Michelson contrast of each aerial image as computed by each metric described in Section 2.1.1 and the expected values as given by theory. Contrast calculations were taken as average values for every fringe across the aerial image.

The variation of intensity fringe height in Figure 6.3.4 and Figure 6.3.5 can be attributed to diffraction from the photon block layer of the mask, as explained in Section 6.2.1. The difference in fringe height variation between aerial images from grating masks with different pitches can be explained by the difference in propagation distance from the mask to aerial image plane (Equation 2.2.2). Thus, when changing grating pitch, the change in envelope of the aerial image must be considered as well as the change in the effect from the source polarisation. Wang *et al* [98], showed that, for a grating with pitch of the order of tens of nm, at 13.5 nm wavelength, the diffraction efficiency is also affected by the polarisation orientation of the incident wavefield.

An alternative explanation for the discrepancy in contrast reduction could be an inadequate number of simulated electrons. The pitch of the grating masks used in this section is smaller than the pitch used when evaluating the necessary number of simulated electrons in Section 5.6. Consequently, the diffraction efficiency of the masks is smaller, and the number of electrons should be increased proportionally to avoid artefacts. This is a practical limitation of the Monte Carlo approach used for the partially coherent propagation method described in Section 3.1.3. The limitation can be overcome with increasing computational cost after the required number of electrons required to avoid artefacts that will affect the simulated contrast is determined.

While the loss of contrast seen in Table 6.2 is significantly less than indicated by theory, it does indicate that the model is sensitive to polarisation effects despite the simplified treatment of the mask diffraction. Further work is required to understand confounding effects in the simulation, and, ultimately, a more rigorous implementation of the mask propagator is required.

6.3.2 Aerial Image Contrast and Source Properties

Figure 6.3.5 and Table 6.2 indicate that the effect of source polarisation on the aerial image manifests only in the reduction of intensity fringe height and not in the increase of minima. The implications of this for the 6.7 nm IL process are that effects due to source polarisation and flux at the mask plane must be considered together to achieve high contrast aerial images when the grating pitch approaches the smallest values that can be fabricated ($p_G \lesssim 14$ nm). As the mask was coherently illuminated for all SSA settings in these

simulations, the effect of reducing the degree of coherence on the aerial image was not sufficiently characterised. Future work will evaluate the effect of partial coherence for grating masks with lateral extent that approaches, or exceeds, the transverse coherence length.

For a two-grating mask with 100 nm pitch, 20 nm thickness and geometry detailed in Section 4.4.1, the effect of increasing the flux at the mask plane by a factor of ~ 2.8 was to increase the RMS contrast by $\sim 3\%$. At this grating pitch, and all grating pitches above 14 nm, no significant change in aerial image contrast was seen due to changes in the polarisation of the illuminating wavefield. However, the uncertainty in this contrast reduction is large because of limitations in the Monte Carlo approach used for partially coherent propagation. The low efficiency of the gratings at ~ 14 nm pitch leads to a high density of numerical artefacts that arise from inadequate sampling of the source electron phase space. More computational resources or optimisation of the propagation codes will then be necessary for future work to evaluate the effect of source polarisation on aerial image contrast for gratings with $p_G \leq 14$ nm.

The polarisation dependent change in contrast described in Section 2.4.2.4 is dependent on the angle of diffraction from the grating mask. Thus, the contrast change is less significant at shorter wavelengths and larger grating pitches (Figure 2.4.5). This Section showed that polarisation will have little effect on contrast for 6.7 nm IL unless the photomask grating pitch approaches the presently achievable fabrication limits. At present, production of sub 20 nm pitch gratings for use at the proposed EUV-IL facility is challenging. This challenge is compounded for the thicker masks generally required for 6.7 nm radiation.

6.4 Effect of Mask Properties on Aerial Image

As described in Section 2.4.1.2, surface roughness is known to introduce phase variation in a coherent transmitted wavefield which manifests as intensity variation in an image known as speckle [191]. Surface roughness of IL masks lead to increased line-width roughness (LWR) in developed patterns in a photoresist. As described in Section 3.3, this photoresist LWR depends not only on the RMS roughness, σ , of the mask, but also the correlation length, $c_{x,y}$, [115,135]. However, how mask surface roughness couples to speckle at the

aerial image plane is not yet fully understood [110]. More research is needed to fully understand the relationship between mask surface roughness and aerial image quality at 6.7 nm wavelength.

Roughness was added to the Ni₃Al absorber layer of the modelled two-beam interference grating mask shown in Section 4.4.1 (Figure 4.4.1 and Figure 4.4.2). The mask had 100 nm grating pitch, 27.5 μm grating separation, and 20 nm thickness. σ and the roughness correlation length parallel to the grating lines, c_y , was changed for each mask surface. The effect of different mask surface roughness was thus evaluated through analysis of the contrast of the aerial image formed by each grating mask.

As shown in Section 3.5 the contrast of an aerial image formed from a beam with polarisation direction parallel to the lines of a grating mask (TE-TE) is expected to produce higher contrast compared to other beam polarisation conditions. Although polarisation effects on contrast were found to be weaker than expected in Section 6.3.1.2, TE-TE illumination was therefore chosen for the simulations with mask roughness so that changes in contrast can be studied independently of polarisation effects. The 100 nm grating pitch described in Section 4.4.1 balances the intended mask resolution for the proposed EUV-IL facility at the Australian Synchrotron and the available model resolution, which is constrained by the available computational resources. A propagation distance of 204.44 μm was used for all simulations involving 100 nm pitch gratings as it is the optimal propagation distance obtained from Equation 2.2.2.

6.4.1 Partially Coherent Illumination of Rough Masks

As seen in Section 5.3 and Section 6.3.1, fully coherent propagation methods are unreliable for accurate representations of aerial images formed by IL. Partially coherent wavefront propagation methods must be applied to characterise the effects of mask surface roughness on the aerial image, even though the degree of coherence was shown to be very high in Section 5.6. In this Section, the partially coherent propagation methods described in Section 3.1.3 were used to propagate a horizontally polarised beam through a horizontally oriented grating mask with surface roughness generated by methods described in Section 4.4.1.2.

A Ni₃Al mask of thickness $t_G = 20$ nm was chosen for two reasons. Firstly, because it has been shown to provide acceptable diffraction efficiency by RCWA calculations for masks with $p_G = 20$ nm [188,189]. Secondly, because fabrication of a Ni₃Al grating is feasible for the ratio $\frac{t_G}{p_G \leq 20 \text{ nm}} = 1$. A thin mask also has the added advantage of reducing the relative significance of systematic errors that arise from the simple approach to propagation of the wavefield through the grating (seen in Section 5.5). Moreover, the relative sensitivity to the effects of nanoscale surface roughness is increased.

The surface roughness of a Ni₃Al grating will depend on the process by which it is deposited and patterned. Roughness on the scale of $\sigma = 0.1 - 0.5$ nm has been reported for 22 nm pitch gratings [125]. Here we assume that this value is smaller than will be achieved in production of Ni₃Al gratings using techniques available locally.

Model masks with substrate, absorber and photon stop layers as shown in Figure 4.4.1 were generated with $p_G = 100$ nm, and dimensions shown in Figure 4.4.2. Surface roughness was added to the Ni₃Al absorber layer using methods described in Section 4.4.1.2. σ was varied from 0.5 nm to 2.5 nm in 0.5 nm steps. For each value of σ , masks were generated with vertical correlation lengths, c_y , (along the grating lines) from 2 nm to 10 nm. The profiles are shown in Figure 4.4.4. A total of 25 distinct masks were used. The horizontal correlation length, c_x , was fixed at 2.5 nm.

The mask illumination was generated for 6.7 nm wavelength using the source and beamline model described in Section 4.3 and SSA dimensions of 200 (h) \times 200 (v) μm . This was shown in Section 5.6 to correspond to transverse coherence lengths of 230 (h) \times 280 (v) μm . Aerial images were generated from propagation through each mask, and the resulting contrast was calculated using metrics described in Section 2.1.1. The relationship between mask roughness properties and the value of each aerial image quality metric described in Section 3.4 was evaluated.

6.4.1.1 Qualitative Description of Aerial Images

The two-dimensional aerial images generated from masks with surface roughness characterised by $c_y = 10$ nm and σ from 0.5 nm to 2.5 nm are shown in Figure 6.4.1. The variation in the intensity distribution both parallel and perpendicular to the intensity fringes

increased significantly with increasing σ . To assess if this corresponded to a change in contrast, line profiles were taken along the horizontal axis at $y = 0$ and the contrast was calculated by each metric described in Section 2.1.1. To limit the effects of the intensity variation due to the diffraction from the photon block mask layer on contrast calculations, the sampled area was reduced to the $8 \mu\text{m} \times 5 \mu\text{m}$ area shown in the right of Figure 6.4.1.

Figure 6.4.2 shows the horizontal profiles taken at $y = 0$ of the aerial images generated from partially coherent propagation of 6.7 nm light through 100 nm pitch, two-grating IL masks with geometry described above. The profiles shown are from masks with σ increasing from 0.5 nm to 2.5 nm in 0.5 nm steps and constant c_y of 2 nm (top profiles) and 10 nm (bottom profiles). For comparison the profile from a mask with no surface roughness ($\sigma = 0 \text{ nm}$) is also shown. The line profiles were taken over a horizontal range shown in the left images of Figure 6.4.1 and are only shown for the central 1 μm .

For both $c_y = 2 \text{ nm}$ (Figure 6.4.2a) and $c_y = 10 \text{ nm}$ (Figure 6.4.2b), the average intensity of fringes can be seen to decrease with increasing σ . The intensity of fringes is also greater

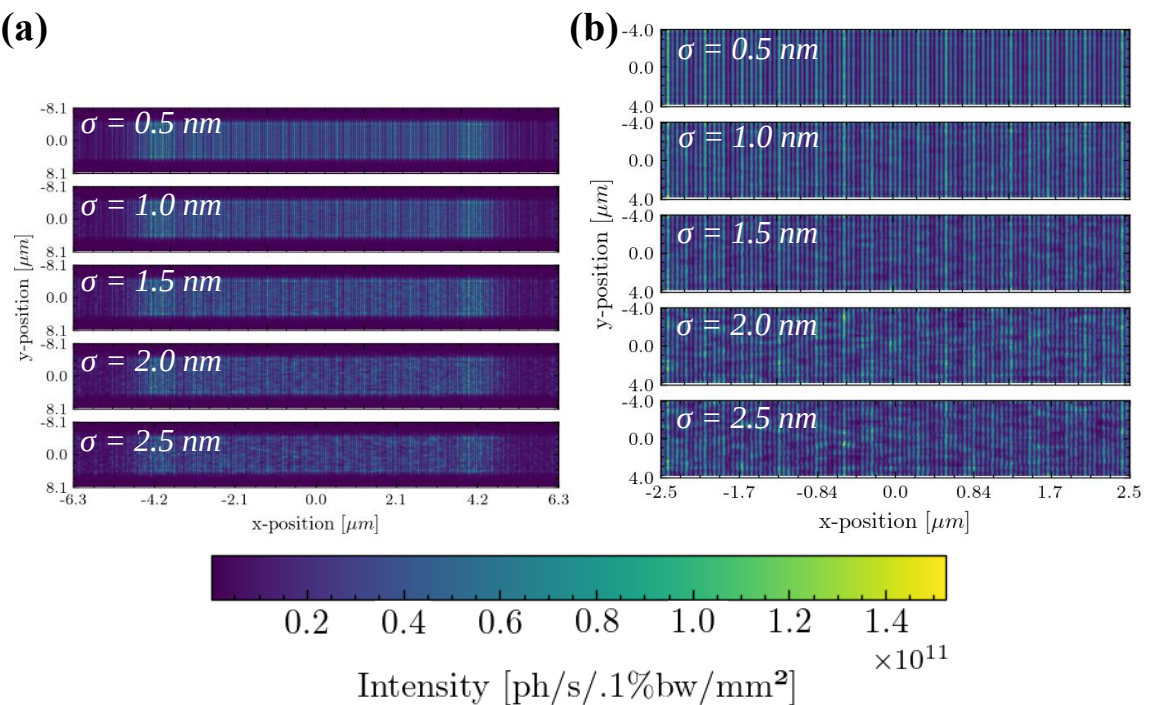


Figure 6.4.1: Aerial images generated from rough masks with $c_y = 10 \text{ nm}$ and σ from 0.5 nm to 2.5 nm. The entire first order aerial images are shown (a), as well as the area sampled for analysis (b). Significant changes are seen in the two-dimensional intensity distribution as σ is increased.

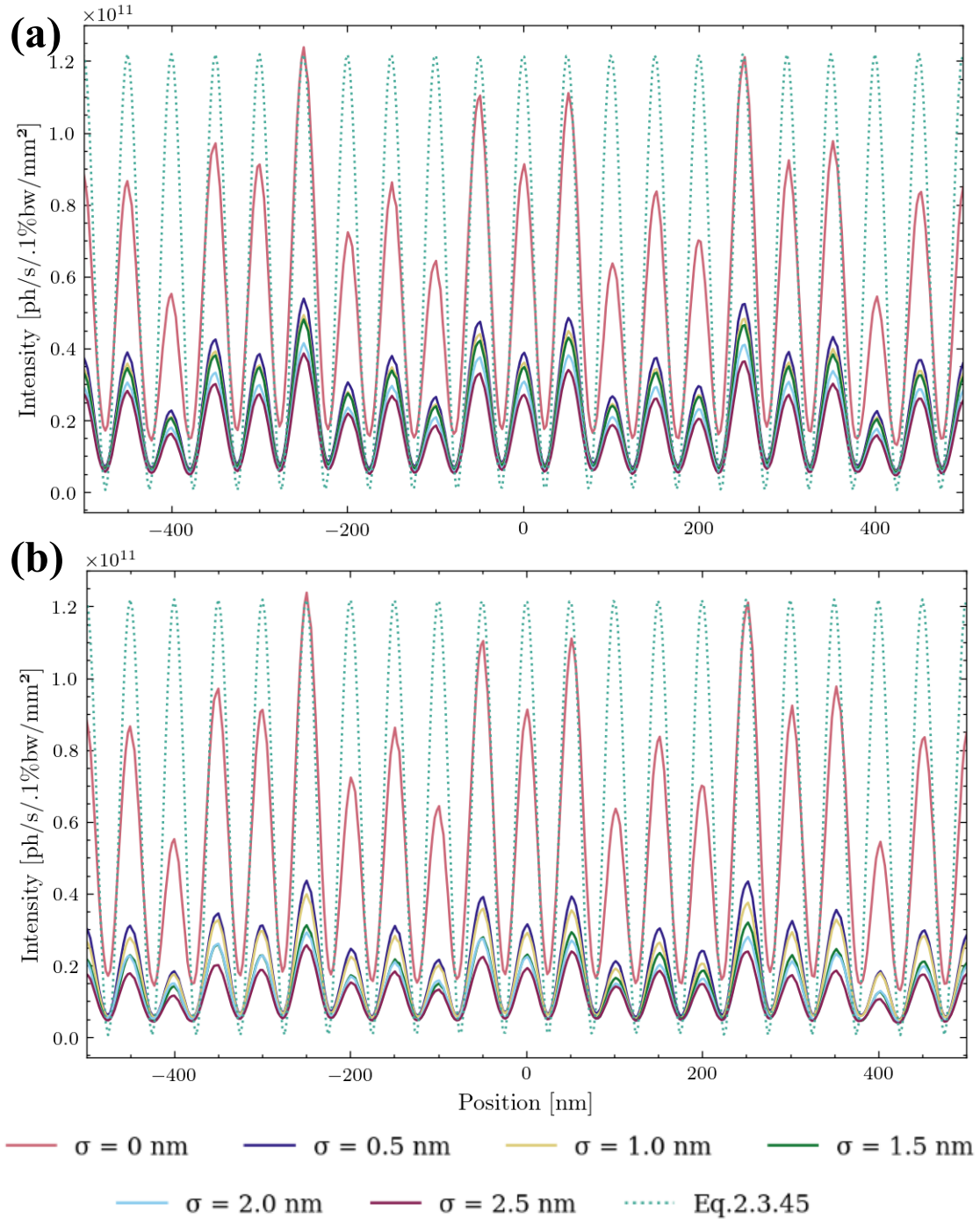


Figure 6.4.2: Comparison of aerial image intensity profiles from masks with different surface roughness. Aerial images were generated from 6.7 nm light incident on two-grating masks with 100 nm pitch, 20 nm thickness and geometry described in Section 4.4.1. Mask surface roughness profiles were added with σ varied from 0.5 nm to 2.5 nm. 2 sets of profiles are shown, each with a constant c_y (a) $c_y = 2 \text{ nm}$, (b) $c_y = 10 \text{ nm}$. The peak-to-peak variation in intensity is significantly increased at $c_y = 10 \text{ nm}$.

for aerial images produces from a mask with smaller c_y . This indicates that the surface roughness profile influences the first-order diffraction efficiency of the mask. Substantial two-dimensional nonuniformity appears in the fringe peak intensity which is varied with σ .

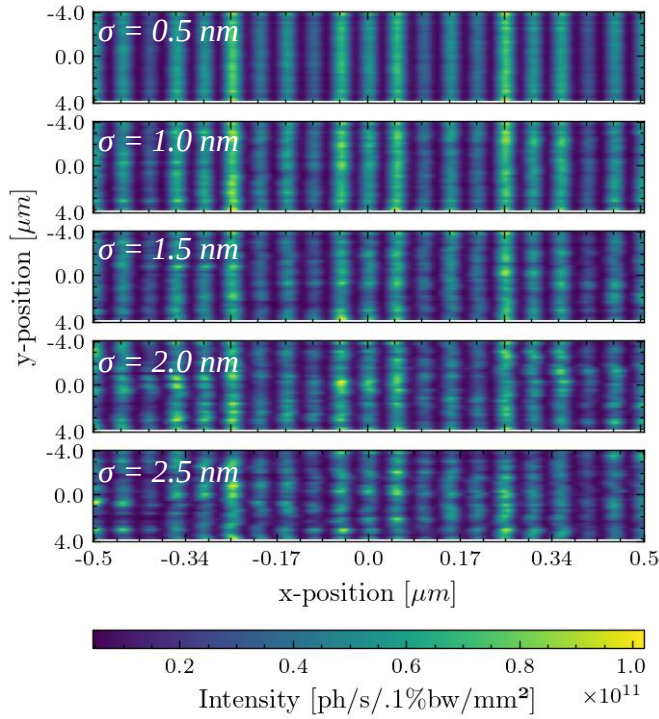


Figure 6.4.3: Close up view of the two-dimensional aerial images shown in Figure 6.4.1 from masks with $c_y = 10$ nm. Aerial images were generated from 6.7 nm light incident on two-grating masks with 100 nm pitch, 20 nm thickness and geometry described in Section 4.4.1. The aerial images show a distinct increase in LWR as σ is increased.

At larger c_y values the variation in peak intensity is more significant and the aperiodic variation introduced in the intensity profile is increased. The width of the intensity fringes can also be seen in Figure 6.4.2 to deviate from the ideal fringe width given by Equation 2.4.44. This is characteristic of line-width roughness (LWR). This is clearer when viewed in two-dimensions at a smaller range, this is shown in Figure 6.4.3 for aerial images obtained from masks with $c_y = 10$ nm.

As shown in Figure 6.4.3, the variation in aerial image fidelity is distributed anisotropically over the aerial image. The LWR introduced in the aerial image intensity due to mask surface roughness is also significantly increased with increasing σ . Qualitative observation of the two-dimensional variation in the aerial image properties suggests that the mean value of quality metrics over the aerial image cannot be used to adequately characterise the effects of mask roughness. The two-dimensional variation also implies that significant sampling error may arise from analysis of small areas, or from one-dimensional line profiles. In addition to the mean value of quality metrics, information about the spread in their values is necessary to adequately characterise the quality of an aerial image generat-

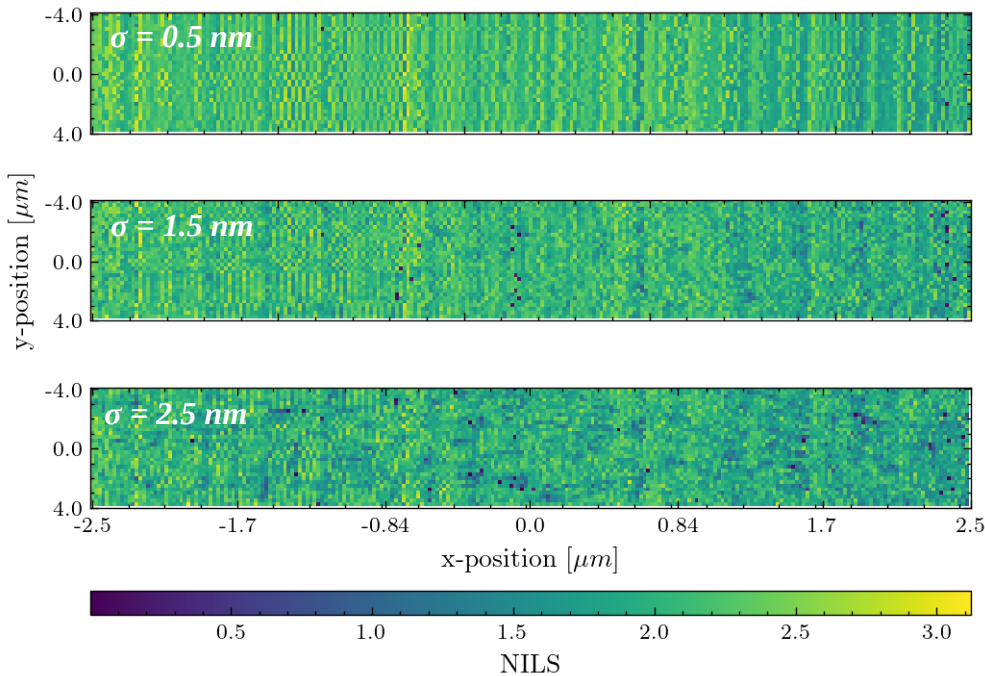


Figure 6.4.4: The two-dimensional NILS distribution for aerial images shown in Figure 6.4.1 from rough two-grating masks with $c_y = 10 \text{ nm}$ and $\sigma = 0.5, 1.5$, and 2.5 nm . NILS values were calculated at each intensity fringe edge.

-ed from a rough mask. The aerial images were thus analysed over the entire sampled area shown in Figure 6.4.1b.

The two-dimensional distribution of NILS values calculated for each intensity fringe edge along every vertical pixel is shown in Figure 6.4.4. The NILS distribution shows variations over the image as σ is increased, which agrees with an increase in LWR seen in Figure 6.4.3. To evaluate the variance in aerial image quality, the mean NILS, and mean normalised NILS standard deviation values were calculated from the two-dimensional distribution for each aerial image. Similarly, the LWR was calculated for every intensity fringe in each aerial image through analysis of the deviation from $p_G/4 = 25 \text{ nm}$, using methods defined in Section 3.4.2.

6.4.1.2 Quantitative Description of Aerial Images

The calculated contrast metrics and LWR for the two-dimensional aerial images is shown in Figure 6.4.5. The fidelity of each aerial image is also shown. This was calculated by comparison with the ideal aerial image generated from Equation 2.4.44 for a mask with the same dimensions and zero roughness. By using the analytical aerial image as a reference,

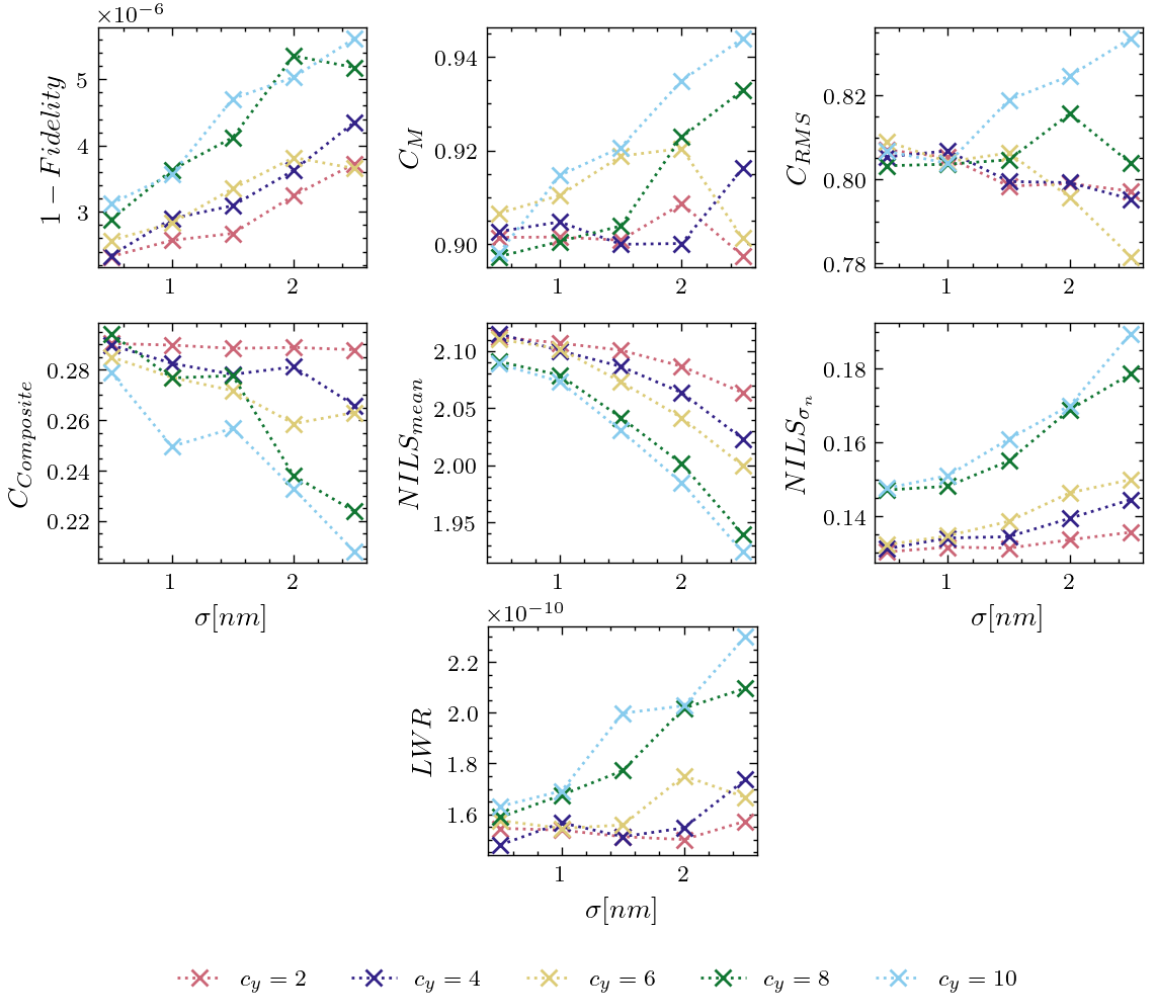


Figure 6.4.5: Contrast metrics for each two-dimensional aerial image generated from rough masks. Fidelity was computed by comparison to the ideal aerial image from Equation 2.4.44. The contrast metrics defined in Section 3.4.3 and LWR are shown for each aerial image. Mean NILS values are shown as well as the mean normalised NILS standard deviation (labelled $NILS_{\sigma_n}$). The mean NILS shows the most correlation to the surface roughness of the mask.

which is only possible in simulation, fidelity provides a direct and reliable indication of how the aerial image is affected by roughness. The quantitative reliability of the other metrics may then be inferred by their correlation with fidelity. Figure 6.4.5 shows the loss in fidelity (plotted as $1 - \text{fidelity}$) as the mask roughness is varied.

As shown in Figure 6.4.5, NILS is the metric most strongly correlated both with aerial image fidelity and with surface roughness qualities of the mask. Each of the combinations of σ and c_y are clearly distinguished. While the mean NILS value shows a very strong correlation to σ and c_y , the mean normalised NILS standard deviation shows a strong correlation with LWR. This shows that as well as the mean NILS value, a measure of the

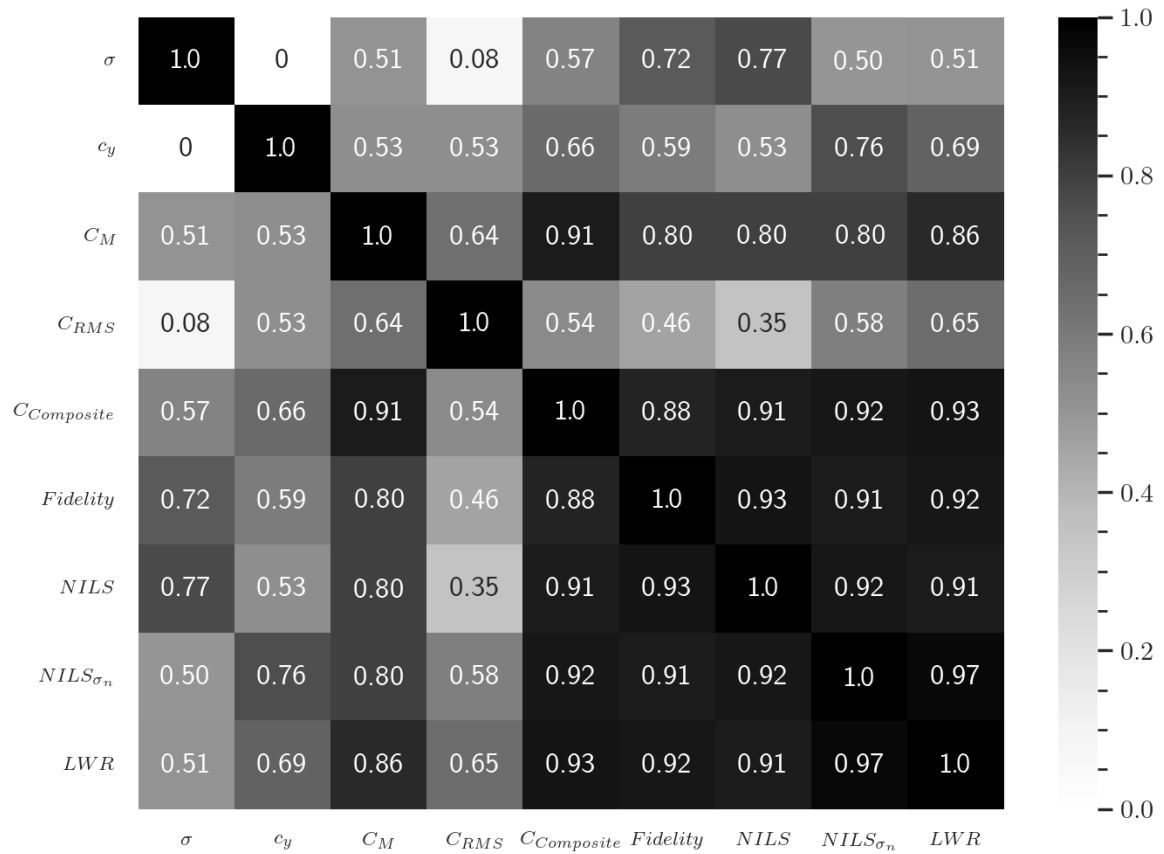


Figure 6.4.6: The correlation between each contrast metric, σ , c_y , LWR, and fidelity when calculated on an aerial image profile.

spread of NILS values over the aerial image is a useful metric for evaluating aerial image quality. The composite contrast metric also shows correlation to surface roughness and aerial image fidelity, although it is not as strong as the correlation seen in NILS. Michelson and RMS contrast metrics do not show any clear correlation with aerial image fidelity or mask surface roughness.

The effect of mask surface roughness on LWR in the aerial image is shown in Figure 6.4.5 to be more significant with larger σ and c_y . LWR below 0.17 nm is seen for all masks with $\sigma = 0.5$ nm, and all masks with $c_y = 2$ nm. While at $\sigma = 2.5$ nm the LWR is seen to increase significantly depending on c_y . For $\sigma = 2.5$ nm, the masks with $c_y = 8$ nm and $c_y = 10$ nm show a LWR of 0.21 nm and 0.23 nm respectively.

Figure 6.4.5 indicated that NILS calculations on the aerial image show the highest correlation to mask surface roughness characteristics. To verify this, a correlation map was calculated for each contrast metric, σ , c_y , LWR, and the fidelity of the aerial images as

computed with respect to an analytical, ideal aerial image generated from Equation 2.4.44. The correlation map shown in Figure 6.4.6 confirms that NILS has the highest correlation (0.93) to aerial image fidelity. The mean normalised NILS standard deviation shows the highest correlation (0.97) to LWR, which is the strongest correlation seen between any two values. This confirms that the mean NILS and the mean normalised NILS standard deviation can be used as reliable metrics to evaluate the quality of an aerial image.

Composite contrast has the second strongest correlation to fidelity (0.88) and LWR (0.93) of any metric. Although its correlation to σ (0.57), is weaker than NILS. This indicates that composite contrast is a satisfactory metric for evaluation of a two-dimensional aerial image formed by a rough mask. Although the correlation to LWR is not as strong as seen in the two-dimensional NILS values, the simplicity in the calculation of composite contrast compared to NILS and LWR means it is a promising candidate for an alternative quality metric for optimisation with the advantage that it is computationally efficient, does not depend on any assumptions regarding the pattern, and is robust to noise.

The Michelson contrast is shown in Figure 6.4.6 to have a strong correlation to LWR (0.86). Although this indicates that Michelson contrast may be a reliable metric, the benefits would be lost in the presence of noise as shown in Section 3.5. The RMS contrast shows no strong correlation to aerial image fidelity or mask surface roughness. Thus, the NILS and composite contrast are determined to be the most reliable metrics in quantifying the quality of an aerial image from a rough, two-grating IL mask.

6.4.2 Aerial Image Quality Metrics and Roughness

The previous sections have shown that the effects of mask roughness on the aerial image depend on both RMS roughness, σ , and correlation length $c_{x,y}$. The correlation length parallel to the orientation of the grating lines, c_y , will have more significant influence on the contrast of the aerial images as σ is increased. For illumination at 6.7 nm wavelength, at σ values below 1 nm, these effects will be less predominant than changes in c_y at σ values between 1 – 2.5 nm for a mask of 20 nm thickness. It has been shown that for evaluation of aerial images resulting from masks with surface roughness, area averaged metrics will be sensitive to sampling error. Thus, they may not sufficiently describe the characteristics

of the aerial image in the presence of the significant two-dimensional variations that arise in the aerial image as the magnitude and correlation of mask roughness increases.

The correlation map shown in Figure 6.4.6 confirms NILS to have a strong correlation to σ (0.77), which agrees with results shown in Section 6.4.1.2. Composite contrast has a weaker correlation to σ (0.57), than NILS. The mean normalised NILS standard deviation is shown in Figure 6.4.6 to have the highest correlation to c_y (0.76), followed by composite contrast (0.66). The RMS contrast shows no strong correlation to aerial image fidelity or mask surface roughness. Thus, the NILS and composite contrast are determined to be the most reliable metrics in quantifying the quality of an aerial image from a rough, two-grating IL mask. The NILS is confirmed to be the superior metric for evaluation of the quality of an aerial image, although composite contrast is a promising candidate for a computationally efficient and robust image evaluation.

In order to define an acceptable threshold of mask surface roughness for high-quality EUV-IL patterning, the properties of the photoresist need to be defined. Without knowing the sensitivity of the photoresist material at 6.7 nm, the minimum value for the mean or RMS NILS of an aerial image cannot be specified. As shown in Figure 6.4.5, if an aerial image mean NILS value was defined for minimum acceptable patterning quality for a particular photoresist, the acceptable upper limit for σ would also depend on the value of c_y . For example, consider if the threshold mean NILS value an aerial image is set to 2.08. The maximum acceptable surface roughness for a 20 nm thick, Ni₃Al, two-grating mask of 100 nm pitch would be $\sigma \leq 0.5$ nm for $c_y \geq 8$ nm, $\sigma \leq 1.0$ nm for $c_y = 6$ nm, $\sigma \leq 1.5$ nm for $c_y = 4$ nm, and $\sigma \leq 2.0$ nm for $c_y = 2$ nm. Experimental verification of these values is needed. These σ and c_y values are significantly larger than the roughness tolerances indicated by Naulleau *et al* [125], the difference could be partly attributed to the shorter wavelength, difference in optical geometry and a shorter correlation length used in this work.

6.5 Discussion

We have shown that the model of the source, SXR-I beamline and mask that was constructed in this work can be used to simulate the formation of a 6.7 nm EUV aerial image, and to explore the effect that source, beamline and mask parameters have on the properties of the image. The results presented in this Chapter confirm that the wavefront

propagation approach, implemented using SRW codes, can satisfactorily represent partially coherent EUV-IL with non-ideal masks. While the source polarisation is accurately modelled, polarisation dependent aerial image contrast was not demonstrated. Further work is required to comprehensively simulate polarisation-dependent diffraction from grating-based photomasks. This provides a computationally feasible and extensible platform for understanding the implementation of EUV-IL at the Australian Synchrotron.

The simulations results presented in this Chapter show that diffraction effects from the photon block layer of the grating mask stack can have a substantial impact on the fidelity of the aerial image for interference lithography at 6.7 nm. For two-beam IL grating masks the effects are characterised by a complicated diffraction envelope that is related to the apertures in the photon block layer that bound each grating.

As shown in Section 5.6, the mask was coherently illuminated for all SSA sizes used in these simulations. Although the coherence length could be reduced, it was always significantly greater than the dimensions of the mask. Thus, the effect of incoherent illumination on the aerial image could not be characterised. The effect of increased flux at the mask plane was an increase in aerial image contrast. Future work will evaluate the effect of partial coherence for grating masks with lateral extent that approaches, or exceeds, the transverse coherence length.

The results have shown that polarisation will have little effect on contrast for 6.7 nm IL for gratings with $p \geq 14$ nm. For all grating pitches above 24 nm, no change in aerial image contrast was seen due to changes in the polarisation of the illuminating wavefield. Aerial image contrast was not found to be as strongly dependent on the polarisation of the illumination as predicted by Ref. 98. More computational resources or optimisation of the propagation codes will be necessary for future work to evaluate the effect of source polarisation on aerial image contrast for gratings with $p_G \leq 14$ nm. However, the production of sub-20 nm pitch gratings for use at the proposed EUV-IL facility is presently a significant challenge, and polarisation-dependent changes in contrast are less important for larger grating pitch gratings.

The simulations presented in this Chapter have shown that mask surface roughness has a significant influence on the characteristics of the aerial image that is formed in 6.7 nm

EUV-IL. This includes an introduction of LWR in the aerial image intensity and a non-negligible reduction in aerial image contrast. The results presented in this chapter also show that the correlation in roughness cannot be ignored for a comprehensive model of aerial image formation, as previously observed by Naulleau *et al* [163]. Very different surface structures may have similar σ . The definition of correlation length in the roughness model for this work cannot distinguish all possible surface structures, but it is a parameter that is relevant to the information that may be obtained by measurement (e.g., by atomic force microscopy) of a rough absorber film.

The most significant factors in determining the contrast of an aerial image formed by the SXR-I beamline were found to be the properties of the grating mask. The dimensions of the mask introduce intensity modulation in the aerial image envelope and the surface roughness map of the mask severely compromising the aerial image quality. While the effect of the grating dimensions on the aerial image intensity was found to be periodic, the intensity modulation introduced by surface roughness was aperiodic and nonuniformly distributed over the two dimensional aerial image. As the wavefield at the mask plane was found to be coherent over a much greater area than the mask, the effect of opening the SSA lead to higher contrast even at a reduction of the coherence at the mask.

It was found that at larger c_y , the σ value of a grating mask is of more importance and will significantly affect the aerial image contrast. As c_y is decreased, the effect of σ in the mask is reduced. While the composite contrast of the aerial images correlated most strongly with changes in c_y , it was found that the NILS correlated most strongly to the effects of increasing σ in the quality of the aerial image. The NILS also showed the strongest correlation to aerial image fidelity of the contrast metrics evaluated, which further confirms its sensitivity to mask roughness.

The NILS, which is widely accepted as the best metric to judge the lithographic quality of an aerial image [156,157], was found to be a satisfactory metric to determine the effect of mask roughness on aerial image contrast. While the mean calculated NILS value gave a good estimate of aerial image quality, the mean normalised NILS standard deviation value provides information about the variation in fidelity across the aerial image. It is potentially useful to use both NILS and its mean normalised standard deviation as a composite figure of merit for simulation-based optimisation.

Michelson contrast showed a relatively weak correlation with σ but strong correlation to c_y . This is expected for simulated date, but it is not given further consideration due to its sensitivity to noise (Section 3.4.3.1) which precludes its application to experimental measurement. In this case other metrics, such as NILS and composite contrast, will be more suitable.

Composite contrast was found to be a satisfactory metric when evaluating a two-dimensional aerial image formed by a rough mask. The strong correlation to LWR indicates that, like LWR, it is capturing information about the speckle introduced in the aerial image. As LWR calculations are sensitive to systematic errors when noise is present in aerial images [154], composite contrast has potential to be a more conveniently computed metric that is more robust to noise.

Other non-ideal mask properties were not investigated, such as particulate contamination, density variations, and voids. The general study of roughness provided in this project will provide insights into these problems as many could be considered similar to mask roughness. For instance, LER could be added to the grating mask model using the same correlated random roughness model than was used for the surface, instead applied to the mask line edge position. This was not included in this work as it requires higher spatial resolution at the mask plane for LER smaller than the 2.5 nm pixel size used. This would lead to greater computational cost. Adding roughness to both the substrate and absorber layer would be beneficial in seeing how the interaction affects the contrast of the aerial image.

Future work should include a more in-depth investigation into the effects of the grating dimensions and the intensity at the aerial image plane caused by diffraction from the photon block layer. The effect of grating dimensions, propagation distance and incident wavelength should also be closely analysed. More work should be done to determine the minimum acceptable coherence for EUV-IL at the SXR-I beamline, and thus the limits on grating dimensions. Future work should also include further simulations of rough masks with a greater range of parameters to identify an allowable threshold for high contrast aerial images. The parameters to investigate should be guided by experimental studies of the nanoscale surface morphology of fabricated masks. The relationship between source coherence and mask roughness effects on aerial image contrast should also be more

thoroughly examined by degrading the coherence at the mask plane and analysing the resulting aerial images from rough masks.

For a particular absorber material, the grating thickness strongly influences the first-order diffraction efficiency. It is also reasonable to assume that surface roughness will have a smaller effect on the aerial image as the mask thickness increases. It is therefore important to investigate the compromise between mask efficiency and sensitivity to mask surface roughness. As indicated in Section 5.5, the assumption of the projection approximation is a known limitation in the beamline model. While it was shown that the thickness dependent efficiency could be obtained with reasonable accuracy under this assumption, the accuracy will deteriorate for thicker masks. Future work should extend the mask model for multislice wavefront propagation through the mask layers, which is straightforward using the computational framework of SRW. Ultimately, a more sophisticated propagator must be implemented for thick masks or when the grating pitch approaches the wavelength [123].

Chapter 7

Conclusion

The semiconductor industry has announced that in order to meet future patterning resolution requirements, for fabricating devices with critical dimensions below 10 nm, a move from 13.5 nm to shorter wavelength radiation is required [15,192]. 6.7 nm radiation is the leading candidate due to progress in developing suitable sources and multilayer mirrors [20]. Synchrotron undulator sources can be used to study lithographic processes at shorter wavelengths due to their high brightness, coherence, and tunability [35]. Extreme ultraviolet (EUV) interference lithography (IL) has been successfully developed at synchrotron radiation facilities. The work in this thesis addressed the need to understand the future implementation of EUV-IL at the Soft X-ray Imaging (SXR-I) beamline of the Australian Synchrotron, which is motivated by the successful development of EUV-IL at other synchrotron facilities [188–190].

A complete source to image plane model of the Australian Synchrotron SXR-I beamline including the proposed EUV/SXR interference lithography optics was constructed. The model represented the primary characteristics of the undulator source and physically accurate but ideal models of each optical component of the 37 m long beamline. The model validation was undertaken by comparison of the spectral distribution and power density of the source, to established undulator radiation theory. It was shown that the source polarisation could be controlled by the parameters of the undulator magnetic structures, and that the partial coherence and intensity of the 6.7 nm wavefront transported through the beamline could be controlled with the size of a secondary source aperture. The coherence properties, polarisation and intensity obtained by simulation were broadly consistent with the known properties of the SXR-I beamline. It was shown that large grating-based photomasks (up to 190 (h) × 160 (v) μm) could be coherently illuminated with sufficient

intensity for EUV-IL. Optimisation of the source collimation, and potentially operating the monochromator in zero-order, may be required to match the (broadband) intensity reported for synchrotron-based 13.5 nm EUV-IL facilities [188–190], if necessary for some applications.

The role of wavefront propagation simulation in understanding the lithographic capabilities at 6.7 nm wavelength was evaluated. Model photomasks based on binary transmission gratings with varied pitch were used to simulate two-beam EUV-IL aerial image formation. Each photomask model was composed of a substrate, absorber (grating lines), and photon block of varying thickness arranged in a stack. A physically relevant representation of correlated random surface roughness was included at the absorber surface.

The complete model was used to obtain aerial images with 2.5 nm resolution in the plane transverse to the optical axis. It was shown that the aerial image obtained from simulating the partially coherent wavefront propagation through a binary grating with 100 nm pitch exhibited the expected periodic structure. The intensity was also in close agreement with the intensity predicted from the grating efficiency calculated using rigorously coupled-wave analysis [188,189]. Fresnel diffraction from the photon block layer of the mask was identified as the source of intensity modulation seen in the aerial image. It was found that the envelope function of the aerial image did not coincide completely with diffraction from a single aperture as described by Meng *et al* [48]. Instead, diffraction from the pair of apertures in the photon block was found to also affect the shape of the aerial image envelope.

A loss of quality in the aerial image, increased line width roughness (LWR), and related deterioration in the aerial image contrast was found for masks with rough surfaces, demonstrating that the wavefront propagation approach can provide insight into the EUV-IL performance that cannot be obtained from existing analytical approaches to modelling.

Multiple metrics were evaluated by investigating their ability to quantify the effect of photomask and grating geometry on the quality of the aerial image. This quantification will guide future mask fabrication for IL. The NILS was found to be the most sensitive metric to changes in the aerial image resulting from variations in RMS roughness. Composite contrast was the metric most sensitive to changes in the roughness correlation length

parallel to the grating lines. Overall, it was found that the NILS was the most reliable metric in predicting the performance of a grating mask in a lithographic system. The work found that σ alone is not a sufficient determination of a mask's ability to form high-contrast interference fringes, but that the grating mask roughness correlation length plays a significant role in the aerial image contrast. This work confirms earlier reports by Naulleau *et al* [161], that both RMS roughness and correlation length of an EUV-IL grating surface must be considered when constructing an accurate lithographic model.

To evaluate the quantitative sensitivity of aerial image quality metrics to the effects of mask surface roughness, their correlation with fidelity, RMS roughness, correlation length, and LWR was examined for aerial images obtained from 25 combinations of RMS roughness and correlation length. It was found that the mean NILS value had the strongest correlation to aerial image fidelity and the mean normalised NILS standard deviation had the strongest correlation to LWR. This confirmed that taking the mean value of a metric over the two-dimensional aerial image is inadequate for a full characterisation of the aerial image quality. The spread in values of metrics that are defined locally, such as NILS, provides information that is complimentary to the mean value, and which may be more sensitive to the effects of mask roughness.

The composite contrast was found to be suitable for computationally efficient evaluation of the loss of aerial image quality, due to mask roughness, owing to its strong correlation with LWR.

7.1 Future Work

The work presented in this thesis establishes an extensible model for EUV-IL that can allow the role of additional properties of the source, optics, and mask to be examined in future work. More work needs to be done to evaluate the model's ability to replicate the effect of source polarisation on the aerial image contrast and examine the consequence of illuminating masks with difference degrees of linear polarisation and elliptical polarisation. Polarisation-dependent aerial image simulations should be evaluated experimentally when the proposed EUV-IL facility at the Australian Synchrotron is commissioned in 2021.

Experimental characterisation of the coherence properties of the 6.7 nm wavefront at the mask plane is also required, together with an evaluation of the compromise between partial coherence and intensity. In anticipation of the requirement to increase the coherent intensity for EUV-IL applications with grating masks of low efficiency, the model presented in this work should be extended to evaluate the use of condenser optics.

The effect of the mask dimensions on the diffraction envelope that affects aerial image uniformity and contrast needs further study. The product of the grating size and spatial resolution was limited in this work by available computational resources. This limitation may be overcome in future work, which will allow a more rigorous exploration of the parameter space. This will also allow investigation into partial coherence effects that will become relevant for large masks. This problem was avoided by Meng *et al* [48], by using a hybrid approach that utilised wavefront propagation by SRW to the mask plane and then a custom mutual optical intensity approach for modelling diffraction from the grating mask and aerial image formation.

Future work in this area should also further investigate effects of both mask surface and line edge roughness on aerial image formation, guided by experimental characterisation of Ni₃Al masks that are currently in development. Evaluation of mask surface roughness profiles with longer correlation length ($c_y > 10$ nm), and smaller RMS roughness ($\sigma < 0.5$ nm) is likely to be most important. Detailed evaluation of the interplay between RMS roughness, roughness correlation length and partial coherence on aerial image contrast can be used to predict the mask roughness that can be tolerated to achieve a critical dimension target by EUV-IL. While the stochastic processes that occur in the resist were outside the scope of this present work, it will ultimately be necessary to interpret the aerial image quality in the context of the complete lithographic process.

References

1. G. D. Hutcheson, "The Economic Implications of Moore's Law," in *Into the Nano Era: Moore's Law Beyond Planar Silicon CMOS*, H. R. Huff, ed., Springer Series in Materials Science (Springer, 2009), pp. 11–38.
2. P. J. Silverman, "The Intel Lithography Roadmap," *Intel Technol. J.* **06**, 55–61 (2002).
3. G. Tallents, E. Wagenaars, and G. Pert, "Optical Lithography: Lithography at EUV Wavelengths," *Nat. Photonics Lond.* **4**, 809–811 (2010).
4. A. R. Neureuther, J. Rubinstein, E. Chin, L. Wang, M. Miller, C. Clifford, and K. Yamazoe, "Modeling Optical Lithography Physics," *Jpn. J. Appl. Phys.* **49**, 06GA01 (2010).
5. M. Rothschild, "Projection Optical Lithography," *Mater. Today* **8**, 18–24 (2005).
6. N. Mojarrad, J. Gobrecht, and Y. Ekinci, "Interference Lithography at EUV and Soft X-Ray Wavelengths: Principles, Methods, and Applications," *Microelectron. Eng.* **143**, 55–63 (2015).
7. Y. Socol, G. N. Kulipanov, A. N. Matveenko, O. A. Shevchenko, and N. A. Vinokurov, "Compact 13.5-nm Free-Electron Laser for Extreme Ultraviolet Lithography," *Phys. Rev. Spec. Top. - Accel. Beams* **14**, 040702 (2011).
8. T. Guest, "Evaluation of an Undulator Soft X-ray Beamline for the Study of 6.x nm Interference Lithography," Latrobe University (2019).
9. IEEE, *International Roadmap for Devices and Systems*, Executive Summary (2017).
10. P. Naulleau, "EUV Lithography," *Synchrotron Radiat. News* **32**, 2–2 (2019).
11. D. T. Attwood, P. Naulleau, K. A. Goldberg, E. Tejnil, Chang Chang, R. Beguiristain, P. Batson, J. Bokor, E. M. Gullikson, M. Koike, H. Medecki, and J. H. Underwood, "Tunable Coherent Radiation in the Soft X-Ray and Extreme Ultraviolet Spectral Regions," *IEEE J. Quantum Electron.* **35**, 709–720 (1999).
12. R. Gronheid, H. H. Solak, Y. Ekinci, A. Jouve, and F. Van Roey, "Characterization of Extreme Ultraviolet Resists with Interference Lithography," *Microelectron. Eng.* **83**, 1103–1106 (2006).
13. L. Wang, H. H. Solak, and Y. Ekinci, "Fabrication of High-Resolution Large-Area Patterns Using EUV Interference Lithography in a Scan-Exposure Mode," *Nanotechnology* **23**, 305303 (2012).
14. C. Xue, X. Meng, Y. Wu, Y. Wang, L. Wang, S. Yang, J. Zhao, and R. Tai, "The Wave Optical Whole Process Design of the Soft X-Ray Interference Lithography Beamline at SSRF," *J. Synchrotron Radiat.* **25**, 1869–1876 (2018).
15. G. D. O'Sullivan and B. Li, "Development of Laser-Produced Plasma Sources for Extreme Ultraviolet Lithography," *J. MicroNanolithography MEMS MOEMS* **11**, 021108 (2012).
16. G. A. van Riessen, "X-Ray Nanolithography Facility: Towards the Ultimate Resolution in Lithography with Synchrotron Radiation and Integrated Metrology," (n.d.).
17. O. Chubar and P. Elleaume, *Synchrotron Radiation Workshop (SRW)* (Brookhaven

- National Lab. (BNL), Upton, NY (United States), 2013).
18. L. Samoylova, A. Buzmakov, O. Chubar, and H. Sinn, "WavePropaGator: Interactive Framework for X-Ray Free-Electron Laser Optics Design and Simulations," *J. Appl. Crystallogr.* **49**, 1347–1355 (2016).
 19. G. O'Sullivan, T. Cummins, P. Dunne, A. Endo, P. Hayden, T. Higashiguchi, D. Kilbane, B. Li, C. O'Gorman, T. Otsuka, E. Sokell, and N. Yugami, "Recent Progress in Source Development for Lithography at 6.x nm," *Phys. Scr.* **T156**, 014105 (2013).
 20. V. Banine, A. Yakunin, and D. Glushkov, "Next Generation EUV Lithography: Challenges and Opportunities, Dublin," *Int. Workshop Extreme Ultrav. Sources* 24 (2010).
 21. N. I. Chkhalo, I. V. Malyshev, A. E. Pestov, V. N. Polkovnikov, N. N. Salashchenko, and M. N. Toropov, "Diffraction Limited X-Ray Optics: Technology, Metrology, Applications," *Phys.-Uspekhi* **63**, 67 (2020).
 22. N. Mojarrad, M. Vockenhuber, L. Wang, B. Terhalle, and Y. Ekinci, "Patterning at 6.5 nm Wavelength Using Interference Lithography," in *Extreme Ultraviolet (EUV) Lithography IV* (International Society for Optics and Photonics, 2013), Vol. 8679, p. 867924.
 23. K. B. Nguyen, "Imaging of Extreme Ultraviolet Lithographic Masks with Programmed Substrate Defects," *J. Vac. Sci. Technol. B Microelectron. Nanometer Struct.* **12**, 3833 (1994).
 24. K. A. Goldberg and I. Mochi, "Wavelength-Specific Reflections: A Decade of Extreme Ultraviolet Actinic Mask Inspection Research," *J. Vac. Sci. Technol. B* **28**, C6E1-C6E10 (2010).
 25. T. Kozawa and A. Erdmann, "Feasibility Study of Chemically Amplified Resists for Short Wavelength Extreme Ultraviolet Lithography," *Appl. Phys. Express* **4**, 026501 (2011).
 26. T. Kozawa and T. Itani, "Wavelength Dependence of Lithography Resolution in Extreme Ultraviolet Region," *Appl. Phys. Express* **4**, 126501 (2011).
 27. T. Otsuka, B. Li, C. O'Gorman, T. Cummins, D. Kilbane, T. Higashiguchi, N. Yugami, W. Jiang, A. Endo, P. Dunne, and G. O'Sullivan, "A 6.7-nm Beyond EUV Source as a Future Lithography Source," in *Extreme Ultraviolet (EUV) Lithography III* (International Society for Optics and Photonics, 2012), Vol. 8322, p. 832214.
 28. B. Li, P. Dunne, T. Higashiguchi, T. Otsuka, N. Yugami, W. Jiang, A. Endo, and G. O'Sullivan, "Gd Plasma Source Modeling at 6.7 nm for Future Lithography," *Appl. Phys. Lett.* **99**, 231502 (2011).
 29. I. Fomenkov, A. Schafgans, and D. Brandt, "Laser-Produced Plasma Sources for High-Volume-Manufacturing EUV Lithography," *Synchrotron Radiat. News* **32**, 3–8 (2019).
 30. A. Endo, H. Hoshino, T. Ariga, and T. Miura, "Development of Short Pulse and High Power CO₂ Laser for EUV Lithography," in *Laser-Generated, Synchrotron, and Other Laboratory X-Ray and EUV Sources, Optics, and Applications II* (International Society for Optics and Photonics, 2005), Vol. 5918, p. 59180I.
 31. H. Tanaka, Y. Hashimoto, K. Tamaru, A. Takahashi, and T. Okada, "Behavior of Debris from Laser-Produced Plasma for Extreme Ultraviolet Light Source Measured by Laser Imaging Technique," *Appl. Phys. Lett.* **89**, 181109 (2006).
 32. L. Wang, B. Terhalle, V. A. Guzenko, A. Farhan, M. Hojeij, and Y. Ekinci, "Generation of High-Resolution Kagome Lattice Structures Using Extreme

- Ultraviolet Interference Lithography," *Appl. Phys. Lett.* **101**, 093104 (2012).
33. A. Isoyan, Y.-C. Cheng, F. Jiang, J. Wallace, M. Efremov, P. Nealey, and F. Cerrina, "Progress in Extreme Ultraviolet Interferometric Lithography at the University of Wisconsin," in *Emerging Lithographic Technologies XII* (International Society for Optics and Photonics, 2008), Vol. 6921, p. 69212R.
34. L. J. Heyderman, H. H. Solak, C. David, D. Atkinson, R. P. Cowburn, and F. Nolting, "Arrays of Nanoscale Magnetic Dots: Fabrication by X-Ray Interference Lithography and Characterization," *Appl. Phys. Lett.* **85**, 4989–4991 (2004).
35. D. T. Attwood, "Synchrotron Radiation," in *Soft X-Rays and Extreme Ultraviolet Radiation: Principles and Applications*, 1. paperback version, digitally printed (with amendments) (Cambridge Univ. Press, 2007), pp. 139–156.
36. A. Heuberger, "X-Ray Lithography with Synchrotron Radiation," *Z. Phys. B Condens. Matter* **61**, 473–476 (1985).
37. I. Mochi and Y. Ekinci, "Lensless EUV Lithography and Imaging," *Synchrotron Radiat. News* **32**, 22–27 (2019).
38. A. M. Goethals, R. Gronheid, F. V. Roey, H. H. Solak, and Y. Ekinci, "Progress in EUV Resist Performance," *J. Photopolym. Sci. Technol.* **19**, 501–506 (2006).
39. Y. Ekinci, M. Vockenhuber, M. Hojeij, L. Wang, and N. Mojarrad, "Evaluation of EUV Resist Performance with Interference Lithography Towards 11 nm Half-Pitch and Beyond," in *Extreme Ultraviolet (EUV) Lithography IV* (International Society for Optics and Photonics, 2013), Vol. 8679, p. 867910.
40. S. Yang and Y. Wu, "EUV/Soft X-Ray Interference Lithography," *MicroNanolithography - Heuristic Asp. Endur. Technol. Intech Open Science Publication*, 83–100 (2018).
41. J. Xu, Z. Wang, Z. Zhang, D. Wang, and Z. Weng, "Fabrication of Moth-Eye Structures on Silicon by Direct Six-Beam Laser Interference Lithography," *J. Appl. Phys.* **115**, 203101 (2014).
42. "Characteristics of EUV-IL," <https://www.psi.ch/en/lmn/characteristics-of-euv-il>.
43. E. Hecht, *Optics*, 2nd ed. (Addison-Wesley, 1987).
44. H. H. Solak, "Nanolithography with Coherent Extreme Ultraviolet Light," *J. Phys. Appl. Phys.* **39**, R171–R188 (2006).
45. W. Karim, S. A. Tschupp, M. Oezaslan, T. J. Schmidt, J. Gobrecht, J. A. van Bokhoven, and Y. Ekinci, "High-Resolution and Large-Area Nanoparticle Arrays Using EUV Interference Lithography," *Nanoscale* **7**, 7386–7393 (2015).
46. C. Vieu, F. Carcenac, A. Pépin, Y. Chen, M. Mejias, A. Lebib, L. Manin-Ferlazzo, L. Couraud, and H. Launois, "Electron Beam Lithography: Resolution Limits and Applications," *Appl. Surf. Sci.* **164**, 111–117 (2000).
47. C. Mack, "Depth-of-Focus and the Alternating Phase-Shift Mask," *Microlithogr. World* **13**, 20–21 (2004).
48. P. P. Naulleau, C. N. Anderson, and S. F. Horne, "Extreme Ultraviolet Interference Lithography with Incoherent Light," in *Emerging Lithographic Technologies XI* (International Society for Optics and Photonics, 2007), Vol. 6517, p. 65172T.
49. X. Meng, H. Yu, Y. Wang, J. Ren, C. Xue, S. Yang, Z. Guo, J. Zhao, Y. Wu, and R. Tai, "Analysis of Partially Coherent Light Propagation Through the Soft X-Ray Interference Lithography Beamline at SSRF," *J. Synchrotron Radiat.* **28**, 902–909 (2021).
50. C. Xue, Y. Wu, F. Zhu, S. Yang, H. Liu, J. (赵俊) Zhao, L. (王连升) Wang, and R. (邵仁忠) Tai, "Development of Broadband X-Ray Interference Lithography Large Area Exposure System," *Rev. Sci. Instrum.* **87**, 043303 (2016).

51. G. N. Kulipanov and A. N. Skrinskiĭ, "Utilization of Synchrotron Radiation: Current Status and Prospects," Sov. Phys. Uspekhi **20**, 559 (1977).
52. H. Shiotani, S. Suzuki, D. G. Lee, P. Naulleau, Y. Fukushima, R. Ohnishi, T. Watanabe, and H. Kinoshita, "Dual Grating Interferometric Lithography for 22-nm Node," Jpn. J. Appl. Phys. **47**, 4881 (2008).
53. E. Buitrago, R. Fallica, D. Fan, T. S. Kulmala, M. Vockenhuber, and Y. Ekinci, "SnO_x High-Efficiency EUV Interference Lithography Gratings Towards the Ultimate Resolution in Photolithography," Microelectron. Eng. **155**, 44–49 (2016).
54. B. Päiväranta, A. Langner, E. Kirk, C. David, and Y. Ekinci, "Sub-10 Nm Patterning Using EUV Interference Lithography," Nanotechnology **22**, 375302 (2011).
55. Y. Fukushima, N. Sakagami, T. Kimura, Y. Kamaji, T. Iguchi, Y. Yamaguchi, M. Tada, T. Harada, T. Watanabe, and H. Kinoshita, "Development of Extreme Ultraviolet Interference Lithography System," Jpn. J. Appl. Phys. **49**, 06GD06 (2010).
56. J. Huang, D. Fan, Y. Ekinci, and C. Padeste, "Fabrication of Ultrahigh Resolution Metal Nanowires and Nanodots Through EUV Interference Lithography," Microelectron. Eng. **141**, 32–36 (2015).
57. A. Langner, B. Päiväranta, B. Terhalle, and Y. Ekinci, "Fabrication of Quasiperiodic Nanostructures with EUV Interference Lithography," Nanotechnology **23**, 105303 (2012).
58. T. Watanabe and T. Harada, "Research Activities of Extreme Ultraviolet Lithography at the University of Hyogo," Synchrotron Radiat. News **32**, 28–35 (2019).
59. G. S. Brown, "Undulators and the Properties of Synchrotron Radiation," in *Synchrotron Radiation Research: Advances in Surface and Interface Science*, R. Z. Bachrach, ed., Synchrotron Radiation Research (Springer US, 1992), pp. 317–333.
60. S. Reiche, "Motion in the Undulator," CERN Yellow Rep. Sch. Proc. 347 Pages (2018).
61. E. G. Bessonov and A. V. Vinogradov, "Undulator and Laser Sources of Soft X Rays," Sov. Phys. Uspekhi **32**, 806 (1989).
62. D. Kilbane, F. de Dortan, G. O'Sullivan, and V. Zakharov, "Reachable Extreme Ultraviolet Wavelengths According to Elements / Atomic Data," in *Short Wavelength Laboratory Sources*, D. Bleiner, J. Costello, F. Dortan, G. O'Sullivan, L. Pina, and A. Michette, eds. (Royal Society of Chemistry, 2014), pp. 42–48.
63. H. Wang, P. Bencok, P. Steadman, E. Longhi, J. Zhu, and Z. Wang, "Complete Polarization Analysis of an Apple II Undulator Using a Soft X-Ray Polarimeter," J. Synchrotron Radiat. **19**, 944–948 (2012).
64. B. Cowie, "Unpublished Report, ANSTO," (2007).
65. D. Attwood, *Soft X-Rays and Extreme Ultraviolet Radiation: Principles and Applications* (Cambridge University Press, 1999).
66. D. Paganin, *Coherent X-Ray Optics* (Oxford University Press, Incorporated, 2006).
67. K. P. Wootton, M. J. Boland, R. Dowd, Y.-R. E. Tan, B. C. C. Cowie, Y. Papaphilippou, G. N. Taylor, and R. P. Rassool, "Observation of Picometer Vertical Emittance with a Vertical Undulator," Phys. Rev. Lett. **109**, 194801 (2012).
68. M. Born and E. Wolf, *Principles of Optics*, 7th Edition, 60th Anniversary Edition (Cambridge University Press, 1959).
69. D. G. Smith, *Field Guide to Physical Optics* (SPIE Press, 2013), Vol. FG17.
70. K. A. Sharma, G. Costello, E. Vélez-Juárez, T. G. Brown, and M. A. Alonso,

- "Measuring Vector Field Correlations Using Diffraction," Opt. Express **26**, 8301 (2018).
- 71. L.-P. Leppänen, K. Saastamoinen, A. T. Friberg, and T. Setälä, "Interferometric Interpretation for the Degree of Polarization of Classical Optical Beams," New J. Phys. **16**, 113059 (2014).
 - 72. M. S. del Rio, "About the Coherent Fraction of Synchrotron Emission," ArXiv180107542 Phys. (2018).
 - 73. "Coherence Properties of Third and Fourth Generation X-Ray Sources. Theory and Experiment (Technical Report)," <https://www.osti.gov/etdeweb/biblio/22119552>.
 - 74. Z. H. Levine, S. E. Grantham, and T. B. Lucatorto, "Design Considerations for a Cascaded Grating Interferometer Suitable for Extreme Ultraviolet Interference Lithography," J. MicroNanolithography MEMS MOEMS **8**, 021202 (2009).
 - 75. G. Bennson, "Handbook on Synchrotron Radiation," Opt. Acta Int. J. Opt. **31**, 979–980 (1984).
 - 76. I. A. Vartanyants and A. Singer, "Coherence Properties of Hard X-Ray Synchrotron Sources and X-Ray Free-Electron Lasers," New J. Phys. **12**, 035004 (2010).
 - 77. P. P. Naulleau, "The Role of Temporal Coherence in Imaging with Extreme Ultraviolet Lithography Optics," Opt. Commun. **219**, 57–63 (2003).
 - 78. G. Geloni, S. Serkez, R. Khubbudinov, V. Kocharyan, and E. Saldin, "Effects of Energy Spread on Brightness and Coherence of Undulator Sources," J. Synchrotron Radiat. **25**, 1335–1345 (2018).
 - 79. R. A. Shore, B. J. Thompson, and R. E. Whitney, "Diffraction by Apertures Illuminated with Partially Coherent Light," J. Opt. Soc. Am. **56**, (1966).
 - 80. D. Paterson, B. E. Allman, P. J. McMahon, J. Lin, N. Moldovan, K. A. Nugent, I. McNulty, C. T. Chantler, C. C. Retsch, T. H. K. Irving, and D. C. Mancini, "Spatial Coherence Measurement of X-Ray Undulator Radiation," Opt. Commun. **195**, 79–84 (2001).
 - 81. E. Wolf and M. Born, eds., "Interference and Diffraction with Partially Coherent Light," in *Principles of Optics: 60th Anniversary Edition*, 7th ed. (Cambridge University Press, 2019), pp. 554–632.
 - 82. J. C. Dainty, "Introduction," in *Laser Speckle and Related Phenomena*, J. C. Dainty, ed., Topics in Applied Physics (Springer, 1975), pp. 1–7.
 - 83. H. Fujii and T. Asakura, "Effect of Surface Roughness on the Statistical Distribution of Image Speckle Intensity," Opt. Commun. **11**, 35–38 (1974).
 - 84. Y. Ohtsuka and Y. Imai, "Partial Coherence Controlled by a Progressive Ultrasonic Wave," JOSA **69**, 684–689 (1979).
 - 85. H. M. Pedersen, "Theory of Speckle Dependence on Surface Roughness," JOSA **66**, 1204–1210 (1976).
 - 86. A. M. Hamed, H. El-Ghandoor, F. El-Diasty, and M. Saudy, "Analysis of Speckle Images to Assess Surface Roughness," Opt. Laser Technol. **36**, 249–253 (2004).
 - 87. B. Dhanasekar, N. K. Mohan, B. Bhaduri, and B. Ramamoorthy, "Evaluation of Surface Roughness Based on Monochromatic Speckle Correlation Using Image Processing," Precis. Eng. **32**, 196–206 (2008).
 - 88. S. Lee, D. Kim, S.-W. Nam, B. Lee, J. Cho, and B. Lee, "Light Source Optimization for Partially Coherent Holographic Displays with Consideration of Speckle Contrast, Resolution, and Depth of Field," Sci. Rep. **10**, 18832 (2020).
 - 89. W. H. McMaster, "Polarization and the Stokes Parameters," Am. J. Phys. **22**, 351–362 (1954).
 - 90. W. A. Shurcliff and S. S. Ballard, *Polarized Light*, Momentum Book No. 7 (D. Van

- Nostrand Company, Inc., 1964).
91. J. Tatum, "4: Stokes Parameters for Describing Polarized Light," in *Physical Optics* (University of Victoria, 2017), pp. 40–55.
 92. F. Perrin, "Polarization of Light Scattered by Isotropic Opalescent Media," *J. Chem. Phys.* **10**, 415–427 (1942).
 93. B. Schaefer, E. Collett, R. Smyth, D. Barrett, and B. Fraher, "Measuring the Stokes Polarization Parameters," *Am. J. Phys.* **75**, 163–168 (2007).
 94. S. Pancharatnam, "Generalized Theory of Interference, and Its Applications," *Proc. Indian Acad. Sci. - Sect. A* **44**, 247–262 (1956).
 95. T. Hassinen, J. Tervo, and A. T. Friberg, "Purity of Partial Polarization in the Frequency and Time Domains," *Opt. Lett.* **38**, 1221–1223 (2013).
 96. E. Wolf, "Optics in Terms of Observable Quantities," *Il Nuovo Cimento 1943-1954* **12**, 884–888 (1954).
 97. A. T. Friberg, J. Tervo, and T. Setälä, "Young's Interference Experiment Reloaded," *AIP Conf. Proc.* **949**, 130–137 (2007).
 98. X. Wang, L.-T. Tseng, D. Kazazis, Z. Tasdemir, M. Vockenhuber, I. Mochi, and Y. Ekinci, "Studying Resist Performance for Contact Holes Printing Using EUV Interference Lithography," in *International Conference on Extreme Ultraviolet Lithography 2018* (International Society for Optics and Photonics, 2018), Vol. 10809, p. 108091Z.
 99. B. L. Henke, E. M. Gullikson, and J. C. Davis, "X-Ray Interactions: Photoabsorption, Scattering, Transmission, and Reflection at E = 50-30,000 Ev, Z = 1-92," *At. Data Nucl. Data Tables* **54**, 181–342 (1993).
 100. A. Akou, I. A. Gural'skiy, L. Salmon, C. Bartual-Murgui, C. Thibault, C. Vieu, G. Molnár, and A. Bousseksou, "Soft Lithographic Patterning of Spin Crossover Complexes. Part 2: Stimuli-Responsive Diffraction Grating Properties," *J. Mater. Chem.* **22**, 3752–3757 (2012).
 101. Shimadzu Corporation, "SHIMADZU DIFFRACTION GRATINGS," <https://www.shimadzu.com/opt/guide/diffraction/10.html>.
 102. C. Palmer and E. G. Loewen, *Diffraction Grating Handbook*, 6th ed. (Newport Corporation, 2005).
 103. J. E. Harvey and R. N. Pfisterer, "Understanding Diffraction Grating Behavior: Including Conical Diffraction and Rayleigh Anomalies from Transmission Gratings," *Opt. Eng.* **58**, 087105 (2019).
 104. M. G. Moharam, E. B. Grann, D. A. Pommet, and T. K. Gaylord, "Formulation for Stable and Efficient Implementation of the Rigorous Coupled-Wave Analysis of Binary Gratings," *JOSA A* **12**, 1068–1076 (1995).
 105. N. Mojarrad, D. Fan, J. Gobrecht, and Y. Ekinci, "Broadband Interference Lithography at Extreme Ultraviolet and Soft X-Ray Wavelengths," *Opt. Lett.* **39**, 2286 (2014).
 106. P. P. Naulleau, J. A. Liddle, E. H. Anderson, E. M. Gullikson, P. Mirkarimi, F. Salmassi, and E. Spiller, "Fabrication of High-Efficiency Multilayer-Coated Gratings for the EuV Regime Using E-Beam Patterned Substrates," *Opt. Commun.* **229**, (2003).
 107. P. P. Naulleau, W. C. Sweatt, and D. A. Tichenor, "Theoretical Efficiency Analysis of a Condenser-Embedded Grating-Based Spectral Purity Filter for EuV Lithography," *Opt. Commun.* **214**, 31–38 (2002).
 108. J. A. Liddle, F. Salmassi, P. P. Naulleau, and E. M. Gullikson, "Nanoscale Topography Control for the Fabrication of Advanced Diffractive Optics," *J. Vac.*

- Sci. Technol. B Microelectron. Nanometer Struct. Process. Meas. Phenom. **21**, 2980–2984 (2003).
- 109. F. Salmassi, P. P. Naulleau, E. M. Gullikson, D. L. Olynick, and J. A. Liddle, "Extreme Ultraviolet Binary Phase Gratings: Fabrication and Application to Diffractive Optics," J. Vac. Sci. Amp Technol. Vac. Surf. Films **24**, 1136 (n.d.).
 - 110. B. M. McClinton and P. P. Naulleau, "Mask Roughness Induced LER: A Rule of Thumb," in *Extreme Ultraviolet (EUV) Lithography* (SPIE, 2010), Vol. 7636, pp. 759–767.
 - 111. M. Paulsen, L. T. Neustock, S. Jahns, J. Adam, and M. Gerken, "Simulation Methods for Multiperiodic and Aperiodic Nanostructured Dielectric Waveguides," Opt. Quantum Electron. **49**, 107 (2017).
 - 112. K. Lai, "Review of Computational Lithography Modeling: Focusing on Extending Optical Lithography and Design-Technology Co-Optimization," Adv. Opt. Technol. **1**, 249–267 (2012).
 - 113. F. H. Dill, W. P. Hornberger, P. S. Hauge, and J. M. Shaw, "Characterization of Positive Photoresist," IEEE Trans. Electron Devices **22**, 445–452 (1975).
 - 114. A. Chunder, A. Latypov, J. J. Biafore, H. J. Levinson, and T. Bailey, "Systematic Assessment of the Contributors of Line Edge Roughness in EUV Lithography Using Simulations," in *Extreme Ultraviolet (EUV) Lithography IX* (International Society for Optics and Photonics, 2018), Vol. 10583, p. 105831N.
 - 115. J. Biafore, M. Smith, C. Mack, J. Thackeray, R. Gronheid, S. Robertson, T. Graves, and D. Blankenship, "Statistical Simulation of Resist at EUV and ArF," Proc. SPIE - Int. Soc. Opt. Eng. **7273**, (2009).
 - 116. S. Friedenthal, A. Moore, and R. Steiner, *A Practical Guide to SysML: The Systems Modeling Language* (Elsevier Science & Technology, 2014).
 - 117. O. Chubar, A. Fluerasu, L. Berman, K. Kaznatcheev, and L. Wiegart, "Wavefront Propagation Simulations for Beamlines and Experiments with "Synchrotron Radiation Workshop,'" J. Phys. Conf. Ser. **425**, 162001 (2013).
 - 118. O. Chubar and R. Celestre, "Memory and CPU Efficient Computation of the Fresnel Free-Space Propagator in Fourier Optics Simulations," Opt. Express **27**, 28750–28759 (2019).
 - 119. O. Chubar, M. Rakitin, Y.-C. K. Chen-Wiegart, A. Fluerasu, and L. Wiegart, "Simulation of Experiments with Partially Coherent X-Rays Using Synchrotron Radiation Workshop," in *Advances in Computational Methods for X-Ray Optics IV* (International Society for Optics and Photonics, 2017), Vol. 10388, p. 1038811.
 - 120. K. S. Morgan, K. K. W. Siu, and D. M. Paganin, "The Projection Approximation Versus an Exact Solution for X-Ray Phase Contrast Imaging, with a Plane Wave Scattered by a Dielectric Cylinder," Opt. Commun. **283**, 4601–4608 (2010).
 - 121. M. Goldstein, A. Wüest, and D. Barnhart, "Partially Coherent Extreme Ultraviolet Interference Lithography for 16nm Patterning Research," Appl. Phys. Lett. **93**, 083110 (2008).
 - 122. M. S. Rakitin, P. Moeller, R. Nagler, B. Nash, D. L. Bruhwiler, D. Smalyuk, M. Zhernenkov, and O. Chubar, "Sirepo: An Open-Source Cloud-Based Software Interface for X-Ray Source and Optics Simulations," J. Synchrotron Radiat. **25**, 1877–1892 (2018).
 - 123. K. Li, M. Wojcik, and C. Jacobsen, "Multislice Does It All—Calculating the Performance of Nanofocusing X-Ray Optics," Opt. Express **25**, 1831 (2017).
 - 124. N. Canestrari, O. Chubar, and R. Reininger, "Partially Coherent X-Ray Wavefront Propagation Simulations Including Grazing-Incidence Focusing Optics," J.

- Synchrotron Radiat. **21**, 1110–1121 (2014).
125. P. P. Naulleau, K. A. Goldberg, E. Gullikson, I. Mochi, B. McClinton, and A. Rastegar, "Accelerating EUV Learning with Synchrotron Light: Mask Roughness Challenges Ahead," in *Photomask Technology 2011* (International Society for Optics and Photonics, 2011), Vol. 8166, p. 81660F.
 126. S. A. George, L. M. Baclea-an, P. P. Naulleau, R. J. Chen, and T. Liang, "Extreme Ultraviolet Mask Surface Cleaning Effects on Lithography Process Performance," J. Vac. Sci. Technol. B **28**, C6E31-C6E35 (2010).
 127. J. R. Maldonado, S. A. Cordes, J. A. Leavey, R. E. Acosta, F. Doany, M. Angelopoulos, and C. Waskiewicz, "Pellicles for X-Ray Lithography Masks," in *Emerging Lithographic Technologies II* (International Society for Optics and Photonics, 1998), Vol. 3331, pp. 245–254.
 128. I. Fomenkov, "EUV Source for Lithography in HVM: performance and prospects," **70** (n.d.).
 129. M. Escudier and T. Atkins, "Discrete Fourier Transform," in *A Dictionary of Mechanical Engineering* (Oxford University Press, 2019).
 130. J. W. Cooley and J. W. Tukey, "An Algorithm for the Machine Calculation of Complex Fourier Series," Am. Math. Soc. **6** (1965).
 131. A. Prošek and M. Leskovar, "Use of Fast Fourier Transform for Sensitivity Analysis," in *Fourier Transform - Signal Processing and Physical Sciences*, S. M. Salih, ed. (InTech, 2015).
 132. C. E. Shannon, "Communication in the Presence of Noise," Proc. IRE **37**, 10–21 (1949).
 133. G. E. Sarty, "The Relationship Between the Nyquist Criterion and the Point Spread Function," Concepts Magn. Reson. Part B Magn. Reson. Eng. **17B**, 17–24 (2003).
 134. J. Miao, T. Ishikawa, Q. Shen, and T. Earnest, "Extending X-Ray Crystallography to Allow the Imaging of Noncrystalline Materials, Cells, and Single Protein Complexes," Annu. Rev. Phys. Chem. **59**, 387–410 (2008).
 135. T. Battula, T. Georgiev, J. Gille, and S. Goma, "Contrast Computation Methods for Interferometric Measurement of Sensor Modulation Transfer Function," J. Electron. Imaging **27**, 013015 (2018).
 136. O. Chubar and P. Elleaume, "Accurate and Efficient Computation of Synchrotron Radiation in the Near Field Region," Proc EPAC98 Conf. **1177**, 3 (1998).
 137. O. Chubar, M.-E. Couprie, M. Labat, G. Lambert, F. Polack, and O. Tcherbakoff, "Time-Dependent FEL Wavefront Propagation Calculations: Fourier Optics Approach," Nucl. Instrum. Methods Phys. Res. Sect. Accel. Spectrometers Detect. Assoc. Equip. **593**, 30–34 (2008).
 138. O. Chubar, "Recent Updates in the ‘Synchrotron Radiation Workshop’ Code, on-Going Developments, Simulation Activities, and Plans for the Future," in *Advances in Computational Methods for X-Ray Optics III* (International Society for Optics and Photonics, 2014), Vol. 9209, p. 920907.
 139. O. Chubar, L. Berman, Y. S. Chu, A. Fluerasu, S. Hulbert, M. Idir, K. Kaznatcheev, D. Shapiro, Q. Shen, and J. Baltser, "Development of Partially-Coherent Wavefront Propagation Simulation Methods for 3rd and 4th Generation Synchrotron Radiation Sources," in *Advances in Computational Methods for X-Ray Optics II* (International Society for Optics and Photonics, 2011), Vol. 8141, p. 814107.
 140. L. Wiegart, M. Rakitin, Y. Zhang, A. Fluerasu, and O. Chubar, "Towards the Simulation of Partially Coherent X-Ray Scattering Experiments," AIP Conf. Proc. **2054**, 060079 (2019).

141. O. Chubar, "Wavefront Calculations," in *X-Ray FEL Optics and Instrumentation* (International Society for Optics and Photonics, 2001), Vol. 4143, pp. 48–59.
142. L. Samoylova, A. Buzmakov, G. Geloni, O. Chubar, and H. Sinn, "Cross-Platform Wave Optics Software for XFEL Applications," in *Advances in Computational Methods for X-Ray Optics II* (International Society for Optics and Photonics, 2011), Vol. 8141, p. 81410A.
143. O. Chubar, Y. S. Chu, X. Huang, S. Kalbfleisch, H. Yan, T. Shaftan, G. Wang, Y. Q. Cai, A. Suvorov, A. Fluerasu, L. Wiegart, Y. K. Chen-Wiegart, J. Thieme, G. Williams, M. Idir, T. Tanabe, P. Zschack, and Q. Shen, "Initial Performances of First Undulator-Based Hard X-Ray Beamlines of NSLS-II Compared to Simulations," AIP Conf. Proc. **1741**, 040002 (2016).
144. D. Laundy, S. G. Alcock, L. Alianelli, J. P. Sutter, K. J. S. Sawhney, and O. Chubar, "Partial Coherence and Imperfect Optics at a Synchrotron Radiation Source Modeled by Wavefront Propagation," in *Advances in Computational Methods for X-Ray Optics III* (International Society for Optics and Photonics, 2014), Vol. 9209, p. 920903.
145. A. He, O. Chubar, J. Dvorak, W. Hu, S. Hulbert, A. Walter, S. Wilkins, and C. Salort, "Wave Optics Simulations for New Soft X-Ray Beamlines at NSLS-II," in *Advances in Computational Methods for X-Ray Optics V* (International Society for Optics and Photonics, 2020), Vol. 11493, p. 1149307.
146. A. Fluerasu, O. Chubar, K. Kaznatcheev, J. Baltser, L. Wiegart, K. Evans-Lutterodt, M. Carlucci-Dayton, and L. Berman, "Analysis of the Optical Design of the NSLA-II Coherent Hard X-Ray Beamline," in *Advances in Computational Methods for X-Ray Optics II* (International Society for Optics and Photonics, 2011), Vol. 8141, p. 81410J.
147. D. A. Shapiro, O. Chubar, K. Kaznatcheev, R. Reininger, C. Sanchez-Hanke, and S. Wang, "Optimization of a Coherent Soft X-Ray Beamline for Coherent Scattering Experiments at NSLS-II," in *Advances in Computational Methods for X-Ray Optics II* (International Society for Optics and Photonics, 2011), Vol. 8141, p. 81410I.
148. B. Nash, O. Chubar, D. L. Bruhwiler, M. Rakitin, P. Moeller, R. Nagler, and N. Goldring, "Undulator Radiation Brightness Calculations in the Sirepo GUI for SRW," in *Advances in Laboratory-Based X-Ray Sources, Optics, and Applications VII* (International Society for Optics and Photonics, 2019), Vol. 11110, p. 11110K.
149. J. Baltser, E. Knudsen, A. Vickery, O. Chubar, A. Snigirev, G. Vaughan, R. Feidenhans'l, and K. Lefmann, "Advanced Simulations of X-Ray Beam Propagation Through Crl Transfocators Using Ray-Tracing and Wavefront Propagation Methods," in *Advances in Computational Methods for X-Ray Optics II* (International Society for Optics and Photonics, 2011), Vol. 8141, p. 814111.
150. M. Hand, H. Wang, F. Maccherozzi, M. Apollonio, J. Zhu, S. Dhesi, and K. Sawhney, "Quantitative Investigation of Linear Arbitrary Polarization in an Apple-II Undulator," J. Synchrotron Radiat. **25**, (2018).
151. E. Collett, "Mathematical Formulation of the Interference Laws of Fresnel and Arago," Am. J. Phys. **39**, 1483–1495 (1971).
152. N. Garcia and E. Stoll, "Monte Carlo Calculation for Electromagnetic-Wave Scattering from Random Rough Surfaces," Phys. Rev. Lett. **52**, 1798–1801 (1984).
153. G. Palasantzas, "Roughness spectrum and surface width of self-affine fractal surfaces via the K-correlation model," Phys. Rev. B **48**, 14472–14478 (1993).
154. P. P. Naulleau, C. N. Anderson, B. L. Fontaine, R. Kim, and T. Wallow, "Lithographic Metrics for the Determination of Intrinsic Resolution Limits in EUV

- Resists," in *Emerging Lithographic Technologies XI* (SPIE, 2007), Vol. 6517, pp. 796–801.
155. T. I. Wallow, J. Fu, J. Liang, J.-S. Wang, J. Fan, M. Delorme, C. Wang, F. Li, V. Jain, and R. Yuan, "Contour-based variability decomposition for stochastic band metrology," in *International Conference on Extreme Ultraviolet Lithography 2021*, K. G. Ronse, P. A. Gargini, E. Hendrickx, P. P. Naulleau, and T. Itani, eds. (SPIE, 2021), p. 42.
 156. I. Mochi, M. Vockenhuber, T. Allenet, and Y. Ekinci, "Open-Source Software for Sem Metrology," in *Photomask Technology 2020* (SPIE, 2020), Vol. 11518, pp. 58–67.
 157. C. Mack, *Fundamental Principles of Optical Lithography: The Science of Microfabrication* (John Wiley & Sons, Incorporated, 2007).
 158. C. A. Mack and F. Technologies, "Using the Normalized Image Log-Slope," *Microlithogr. World* **23**, 1–6 (2001).
 159. C. A. Mack, "Understanding Focus Effects In Submicron Optical Lithography," in *Optical/Laser Microlithography* (International Society for Optics and Photonics, 1988), Vol. 0922, pp. 135–148.
 160. A. F. Herrero, M. Pflüger, F. Scholze, and V. Soltwisch, "Fingerprinting the Type of Line Edge Roughness," in *Modeling Aspects in Optical Metrology VI* (SPIE, 2017), Vol. 10330, pp. 175–183.
 161. Z. Belete, P. D. Bisschop, U. Welling, and A. Erdmann, "Stochastic Simulation and Calibration of Organometallic Photoresists for Extreme Ultraviolet Lithography," *J. MicroNanopatterning Mater. Metrol.* **20**, 014801 (2021).
 162. L. S. Melvin and R. Jonckheere, "Contribution of Mask Defectivity in Stochastics of EUVL-Based Wafer Printing," *J. MicroNanopatterning Mater. Metrol.* **20**, 021003 (2021).
 163. P. Naulleau, B. McClinton, K. A. Goldberg, I. Mochi, and A. Rastegar, "Mask Roughness Challenges in Extreme Ultraviolet Mask Development," *J. Vac. Sci. Technol. B* **29**, 06F501 (2011).
 164. P. P. Naulleau and G. Gallatin, "Spatial Scaling Metrics of Mask-Induced Line-Edge Roughness," *J. Vac. Sci. Technol. B Microelectron. Nanometer Struct. Process. Meas. Phenom.* **26**, 1903–1910 (2008).
 165. P. P. Naulleau and S. A. George, "Implications of image plane line-edge roughness requirements on extreme ultraviolet mask specifications," in *Photomask and Next-Generation Lithography Mask Technology XVI* (SPIE, 2009), Vol. 7379, pp. 166–176.
 166. G. F. Lorusso, V. Rutigliani, F. Van Roey, and C. A. Mack, "Unbiased Roughness Measurements: Subtracting Out SEM Effects, Part 2," *J. Vac. Sci. Technol. B* **36**, 06J503 (2018).
 167. G. Papavarios, V. Constantoudis, and E. Gogolides, "Allowable Sem Noise for Unbiased LER Measurement," in *Metrology, Inspection, and Process Control for Microlithography XXXII* (SPIE, 2018), Vol. 10585, pp. 471–480.
 168. S. Lai and G. von Bally, "Fringe Contrast Evaluation by Means of Histograms," in *OPTIKA '98: 5th Congress on Modern Optics* (International Society for Optics and Photonics, 1998), Vol. 3573, pp. 384–387.
 169. J. Shin, G. Han, Y. Ma, K. Moloni, and F. Cerrina, "Resist Line Edge Roughness and Aerial Image Contrast," *J. Vac. Sci. Technol. B Microelectron. Nanometer Struct. Process. Meas. Phenom.* **19**, 2890–2895 (2001).
 170. M. D. Shumway, P. Naulleau, K. A. Goldberg, and J. Bokor, "Measuring Line

- Roughness Through Aerial Image Contrast Variation Using Coherent Extreme Ultraviolet Spatial Filtering Techniques," *J. Vac. Sci. Technol. B Microelectron. Nanometer Struct. Process. Meas. Phenom.* **23**, 2844–2847 (2005).
- 171. P. J. Bex and W. Makous, "Spatial Frequency, Phase, and the Contrast of Natural Images," *J. Opt. Soc. Am. A* **19**, 1096 (2002).
 - 172. R. Jyrki, R. Franssila, and R. Nasanen, "Contrast Sensitivity as a Function of Spatial Frequency, Viewing Distance and Eccentricity with and Without Spatial Noise," *Vision Res.* **32**, 631–637 (1992).
 - 173. J. K. Alexander, B. Fuss, and R. J. Colello, "Electric Field-Induced Astrocyte Alignment Directs Neurite Outgrowth," *Neuron Glia Biol. Camb.* **2**, 93–103 (2006).
 - 174. K. A. Goldberg, P. Naulleau, and J. Bokor, "Fourier Transform Interferometer Alignment Method," *Appl. Opt.* **41**, 4477–4483 (2002).
 - 175. "Photo Chemical Investigation and a New Method of Determination of the Sensitiveness of Photographic Plates," *J. Soc. Chem. Ind.* **9**, 455–469 (1890).
 - 176. V. Patrascu and V. V. Buzuloiu, "The Mean Dynamic Range Optimization in the Framework of Logarithmic Models," in *Advanced Topics in Optoelectronics, Microelectronics, and Nanotechnologies* (International Society for Optics and Photonics, 2003), Vol. 5227, pp. 73–80.
 - 177. D. Ong, S. Solanki, X. Liang, and X. xu, "Analysis of Laser Speckle Severity, Granularity, and Anisotropy Using the Power Spectral Density in Polar-Coordinate Representation," *Opt. Eng.* **51**, 4301 (2012).
 - 178. "Technical Information - Soft X-ray | ANSTO," <https://www.ansto.gov.au/user-access/instruments/australian-synchrotron-beamlines/soft-x-ray-spectroscopy/technical>.
 - 179. G. A. van Riessen, M. Junker, N. W. Phillips, and A. G. Peele, "A Soft X-Ray Beamline for Quantitative Nanotomography Using Ptychography," in *X-Ray Nanoimaging: Instruments and Methods* (International Society for Optics and Photonics, 2013), Vol. 8851, p. 885117.
 - 180. M. W. M. Jones, K. D. Elgass, M. D. Junker, M. D. de Jonge, and G. A. van Riessen, "Molar Concentration from Sequential 2-D Water-Window X-Ray Ptychography and X-Ray Fluorescence in Hydrated Cells," *Sci. Rep.* **6**, 24280 (2016).
 - 181. G. Kourousias, B. Bozzini, A. Gianoncelli, M. W. M. Jones, M. Junker, G. van Riessen, and M. Kiskinova, "Shedding Light on Electrodeposition Dynamics Tracked in Situ Via Soft X-Ray Coherent Diffraction Imaging," *Nano Res.* **9**, 2046–2056 (2016).
 - 182. B. C. C. Cowie, A. Tadich, and L. Thomsen, "The Current Performance of the Wide Range (90–2500 eV) Soft X-ray Beamline at the Australian Synchrotron," *AIP Conf. Proc.* **1234**, 307–310 (2010).
 - 183. K. P. Wootton and R. P. Rassool, "APPLE-II Undulator Magnetic Fields Characterised from Undulator Radiation," **4** (2013).
 - 184. O. Reichel and F. Mueller, "Functional Specification - SXR 2nd Branchline," (2011).
 - 185. G. LeBlanc, "Fact Sheet - Australian Synchrotron Light Source," (2020).
 - 186. V. Luong, V. Philipsen, E. Hendrickx, K. Opsomer, C. Detavernier, C. Laubis, F. Scholze, and M. Heyns, "Ni-Al Alloys as Alternative EUV Mask Absorber," *Appl. Sci.* **8**, 521 (2018).
 - 187. R. Kesarwani, P. P. Dey, and A. Khare, "Correlation Between Surface Scaling

- Behavior and Surface Plasmon Resonance Properties of Semitransparent Nanostructured Cu Thin Films Deposited Via PLD," RSC Adv. **9**, 7967–7974 (2019).
- 188. B. Haydon, "Evaluation of Photomask Material for 6.7 nm Interference Lithography," (2021).
 - 189. B. Haydon, J. Knappett, and G. van Riessen, "Evaluation of Photomask Absorber Materials for 6.7 nm EUV Lithography," Manuscr. Prep. (2022).
 - 190. G. N. Tran, G. A. van Riessen, and A. G. Peele, "Modal Approach for Partially Coherent Diffractive Imaging with Simultaneous Sample and Coherence Recovery," Opt. Express **25**, (2017).
 - 191. D. Fan, E. Buitrago, S. Yang, W. Karim, Y. Wu, R. Tai, and Y. Ekinci, "Patterning of Nanodot-Arrays Using EUV Achromatic Talbot Lithography at the Swiss Light Source and Shanghai Synchrotron Radiation Facility," Microelectron. Eng. **155**, 55–60 (2016).
 - 192. Y. Ekinci, T. Garvey, A. Streun, A. Wrulich, and L. Rivkin, "A High-Brightness Accelerator-Based EUV Source for Metrology Applications," in *Photomask Technology 2018* (SPIE, 2018), Vol. 10810, pp. 126–134.
 - 193. Yang Shumin, Wang Liansheng, Zhao Jun, Xue Chaofan, Liu Haigang, Xu Zijian, Wu Yanqing, and Tai Renzhong, "Developments at SSRF in Soft X-Ray Interference Lithography," Nucl. Sci. Tech. **26**, 7 (2015).
 - 194. S. A. George, P. P. Naulleau, I. Mochi, F. Salmassi, E. M. Gullikson, K. A. Goldberg, and E. H. Anderson, "Extreme Ultraviolet Mask Substrate Surface Roughness Effects on Lithographic Patterning," J. Vac. Sci. Technol. B **28**, C6E23-C6E30 (2010).
 - 195. "IRDSTM 2020: Lithography - IEEE International Roadmap for Devices and SystemsTM," <https://irds.ieee.org/editions/2020/lithography>.
 - 196. A. R. Hare and G. R. Morrison, "Near-field Soft X-ray Diffraction Modelled by the Multislice Method," J. Mod. Opt. **41**, 31–48 (1994).
 - 197. S. S. Ali, K. Li, M. Wojcik, and C. Jacobsen, "Zone Plate Performance as a Function of Tilt Analyzed via Multislice Simulations," Microsc. Microanal. Camb. **24**, 298 (2018).

Appendix

Multi-slice Scalar Wave Propagation

Multi-slice scalar wave propagation is a tool that has been successfully used to analyse the optical performance of X-ray focusing optics [123]. A three-dimensional object is represented as many layers of atoms, represented by voxels with position. Each voxel is assigned a complex refractive index with an absorption and transmission coefficient. A beam is generated as x-rays are either absorbed or scattered at each voxel [106,143].

The necessary thickness of a slice needed for multi-slice propagation, Δz , is dependent on the sampling rates ϵ_1 & ϵ_2 and the resolution Δx in the plane of the object being propagated through. It is given by [123]:

$$\Delta z = \frac{\epsilon_1}{\epsilon_2} \frac{\Delta x^2}{\lambda}.$$

7.1.1

Multi-slice propagation is suitable for any structure that can be defined by a three-dimensional refractive index distribution and has a greater scope than originally realised. Multi-slice can accurately represent complicated systems involving high aspect ratio gratings, Fresnel Zone plates tilted off-axis and flawed x-ray nanofocusing optics [123,193,194].

This method is included as a basis for identifying criterion for using a single-slice approximation of masks.

Propagation Parameters used for Propagation

Element	Propagator 	Do any resizing on fourier side, using FFT	Horizontal range modification factor at resizing 	Horizontal resolution modification factor at resizing	Vertical range modification factor at resizing	Vertical resolution modification factor at resizing	
WBS	0 - Standard		<input type="checkbox"/>	1	1	1	1
Drift 12.12m	1 - Quadratic Term		<input type="checkbox"/>	3	1	3	1
Toroidal Mirror	0 - Standard		<input type="checkbox"/>	2	1	2	1
Drift 3.38m	1 - Quadratic Term		<input type="checkbox"/>	1	1	1	1
Planar Mirror	0 - Standard		<input type="checkbox"/>	1	1	1	1
Drift 0.2m	1 - Quadratic Term		<input type="checkbox"/>	1	1	1	1
Grating	0 - Standard		<input type="checkbox"/>	2	1	2	1
Drift 1m	1 - Quadratic Term		<input type="checkbox"/>	3	1	3	1
Exit Aperture	0 - Standard		<input type="checkbox"/>	0.03	20	0.03	20
Drift 0.6m	1 - Quadratic Term		<input type="checkbox"/>	2	0.5	2	0.5
Cylindrical Mirror	0 - Standard		<input type="checkbox"/>	1	1	1	1
Drift 7m	1 - Quadratic Term		<input type="checkbox"/>	10	0.4	8	0.4
SSA	0 - Standard		<input type="checkbox"/>	0.7	8	0.7	8
Drift 9.7m	1 - Quadratic Term		<input type="checkbox"/>	1.2	1.5	0.05	3.2
BDA	0 - Standard		<input type="checkbox"/>	0.03	133.63	0.028	25
Mask	0 - Standard		<input type="checkbox"/>	1	1	1	1
Drift 0.0002m	1 - Quadratic Term		<input type="checkbox"/>	1	1	1	1
Final post- propagation	0 - Standard		<input type="checkbox"/>	1	1	1	1

Figure 7.1.1-A: Propagation parameters used for each element in the model including drifts between optical elements. Screenshot taken from SRW [17].